Universidad del País Vasco
Euskal Herriko Unibertsitatea

FACULTY OF SCIENCE AND TECHNOLOGY
UNIVERSITY OF THE BASQUE COUNTRY

FACULTY OF SCIENCE AND TECHNOLOGY

CHEMICAL ENGINEERING DEPARTMENT

EXPERIMENTAL DEVELOPMENT AND MODELING OF A MEMBRANE REACTOR FOR THE DIRECT SYNTHESIS OF DME WITH CO_2 VALORIZATION

PhD Thesis

Pablo Rodríguez Vega

Leioa, June 2019

Universidad del País Vasco Euskal Herriko Unibertsitatea

NAZIOARTEKO BIKAINTASUN CAMPUSA
CAMPUS DE EXCELENCIA INTERNACIONAL

AUTORIZACIÓN DE LOS DIRECTORES DE TESIS

PARA SU PRESENTACIÓN

Dr. **ANDRÉS T. AGUAYO URQUIJO** con N.I.F. 14703582G y el Dr. **JAVIER BILBAO ELORRIAGA** con N.I.F. 14548967H como Directores de la Tesis Doctoral: **EXPERIMENTAL DEVELOPMENT AND MODELING OF A MEMBRANE REACTOR FOR THE DIRECT SYNTHESIS OF DME WITH CO_2 VALORIZATION** realizada en el Programa de Doctorado de **INGENIERÍA QUÍMICA** por el Doctorando Don **PABLO RODRÍGUEZ VEGA**, autorizamos la presentación de la citada Tesis Doctoral, dado que reúne las condiciones necesarias para su defensa.

En Leioa a _____ de Junio de 2019

LOS DIRECTORES DE LA TESIS

Fdo.: **ANDRÉS T. AGUAYO URQUIJO** Fdo.: **JAVIER BILBAO ELORRIAGA**

Universidad del País Vasco Euskal Herriko Unibertsitatea

NAZIOARTEKO BIKAINTASUN CAMPUSA
CAMPUS DE EXCELENCIA INTERNACIONAL

AUTORIZACIÓN DE LA COMISIÓN ACADÉMICA DEL PROGRAMA DE DOCTORADO

La Comisión Académica del Programa de Doctorado en **INGENIERÍA QUÍMICA** en reunión celebrada el día ___de Junio de 2019, ha acordado dar la conformidad a la presentación de la Tesis Doctoral titulada: **EXPERIMENTAL DEVELOPMENT AND MODELING OF A MEMBRANE REACTOR FOR THE DIRECT SYNTHESIS OF DME WITH CO_2 VALORIZATION** dirigida por el Dr. **ANDRÉS T. AGUAYO URQUIJO** y el Dr. **JAVIER BILBAO ELORRIAGA** y presentada por Don **PABLO RODRÍGUEZ VEGA** adscrito o adscrita al Departamento de **INGENIERÍA QUÍMICA**.

En _____a _____de _____de _____

EL/LA RESPONSABLE DEL PROGRAMA DE DOCTORADO

Fdo.: _____

Universidad del País Vasco Euskal Herriko Unibertsitatea

NAZIOARTEKO BIKAINTASUN CAMPUSA
CAMPUS DE EXCELENCIA INTERNACIONAL

AUTORIZACIÓN DEL DEPARTAMENTO

El Consejo del Departamento de **INGENIERÍA QUÍMICA** en reunión celebrada el día ___ de Junio de 2019 ha acordado dar la conformidad a la admisión a trámite de presentación de la Tesis Doctoral titulada: **EXPERIMENTAL DEVELOPMENT AND MODELING OF A MEMBRANE REACTOR FOR THE DIRECT SYNTHESIS OF DME WITH CO_2 VALORIZATION** dirigida por el Dr. **ANDRÉS T. AGUAYO URQUIJO** y el Dr. **JAVIER BILBAO ELORRIAGA** y presentada por Don **PABLO RODRÍGUEZ VEGA** ante este Departamento.

En Leioa a _____ de Junio de 2019

VºBº DIRECTOR DEL DEPARTAMENTO	SECRETARIO DEL DEPARTAMENTO

Fdo.: **ROBERTO AGUADO ZARRAGA** Fdo.: **RUBÉN LÓPEZ FONSECA**

Universidad del País Vasco Euskal Herriko Unibertsitatea

NAZIOARTEKO BIKAINTASUN CAMPUSA
CAMPUS DE EXCELENCIA INTERNACIONAL

ACTA DE GRADO DE DOCTOR O DOCTORA
ACTA DE DEFENSA DE TESIS DOCTORAL

DOCTORANDO DON **PABLO RODRÍGUEZ VEGA**

TITULO DE LA TESIS: **EXPERIMENTAL DEVELOPMENT AND MODELING OF A MEMBRANE REACTOR FOR THE DIRECT SYNTHESIS OF DME WITH CO_2 VALORIZATION**

El Tribunal designado por la Comisión de Postgrado de la UPV/EHU para calificar la Tesis Doctoral arriba indicada y reunido en el día de la fecha, una vez efectuada la defensa por el doctorando y contestadas las objeciones y/o sugerencias que se le han formulado, ha otorgado por_____la calificación de:

unanimidad ó mayoría

SOBRESALIENTE / NOTABLE / APROBADO / NO APTO

Idioma/s de defensa (en caso de más de un idioma, especificar porcentaje defendido en cada idioma): Inglés

En Leioa a _____de _____de _____

EL/LA PRESIDENTE/A,

Fdo.:
Dr/a:_____

EL/LA SECRETARIO/A,

Fdo.:
Dr/a:_____

VOCAL 1º,

Fdo.:
Dr/a:_____

VOCAL 2º,

Fdo.:
Dr/a:_____

VOCAL 3º,

Fdo.:
Dr/a:_____

EL DOCTORANDO,

Fdo.: _____

Este trabajo ha sido posible gracias a la financiación del Ministerio Economía y Competitividad (Proyectos CTQ2013-46173-R y CTQ2016-77812-R).

De igual modo, agradecer a los *Servicios Generales de Investigación* (SGIker) de la UPV/EHU y a los *Servicios Centrales de Apoyo a la Investigación* (SCAI) de la UMA por su aportación a este trabajo.

Contents

ABSTRACT

Abstract

The direct synthesis of dimethyl ether (DME) has been studied from $H_2 + CO + CO_2$ systems with a packed bed membrane reactor (PBMR). The experimental work for the design and tuning of the reactor has consisted in the following steps: selection of the suitable material for the membrane based on its characterization; development of a reproducible method of the crystallization of the zeolite on a porous support; configuration of the membrane reactor system in the laboratory; adaptation of the chromatographic analysis equipment of the new experimental system.

The experiments with the conventional (PBR) and membrane (PBMR) reactors have been carried out at the following reaction conditions: 10 - 40 bar; 250 - 350 °C; space time, until 10 $g_{cat}\,h\,(mol_C)^{-1}$; feed, $CO_2/(CO+CO_2)$ ratio, 0 - 1; $H_2/(CO+CO_2)$ ratio, 3; time on stream, until 5 h. Based on the results, the improvement of the performances with regard to the conventional reactor (PBR) has been evaluated. This enhancement is justified by the alteration of the thermodynamic equilibrium, due to the permeation of medium reaction components and the resulting change of the composition in the reactor.

The used catalyst was CuO-ZnO-ZrO_2/SAPO-11 and it has been characterized by different techniques: N_2 adsorption-desorption; scanning electron microscopy

(SEM); inductively coupled plasma optical emission spectroscopy (ICP-OES); X-ray diffraction (XRD); temperature programmed reduction (TPR); TPR / N_2O chemisorption; temperature programmed desorption (TPD) of NH_3 and thermogravimetry and calorimetry of NH_3 adsorption. Its performance has been quantified, within the aforementioned range of conditions, with a kinetic model determined for a PBR that considers the individual steps of the reaction scheme (methanol and DME synthesis from CO and CO_2, methanol dehydration towards DME, water gas shift (WGS) reaction and paraffins formation), as well as the catalyst deactivation (mainly by coke deposition). The accurate adjustment of the kinetic model and its capacity to predict the evolution with time on stream of the components distribution has been proven, through the whole considered range of conditions.

An original mathematical model has been established for the simulation of the PBMR, with LTA as selected membrane. The simulation model considers both the equations of the kinetic model and the mass transport of each component between the reaction and permeate sections. This model has been employed firstly to determine the transport properties in the membrane, through experiments without catalyst in the reaction section. Secondly, the simulation of the PBMR has been performed with the kinetic parameters along with the membrane transport ones, previously calculated. The advantages of the PBMR in comparison with the PBR have been evaluated for DME and oxygenates (methanol and DME) production and CO_2 conversion, and demonstrating the capacity of the simulation model on scale-up studies and future analysis of the optimization of sweeping and recirculation strategies.

OBJECTIVES

Objectives

The overall objective of this thesis is the experimental development and modeling of an original catalytic membrane reactor, at lab-scale, for the direct synthesis of dimethyl ether (DME) from synthesis gas, carbon dioxide and their mixtures.

The principal originality of this work is based on the lack of experimental precedents for the employment of a membrane reactor in this process. This absence can be mainly attributed to the difficulty of preparing a hydrophilic membrane, which should be stable under high pressure (over 30 bar) and in the temperature range between 200 - 325 °C, required conditions in DME synthesis.

With this initiative the continuation of over 20 years group investigation on the direct synthesis of DME is provided, as an attractive route for the production of this oxygenate (alternative to methanol as fuel and raw material). This direct synthesis route on a bifunctional catalyst requires only one reactor and presents remarkable thermodynamic advantages regarding methanol synthesis, facilitating the use of synthesis gas derived from different sources (carbon, natural gas and biomass) and CO_2 valorization, co-fed with synthesis gas. It is precisely this capacity of the process, for CO_2 valorization towards a product of commercial interest, what has promoted its development, given the urgent necessity of reducing the emissions of this greenhouse gas.

Consequently, in parallel to the vision of the process on the international stage, the focus of the investigation group has evolved, progressively contributing to the development of the bifunctional catalyst through the design of new functions (metallic and acid). Furthermore, improving the combination of these functions to obtain active catalysts, selective and stable, with conventional (hybrid) and core-shell configurations. The kinetic model has been also developed, considering the catalyst deactivation, as well as the simulation of isothermal fixed bed reactors.

The interest of the hydrophilic membrane reactor is based on the advantages of the selective separation of water from the reaction medium, as a strategy to displace the thermodynamic equilibrium of the steps of methanol synthesis and its dehydration towards DME. These advantages have been studied through simulation in the bibliography by different authors and also by the group where this thesis has been carried out, but without an experimental implementation.

From the previous experience of the group to achieve the objective of the development of the membrane reactor, the work has been programmed to complete successively the following specific objectives:

- Preparation and characterization of the different alternative membranes, selected based on the literature and in collaboration with the Yamaguchi University (Japan). This stage of the Thesis was performed at this University, where the author of this Thesis carried out his predoctoral stay, and it was continued at the home University applying the acquired knowledge.
- Fine-tuning, adjusting procedures described in the literature, of an adequate technology to prepare and crystallize a zeolite on the outer surface of a metallic cylindrical support, as well as the sealing of the membrane-reactor surface.

- Implementation of the original lab-scale system, adapting an equipment, designed for conventional fixed bed reactors, to the requirements of a reactor with reaction (catalytic fixed bed) and permeate sections. Hence, it is necessary to readjust the feeding systems and flows control, as well as the sample collection and products flow analysis.
- Preparation and characterization of a hybrid catalyst of CuO-ZnO-ZrO_2 / SAPO-11 for DME synthesis. This stage of the study was based on the previous knowledge of the group in the preparation of this catalyst, which was selected due to its activity, selectivity (with minimal paraffins yield), stability and capacity for CO_2 conversion.
- Kinetic modeling of DME synthesis with CuO-ZnO-ZrO_2 / SAPO-11 catalyst within a wide range of conditions (pressure, temperature, space time, CO_2 / ($CO + CO_2$) and H_2 / ($CO + CO_2$) ratio in the feed, and time on stream, in order to consider the deactivation).
- Development of a design model of the membrane reactor that integrates, on one side, the components transport equations from the reaction medium through the membrane and, on the other side, the kinetic model.
- Calculation of the transport parameters of the membrane through the implementation of the simulation model of the membrane reactor, and operating without reaction (in absence of catalyst).
- Validation of the design model with experimental results.
- Application through simulation of the model, in order to study the effect of the process conditions. Moreover, this implementation enables the comparison of the membrane reactor performance and the conventional fixed bed one for DME production and CO_2 conversion, as main objectives of interest, and additionally for studies oriented to the scale-up.

LIST OF FIGURES

List of Figures

1 Introduction

2 Experimental

3 Kinetic Modeling

LIST OF TABLES

List of Tables

I

1

INTRODUCTION

1 Introduction

At the present time, the anthropogenic emissions of CO_2, derived from the combustion of fossil fuels, correspond to the following different sectors worldwide (Alper and Orhan, 2017): power generation (42 %), transport (23 %), industrial production and construction (20 %), and other sectors (including the residential one) (15 %). Due to the increasing estimates of CO_2 emissions, up to 43 GT by 2030 and CO_2 concentration of 570 ppm by the end of the 21st century, and given the serious consequences of the derived climate change (which leads to deforestation) for humankind, various commitments have been adopted by the developed countries (Kyoto Protocol and Paris Agreement among others). These agreements are focused on the mitigation of emissions, strengthening the efficient use of energy, the circular economy, rational symbiosis of the industrial development and the preservation of the natural environment as the main strategies, along with the progressive substitution of fossil fuels for renewable sources. More recent is the initiative for normalizing the automotive fuels based on its environmental impact. In these initiatives aimed at the reduction of mobile sources emissions (automotive and transport vehicles), the European Union has taken the lead regarding the severity of the measures that are adopted, having a major bearing on the automotive and oil industry. Therefore, in the year 2016 has been established the deadline of 2020

for reducing the CO_2 emissions by 20 % compared to 1990 levels, and further more ambitious targets are to be considered (Global Greenhouse Gas Emissions Data). Unfortunately, these before described initiatives do not progress as planned given the urgency and magnitude of the problem. The causes that may hinder its implementation are mainly socioeconomic factors, such as the increased industrial activity in the developed countries, the difficulties transitioning away from the oil economy and the recent discovery of fossil fuel deposits, particularly of natural gas.

In this scenario, a deep transition period towards a zero-emissions energetic model, based on the main utilization of renewable energy sources, may be expected. It is essential, therefore, to promote the implementation of CO_2 capture and storage technologies (CCS). Since the current capacity of these strategies is limited up to 14 % of CO_2, its capture and utilization (CCU) and the integration of both concepts (CCUS) should be progressed, which is described in Figure 1.1.

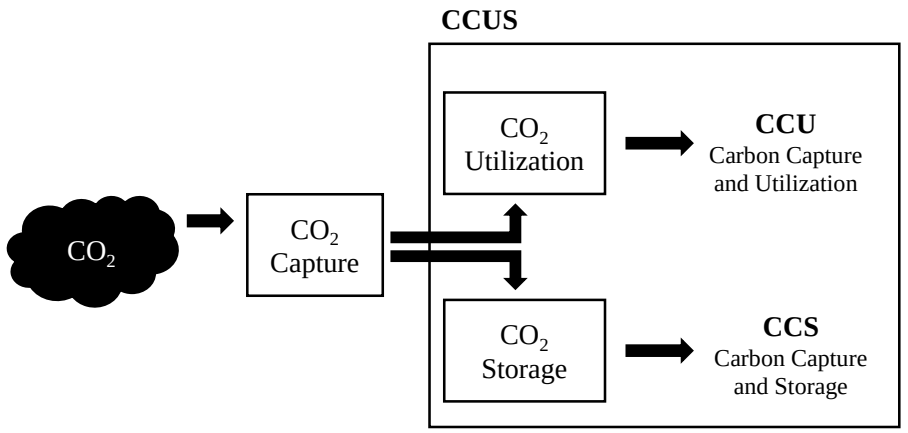

Figure 1.1: Integration of CO_2 capture, utilization and storage (CCUS) concepts (Alper and Orhan, 2017).

The integration of CO_2 capture and storage units (with high costs) and CO_2 valorization systems towards products of commercial interest, through net energy

generation processes, is key for the viability of CCUS strategies (Dutta et al., 2017). Among these strategies, Luu et al. (2016) have studied the integration of CO_2 geologic storage (energy production from natural gas) with its utilization in the intensification of natural gas extraction and methanol synthesis. This integration concept permits in Iceland the reutilization of 5500 t / year using H_2 obtained through H_2O electrolysis (Rafiee et al., 2018). The unification of non-fossil energy generation technologies (like solar energy) for the disassociation of H_2O from CO_2, allows the reduction of CO_2 net emission within the integrated processes (Chen et al., 2016a).

CO_2 capture technologies can be classified (Leonzio, 2018) into:

- *Absorption*: CO_2 is absorbed in a liquid solvent, either through solubility or by formation of a chemical bond, using packed bed towers, tray towers, bubble columns, spray columns or rotating packed beds. The solvent is conducted to a section where CO_2 is released by heating, so that it can be reutilized in successive absorption cycles. The solvent should have the following properties: high reactivity and absorptivity towards CO_2, great thermal and chemical stability, low vapor pressure, regenerability and low environmental impact. As physical adsorbents rectisol, selexol and purisol are used. However, the chemical absorption capacity is higher, under low CO_2 partial pressure, through amines (MEA, DEA, MDEA, DIPA, AMP, PZ, EDA, TEPA, DETA, HAD, DMEA), mixtures (MDEA-DEA, AMP-PZ, AMP-DEA), ionic liquids, aqueous solutions (K_2CO_3, CaO, DMC) and NH_3. Some of the advantages of the amines are their low cost, highlighting MEA reactivity (the most used one due to its capacity for retaining even CO_2 traces) and the AMP-PZ mixture (2-amino-2-methyl-1-propanol / piperazine), easily regenerable. On the contrary, the disadvantages are:

1) the addition of H_2O into the medium requires a dehydration step of the treated gas, which demands a high energetic cost; 2) the environmental impact of the degradation products.

- *Ionic liquids (ILs) (ions with melting point below 100 °C)*: These liquids have a low volatility, a wide temperature range in liquid phase, high thermal and chemical stability and adjustable physical-chemical properties. The difficulties, in contrast, are their high viscosity, elevated cost, their complicated preparation and the great energetic requirements for their regeneration.
- *Membranes*: Membrane separation equipments for CO_2 gas flows offer the following advantages: absence of solvents, modular and scalable compact configuration, flexibility within the operation conditions and their applicability in remote regions. The different types of membranes are microporous, dense (ceramic or polymeric) and liquid supported (MEA, DEA, MDEA, AMP, among others).
- *Molten carbon fuel cells (MCFC)*: On the anode H_2 (used as energetic vector) is oxidized producing CO_2 and H_2O (Eq. 1.1), meanwhile, on the cathode O_2 is reduced with CO_2 forming carbonate ions (Eq. 1.2). Overall (Eq. 1.3), CO_2 is separated on the cathode and concentrated on the anode. This CO_2 concentration is an advantage in comparison with other CCS strategies.

$$H_2 + {CO_3}^{2-} \longrightarrow CO_2 + H_2O + 2e^- \tag{1.1}$$

$$\frac{1}{2}O_2 + CO_2 + 2e^- \longrightarrow {CO_3}^{2-} \tag{1.2}$$

$$\frac{1}{2}O_2 + H_2 + CO_2\,(\text{cathode}) \longrightarrow CO_2\,(\text{anode}) + H_2O \tag{1.3}$$

- *Cryogenic separation*: Due to the high cost of the energetic requirements for both compression and refrigeration, this technology is limited to high

pressure flows and high CO_2 concentrations. Particularly interesting is the combination with a separation membrane for a CO_2 previous preconcentration.

- *Mineralization*: Within the carbonation reaction, CO_2 is converted to ${CO_3}^{2-}$ releasing energy. The calcium sulfoaluminate carbonation in cement or fly ashes turns out to be very interesting, considering its scale-up possibilities (Jang et al., 2016).

The main strategies that are employed for the capture of CO_2 are "physical". Either it can be injected directly into carbonated beverages and, at a major scale, into oil and natural gas deposits (increasing the production up to 15 %), or using it as solvent, due to its high solubility in supercritical state (Dai et al., 2013). CO_2 can also be used as coolant, for the production through photosynthesis of microalgae or as gas-producing agent in the active carbons production. The valorization of CO_2 on a large scale, nonetheless, is more interesting through its "chemical" routes, converting CO_2 into fuels and raw materials. The stability of CO_2 may not be interpreted as no reactivity and that a considerable energetic requirement would be necessary for its conversion. Nonetheless, CO_2 is a carbon and oxygen source in the chemical synthesis of numerous compounds and its valorization is an opportunity for the development of new sustainable catalytic processes. Styring and Armstrong (2011) have classified CO_2 conversion reactions into: 1) reduction; 2) insertion; 3) condensation, and; 4) addition.

These CO_2 valorization chemical processes are, on the other hand, classified based on their energetic requirements (Alper and Orhan, 2017). Thus, the carboxylation reactions do not demand a high energy input, where CO_2 is incorporated within the structure of another reactant producing carboxylates and lactones (RCOOR), carbamates ($R_1R_2NCOOR_3$), ureas (RRNCONRR), isocyanates (RNCO), and car-

bonates (ROC(O)OR). In contrast, the reactions that require a great energy demand are the ones involved in the production of CO, CH_4, CH_3OH, DME, formates ($HCOO^-$), oxalates ($[C(O)O]^{2-}$), formaldehydes (H_2CO) or hydrocarbons. This external energy source can be thermal, electrocatalytic or photocatalytic, providing opportunity to the processes to be intergrated with renewable energy production (solar, wind and marine). The same authors have distinguished CO_2 conversion processes attending to their technology state: 1) consolidated, like the urea production (110 Mt / year), methanol (2.5 Mt / year), cyclic carbonates (0.05 Mt / year) and salicylic acid (0.03 Mt / year); 2) emerging, like methane dry reforming, formic acid production, polymers and fuels (hydrocarbonated and dimethyl ether (DME)); 3) at laboratory-scale research stage, like the isocyanates synthesis, organic carbonates, lactone and carboxylic acid. Furthermore, also emerging are the biotechnological routes of methanol production, carboxylates, urea and esters through RuBisCO (Ribulose Bisphosphate Carboxylase Oxidase) subject to genetic modifications (Aresta et al., 2005), and the utilization of plasma technologies.

1.1 Catalytic processes for CO_2 conversion

The different catalytic and electrocatalytic processes for CO_2 conversion into fuels and chemical products have been reviewed several times (Alper and Orhan, 2017; Homs et al., 2013; Leonzio, 2018; Rafiee et al., 2018), and these are schematized in Figure 1.2. It can be observed that some products are, at the same time, raw materials for other processes. Thus, oxygenates (methanol and DME) with interest as fuels, are converted into olefins (MTO and DTO processes) or into hydrocarbons in the range of the boiling point of gasoline pool (MTG and DTG processes), and are additionally hydrogen vectors (through reforming). Moreover, methanol can

be selectively dehydrogenated towards formaldehyde, which will be used in the polymers and resin production.

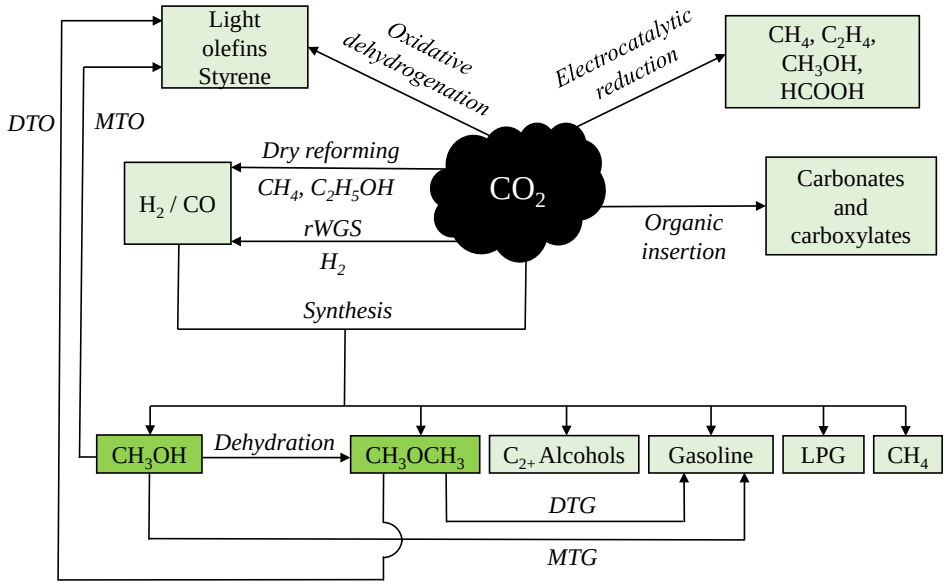

Figure 1.2: Catalytic and electrocatalytic routes to obtain fuels and raw materials from CO_2.

CO_2, furthermore, allows the production of synthesis gas (H_2 / CO) through rWGS reaction (where CO_2 takes the role of H_2 acceptor) or by dry reforming of methane, hydrocarbons or oxygenates (where CO_2 acts as oxidant agent). In addition, synthesis gas is converted into a hydrocarbons mixture, either through Fischer-Tropsch (FT) or with MeOH / DME as intermediates. In this latter case, for the selective production of C_{2+} alcohols or isoparaffinic gasoline. The characteristics of CO_2 conversion processes, which have received greater interest, are described next in more detail.

1.1.1 Oxidative dehydrogenation

1.1.1.1 Methane

The direct conversion of methane into ethane (Eq. 1.4) or into ethylene, (Eq. 1.5) through oxidative coupling (OCM) forming C-C bonds, has a growing interest in valorizing burgeoning natural gas reserves. Moreover, CH_4 valorization, co-responsible of the *greenhouse effect*, contributes to mitigate the climate change.

$$2\,CH_4 + CO_2 \longrightarrow CH_3CH_3 + CO + H_2O \qquad \Delta H^0 = 62.1\,KJ\,mol^{-1} \qquad (1.4)$$

$$2\,CH_4 + 2\,CO_2 \longrightarrow CH_2CH_2 + 2\,CO + 2\,H_2O \qquad \Delta H^0 = 196.2\,KJ\,mol^{-1} \qquad (1.5)$$

These reactions occur through the following mechanism (Carlos Colmenares, J., 2010): 1) cleavage of methane C-H bonds in the active sites of the catalyst, forming $CH_3\cdot$ and $CH_2\cdot$ radicals; 2) dissociation of CO_2 towards CO and oxygen atoms; 3) coupling of these radicals; 4) recombination of $CH_3\cdot$ and $CH_2\cdot$ radicals; 5) dehydrogenation, either oxidative or radical, of ethane to ethylene.

The catalysts used are strong basic metallic oxides and they can be grouped into (Aresta et al., 2016): 1) pure oxides of the lanthanide series, of which La_2O_3 performance is the greatest; 2) basic oxides loaded with Group 1 or 2 cations (Li / MgO, Ba / MgO, and Sr / La_2O_3); 3) transition metal oxides that contain Group 1 cations, and; 4) redox catalysts, like CeO_2 modified by Group 1 and 2 cations.

1.1.1.2 Paraffins

The production of olefins (ethylene, propylene and butenes) through oxidative dehydrogenation of their corresponding paraffins (Eq. 1.6), represents an added value

for them. In this manner, raw materials are obtained in the production of polyolefins and, at the same time, avoiding the high energetic requirement of steam cracking, as well as the rapid deactivation of the catalyst due to coke deposition (attenuated by the gasification capactiy of CO_2).

$$C_nH_{n+2} + CO_2 \longrightarrow C_nH_n + CO + H_2O \tag{1.6}$$

It should be pointed out that the dehydrogenation of C_{5+} paraffins is not viable due to the rapid catalyst deactivation by coke deposition.

The most studied catalysts are based on redox properties, principally MoO_3, Cr_2O_3 and V_2O_5. The basic character of these materials favors CO_2 adsorption and olefins desorption. CeO_2 (with well-established redox properties), ZrO_2, TiO_2, SiO_2 and zeolites (HZSM-5, MCM-41) have been used as supports. Paraffins are activated by the presence of acid sites, and hence, their dehydrogenation. The mesoporosity of the support (MCM-41, SBA-15) favors the metallic oxide dispersion (Liu et al., 2004).

Paraffins dehydrogenation mechanism (Zheng et al., 2005) considers rWGS (Eq. 1.8) where H_2, product of the dehydrogenation, is oxidized by CO_2. Furthermore, paraffin dry reforming (Eq. 1.10) and coke deposits oxidation through Boudouard reaction (Eq. 1.11) are considered.

$$C_nH_{n+2} \longleftrightarrow C_nH_n\,H_2 \tag{1.7}$$

$$H_2 + CO_2 \longleftrightarrow CO + H_2O \tag{1.8}$$

$$C_nH_{n+2} + CO_2 \longrightarrow C_nH_n + CO + H_2O \tag{1.9}$$

$$C_nH_{n+2} + 2\,CO_2 \longrightarrow 4\,CO + 3\,H_2 \tag{1.10}$$

$$CO_2 + C \longleftrightarrow CO \tag{1.11}$$

Michorczyk et al. (2012) have proposed the following mechanism for Cr, which is dehydrogenated during the reaction to CrO_{x-1} and oxidized (regenerated) towards CrO_x:

$$C_3H_8 + CrO_x \longleftrightarrow CrO_{x-1} + C_3H_6 + H_2O \tag{1.12}$$

$$CO_2 + CrO_{x-1} \longleftrightarrow CO + CrO_x \tag{1.13}$$

$$H_2 + CrO_x \longleftrightarrow CrO_{x-1} + H_2O \tag{1.14}$$

1.1.1.3 Ethylbenzene

The oxidative dehydrogenation of ethylbenzene (EB) to styrene (ODE) is of great interest to avoid selectivity limitations and catalyst deactivation by coke in the conventional industrial process, which requires a vapor excess. ODE with CO_2 as dehydrogenating agent, with the described steps in Eqs. 1.15 - 1.17, shows a styrene selectivity of 97 % and demands approximately a tenth of the energetic requirement compared to the conventional process. Therefore, it offers an attractive option for satisfying the growing demand of styrene (yearly production of 14.6 Mt) in the production of synthetic rubber, polystyrene and styrene-acrylonitrile copolymers.

$$C_6H_5CH_2CH_3 + CO_2 \longrightarrow C_6H_5CH{=}CH_2 + H_2O + CO \tag{1.15}$$

$$C_6H_5CH_2CH_3 \longrightarrow C_6H_5CH{=}CH_2 + H_2 \tag{1.16}$$

$$H_2 + CO_2 \longrightarrow CO + H_2O \tag{1.17}$$

The sintering of Fe based catalyst has been reduced with the addition of Ti, Al or Zr. In the case of Ti, it shows a greater result leading to stable phases of $FeTiO_3$,

Fe_2TiO_5 and $FeTi_2O_5$, albeit with an increase in the coke formation (Castro et al., 2013). The incorporation of Mg and Al allows the formation of $MgFe_{0.1}Al_{0.9}O_4$ spinel, stable against sintering and with an activity favored by the presence of Lewis sites (Zhu et al., 2004). Fe/CeO_2 catalyst has a high activity attributable to the redox activity of the Ce sites (changing Ce^{4+} and Ce^{3+}), promoted by Fe^{3+} and whose presence improves the Ce storage capacity of oxygen (Reddy et al., 2012). The importance of both the redox efficiency and the mesoporous structure of the support has been proven using CeO_2-ZrO_2 supported on SBA-15 (Burri et al., 2007). Vanadium catalysts have been also studied, on one hand, supported on microporous zeolite (MCM-41) and, on the other hand, supported on active carbon incorporated in hydrotalcite (Mg-V-Al structures). With this latter Yoshihiro et al. (2000) obtained a EB conversion of 67.1 % and a styrene selectivity of 80 %.

Different mechanisms have been proposed for ODE from EB, considering the three steps mechanism the most thermodynamically favorable (Liu et al., 2011):

$$C_8H_{10} + \circ \longleftrightarrow C_8H_{10}{}^{\circ} \tag{1.18}$$

$$C_8H_{10}{}^{\circ} + \bullet \longrightarrow C_8H_8{}^{\bullet} + 2\,H^{\circ} \tag{1.19}$$

$$H^{\circ} + H^{\circ} \longrightarrow H_2 + 2\circ \tag{1.20}$$

$$CO_2\,(g) + O^{\bullet} \longleftrightarrow CO\,(g) + O^{\bullet} \tag{1.21}$$

$$H_2\,(g) + O^{\bullet} \longleftrightarrow H_2O\,(g) + \bullet \tag{1.22}$$

$$C_8H_8{}^{\bullet} \longrightarrow C_8H_8 + \bullet \tag{1.23}$$

where $\circ$ = oxidizing sides and $\bullet$ = reducing sites.

1.1.2 Methane dry reforming

Methane dry reforming (DRM) produces synthesis gas with a lower H_2 / CO ratio than steam reforming (SRM), which is the main H_2 production process at industrial scale. For this reason, its interest resides in the CO_2 conversion achieved in parallel to the production of H_2. The reaction steps are: methane reforming (Eqs. 1.24 and 1.25), rWGS (Eq. 1.26), gasification of the deposited coke (C) (Eq. 1.27), and the steps of the formation of this coke (that deactivates the catalyst), which are the methane decomposition (Eq. 1.28) and Boudouard reaction (Eq. 1.29):

$$CO_2 + CH_4 \longleftrightarrow 2\,CO + 2\,H_2 \tag{1.24}$$

$$CH_4 + H_2O \longleftrightarrow CO + 3\,H_2 \tag{1.25}$$

$$CO_2 + H_2 \longleftrightarrow CO + H_2O \tag{1.26}$$

$$C + H_2O \longleftrightarrow CO + H_2 \tag{1.27}$$

$$CH_4 \longleftrightarrow C + 2\,H_2 \tag{1.28}$$

$$2\,CO \longleftrightarrow C + CO_2 \tag{1.29}$$

The main limitations of DRM are the high energetic requirement, inherent in the endothermicity of the reforming steps (reaction heats of the reactions in Eqs. 1.24 and 1.25 are 247 kJ·mol^{-1} and 228 kJ·mol^{-1}, respectively), and the catalyst stability, affected by sintering and coke formation. This coke formation is quite rapid in Ni catalysts, industrially used as a result of their high activity and low cost. The energetic demand is reduced and, moreover, the coke formation is attenuated combining DRM with SRM and POM (methane partial oxidation). For that purpose, accordingly to the tri-reforming concept, methane is co-fed with H_2O and

O_2 (Song and Pan, 2004). Numerous efforts have been performed to improve the stability of Ni catalysts in DRM on their different conformations: supported oxides, incorporated within perovskites or with bifunctional structures, spinel and core shell. Consequently, the stability has been enhanced through the incorporation of oxides (La_2O_3, MgO, BaO, CaO, Ga_2O_3) that promote Ni dispersion, metal-support interaction and dispersion of oxygen.

Noble metal catalysts show a higher activity and stability. Comparing the results with supported catalysts on MgO-Al_2O_3, Rezaei et al. (2006) have determined the following activity order: Rh $\geq$ Ru $>$ Ir $>$ Pt $>$ Pd. On the other hand, the effect of the support in the activity of Rh catalysts follows the order: $Al_2O_3 > TiO_2 > SiO_2 >$ MgO (Hou et al., 2006).

Ni perovskite-type catalysts (ABO_3, where A is a lanthanide and B a transition metal) exhibit a great thermal stability (Sutthiumporn et al., 2012), as well as La_2NiO_4. With an spinel-like structure, Sierra Gallego et al. (2008) have obtained methane and CO_2 conversions of 85 % and 93 %, respectively, in DRM at 700 °C, with an insignificant coke deposition for 160 h. It is well established that the high dispersion of Ni favors the metal-support interaction and minimizes sintering, as Corma et al. (2000) have proven with Ni / ITQ-6, in which Ni is dispersed in nanoparticles. Core-shell configuration was also found by Li et al. (2014b) to be effective against Ni sintering using Ni@SiO_2. Furthermore, Mo et al. (2014) have proposed a reproducible method for the preparation of these catalysts.

Different mechanisms have been developed for DRM, usually Langmuir-Hinshelwood type. These consider the main steps of methane and CO_2 dissociation (or activation), followed by the intermediates adsorption in the active sites, resulting in the formation of products (CO, H_2 and H_2O), which are desorbed. The controlling

steps of the reaction are those of the dissociation of methane (Eqs. 1.30 - 1.33) and CO_2.

$$CH_4\,(g) \longrightarrow CH_3\,(a) + H\,(a) \tag{1.30}$$

$$CH_3\,(g) \longrightarrow CH_2\,(a) + H\,(a) \tag{1.31}$$

$$CH_2\,(a) \longrightarrow CH\,(a) + H\,(a) \tag{1.32}$$

$$CH\,(g) \longrightarrow C\,(a) + H\,(a) \tag{1.33}$$

These reaction steps are considered to be proceeding on the metallic sites, even though the support acid sites have a synergetic effect on the successive cracking towards adsorbed (a) species. Furthermore, the adsorbed coke species on the support contribute to the deactivation of the catalyst. On a deactivated catalyst three types of coke can be distinguished (Rostrup-Nielsen, 1994): 1) the so-called whisker type formed over 723 K; 2) amorphous and encapsulating of Ni sites, which is formed below 773 K, and; 3) filamentous and graphitic, along with the presence of carbon nanotubes, produced over 873 K.

The second step, CO_2 dissociation, for a Ni catalyst supported on SiO_2 or on an acid support, occurs with the formation of an anionic precursor of adsorbed CO_2 (Eq. 1.34), from which an oxygen atom is dissociated (Eq. 1.35). This adsorbed oxygen reacts either with the methyl radicals formed in the methane dissociation (Eq. 1.36), or the adsorbed hydrogen atoms (Eq. 1.37). Aditionally, H_2O is formed (Eq. 1.38), and H_2 (Eq. 1.39) and CO (Eq. 1.40) are released (Bradford and Vannice, 1999).

$$CO_2\,(g) \longleftrightarrow CO_2\,(a) \tag{1.34}$$

$$CO_2\,(a) \longleftrightarrow CO\,(a) + O\,(a) \tag{1.35}$$

$$CH_x\,(a) + O\,(a) \longrightarrow CO\,(a) + xH\,(a) \tag{1.36}$$

$$H\,(a) + O\,(a) \longrightarrow OH\,(a) \tag{1.37}$$

$$H\,(a) + OH\,(a) \longleftrightarrow H_2O\,(a) \tag{1.38}$$

$$2\,H\,(a) \longrightarrow H_2\,(g) \tag{1.39}$$

$$CO\,(a) \longrightarrow CO\,(g) \tag{1.40}$$

It should be firstly noted that coke is considered to be formed from a CO excess adsorbed on the metallic sites. And secondly, that the presence of oxygen adsorption promotors favors its gasification, attenuating the deactivation. Also the presence of H_2O contributes to the gasification of coke:

$$C + H_2O \longleftrightarrow CO + H_2 \tag{1.41}$$

From an energetic efficiency point of view, dry reforming technology through "chemical looping" is very encouraging. It takes place along the methane reduction steps with the metallic oxide (Eq. 1.42), CO_2 reduction (Eq. 1.43) and oxidation of the metal with air (Eq. 1.44), leading to the global reaction in the Eq. 1.45:

$$4\,MeO + CH_4 \longrightarrow 4\,Me + CO_2 + H_2O \tag{1.42}$$

$$Me + (1\text{-}\delta)\,CO_2 \longrightarrow 4\,MeO_{1-\delta} + (1\text{-}\delta)\,CO \tag{1.43}$$

$$2\,MeO_{1-\delta} + \delta O_2 \longrightarrow 2\,MeO \tag{1.44}$$

$$CH_4 + (3-4\,\delta)\,CO_2 + 2\,\delta O_2 \longrightarrow (4-4\,\delta)\,CO + 2\,H_2O \tag{1.45}$$

$NiFe_2O_4$ spinel and the combination CeO_2-Fe_2O_3 show a good performance as oxygen carriers (Huang et al., 2016).

1.1.3 Hydrogenation

The most attractive considered routes for CO_2 valorization at a large scale (Figure 1.3) are the production of hydrocarbon fuels.

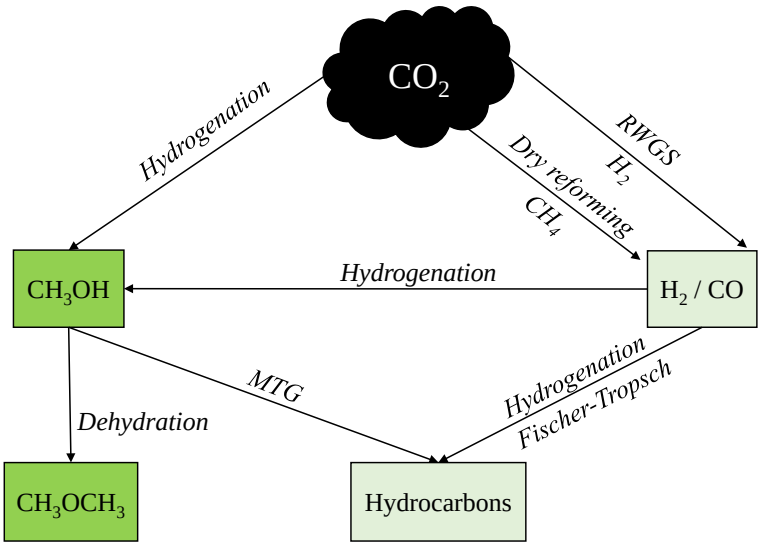

Figure 1.3: Production routes of fuels through CO_2 direct hydrogenation (Naik et al., 2010).

For this purpose and due to the low CO_2 reactivity, its hydrogenation is interesting either through rWGS reaction, valorizing afterwards the produced CO by hygrogenation reactions (methanation, methanol synthesis, Fischer-Tropsch, C_{2+} alcohols and gasoline / isoparaffins synthesis, and others); or through its direct hydrogenation. Among these direct and indirect hydrogenation routes is the DME synthesis, which will be described in Section 1.2.

1.1.3.1 Methane production

The interest in this route is associated with the availability of solar photovoltaic and wind energy for H_2 generation. It proceeds with the stoichiometry:

$$CO_2 + 4H_2 \longleftrightarrow CH_4 + 2H_2O \tag{1.46}$$

The catalysts used are made of Ni, Ru or Rh supported on Al_2O_3, either bare or modified with CeO_2 and ZrO_2. A CH_4 yield of 70 % can be achieved within the temperature range of 460 - 620 K (García-García et al., 2016).

1.1.3.2 Reverse water gas shift (rWGS)

rWGS reaction (Eq. 1.47) is endothermic and requires a temperature higher than 973 K in order to be able to obtain a considerable CO_2 conversion. The reaction proceeds together with the secondary reactions of Sabatier (Eq. 1.48), Boudouard (Eq. 1.49) and methanation (Eq. 1.50).

$$CO_2 + H_2 \longleftrightarrow CO + H_2O \tag{1.47}$$

$$CO_2 + 4H_2 \longleftrightarrow CH_4 + 2H_2O \tag{1.48}$$

$$2CO \longleftrightarrow C + CO_2 \tag{1.49}$$

$$CO + 3H_2 \longleftrightarrow CH_4 + H_2O \tag{1.50}$$

The proposed reaction mechanisms for rWGS reaction (similar to those of WGS reaction) are redox and dissociative. In the redox mechanism Cu^0 crystals are active sites for CO_2 dissociation (Eq. 1.51), and the oxidized Cu sites are reduced

releasing H_2O and being the metallic Cu sites regenerated (Eq. 1.52):

$$CO_2\,(g) + 2\,Cu^0\,(s) \longrightarrow CO\,(g) + Cu_2O\,(s) \tag{1.51}$$

$$H_2\,(g) + Cu_2O\,(s) \longrightarrow H_2O\,(g) + Cu^0\,(s) \tag{1.52}$$

H_2 dissociation mechanism provides OH^- and H^+ ions, leading to the subsequent formation of formate species (HCO_2-M). These are formed by the attack of OH^- groups on M-CO species and MO_2H species, formed through intermediates CO_2-metal protonation (Chen et al., 2010).

1.1.3.3 Direct synthesis of methanol

The worldwide production of methanol (around 65 Mt) (Leonzio, 2018) takes place principally from synthesis gas (Eq. 1.53). This reaction is key in the development of the GTL (Gas to Liquid) concept, along with the secondary reactions of rWGS (Eq. 1.47) and the synthesis from CO_2 (Eq. 1.54) that requires 3 hydrogen molecules for each CO_2 molecule.

$$CO + 2\,H_2 \longleftrightarrow CH_3OH \tag{1.53}$$

$$CO_2 + 3\,H_2 \longleftrightarrow CH_3OH + H_2O \tag{1.54}$$

Methanol is an energetic vector according to its utilization as fuel, pure or mixed with gasoline, and the production of H_2 by reforming. Additionally, it is an important raw material for the production of other fuels, solvents and base-chemical products (Figure 1.4), such as light olefins (MTO process, BTX aromatics, formaldehyde, acetic acid, methyl methacrylate, dimethyl terephthalate, methylamines, chloromethane, dimethyl carbonate, methyl tertbutyl ether (MTBE) and others).

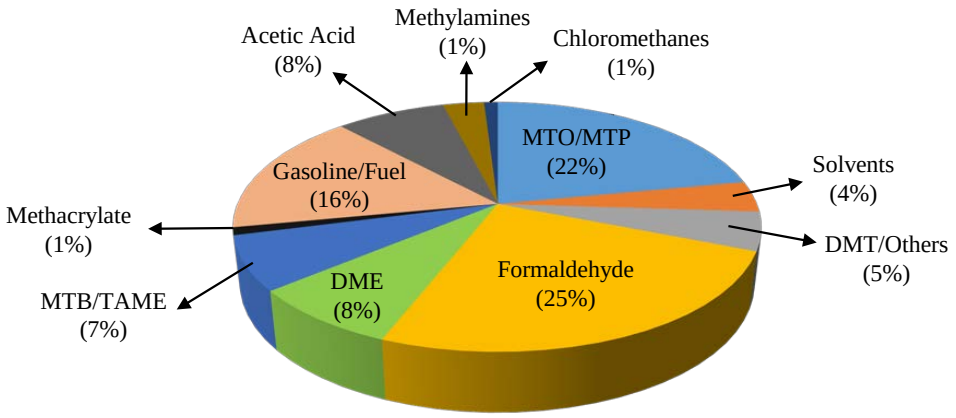

Figure 1.4: Distribution of methanol demand in 2016.

For this reason, the extensive utilization of methanol (methanol economy) represents a sustainable complement to the established oil economy (Olah, 2005).

A methanol production unit from natural gas (GTM process) or from carbon (CTM) has three sections aimed for synthesis gas production, methanol synthesis and methanol purification. The challenge of CO_2 valorization is its co-feed within the first two sections (Figure 1.5). Furthermore, the utilization of biomass as raw material is very important to implement a non-carbon production process (Wender, 1996).

In synthesis gas production from natural gas, CH_4 reforming proceeds by steam reforming reactions (SRM), autothermal (ATR) and partial oxidation (POM), and with the incorporation of CO_2 also by dry reforming (DRM) (described in Section 1.1.2). The second section of the scheme in Figure 1.5 corresponds to methanol synthesis. The first commercial catalyst for synthesis gas conversion, formed by ZnO-Cr_2O_3, was produced by BASF in 1923. It required a high temperature (623 - 673 K) and pressure (240 - 350 bar), and it was rapidly poisoned by S, Cl and heavy metals in the feed (derived from carbon gasification). Currently, the catalysts used

are ternary, basically Cu-ZnO-Al_2O_3 (CZA), resulting from the commercialized ones by Imperial Chemical Industry (ICI) in 1966.

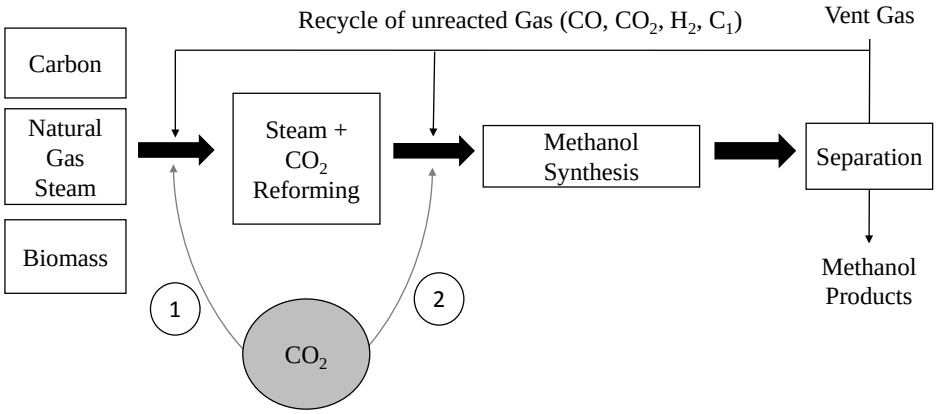

Figure 1.5: Steps in methanol production (Zhang et al., 2017).

The reaction takes place under 50 - 100 bar and at 473 - 523 K, adequate conditions in order to minimize the formation of by-products (specially hydrocarbons) and to enhance its stability, minimizing Cu sintering (remarkable above 573 K). ZnO provides the following improvements (Bae et al., 2008): 1) Cu sintering is attenuated and the interaction Cu-support is increased; 2) an appropiate Cu^+ / Cu^0 is maintained through the creation of stable active species Cu^+-OZn; 3) ZnO acts as dispersed agent against poisons in the feed. Nevertheless, ZnO has limited activity for rWGS reaction. The incorporation of Al_2O_3 improves Cu dispersion and enhances its stability.

By co-feeding CO_2 with synthesis gas rises H_2O content in the reaction medium, which is a product of rWGS (Eq. 1.47) and methanol synthesis (Eq. 1.54) reactions. This H_2O content increase diminishes both the activity and stability of Cu-ZnO-Al_2O_3 catalyst. This decrease has motivated a great research effort, being used as additional promotors the oxides of Zr, Ga, Si, B, Cr, Ce, La, Mn, V,

Ti, Au and Pd (and mixtures of them) (Arena et al., 2007; Ban et al., 2014; Bonura et al., 2011; Li et al., 2016; Liu et al., 2007; Saito and Murata, 2004; Toyir et al., 2015; Wang et al., 2011; Zhang et al., 2014).

Arena et al. (2008) have established a mechanism for Cu-ZrO_2 and CuO-ZnO-ZrO_2 catalysts, considering that ZnO favors Cu dispersion and facilitates CO_2 adsorption. It was determined by FTIR analysis that the rate-determining step is the hydrogenation of the intermediate formate in the ZnO and ZrO_2 sites, close to the Cu ones. Figure 1.6 shows the mechanism based on elementary steps proposed by Lim et al. (2009) for the methanol synthesis on Cu-ZnO-Al_2O_3-ZrO_2 catalyst.

Surface reaction	Elementary steps	
(A) CO hydrogenation reaction	Step 1: $CO \cdot s_1 + H \cdot s_2 \leftrightarrow HCO \cdot s_1 + s_2$	
	Step 2: $HCO \cdot s_1 + H \cdot s_2 \leftrightarrow H_2CO \cdot s_1 + s_2$	
	Step 3: $H_2CO \cdot s_1 + H \cdot s_2 \leftrightarrow H_3CO \cdot s_1 + s_2$	
	Step 4: $H_3CO \cdot s_1 + H \cdot s_2 \leftrightarrow CH_3OH + s_1 + s_2$	**(RDS)**
(B) water-gas shift reaction	Step 1: $CO_2 \cdot s_3 + H \cdot s_2 \leftrightarrow HCO_2 \cdot s_3 + s_2$	
	Step 2: $HCO_2 \cdot s_3 + H \cdot s_2 \leftrightarrow CO \cdot s_3 + H_2O \cdot s_2$	**(RDS)**
(C) CO_2 hydrogenation reaction	Step 1: $CO_2 \cdot s_3 + H \cdot s_2 \leftrightarrow HCO_2 \cdot s_3 + s_2$	
	Step 2: $HCO_2 \cdot s_3 + H \cdot s_2 \leftrightarrow H_2CO_2 \cdot s_3 + s_2$	**(RDS)**
	Step 3: $H_2CO_2 \cdot s_3 + H \cdot s_2 \leftrightarrow H_3CO_2 \cdot s_3 + s_2$	
	Step 4: $H_3CO_2 \cdot s_3 + H \cdot s_2 \leftrightarrow H_2CO \cdot s_3 + H_2O \cdot s_2$	
	Step 5: $H_2CO \cdot s_3 + H \cdot s_2 \leftrightarrow H_3CO \cdot s_3 + s_2$	
	Step 6: $H_3CO \cdot s_3 + H \cdot s_2 \leftrightarrow CH_3OH + s_3 + s_2$	

Figure 1.6: Methanol synthesis mechanism on a Cu-ZnO-Al_2O_3-ZrO_2 catalyst (Lim et al., 2009).

The rate-determining steps (RDS) are: for CO hydrogenation, an adsorbed methoxy species ($H_3CO{\cdot}s_1$) hydrogenation; in the case of WGS reaction, the formation of

an intermediate formate ($HCO_2 \cdot s_3$), and; for CO_2 hydrogenation, an intermediate formate hydrogenation ($HCO_2 \cdot s_3$).

1.1.4 Fine chemical products

Acetic acid production is an example of opportunity to valorize low cost reactants like CO_2 and CH_4. Equally interesting is the production of benzoic acid from CO_2 and benzene. Furthermore, the acrylic acid production has become a great interest through ethylene direct carboxylation with CO_2 on Ni catalysts (Eq. 1.55). This reaction is particularly interesting to valorize CO_2 generated in the ethylene production units by steam cracking with naphthas (Yu et al., 2013).

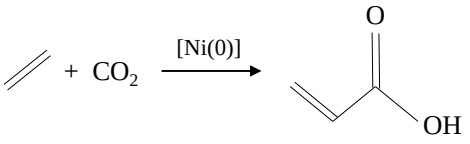

(1.55)

CO_2 is raw material for the production of lineal and cyclic carbonates. Among the first ones, dimethyl carbonate (DMC) $(CH_3O)_2CO$, well known for its properties, such as low toxicity, is used as solvent, gasoline additive and reactant in alkylation and acylation reactions. It is produced by reaction with methanol (Eq. 1.56) with supported Cu catalysts, although SnO_2 and Zr_2 supported on SiO_2 have shown great performance (Ballivet-Tkatchenko et al., 2011).

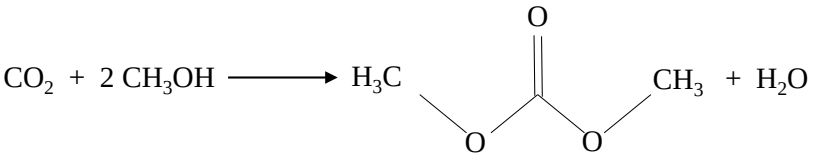

(1.56)

Cyclic carbonates (of ethylene, propylene, cyclohexane, styrene and others), with

an annual market of 20 Mt, are produced by the addition of CO_2 to an epoxy (Eq. 1.57)

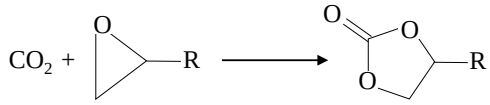

R = H for ethylene carbonate
R = CH_3 for propylene carbonate (1.57)

They are used as solvents, electrolytes and raw material in the production of polycarbonates, other polymeric materials and fine chemicals (dialkyl carbonates, glycols, carbamates, pyrimidines, etc.) The formation reactions are catalyzed by alkali metal halides, metal oxides, zeolites and organic bases (Jutz et al., 2009).

Acetylsalicylic synthesis ($CH_3COOC_6H_4COOH$) is an example of the insertion capacity of CO_2 in C-H bonds of alkenes, aromatics or olefins. The products of greatest interest are carbonic acids, esters, lactones, and heterocyclic; in other words, compounds with functional groups potentially applicable as solvents, plasticizers, detergents, antioxidants, sun-protection agents, etc. (Gu and Cheng, 2015).

1.1.5 Urea and polymers synthesis

These routes have the attractiveness of incorporating CO_2 in materials with a high production. Specially, in those where CO_2 molecule is sufficient as C1 unique source in order to build the macromolecule, as in the case of the formation of urea-formaldehyde (UF) and melamine-formaldehyde (MF) resines, with great CO_2 fixation capacity. Those resines have multiple applications, among them are their use as food additive and electric insulator.

CO_2 can be valorized in NH_3 production industry itself for the synthesis of urea (carbamide, $(NH_2)_2CO$). This consists of the formation reactions of carbamate (H_2N-$COONH_4$) (Eq. 1.58), which is dehydrated towards urea (Eq. 1.59). Ac-

cording to the stoichiometry, to obtain 1 t of urea 0.75 t of CO_2 is required. Nevertheless, urea is principally used as fertilizer, with the role of release CO_2 and NH_3 (adsorbed by plants). Therefore, this route is not adequate to diminish CO_2 emissions.

$$2\,NH_3 + CO_2 \longleftrightarrow H_2N{-}COONH_4 \tag{1.58}$$

$$H_2N{-}COONH_4 \longleftrightarrow (NH_2)_2CO + H_2O \tag{1.59}$$

Other polymers, like aliphatic polycarbonates, are produced by the reaction of CO_2 with epoxides or through transesterification of diols with DMC. They are substitutes of polyethers for the fabrication of polyurethane (formed by urethane bonds, -NH-(C=O)-O-) (von der Assen et al., 2015). In the same way, by reaction of CO_2 with epoxides, aromatics polycarbonates based on bisphenol can be synthesized. Polyoxymethylene (POM) is another polycondesation polymer that can be produced from CO_2 (in this case with formic acid as intermediate) and 1,3,5-trioxane. Although POM incurs a higher cost than polyethylene and propylene, it provides a higher mechanical resistance. Moreover, using another intermediate (such as methanol), CO_2 can be applied in the production on a large scale of polymethylmethacrylate (PMMA).

1.1.6 Electrochemical and photochemical valorization

The electrochemical reduction or activation of CO_2 can produce different compounds of interest like CO, oxalic acid, formic acid, methane, methanol, ethane, ethylene, ethanol and other hydrocarbons and oxygenates (Eqs. 1.60 - 1.63). The best economical prospects are CO and formic acid production (Jhong et al., 2013), even though, in relation to its importance within the petrochemical industry, the production of ethylene becomes more interest.

$$CO_2 + 2H^+ + 2e^- \longrightarrow HCO_2H \qquad E^0 = -0.85\,V \tag{1.60}$$

$$CO_2 + 4H^+ + 4e^- \longrightarrow H_2CO + H_2O \qquad E^0 = -0.72\,V \tag{1.61}$$

$$CO_2 + 6H^+ + 6e^- \longrightarrow CH_3OH + H_2O \qquad E^0 = -0.85\,V \tag{1.62}$$

$$CO_2 + 8H^+ + 2e^- \longrightarrow CH_4 + 2H_2O \qquad E^0 = -0.48\,V \tag{1.63}$$

The best future technology prospects are associated with the utilization of solar energy for generating the required electricity, being Cu catalysts the most interesting for the production of selective hydrocarbons (Kortlever et al., 2015).

The photocatalytic reduction of CO_2 makes possible to achieve the objectives of CO_2 fixation and hydrocarbons production. Uner and Oymak (2012) have proposed the mechanism of two active sites, shown in Figure 1.7, for the production of CH_4 through CO_2 photocatalytic reduction on a TiO_2 catalyst with Pt as promoter. However, the low energetic efficiency is an important limitation of this technology.

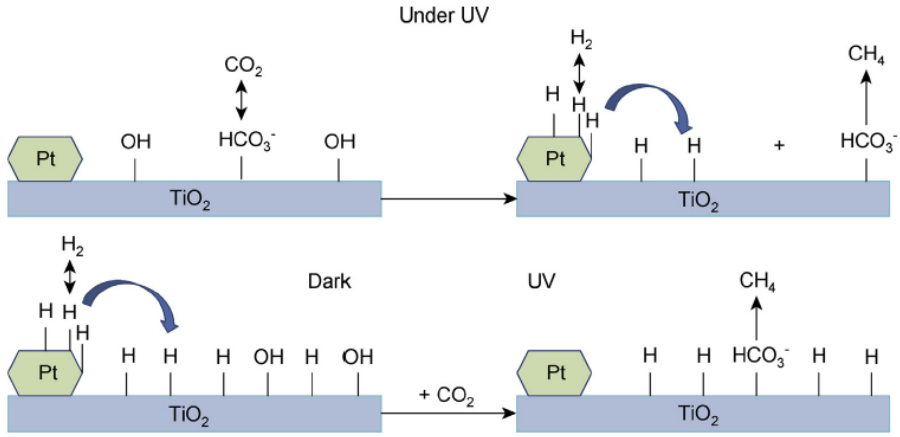

Figure 1.7: Mechanism of CH_4 formation through CO_2 photocatalytic reduction on a TiO_2-Pt catalyst (Uner and Oymak, 2012).

1.2 Dimethyl Ether synthesis

1.2.1 Interest of DME

DME (CH_3-O-CH_3) has been universally used as aerosol (substituting chlorofluorocarbons) (Sciarra and Sciarra, 2001) and as "ecological" refrigerant (Restrepo et al., 2008). According to its interest as domestic fuel, the demand projection will grow to 80 Mt by 2020, considering that 90 % will be destined to its use in Asia (mixed with LPG). Currently there are 60 units of DME production in China, by the two steps process, with a capacity over 250 thousand t / year each one.

Its implementation on a large scale, based on its properties (Arcoumanis et al., 2008; Semelsberger et al., 2006), has been in the form of fuel. Not only for domestic use but also in the automotive industry and for electrical energy generation, even though its calorific value is lower than the hydrocarbons one. In spite of its low heating value (LHV) of 27.6 MJ/kg, inferior to the diesel fuel one (42.5 MJ/kg), its high cetane number (55 - 69) and the short delay time in the injection, make DME suitable for diesel engines. It does not contain sulfur and gives rise to very low emissions, both of particles (Kim et al., 2008) and NO_x (Song et al., 2009). Due to its low viscosity and the capacity of dissolving some elastomers and plastics, different modifications in the injectors and in the selection of the materials are required. The low emissions of its combustion makes DME very interesting as fuel blended with liquefied petroleum gases (LPG: propane and butane), being favored by the similar vapor pressure and the same storage and transport characteristics (Lee et al., 2009; Parkash, 2010). Furthermore, by its combustion in a gas turbine a high energetic efficiency (61 - 62 %) is obtained and, additionally, it has the attractive of non-requiring high purity DME, due to the small energetic

requirement of the vaporization (Fleisch et al., 2012).

With this in mind, the evolution towards a DME economy is based not only on its use as fuel, but also on its future as intermediate raw material. This latter leads to the production of fuels, raw materials in the petrochemical industry and H_2, substituting petroleum products as well as methanol. Thus, MTO (methanol to olefins) process, developed by UOP/Mobil and successively improved (Tian et al., 2015), and MTP, developed by Lurgi (to selectively obtain propylene) (Khadzhiev et al., 2008), have met the growing implementation to satisfy the burgeoning demand of light olefins. Currently this demand is being met by petroleum products, through naphta steam cracking (Sadrameli, 2015), and fluid catalytic cracking (FCC) (Awayssa et al., 2014). The replacement of methanol by DME, through the DTO (DME to olefins) process, is an interesting alternative and can offer advantages with respect to MTO process.

DTO process presents many analogies to MTO, because in fact, DME is an intermediate in the transformation of methanol into olefins, which takes place by a well established mechanism commonly referred to as "hydrocarbon pool" (Dahl and Kolboe, 1993, 1994). The knowledge of this mechanism has been developed, based on the intermediates determination, through spectroscopic techniques denominating the updated version "double cycle mechanism". Two routes of olefins formation are distinguished: aromatics intermediates (polymethylbenzenes) methylation-dealkylation and olefins methylation-cracking. Both occur along with different secondary reactions (isomerization, cyclization and hydrogen transfer), forming, together with olefins, other by-products: light paraffins, BTX aromatics, C_5^+ aliphatics and coke (Bjørgen et al., 2004; Ilias and Bhan, 2013; Sun et al., 2014a; Wang et al., 2015a). Consequently, the investigation of new catalysts have received a considerable attention in order to improve both their selectivity and stability (less

deactivation). This research is mainly focused on SAPO-34 catalysts (when the objective is the selectivity of olefins) and HZSM-5 (to obtain propylene and with less coke deactivation).

The reaction scheme of DTO process is similar to MTO one. The sensitivity of MTO process regarding the reaction conditions and the catalyst remains also in DTO process, but with significant differences. Among these, it should be emphasized (Al-Dughaither and de Lasa, 2014; Pérez-Uriarte et al., 2016a,b,c,d):
1) higher DME reactivity, with a kinetic constant in the olefins formation step 20 times greater than the one of methanol at 350 °C; 2) higher catalyst deactivation by coke; 3) the need for a catalyst with moderate acid strength; 5) enhanced performance of HZSM-5 catalyst in comparison to others (SAPO-34 and SAPO-18) with greater severity of form selectivity and whose deactivation is extremely rapid. The analogies lead to consider that the MTO process technology (fluidized bed with catalyst circulation) can be adequate for DTO process, although different operation conditions should be established.

Another application for DME with development potential is as H_2 vector, because its characteristics (high hydrogen content, absence of C-C bonds and low toxicity) facilitate the reforming at low temperature (< 300 °C) with high H_2 yield (Hočevar and Summers, 2008). This can be applied for PEM fuel cells on a vehicle, as well as to cover, on a large scale, the growing demand in the petrochemical industry. Steam reforming takes place on a bifunctional catalyst, through DME hydrolysis in the acid function (Eq. 1.64), followed by methanol reforming in the metallic function (Eq. 1.65).

$$CH_3OCH_3 + H_2O \longleftrightarrow 2\,CH_3OH \tag{1.64}$$

$$CH_3OH + H_2O \longleftrightarrow 3\,H_2 + CO_2 \tag{1.65}$$

Additionally, the reactions of water gas shift (WGS) (Eq. 1.66) and DME partial decomposition (Eq. 1.67) are also considered.

$$CO + H_2O \longleftrightarrow CO_2 + H_2 \tag{1.66}$$

$$CH_3OCH_3 \longleftrightarrow CH_4 + H_2 + CO \tag{1.67}$$

The most used catalysts in a lab-scale have been prepared with the metallic function CuO-ZnO-Al_2O_3 (CZA), based on the commercial one for methanol synthesis and methane reforming (Badmaev et al., 2007; Feng et al., 2009; Kawabata et al., 2006). The main innovations have mainly consisted of the utilization of CuM_2O_4 spinels (M = Fe, Mn, Cr, Ga, Al, etc). Among these, $CuFe_2O_4$ spinel has received a great attention due to its thermal stability (Faungnawakij et al., 2007; Oar-Arteta et al., 2014; Shimoda et al., 2011), which recovers its activity in reaction-regeneration cycles (Oar-Arteta et al., 2015a, 2016).

As acid function γ-Al_2O_3 has been the most used for DME hydroxylation (Faungnawakij et al., 2008a,b, 2010; Wang et al., 2010), but it has been progressively substituted by HZSM-5 (more active). HZSM-5 has to be adequately treated (like the desilication by alkaline treatment) in order to avoid the formation of hydrocarbons and the consquent formation of coke (Ereña et al., 2013a,b; Gayubo et al., 2014; Vicente et al., 2013). Oar-Arteta et al. (2015a,b) have improved the properties of γ-Al_2O_3, obtaining it by calcination of pseudoboehmite. This treatment provides the catalyst with high mechanical resistance (a deficiency of $CuFe_2O_4$ spinel) and also with moderate acidity, limiting the formation of hydrocarbons. Therefore, it allows to operate achieving a yield of 82 % at 350 °C and with stability in reaction-regeneration cycles. Filling the gap in kinetic modeling for oxygenates reforming, Oar-Arteta et al. (2016) have proposed a kinetic model based

on Langmuir-Hishelwood-Hougen-Watson expressions for each step, establishing optimal reforming conditions: 360 - 380 °C and a steam / DME ratio of around 6.

1.2.2 Indirect synthesis of DME

DME production is industrially carried out in a process with two units (indirect synthesis) (Catizzone et al., 2017c), through a two steps process. Methanol is synthesized in the first unit (under reaction conditions described in Section 1.1.3.3) and dehydrated towards DME in the second unit (MTD process). The indirect synthesis of DME is a reversible exothermic reaction on acid catalysts, whose thermodynamic is not favored increasing the pressure, but rather decreasing the temperature. The industrial process has different licensees (Haldor Topsoe, Linde/Lurgi, Toyo Engineering, Uhde, Mitsubishi Gas Chemical Company (MGC), China Energy, China Southwestern Research Institute of Chemical Industry) and an extensive implementation in asiatic countries since the beginning of the 21st century (Fleisch et al., 2012), with carbon as raw material. It is performed under moderate pressure (below 20 bar) and within the temperature range 150 - 300 °C, being γ-Al_2O_3 generally used as catalyst due to its reduced cost, high specific surface, mechanical resistance and thermal stability. The nature of Lewis sites (weakly acid) of γ-Al_2O_3 is appropriate to achieve a high DME selectivity, inhibiting the formation of hydrocarbons as by-products, nonetheless the activity is moderate and a temperature above 250 °C is required. This activity has increased modifying γ-Al_2O_3 with P, Ti, Nb, B, etc. (Yaripour et al., 2015).

Catalysts with higher acidity than γ-Al_2O_3 have been also studied, which allows the reaction to take place at lower temperature, avoiding the formation of hydrocarbons. For this purpose, the optimal performance of heteropolyacids (HPAs) (more active than HZSM-5 catalyst) has been proven, which is enhanced with the incor-

poration of W and P (Alharbi et al., 2015) and supporting HPAs on TiO_2 (Ladera et al., 2014).

The greatest research effort in the design of catalysts for methanol dehydration has been focused on zeolites, whose performance (activity, DME selectivity and stability) is influenced by the channels configuration of their crystalline structures and the quantity and strength of acid sites (Catizzone et al., 2017a). HZSM-5 zeolite, which is less hydrophilic than γ-Al_2O_3, has received a special attention. It contains pores with moderate severity of the form selectivity and an acidity dependent on $Si\,/\,Al_2O_3$ ratio, with sites that mainly have a moderate acid strength. It is remarkable the acidity adaptability of this zeolite (in this case to reduce the acid strength), by the selection of the calcination temperature, steaming or incorporation of different metals. It is also of interest the behavior of hybrid catalysts of HZSM-5 zeolite, impregnated with γ-Al_2O_3, being more active and selective than each separate catalyst, due to the dilution of the zeolite strong sites (Kim et al., 2006). Catizzone et al. (2017b) have proposed ferrierite (FE) as ideal catalyst, whose crystalline structure with two dimension channels makes it highly selective and, additionally, coke deposition is reduced. This zeolite, prepared with a high Al content, allows achieving a DME selectivity close to 100 % at 200 °C and a high methanol conversion (up to 82 %), in contrast to γ-Al_2O_3 conversion of 25 %.

Methanol dehydration mechanism on zeolites is carried out by methanol adsorption and the formation of methoxy ions. These ions are combined with another methanol molecule forming a DME one. Nevertheless, it should not be disregarded that methanol adsorption mechanism can be associative by the adsorption of two methanol molecules in the same active site (Migliori et al., 2014).

1.2.3 Direct synthesis of DME

During the last two decades the interest of DME production in one step has been growing. DME is synthesized through STD (syngas to dimethyl ether) process, using a bifunctional catalyst, simplifying the process with only one reactor and, particularly, favoring the thermodynamics. The interest has increased with the perspective of valorizing CO_2 (pure or co-fed with CO).

The reactions involved in STD process are:

Methanol synthesis

$$CO + 2\,H_2 \longleftrightarrow CH_3OH \tag{1.68}$$

$$CO_2 + 3\,H_2 \longleftrightarrow CH_3OH + H_2O \tag{1.69}$$

Reverse water gas shift (rWGS)

$$CO_2 + H_2 \longleftrightarrow CO + H_2O \tag{1.70}$$

Methanol dehydration towards DME

$$2\,CH_3OH \longleftrightarrow CH_3OCH_3 + H_2O \tag{1.71}$$

Paraffins formation secondary reaction (mainly methane)

$$n\,CO + (2\,n + 1)\,H_2 \longleftrightarrow C_nH_{2n+2} + n\,H_2O \quad (n = 1 - 3) \tag{1.72}$$

The interest in STD process is based on different factors: 1) lower cost of DME and methanol (by-product) production in comparison to DME synthesis in two steps and the synthesis of methanol (Trippe et al., 2013); 2) possibility of synthesis gas generation from various hydrocarbonated raw materials, carbon, natural gas,

biomass or consumer society residues (Figure 1.8); 3) boost biomass gasification in order to contribute to neutral carbon balance; 4) opportunity to maximize the natural gas operating profit, integrating its valorization with DME synthesis. Thus, the energetic efficiency is around 64 - 68 % for a 2500 equivalent t/day plant, higher than methanol synthesis with a energetic requirement 5 % lower and a lower capital cost (8 % lower for DME with methanol as by-product) (Kabir et al., 2013; Pontzen et al., 2011).

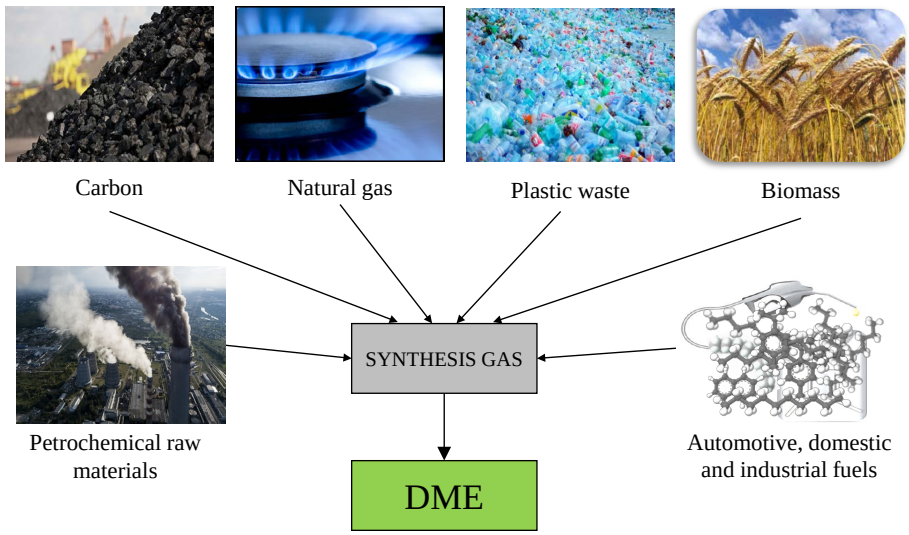

Figure 1.8: DME production from fossil sources, biomass and waste.

While there has been a marked technological development of DME synthesis in one step (principally with natural gas and carbon as raw materials) (Azizi et al., 2014; Bhattacharya et al., 2013), the implementation of the process has been limited to demonstration units. Nonetheless, industrial units in gas natural producers regions (Middle East, South-East Asia and Oceania) are at study stage.

The most studied catalysts for STD process, fed with synthesis gas, have a metallic function of CuO-ZnO-Al_2O_3 (CZA), being the usual composition for methanol synthesis (Moradi et al., 2007). Nevertheless, Al_2O_3 has been replaced, partially

or totally, by other materials such as MnO or ZrO_2, and ZnO (used to establish Cu) has been substituted by La_2O_3 (Li et al., 2014a). On the other hand, the acid functions used to prepare the catalyst are different based on their porous structures (γ-Al_2O_3, silica-alumina, HZSM-5, mordenite and HY zeolites, ferrierite, HMCM-22 and SAPOs), sharing all of them the characteristic of a limited acid strength, avoiding the formation of hydrocarbons (Sun et al., 2014b). For the preparation of the catalyst, the most used technique is the sol-gel co-precipitation and the overall strategy is to provide an acid function excess. In this way, the equilibrium displacement of methanol synthesis is ensured and the reaction is controlled by methanol formation, which is the slowest step.

Given its importance in the viability of the process, the deactivation of the catalyst has received a significant attention, whose causes are: 1) partial blockage by coke of Cu-ZnO metallic sites (being considered as the fastest step in the deactivation); 2) coke deposition on the micro and mesopores of the acid function; 3) Cu sintering of the metallic function. The mechanism of coke deposition takes place presumably by condensation towards aromatic structures of methoxy ions, which are key intermediates formed in the metallic and acid sites by methanol adsorption. Therefore, it is considered that there is a synergy between the two coke formation mechanisms on each function of the catalyst (García-Trenco et al., 2012). The verification (well established in the research literature) that the increase of H_2O content in the reaction medium attenuates coke deposition is consistent with this hypothesis of the key role of methoxy ions as precursors, whose formation is thermodynamically limited with the increase of H_2O concentration (Ereña et al., 2008). Moreover, irreversible deactivation, by Cu sintering, is considerable around 300 °C, which limits the reaction temperature and is an issue for regeneration by coke combustion, really low below this temperature (Sierra et al., 2010).

Coke characterization studies (Ereña et al., 2008) have determined its presence both on the metallic and acid sites, as well as on the interphase between them (corresponding to the inert Al_2O_3 in the CuO-ZnO-Al_2O_3 / γ-Al_2O_3 catalyst). However, coke is presented on the metallic function from the initial stages of the reaction, achieving a limit value in a short period of time. This dynamic can be explained because hydrogenation of coke precursors slows down its evolution. Nevertheless, the amount of deposited coke on the acid function increases with the reaction time, approaching a value corresponding to an equilibrium, in this case between its formation and its diffusion to the exterior of the catalyst particles. Consequently, the activity of the metallic sites is important to hydrogenate coke intermediate compounds. In like manner, the properties of the acid function are also important both to attenuate coke formation and favor the circulation of the intermediates towards the exterior of the micropores.

The most studied technology is the one of Haldor Topsoe, which consists of an adiabatic fixed bed reactors bank similar to the commercialized one for methanol synthesis (Hu et al., 2008). As an alternative, a slurry reactor technology for the synthesis in liquid phase (LPDME) has been developed (`www.oberon.fuels.com`), in order to ensure the isothermicity (Gao et al., 2009; Han et al., 2009). Even though the utilization of an agitated slurry reactor limits the scale-up until a considerate limit of 100 t / day (Ohno et al., 2007), it can be enhanced based on other variables of the slurry reactor, like the bubbly flow (Chen et al., 2006). It is worth mentioning that the difficulty of operating under high pressure has limited the utilization of fluidized reactors (Kumar and Srivastava, 2010; Lu et al., 2004). The potential of these reactors is great and are being developed by Unitel Technologies in Australia (`www.unitelch.com`).

1.2.4 CO_2 valorization in DME synthesis

The integration in the same reactor of the reactions (Eqs. 1.68 - 1.71) exhibits the disadvantage of operating at intermediate pressure and temperature conditions from the optimal ones for methanol synthesis and its dehydration steps. However, the advantage of the methanol synthesis equilibrium displacement is greater, diminishing thermodynamic restrictions. Consequently, it allows to operate, in comparison with methanol synthesis, under lower pressure, higher temperature and a lesser H_2/CO ratio in the feed (Aguayo et al., 2007; Jia et al., 2006). This last advantage is important to valorize synthesis gas derived from biomass (Olah et al., 2009). But, especially, the lower thermodynamic limitation is considered more favorable for CO_2 incorporation in the feed, enhancing its conversion regarding that in the synthesis of methanol at the same reaction conditions.

Olah et al. (2009) have considered that one step DME synthesis (Figure 1.9) is a key route for CO_2 catalytic valorization on a large scale. Furthermore, these authors have placed great emphasis on the sustainability of the process when CO_2 is co-fed with synthesis gas, produced from lignocellulosic biomass.

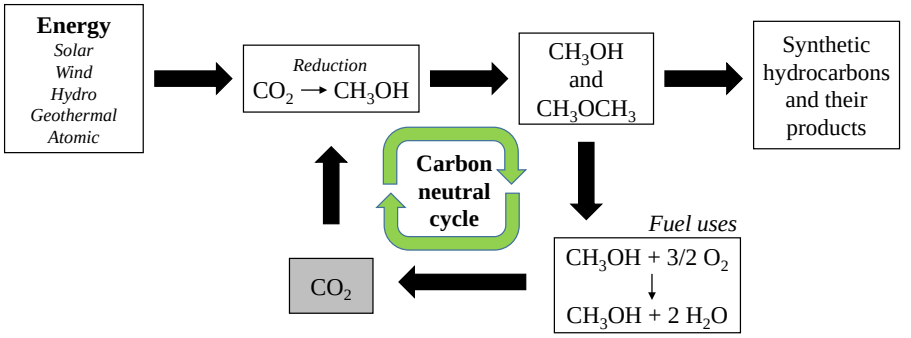

Figure 1.9: Methanol and DME production valorizing CO_2 (Olah et al., 2009).

The consideration of the process of the direct synthesis of DME as one of the most viable routes to mitigate CO_2 emissions in short-term and on a large scale, has given a considerable boost in the study of the process. In particular, it has aroused the need for performing significant innovations in the catalyst and in the reactor, due to the effect of CO_2 co-feeding in the conversion, selectivity and stability of the catalyst, and in the decrease of the yields in comparison to synthesis gas feeding.

Two factors that condition the process are: 1) low reactivity of CO_2 hydrogenation, and; 2) increase of H_2O content in the reaction medium, being WGS reaction displaced, and consequently resulting in the displacement of methanol dehydration. H_2O is adsorbed in the metallic sites, decreasing their activity and, additionally, favoring the irreversible deactivation (sintering) of these metallic sites. Furthermore, the activity of the acid sites also diminishes and, to a greater extent, when the acid function is hydrophilic. Therefore, research efforts have been focused on the activity intensification and catalyst stability.

1.2.4.1 Catalysts

In addition to the required properties of the catalyst in the direct synthesis of DME, by feeding CO_2 deactivation problem assumes greater relevance. Thus, higher CO_2 and H_2O concentrations in the reaction medium favors CuO oxidation and its sintering. The first effect attenuates the rates of CO and CO_2 hydrogenation and WGS reactions, but the second one is more important due to its irreversibility. However, these unfavorable effects should not fade the main positive one, which is the attenuation of coke deposition caused by the before described role of H_2O in the reaction medium (Section 1.2.3), controlling the concentration of superficial methoxy species, as well as the ability of H_2O to diffuse coke precursors. Ateka et al. (2016a) have determined, using a CuO-ZnO-MnO / SAPO-18 catalyst, that

coke on the metallic function is completely eliminated by combustion with air at 300 °C for 48 h. It means that the limiting factor to use these type of catalysts is the sintering. Among the initiatives to attenuate Cu sintering, it is worth noting the incorporation of promotors like MgO (Oyola-Rivera et al., 2015) and CeO_2 (Zhou et al., 2016b), whose principal purpose is to enhance CuO crystallites dispersion and to stabilize its interaction with the support.

Within the research work to improve the catalyst, two pathways can be distinguished : 1) focused on improving each function of the catalyst, and; 2) oriented towards changing the structure of the bifunctional catalyst particle. Regarding the first one, in order to enhance the activity and/or stability of CuO-ZnO sites, have shown interesting results: 1) increase of the CO_2 hydrogenation rate, substituting ZnO by Fe_2O_3 and using CeO_2 as promotor (Qin et al., 2016; Zhou et al., 2016b); 2) increment of the activity in rWGS by incorporating MnO instead of Al_2O_3 (Arena et al., 2009; Zhang et al., 2014); 3) increase of the $Cu^{\delta+}$ sites stability by incorporation of ZrO_2 (An et al., 2008; Bonura et al., 2016; Frusteri et al., 2015; Peng et al., 1999; Sun et al., 2004).

Regarding the research focused on the acid function, in order to mitigate the activity decrease by H_2O adsorption and to facilitate its desorption from the acid sites, hydrophilicity has been progressively diminished, being the replacement of γ-Al_2O_3 by zeolites the most notable measure. HZSM-5 zeolite, subjected to numerous modifications has been widely studied (Cai et al., 2016; García-Trenco and Martínez, 2012; Zhang et al., 2013) and also silicoaluminophosphates (SAPO-18, SAPO-11), which are materials with less H_2O adsorption capacity. Frusteri et al. (2017) have tested the optimal performance of ferrierite, justified by its porous and acid structure.

Our research group has been focused on conventional (hybrid) catalysts preparation, underlining that Ateka et al. (2017a, 2016b) have proven the great behavior of CuO-ZnO-MnO (CZMn) and CuO-ZnO-ZrO_2 (CZZr) metallic functions and SAPO-18 as acid function to valorize CO_2 co-fed with synthesis gas, emphasizing the low cost of the former. It was determined that the optimal mass ratio (metallic function / acid function) was 2 / 1. Based on the results using both catalysts (CZMn and CZZr) within a wide range of operation conditions, it should be pointed out the following effects of CO_2 co-feeding (Ateka et al., 2016b): 1) reaction rate decrease of methanol synthesis reactions from CO and CO_2; 2) attenuation of the catalyst deactivation by coke and increase of H_2O concentration in the reaction medium; 3) optimal reaction conditions for valorizing CO_2 correspond to less DME production; 4) CO_2 conversion achieves a minimum under an intermediate pressure, and a maximum with a relatively low space time.

Sánchez-Contador et al. (2018c) have studied the effect of the incorporation of ZrO_2 in the CuO-ZnO metallic function, synthesizing MeOH from CO_2 / CO / H_2 mixtures under the reaction conditions of the direct synthesis of DME. The determined most suitable ratio was Cu:Zn:Zr = 2:1:1 achieving an optimal agreement between CO_x conversion (8.14 %), methanol yield and selectivity (over 98 %) and catalyst stability. The addition of ZrO_2 has been proven effective to stabilize $Cu^{\delta+}$ sites in a reaction medium with high H_2O content, like by CO_2 hydrogenation.

Same authors (Sánchez-Contador et al., 2018a) have shown the interest in SAPO-11 for methanol dehydration towards DME, comparing its behavior (at DME synthesis reaction conditions) with the one of SAPO-18 (moderate acid strength), and with HZSM-5 zeolites with different SiO_2 / Al_2O_3 ratios and subjected to acidity passivation treatments. This focus on SAPO-11 in methanol dehydration is well established in the literature (Chen et al., 2018; Dai et al., 2011) and is justified by

its acidity (high number of sites of low acid strength) and its AEL topology (Figure 1.10).

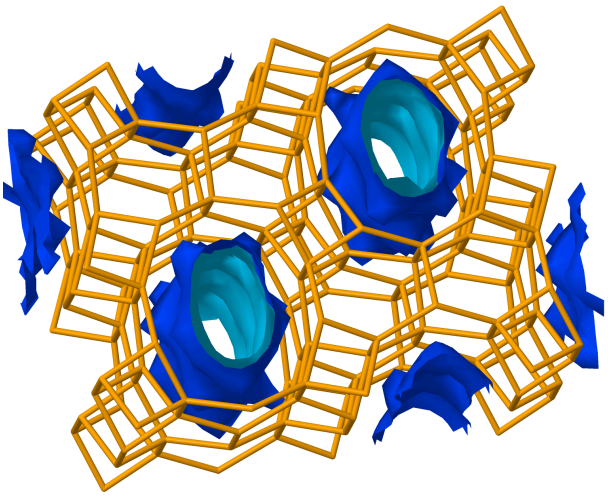

Figure 1.10: Structure of the channels of SAPO-11 (Sánchez-Contador, 2017).

It contains unidimensional channels of 0.4 x 0.6 nm and without intersections (Lok et al., 1984). These properties minimize the adsorption and retention of hydrocarbon molecules, as well as their condensation to form polyaromatic components from coke.

From the research works carried out by Sánchez-Contador et al. (2018a,c), the interest in these functions (CuO-ZnO-ZrO_2 and SAPO-11) has been proven. This catalyst presents an enhanced performance, in comparison with other previous studied compositions by the authors in the direct synthesis of DME from CO_2 / CO / H_2 mixtures.

Comparatively, in the direct synthesis of DME, a core-shell structure for each catalyst particle, as an alternative to bifunctional (hybrid) catalysts, is being explored. These hybrid catalysts are prepared by extrusion of the metallic and acid functions particles configuring each catalyst particle, whereas core-shell structure consists

of depositing the acid function on a nucleus, previously prepared by the metallic function (Figure 1.11).

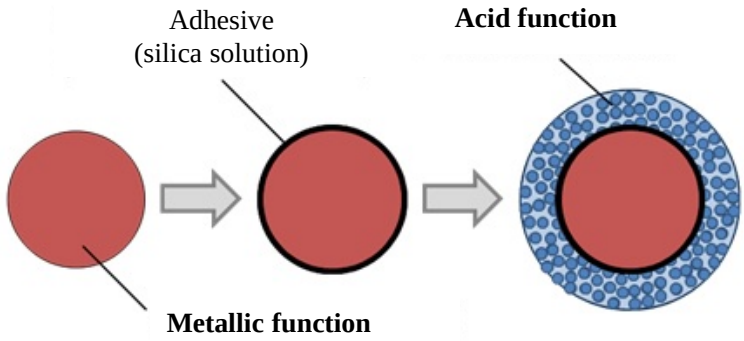

Figure 1.11: Configuration of a bifunctional catalyst particle with a core-shell structure (Sánchez-Contador et al., 2018b).

The general objective of core-shell structure in catalytic processes is to protect the catalyst by coating with a material, either preserving it from poisons adsorption or attenuating metallic particles sintering by separating them physically. In multiple steps reactions (cascade reactions), a more favorable reaction medium is achieved for each step. There are precedents in the literature for this initiative in the direct synthesis of DME, with core-shell catalysts prepared with CuO-ZnO-Al_2O_3 and using as acid function HZSM-5 zeolite (Yang et al., 2011), γ-Al_2O_3 (Wang et al., 2013a,b), SiO_2-Al_2O_3 (Wang et al., 2014) or SAPO-11 (Phienluphon et al., 2015a). Among the causes of the better performance of core-shell catalysts in comparison to hybrid ones, it is emphasized, on these before cited works, the higher availability of acid sites on the catalyst particle surroundings for the conversion of the methanol formed in the nucleus. A greater resistance towards sintering of Cu species in the nucleus has been also observed (Sánchez-Contador et al., 2019). Moreover, with a core-shell structure the adverse effects of the phases interaction can be minimized, which different authors have related to deactivation. Thus, Nie et al. (2012) have highlighted the advantage of the Cu species confinement in the

nucleus, avoiding their migration towards the acid function. García-Trenco and Martínez (2014) have proven through XPS analysis and 27 AlMAS-NMR spectra the migration of Al^{3+} species from HZSM-5 zeolite towards CuO-ZnO-Al_2O_3 metallic function, giving this migration a relevant role in the catalyst deactivation by Cu sintering.

Sánchez-Contador et al. (2018b) have prepared a new CuO-ZnO-ZrO_2@SAPO-11 catalyst by "physical coating" methodology with SiO_2 solution as adhesive (Phienluphon et al., 2015b; Pinkaew et al., 2013). This procedure avoids Cu species sintering problems in the conventional (hybrids) catalysts preparation, as a result of the required high temperature and the alkaline medium. The great performance of CuO-ZnO-ZrO_2@SAPO-11 can be explained by the advantages offered by the separation of methanol synthesis and its dehydration reactions, generating a favorable reaction medium for the activity of each catalyst function. On this matter, it is important the limitation of H_2O presence in the metallic nucleus and the greater ease of the contact of methanol in the acid sites on its circulation towards the catalyst particle periphery. Sánchez-Contador et al. (2018b) have corroborated that the preparation method of core-shell particle prevents the partial blockage of SAPO-11 mesopores by CuO-ZnO-ZrO_2 particles in the pelletization step preparing hybrid catalysts. As a consequence of these advantages, core-shell catalyst performance improves (higher activity, DME selectivity and stability) in comparison to the hybrid one with the same components. It is noteworthy the greater stability as a result of less sintering and lower coke deposition.

1.2.4.2 Thermodynamics

In the literature regarding methanol synthesis thermodynamics (Chang et al., 1986; Iyer et al., 2015; van Bennekom et al., 2012) and one step DME synthesis (Chen

et al., 2013; Jia et al., 2006; Moradi et al., 2011), the studied feed gas has been synthesis gas whereas little attention has been given to CO_2 conversion capacity, whose role has been restricted to secondary product of the reaction. The interest in CO_2 conversion processes on a large scale requires new studies regarding the thermodynamics and kinetics, aimed at establishing the appropriate conditions and the reactor design. Chen et al. (2016b) have compared the DME synthesis thermodynamic in two steps and in a single step, co-feeding CO_2 with synthesis gas. The results support that with both strategies CO_2 co-feeding decreases DME yield, and, furthermore, the direct synthesis of DME has lower thermodynamic limitations and allows achieving higher CO_2 conversion.

Ateka et al. (2017b) have compared in depth the thermodynamics of both methanol synthesis and the direct synthesis of DME, from the perspective of the capacity of these processes to valorize CO_2. It was determined the effect of the reaction conditions (temperature, pressure and CO_2 / (CO+CO_2) ratio in the feed) in regard to CO_2 conversion, oxygenates yield and selectivity (MeOH and DME) and generated heat in each process. These reaction indexes are fundamental to design the kinetic model and to establish the appropriate reaction conditions.

CO_2 conversion

In Figure 1.12 the effect of the reaction temperature on CO_2 conversion in methanol synthesis (MS) with the corresponding one in the direct synthesis (DS) of DME are compared, varying CO_2 / CO_x molar ratio in the feed. The results show that CO_2 valorization is feasible in both processes within the studied temperature range, feeding a high CO_2 concentration ($CO_2 / CO_x > 0.50$). On the other hand, CO_2 conversion reaches a minimum within 250 - 300 °C range (at higher temperature increasing CO_2 concentration), which is more pronounced in DME synthesis.

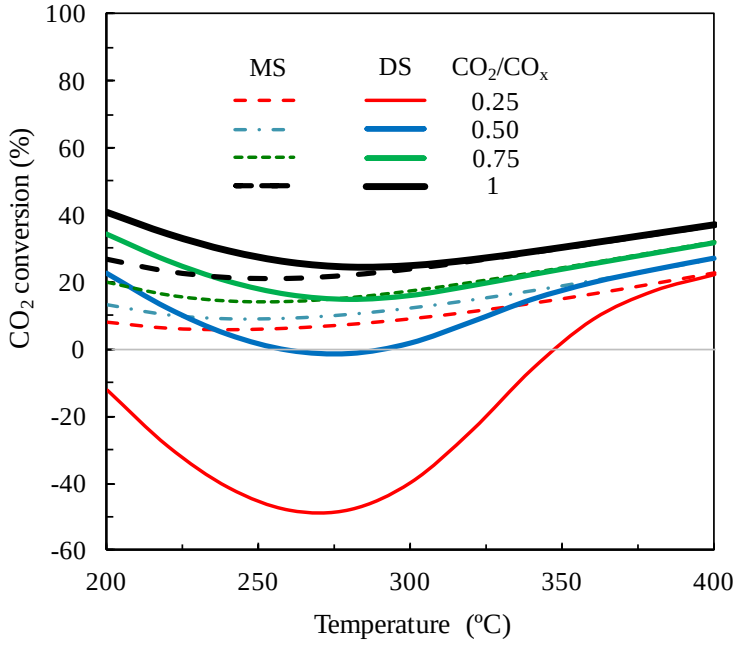

Figure 1.12: Comparison of the evolution with CO_2 conversion temperature between methanol synthesis (MS) and direct synthesis (DS) of DME, varying CO_2 / CO_x ratio in the feed. Reaction conditions: 30 bar; H_2 / CO_x, 3 (Ateka et al., 2017b).

Comparing both results, it can be observed on Figure 1.12 that the differences depend significantly on CO_2 concentration in the feed. Thus, feeding only CO_2 (results for CO_2 / CO_x = 1), CO_2 conversion is greater in DME synthesis below 300 °C. Conversely, decreasing CO_2 concentration in the feed, the advantage of DME synthesis is achieved at lower temperature (for example, at 275 °C for CO_2 / CO_x = 0.75 and at 225 °C for CO_2 / CO_x = 0.50).

In order to be able to give value to those results within real operating possibilities, it might be considered that there is a temperature range where it can be operated attending to activity and stability of current catalysts (Cu in the metallic function). For this reason, the predictable limit temperature with these catalysts is 300 °C in order to avoid Cu catalysts sintering (Sierra et al., 2010).

At the same time, below 250 °C the reaction rate with these catalysts is very low (Ng et al., 1999). Consequently, thermodynamic results indicate that the temperature interval from 250 - 300 °C, which is of greater interest from the point of view of the catalyst and to obtain high methanol and DME yields, even though they are not the optimal ones, is suitable to achieve remarkable CO_2 conversion values. These values are higher in DME synthesis than in methanol one and, additionally, they are greater upon increasing CO_2 concentration in the feed.

In Figure 1.13 is shown an overall perspective of the equilibrium conversion of CO_2 with reaction temperature and CO_2 concentration in the feed synthesizing DME.

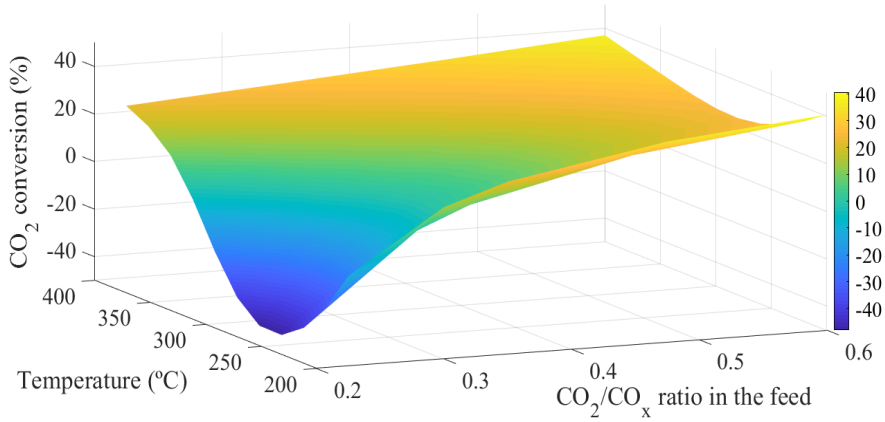

Figure 1.13: Evolution of the equilibrium of CO_2 conversion with reaction temperature and CO_2 concentration (CO_2 / CO_x ratio) in the feed, in the direct synthesis of DME. Reaction conditions: 30 bar; H_2 / CO_x, 3 (Ateka et al., 2017b).

Oxygenates yield

Figure 1.14 gathers the comparison between the effect of temperature on oxygenates yield (methanol and DME) in methanol synthesis (dotted lines) and DME synthesis (solid lines) for different pressures (Ateka et al., 2017b).

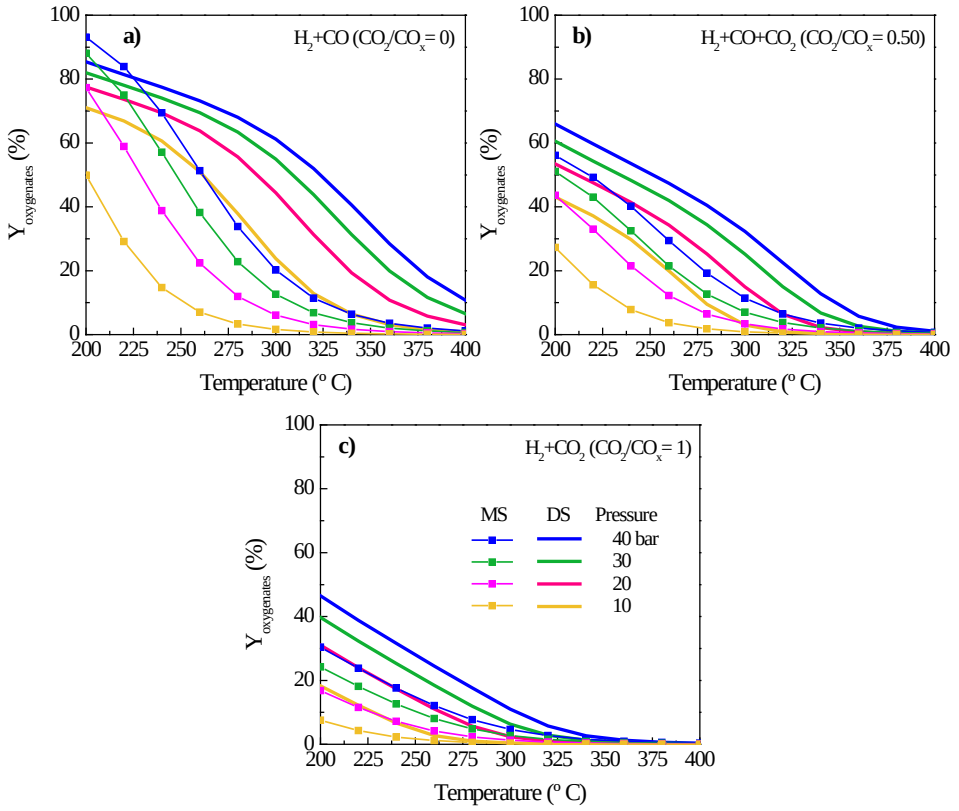

Figure 1.14: Comparison of temperature and pressure effect within the oxygenates yield values in thermodynamic equilibrium, for methanol synthesis (MS, dotted lines) and direct synthesis of DME (DS, solid lines), varying CO_2 concentration in the feed. CO_2 / CO_x = 0 (a) ; CO_2 / CO_x = 0.50 (b) ; CO_2 / CO_x = 1 (c). H_2 / CO_x, 3 (Ateka et al., 2017b).

Each graphic corresponds to a CO_2 concentration in the feed, maintaining H_2 / CO_x ratio = 3 constant. Focusing on the methanol synthesis results, it can be observed

that the pressure increase has a favorable effect in methanol yield (consequence of the reduction in the number of moles), whereas the temperature increase is unfavorable, due to the exothermic character of the reaction. Furthermore, the reaction thermodynamic limitations when increasing CO_2 concentration in the feed can also be observed. This is due to the fact that the methanol formation equilibrium constant is low for CO_2 feeds and that methanol formation is controlled by the rWGS reaction. Attending to these results it can be observed that DME synthesis (solid lines) is more thermodynamically favorable than methanol synthesis regarding oxygenates production.

The effect of temperature and pressure on DME yield are shown in Figure 1.15. A favorable effect can be observed increasing the pressure, whereas there is a remarkable DME yield decrease the higher the temperature is. DME production is lower increasing CO_2 concentration in the feed.

The results in DME selectivity at the same reactions conditions than in Figure 1.15 are given in Figure 1.16. It shows that the effect of pressure and temperature effect on DME selectivity is similar to the one observed for oxygenates yield. That is, lower upon increasing reaction temperature, while favored by incrementing the reaction pressure.

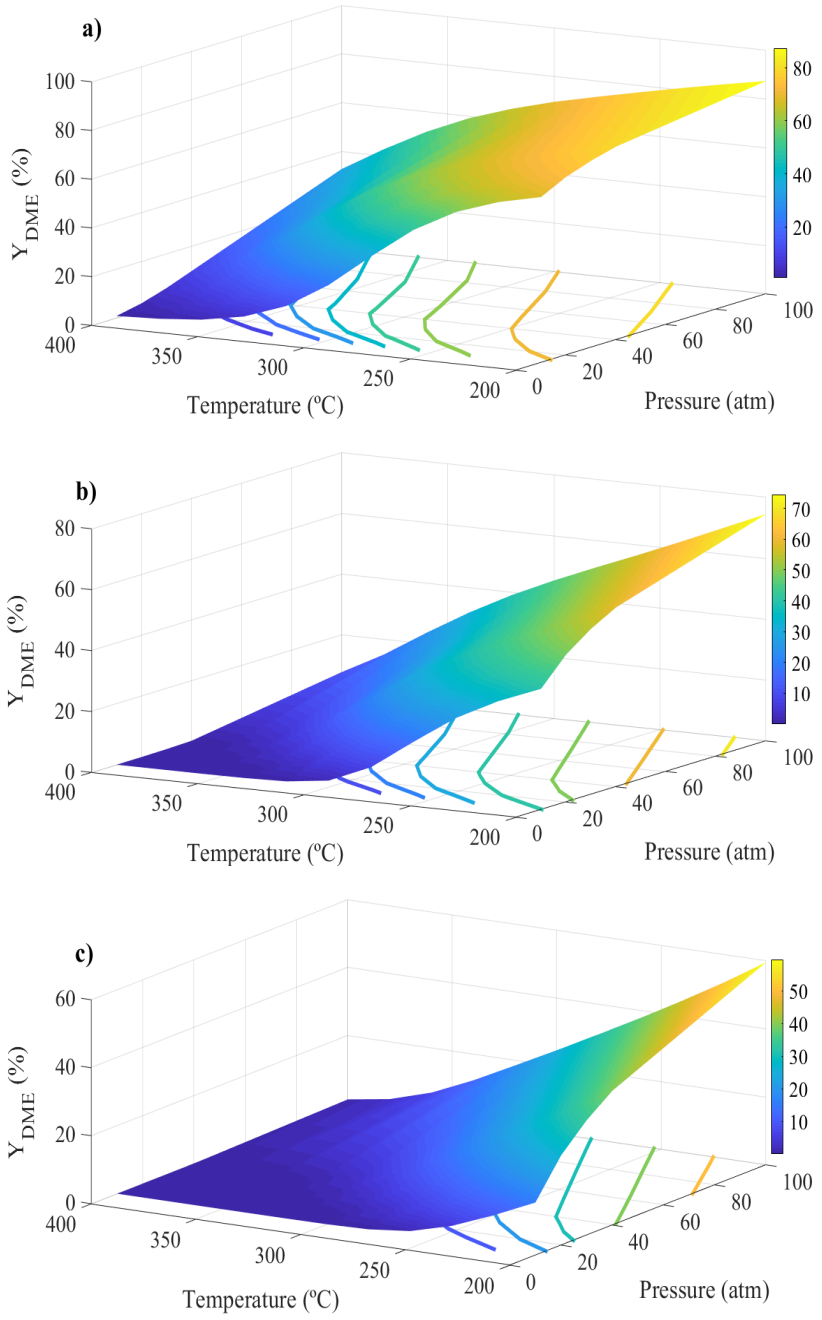

Figure 1.15: Evolution with temperature and pressure of DME yield in its direct synthesis thermodynamic equilibrium, varying CO_2 concentration in the feed. CO_2 / CO_x = 0 (a); CO_2 / CO_x = 0.50 (b); CO_2 / CO_x = 1 (c). H_2 / CO_x, 3 (Ateka et al., 2017b).

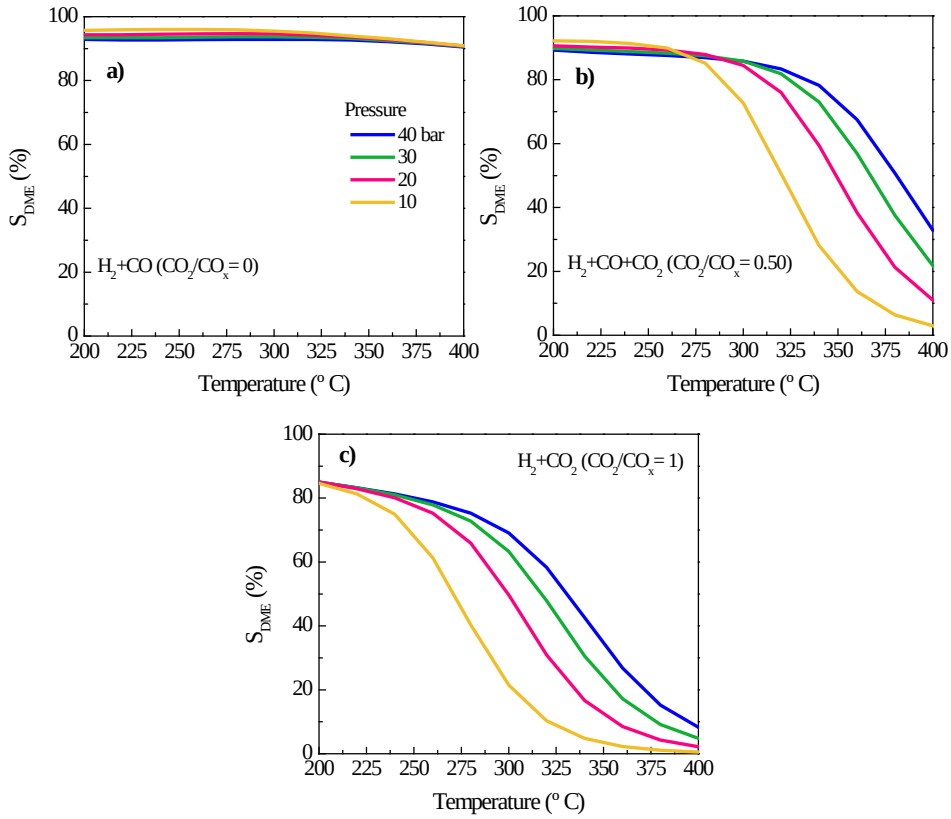

Figure 1.16: Evolution with temperature and pressure of DME selectivity in its direct synthesis thermodynamic equilibrium, varying CO_2 concentration in the feed. CO_2 / CO_x = 0 (a); CO_2 / CO_x = 0.50 (b); CO_2 / CO_x = 1 (c). H_2 / CO_x, 3 (Ateka et al., 2017b).

Reaction heat

In their interest to simplify the reactor design, Ateka et al. (2017b) have studied the feasibility of reaching thermo-neutral regime when co-feeding CO_2 with syngas, taking into account, on one side, the exothermic nature of CO and CO_2 hydrogenation and MeOH dehydration reactions and, on the other side, the endothermic nature of rWGS reaction. Figure 1.17 illustrates the isoquant curves of the generated heat in MeOH (Graph a) and DME synthesis (Graph b), for various CO_2 / CO_x

ratios in the feed and different reaction temperatures. It is observed that at a determined temperature in both processes, an increase of CO_2 concentration in the feed leads to a decrease in the generated heat. In methanol synthesis this decay is about from 80 KJ mol_C^{-1} without CO_2 in the feed and until 45 KJ mol_C^{-1} for feeds with a CO_2 / CO_x ratio = 0.5 (Figure 1.17a). Making the same comparison synthesizing DME, it decreases from 90 until 60 KJ mol_C^{-1} (Figure 1.17b). This effect is remarkable because it concludes that CO_2 co-feeding is a design variable to avoid the formation of hot spots in the reactor and in catalyst particles, which derives in control problems and Cu catalyst sintering. For this reason, CO_2 co-feeding contributes to preserve the catalyst thermal stability.

On the other hand, the comparison between the results in Figure 1.17 for the two processes shows that the direct synthesis of DME is more exothermic than that of methanol.

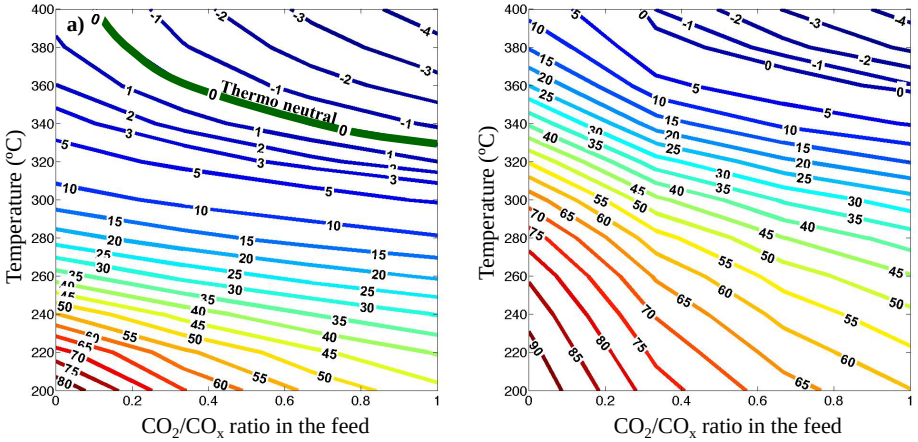

Figure 1.17: Isoquant curves of the generated heat in a temperature diagram vs. CO_2 concentration (CO_2 / CO_x ratio) in the feed for methanol synthesis (a) and DME synthesis (b). Reaction conditions: 30 bar, H_2 / CO_x, 3 (Ateka et al., 2017b).

The thermo-neutral operation requires temperatures higher than 300 °C for methanol synthesis and higher than 360 °C for DME synthesis. Consequently, to be able to work in thermo-neutral regime the catalyst should be drastically modified, considering the maximal temperature (300 °C) to avoid current Cu catalyst sintering.

1.2.4.3 Kinetic modeling

The model proposed by Ateka et al. (2018a) for the direct synthesis of DME from CO_2 / CO / H_2 on a CuO-ZnO-MnO / SAPO-18 hybrid catalyst is based on previous works feeding synthesis gas (Aguayo et al., 2007) and CO_2 (Ereña et al., 2011). This model considers the following kinetic equations for the reaction single steps:

Methanol synthesis through CO and CO_2 hydrogenation (steps in Eqs. 1.68 and 1.69):

$$r_{MeOH} = k_1 \left[p_{H_2}^2 \, p_{CO} - \frac{p_{CH_3OH}}{K_1} \right] \Theta \tag{1.73}$$

$$r_{MeOH} = k_1 \left[p_{H_2}^3 \, p_{CO_2} - \frac{p_{CH_3OH} \, p_{H_2O}}{K_1} \right] \Theta \tag{1.74}$$

Methanol dehydration towards DME (step in Eq. 1.71):

$$r_{DME} = k_2 \left[p_{CH_3OH}^2 - \frac{p_{CH_3OCH_3} \, p_{H_2O}}{K_2} \right] \tag{1.75}$$

WGS reaction (CO_2 formation) (step in Eq. 1.66):

$$r_{CO_2} = k_3 \left[p_{CO} \, p_{H_2O} - \frac{p_{CO_2} \, p_{H_2}}{K_3} \right] \tag{1.76}$$

Hydrocarbons synthesis (C_1 - C_4 paraffins) (step in Eq. 1.72):

$$r_{HC} = k_4 \left[p_{H_2}^3 \, p_{CO} - \frac{p_{CH_4} \, p_{H_2O}}{K_4} \right] \Theta \tag{1.77}$$

It should be noted that the expressions in Eqs. 1.73 - 1.77 are considered to be the elemental reactions, and that the hydrocarbons formation stoichiometry adopted in Eq. 1.77 corresponds to CH_4 formation (main hydrocarbon). Moreover, based on a study about the significance of the individual reactions, Ateka et al. (2018a) have proven that the contribution of CO_2 to methanol synthesis is less than 1 % of the contribution of CO, under the most favorable conditions, which allows disregarding Eq. 1.74.

Conversely, the model of Ateka et al. (2018a) includes a factor (Θ) in the kinetic equations of methanol and hydrocarbons formation. This term quantifies with Eq. 1.78 the limitation of these two steps activated with the metallic function, as consequence of the competition for the adsorption of H_2O and CO_2 with CO in the metallic sites.

$$\Theta = \frac{1}{1 + K_{H_2O}\, p_{H_2O} + K_{CO_2}\, p_{CO_2}} \tag{1.78}$$

The catalyst deactivation kinetic is quantified by Ateka et al. (2018a) considering that it affects directly and exclusively the methanol synthesis, whose velocity considers the catalyst activity with the expression:

$$r_{CH_3OH} = k_1 \left[p_{H_2}^2\, p_{CO} - \frac{p_{CH_3OH}}{K_1} \right] \Theta\, a \tag{1.79}$$

where the activity is the quotient of the reaction velocity at t time and at zero time on stream:

$$a = \frac{r_{MeOH}}{(r_{MeOH})_0} \tag{1.80}$$

The deactivation kinetic equation has been established as:

$$-\frac{da}{dt} = \frac{k_d (p_{CH_3OH} + p_{DME})}{1 + (K_{H_2O})_d\, p_{H_2O} + (K_{CO_2})_d\, p_{CO_2}}\, a^d \tag{1.81}$$

Eq. 1.81 corresponds to a deactivation in parallel with the progress of the reaction, where the methoxy ions precursors of coke are formed through methanol and DME adsorption in the metallic and acid sites. The formation of methoxy ions is attenuated by the competitive H_2O and CO_2 adsorption and it is described by a Langmuir-Hinshelwood type expression.

Ateka et al. (2018a) have used the kinetic model for the simulation (using MATLAB simulation program) of the direct synthesis of DME in an isothermal fixed bed reactor. Figure 1.18 shows the evolution of CO_2 conversion (fraction of fed CO_2 that is converted into oxygenates) with space time and time on stream, for different CO_2 / CO_x ratios (0.3, 0.5 and 0.8) and constant reaction conditions (275 °C; 30 bar; H_2 / CO_x, 3).

The results shown in Figure 1.18 highlight that the efficacy of CO_2 conversion is strongly dependent on CO_2 / CO_x ratio in the feed, which determines the required conditions for the conversion. Thus, for a low CO_2 / CO_x ratio in the feed (CO_2 / CO_x = 0.5 / 0.7, Figure 1.18a) the maximal CO_2 sequestration (around 3 %) is obtained with a small space time value, 1 $g_{cat}h(mol_C)^{-1}$, and is a well defined maximum. Regarding CO_2 / CO_x ratio = 0.5 (Figure 1.18b), CO_2 conversion achieves a maximum of 6 % and is obtained within a wider range of space time (between 1 and 4 $g_{cat}h(mol_C)^{-1}$).

Increasing the CO_2 / CO_x ratio until 0.8 (Figure 1.18c), CO_2 conversion is higher ($\approx$ 15 %) and enhances slightly with space time value between 4 and 10 $g_{cat}h(mol_C)^{-1}$. On the other hand, on Figure 1.18 can be observed that CO_2 conversion is quasi independent of time on stream, except when CO_2 / CO_x ratio is less than 0.5 and for high space time values, in which case it decreases with the time on stream due to the catalyst deactivation at these conditions.

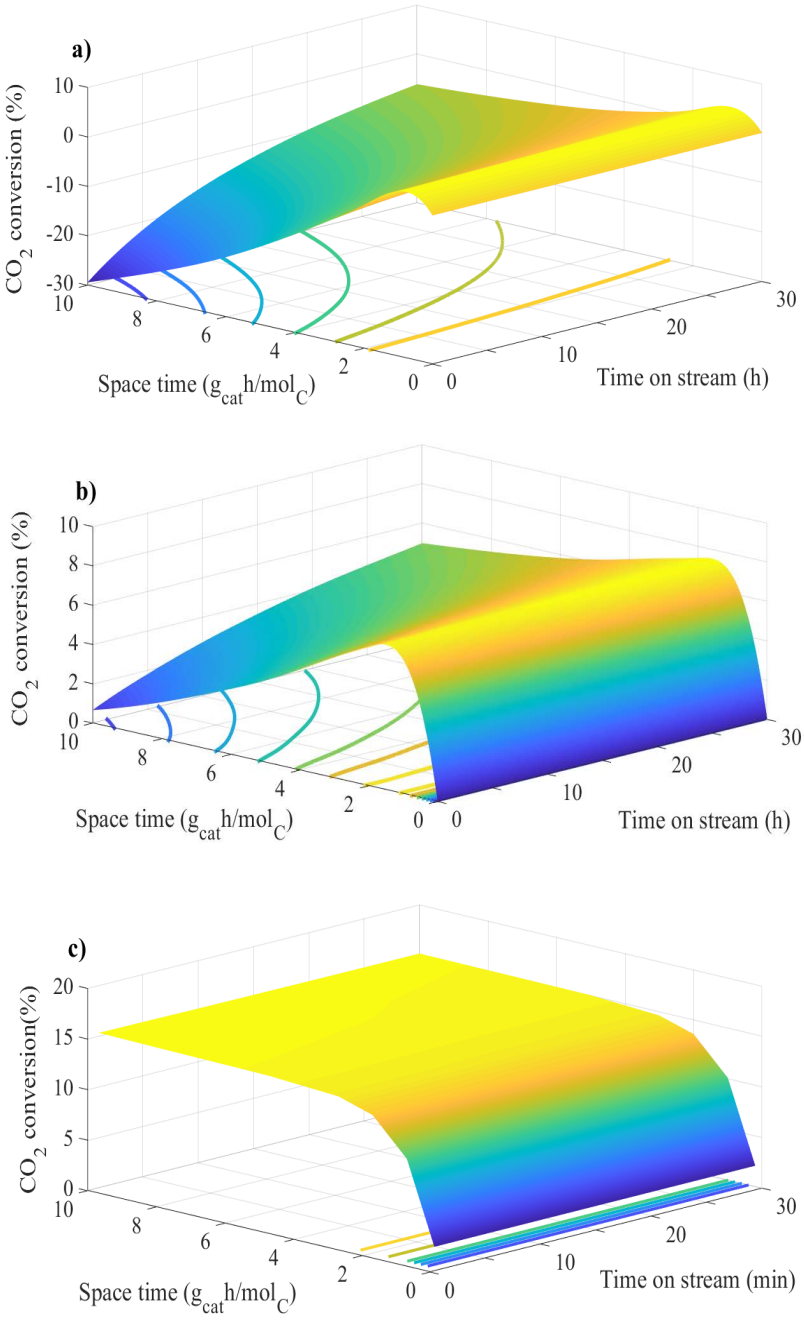

Figure 1.18: CO_2 conversion evolution with space time and time on stream for CO_2 / CO_x of 0.3 (a), 0.5 (b) and 0.8 (c). Reaction conditions: 275 °C; 30 bar; 10.18 $g_{cat}h(mol_C)^{-1}$; H_2 / CO_x, 3 (Ateka et al., 2018a).

At the same time, Ateka et al. (2018a) emphasize that CO_2 co-fed with synthesis gas, despite its conversion, has an adverse effect of decreasing DME yield that must be taken into account for the process profitability.

Figure 1.19 shows that even though increasing CO_2 / CO_x ratio in the feed allows achieving higher CO_2 sequestration for a determined space time value, DME yield decreases.

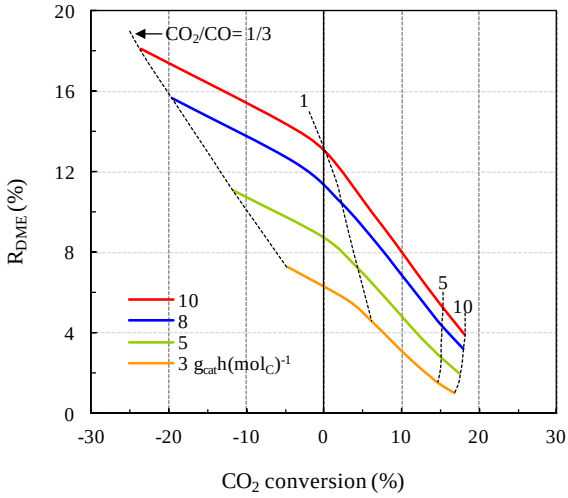

Figure 1.19: Relationship between CO_2 conversion and DME yield at zero time on stream, for different values of CO_2 / CO_x ratio in the feed and space time. Reaction conditions: 275°C, 30 bar; 5h time on stream; H_2 / CO_x, 3 (Ateka et al., 2018a).

On the other side, with a CO_2 / CO_x ratio less than 0.8, the enhancement in CO_2 conversion requires decreasing space time value, with the consequent decrease of DME yield. Increasing CO_2 / CO_x ratio (higher than 0.8), this tendency is slightly reversed and the increase of space time favors also DME yield enhancement.

1.3 Membrane reactor for DME synthesis

The initiative of the membrane reactor arises in this thesis for the direct synthesis of DME, principally in order to displace the thermodynamic equilibrium of methanol synthesis, rWGS reaction and methanol dehydration, whose thermodynamic equilibrium is disfavored with CO_2, co-fed with synthesis gas. The theoretical advantages of this initiative have been studied by simulation (Ateka, 2014; De Falco et al., 2017a,b; Diban et al., 2013, 2014; Iliuta et al., 2010).

1.3.1 General concepts

The membrane reactor design is an interesting implementation within the concept of processes integration, by the function of a selective membrane to modify the composition of the reaction medium. In this sense, the thermodynamic limitations due to the composition are reduced, the reaction rate and/or selectivity are enhanced and, furthermore, the energetic requirement decreases. The basic goal of the reactor design is to obtain a compact, stable and versatile equipment. To achieve these objectives, the relative simplicity of the membrane reactor presents remarkable advantages in comparison with other processes integration alternatives, also studied for the removal of H_2O from the reaction medium. These alternatives require great innovations in the reactor design regarding the conventional fixed bed reactors. Thus, the combination with reactive distillation (Silva et al., 2011) is a more complex system and the adsorption demands reactors with catalyst and adsorbent circulation (Abashar and Al-Rabiah, 2018).

Diban et al. (2013) have reviewed the application of membranes in catalytic reactors, where generally the catalyst is placed in a fixed bed and the membrane is

located co-axially, with the following roles: 1) longitudinal distribution control of a reactant, for which the membrane is selective (reactor "crossed" flows concept), and; 2) longitudinally and selectively separate a component of the reaction medium, decreasing thereby its concentration in the medium through the feed or products flow sweep, with the subsequent energetic contribution (Rahimpour and Dehghani, 2016). Conversely, the concentric tube with the membrane can be on the outer or the inner part of the catalytic bed. Figure 1.20 shows the two strategies scheme for methanol synthesis with the membrane in the middle of the reactor. A hydrophilic membrane, H_2O permselective, that facilitates the removal of H_2O is used in Figure 1.20a. In the permeate section, H_2O is subsequently eliminated by the sweep gas, favoring the equilibrium displacement in methanol formation (Farsi and Jahanmiri, 2012; Rahimpour and Dehghani, 2016). Mardanpour et al. (2012) have simulated this strategy for the direct synthesis of DME. In Figure 1.20b a H_2 permselective Pd membrane is applied. Synthesis gas is injected within the catalytic bed and the gas product is compressed and recirculated towards the permeation central region, allowing feeding H_2 with the suitable concentration in each longitudinal position (Bayat et al., 2014).

Furthermore, Diban et al. (2013) distinguish between inert and catalytic membranes (with an embedded catalyst or with catalytic activity), that combines the actions of a component separation and the activation of one of the single reactions, in order to intensify the selective formation of products.

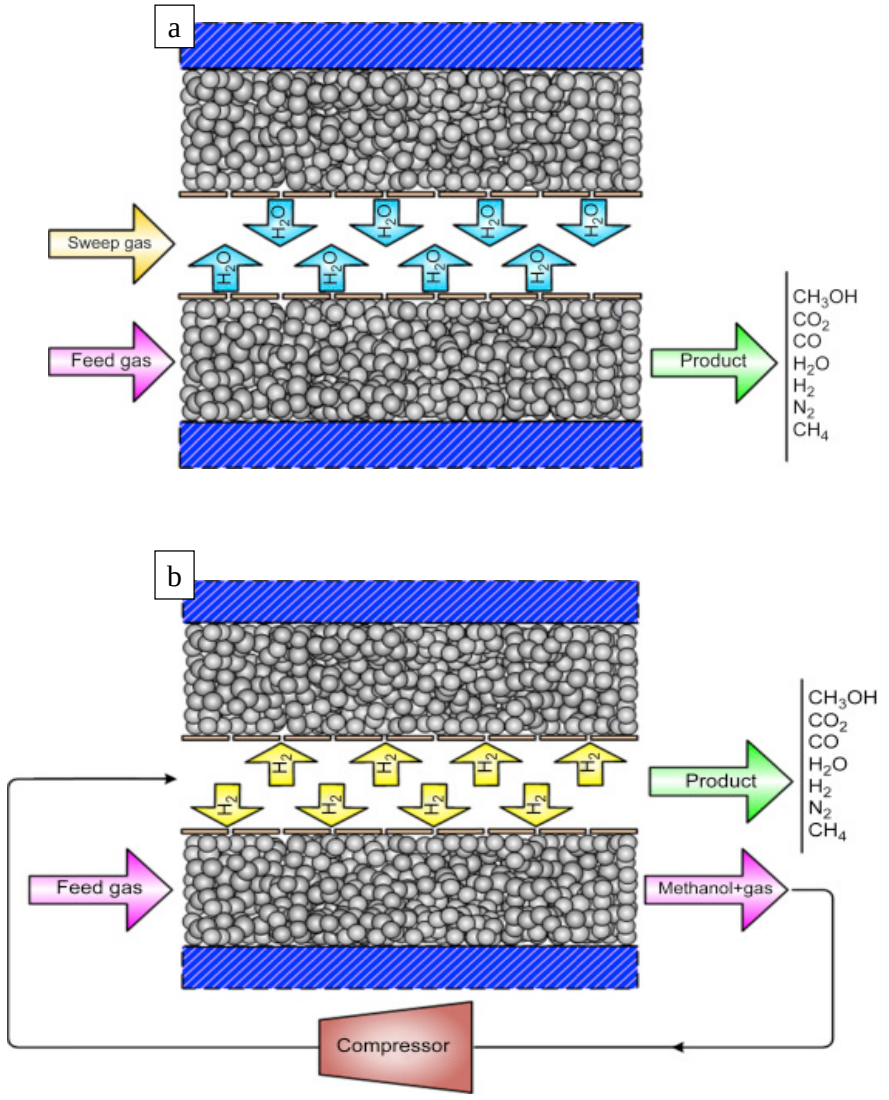

Figure 1.20: Methanol synthesis schemes with H_2O (a) and H_2 (b) permselective membranes (Bayat et al., 2014; Farsi and Jahanmiri, 2012).

1.3.2 Hydrophilic membranes

The main requirements to integrate a hydrophilic membrane in a catalytic reactor are: 1) thermal stability at high temperature and under high pressure; 2) great H_2O selectivity, and; 3) high H_2O flux and permeability. H_2O permselective membranes have been extensively used in processes at low temperatures (< 150 °C), in desalination, and in natural gas, air or organic compounds dehydration. Focusing on the requried conditions for DME synthesis (> 200 °C and high pressure), polymeric membranes have been discarded, whose performances diminish increasing the temperature from 50 °C to 200 °C (permeability from $4{\cdot}10^{-7}$ to $4{\cdot}10^{-8}$ mol s^{-1} m^{-2} Pa^{-1} and H_2O/H_2 selectivity from 150 to 18) (Struis and Stucki, 2001). Above 200 °C, amorphous microporous membranes (supported on ceramic materials) have a moderate permeability (around 10^{-7} mol s^{-1} m^{-2} Pa^{-1}) and low H_2O/H_2 selectivity (< 10) (Lee et al., 2006). Sea and Lee (2006) have used a silica-alumina membrane (permeability of 10^{-7} mol s^{-1} m^{-2} Pa^{-1} and H_2O/H_2 selectivity of 8.4) in methanol dehydration towards DME, achieving a methanol conversion of 82.5 % (68 % in fixed bed reactor without membrane). It is remarkable that these membranes have a limited thermal stability.

Membranes considered more adequate to operate above 200 °C are the microporous zeolites, crystallines, with a uniform pore size, high mechanical resistance, and chemical and thermal stability. Moreover, with the selection of the zeolite and its composition (particularly controlling Si / Al ratio) properties such as permeability or selectivity can be modeled. H-SOD (sodalite) and MOR (mordenite) can achieve a permeability within the range of 10^{-7} - 10^{-6} mol s^{-1} m^{-2} Pa^{-1} and a H_2O/H_2 selectivity higher than 10 at 250 °C (Espinoza et al., 2000, 2002; Rohde et al., 2008), although it was tested that H-SOD has a limited thermal stability

above 200 °C. Diban et al. (2013) have presented in their review the zeolite applications with different crystalline structure (LTA, MFI or HZSM-5, MOR, MER or merlionite, PHI or phillipsite and CHA or chabazite) in the alcohol esterification. Fedosov et al. (2015) have used a LTA membrane (NaA) for the dehydration of methanol towards DME, achieving a methanol conversion of 88 % (80 % without membrane) at 250 °C.

The fuel production processes, where the utilization of zeolite membranes have received more attention, are the Fischer-Tropsch (FT) synthesis, and, to a lesser extent, the WGS reaction (Reddy and Smirniotis, 2015) and methanol synthesis (Rahimpour and Dehghani, 2016).Espinoza et al. (1999) have described in their patent the comparison between the properties of different zeolites (MOR, MFI, A, CHA) and silicalite at FT synthesis conditions. On one side, at low temperatures (200 - 250 °C) and therefore with gas-liquid-solid (G-L-S) contact due to the wax formation, and, on the other side, at high temperature (300 - 360 °C) when the reaction is G-S. The great performance of hydrophilic zeolites in this reaction have been investigated by different authors (Rohde et al., 2005). Gallucci et al. (2004) have experimentally demonstrated the higher yield of methanol synthesis using a LTA membrane reactor. Recently, Gorbe et al. (2018) have analyzed H_2O separation capacity of zeolite A from H_2, CO_2 and H_2O mixtures within a wide range of pressure (100 - 270 kPa), temperature (160 - 260 °C) and H_2O partial pressure, observing a remarkable limitation of this separation capacity above 240 °C.

1.3.3 Simulation of the direct synthesis of DME

The utilization of membrane reactors in the direct synthesis of DME has been studied by theoretical modeling and simulation, giving special attention to the efficiency of this reactor for CO_2 conversion. Figure 1.21 shows the block diagram of the membrane reactor system, and CO_2 flow separation and recirculation units. In this scheme proposed by De Falco et al. (2017a,b), condensation and gas separation systems are described. Two recirculation loops are established through a H_2O condensation unit from the permeate flow and a non-condensable gases (H_2, CO_2 and CO) separation unit from the reaction flow. Methanol, DME and H_2O vapors are condensed, from which subsequently DME and methanol are successively separated through each distillation steps.

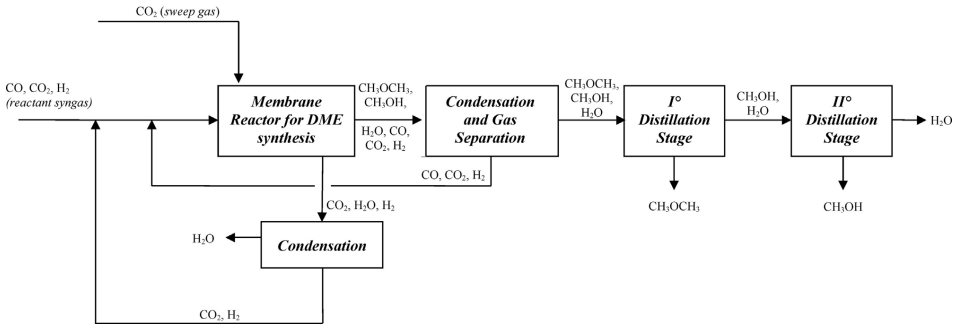

Figure 1.21: Layout of the membrane reactor and the separation and recirculation units for the direct synthesis of DME (De Falco et al., 2017a,b).

The membrane reactor simulation study proposed by Iliuta et al. (2010) is pioneer determining the importance of the increase of CO_2 ratio in the feed with the membrane efficiency, in order to favor the enhancement in methanol yield and DME selectivity, justified by the displacement of the rWGS reaction. These authors have considered gas plug flow in both reaction and permeate regions, bed isothermicity, using the kinetic of a CuO-ZnO-Al_2O_3 / HZSM-5 catalyst and considering

only H_2O and H_2 involved through the membrane transport.

Diban et al. (2013) have studied in more detail the utilization of a packed bed membrane reactor (PBMR) design model. This research study has evaluated the effect of the membrane transport properties (H_2O permeability and H_2O / H_2, H_2O / CO, H_2O / CO_2, H_2O / CH_3OH, H_2O / DME, H_2O / hydrocarbons selectivity) using the appropiate kinetic of a CuO-ZnO-Al_2O_3 / γ-Al_2O_3 catalyst. Gas plug flow and reactor isothermicity are considered in this model. Based on HZSM-5, MOR and SIL zeolite membranes properties, collected from the literature for FT synthesis, it was determined an increase in CO_2 conversion of 34 %. Nevertheless, the limited selectivity of these membranes decreases DME yield comparing to the values obtained without using a membrane. This decrease is due to the permeation of methanol, which can be reduced using the same reactants partial pressure both in the reaction and permeate sections. Therefore, Diban et al. (2013) have defined the required permeability range ("ideal" membranes) between $0.5 \cdot 10^{-7}$ - $1.2 \cdot 10^{-7}$ mol s^{-1} m^{-2} Pa^{-1} for obtaining considerable enhancements both in CO_2 conversion and DME yield, which requires the improvement of the permeation properties of these microporous materials.

The simulation has allowed Diban et al. (2014) to study the effect of the sweep conditions, such as the flow (within the range from 0.06 - 1.80 mol_{CO_x} h^{-1}) and the gas recirculation factor ($0 < \alpha < 1$). The enhancement in CO_2 conversion has been determined increasing the sweep flow above 0.18 mol_{CO_x} h^{-1}. Additionally, the sweep gas recirculation should be controlled due to its effect on DME yield, as a result of the synergy between H_2O and methanol removal from the reaction medium.

In the simulation of De Falco et al. (2017a,b) a CO_2 flow in the sweep stream

has been incorporated, which connects to the permeate section (Figure 1.21). In contrast, the approach of Iliuta et al. (2010) and Diban et al. (2013, 2014) aims at that the sweep flow contains the same H_2 / CO_x ratio than the feed in the reaction section. The equations in the model include the mass balances for 6 components in the reaction medium and the heat balance (different from previous models considering isothermal reactors), calculated with the assumption of a plug flow reactor (1 m length and 0.038 m of diameter). The implemented kinetic that of a CuO-ZnO-Al_2O_3 / HZSM-5 catalyst. The studied variables by De Falco et al. (2017a,b) are: temperature, 200 - 300 °C; pressure, 5 - $7{\cdot}10^6$ Pa; space velocity (GHSV), up to 7 10^3 h^{-1}; CO_2 / CO_x ratio in the feed, 0.5 - 0.8; H_2 / CO_2 ratio, 1 - 3; and, sweep flow (in co-current mode regarding the reaction flow). The authors have determined the following optimal reaction conditions: inlet temperature, 200 °C; pressure, $7{\cdot}10^6$ Pa; space velocity (GHSV), $7{\cdot}10^3$ h^{-1}; CO_2 / CO_x ratio in the feed, 3; H_2 / CO_2 ratio, 0.7; and, sweep steam / total stream ratio, 5. At these conditions DME yield achieves 75 % (57 % in the conventional reactor), DME selectivity of 99 % (88 % in the fixed bed reactor), CO_2 conversion of 69 % (53 %) and CO_x conversion of 75 % (65 %).

2

EXPERIMENTAL

2 | Experimental

2.1 Membrane reactor design

2.1.1 Equipment description

The membrane reactor system has been designed, built up and put into operation through the appropriate adjustment of a commercial equipment for catalytic reactions (Microactivity Reference from PID Eng&Tech., Madrid, Spain). Its configuration is shown in Figure 2.1.

This configuration enables the feeding of both liquids and gases, as well as to work in two separate zones, reactor and permeate sections. The feed gases enter the system through two sets of mass flow controllers (Bronkhorst High-Tech B.V. Series). One is in charge of feeding the reaction section whereas the other manages the permeate section feed. In order to measure and control the flow rates in both sections, the sets are equipped with shut-off and non-return valves, as well as reading systems. The feed gases are N_2 (inert gas), He (carrier gas towards the gas chromatograph (Varian CP-490)) and the reactive gases H_2, CO_2, CO_2 / CO and synthesis gas (H_2 / CO).

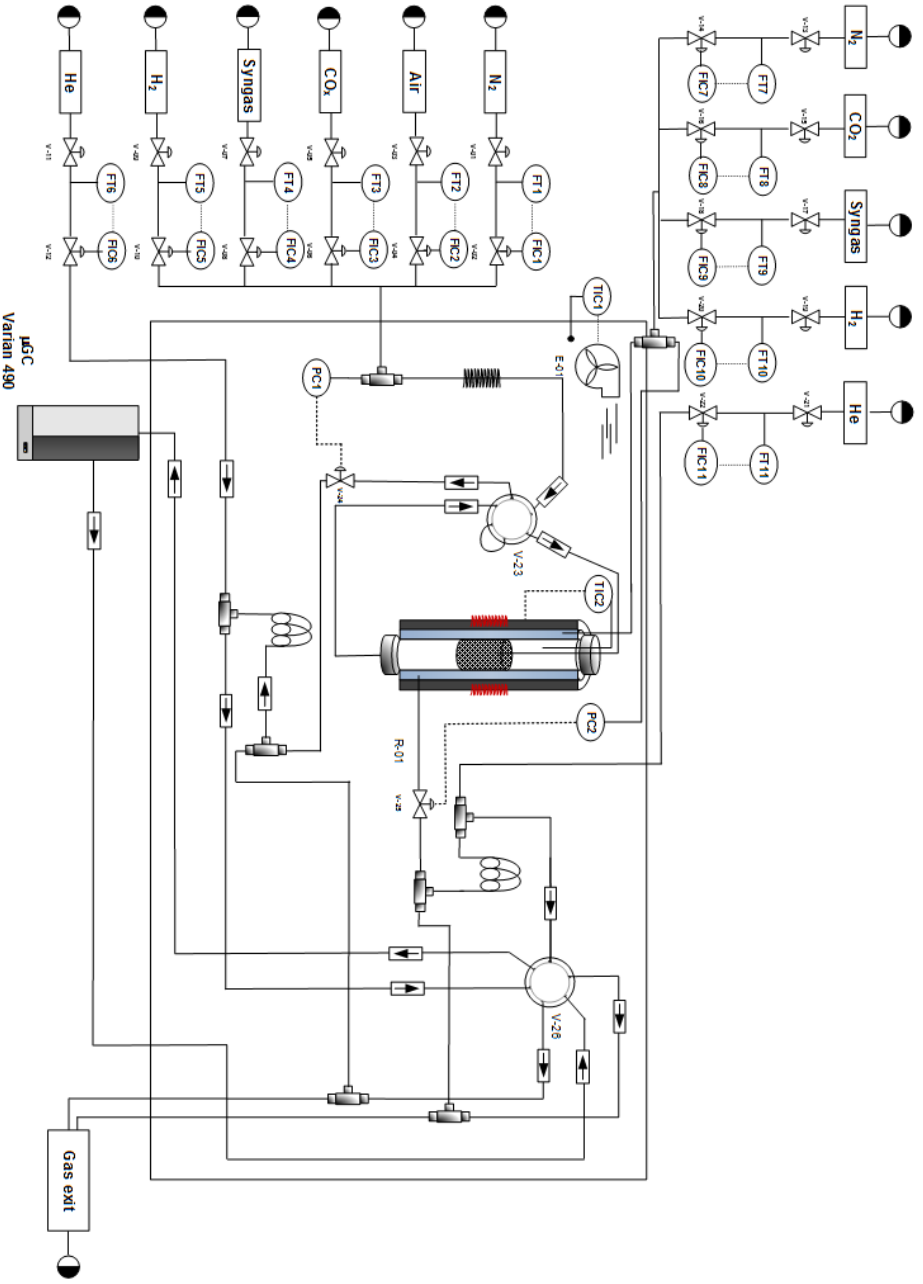

Figure 2.1: Flow diagram of the reaction equipment.

Inlet gases (and/or liquids) are firstly introduced, in each experiment, into the hot box (limited by a rectangle in Figure 2.1), where they are homogenized and pre-heated to avoid any condensation. On one side, in the case of the reaction section, the feed is mixed in a T-type connection, which on one end the pressure is measured and the other is connected to the bypass valve V-23 (Figure 2.2), through which subsequently flows into the reactor. On the other side, the feed gases initially enter the permeate section without circulating through any valve. The other bypass valve V-26 (Figure 2.2) is placed at the outlet of the reactor and controls which section (reaction or permeate) is analyzed in the gas chromatograph.

The temperature is controlled and monitored by TOHO TTM-005 controllers and is measured by thermocouples K-Type (TIC-1 and TIC-2). One of them is placed in the catalytic bed within the reactor tube controlling the surrounded thermal resistance, and the other is located in the hot box of the reactor system. Additionally, there is a heating system surrounding the outlet flow of gases, in order to avoid any condensation before entering the gas chromatograph.

Two transducers, PIC-1 and PIC-2 (Sensor-Technik-Wiedemann GmbH), were used to control the pressure of the system. They act simultaneously on two needle pressure valves (V-14 and V-15), placed at the reactor outlet, which regulate the pressure in both sections. The reaction feed gases pass through the 6-port bypass valve V-23 (Figure 2.2a), which determines if they are conducted towards either the gas chromatograph or the gas exit (bypass connected), or enter the reactor (bypass disconnected). The packed bed membrane reactor (PBMR) system, in comparison with a packed bed reactor (PBR) one, requires a second bypass valve V-26 within it (Figure 2.2b). This regulates if either the reaction or the permeate section will be analyzed. If the bypass is connected, the permeate sample is conducted to the gas chromatograph and the reaction one towards the gas exit. Otherwise (bypass

disconnected), the reaction sample will be transported to be analyzed.

Once the reaction has taken place, a small part of the reaction and permeate fluxes (around 1 cm^3) are diluted in a He stream and are sent to the gas chromatograph to be analyzed continuously in-line every 2.5 min.

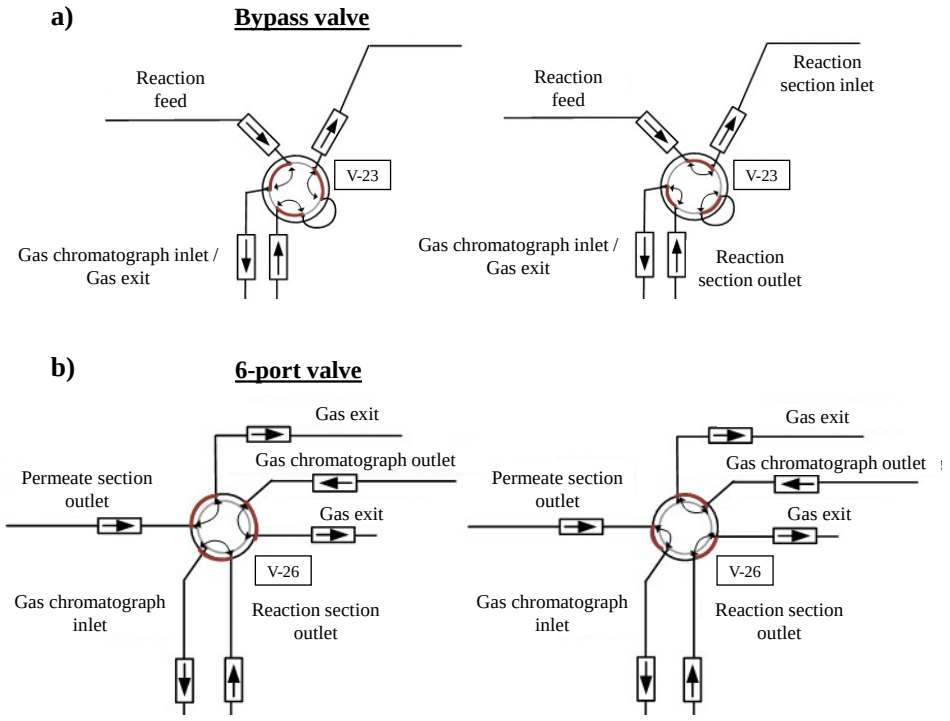

Figure 2.2: Operation schemes of the bypass valve V-23 (a) and the 6-port valve V-26 (b).

2.1.2 Packed bed membrane reactor (PBMR)

The stainless steel packed bed membrane reactor (PBMR), shown in Figure 2.3, structurally presents two concentric sections: the reaction one, in which the catalytic bed is located, surrounded by another concentric system that allows the

sweep of the permeate flow (permeate section). The different components of the PBMR are: 1) thermocouple, to measure the temperature in the catalytic bed; 2) inlet of the reaction section; 3) reaction section, membrane tube with the central porous region; 4) inlet of the permeate section; 5) thermal resistance; 6) outlet gases from the reaction area; and 7) outlet flow of the permeate section.

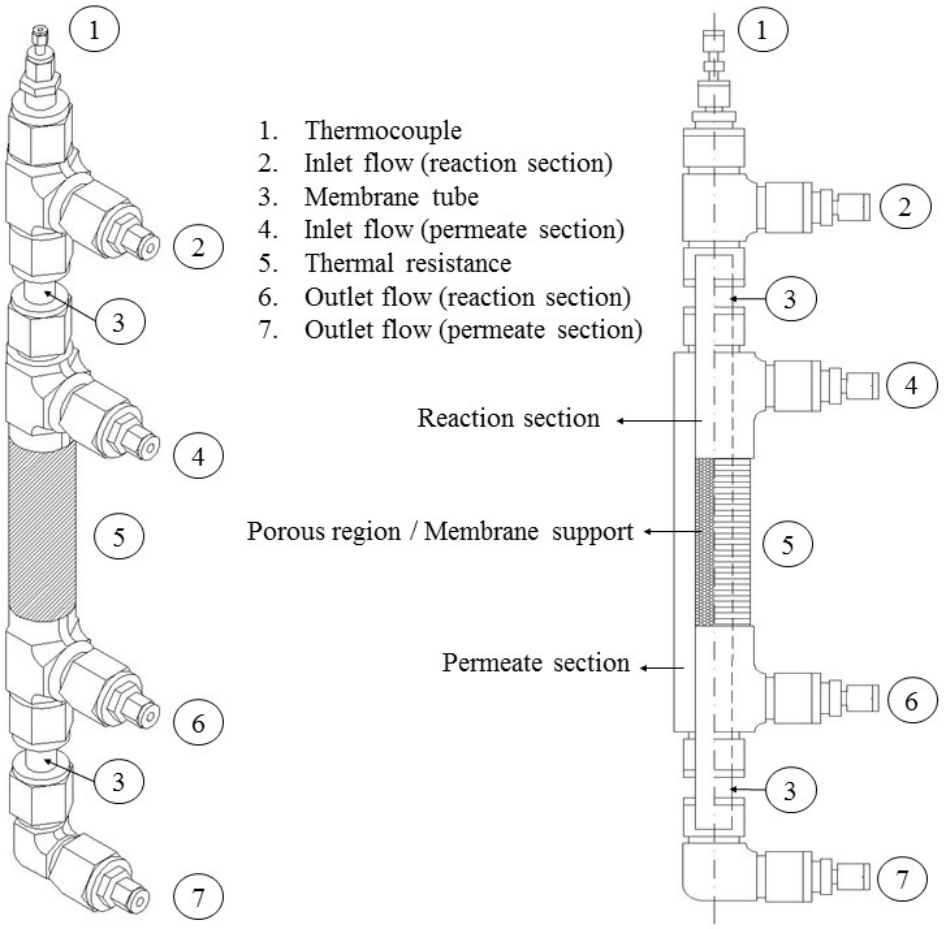

Figure 2.3: Isometric and section view of the packed bed membrane reactor (PBMR).

The reaction section, shown in Figure 2.4, is limited by the stainless steel membrane tube (*Mott Corporation*).

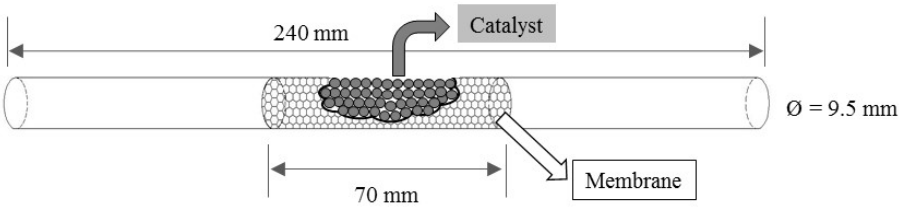

Figure 2.4: Dimensions of the reaction section and the catalytic bed

Its inner diameter is 9.5 mm and its length, 240 mm. It has a central region of 70 mm, that corresponds to the catalytic bed, and its outer surface, allows the permeation of water vapour from the reaction medium towards the permeate section.

The catalytic bed is composed of a mixture of catalyst and solid inert, carborundum (CSi) with an average particle diameter > 0.5 mm, obtaining a sufficient bed length in order to ensure a homogeneous distribution through it and its isothermicity when operating with a low space times.

2.1.3 Control system

The PBMR system is equipped with a process control software called Process@, which allows to handle and program the operating conditions creating automatic sessions. This application enables designing, configure and perform sequentially operating sessions. The main sessions, from which other subsequent ones are derived varying feed, pressure and temperature among others, are described in the subsequent sections.

2.1.3.1 Catalyst reduction step

1. Establishment of the appropriate communication with the reactor system and launch of the process.
2. Reduction for 14 h at 200 °C with a low H_2 (10 %), diluted in N_2.
3. Reduction for 1.5 h at 250 °C with a higher H_2 concentration (20 %).
4. Sweep with N_2 for 20 min.
5. Stabilization of the operating conditions (reactor and hot box temperature, and pressure), with V-23 bypass valve connected, for the subsequent reaction step.

2.1.3.2 Reaction step

1. Establishment of the appropriate communication with the reactor system and the operating conditions, with V-23 bypass connected.
2. N_2 and He flows stabilization. The first one is equivalent to the sum of the reactants flow, and the second one acts as a carrier to conduct the gas samples towards the gas chromatograph.
3. Stop of N_2 flow and stabilization of the following reactants flows in independent sessions for each one.
4. Once all the reactants flows are stabilized, the V-23 bypass valve is disconnected and the reaction starts.
5. End of the reaction and sweep with N_2 in reaction conditions (temperature and pressure).
6. Reaction and permeate sections cooling until 200 °C under the reaction pressure.
7. Sections and hot box cooling, and pressure diminishing.
8. Reactor system shutdown.

2.1.4 Reaction products analysis

The reaction products are analyzed at the system outlet in a gas micro-chromatograph (micro-GC Varian CP-490), equipped with fixed injectors and TCD detectors implemented in two analytic modules. Each module is provided with one of the following columns:

- Molecular sieve (MS-5): (10 m x 12 μm) where H_2, O_2, N_2 and CO are quantified.
- Porapak Q (PPQ): (10 m x 20 μm) where CH_4, CO_2, ethane, H_2O, propane, methanol and DME are analyzed.

The obtained products results are displayed in chromatograms like the ones shown in Figures 2.5 and 2.6.

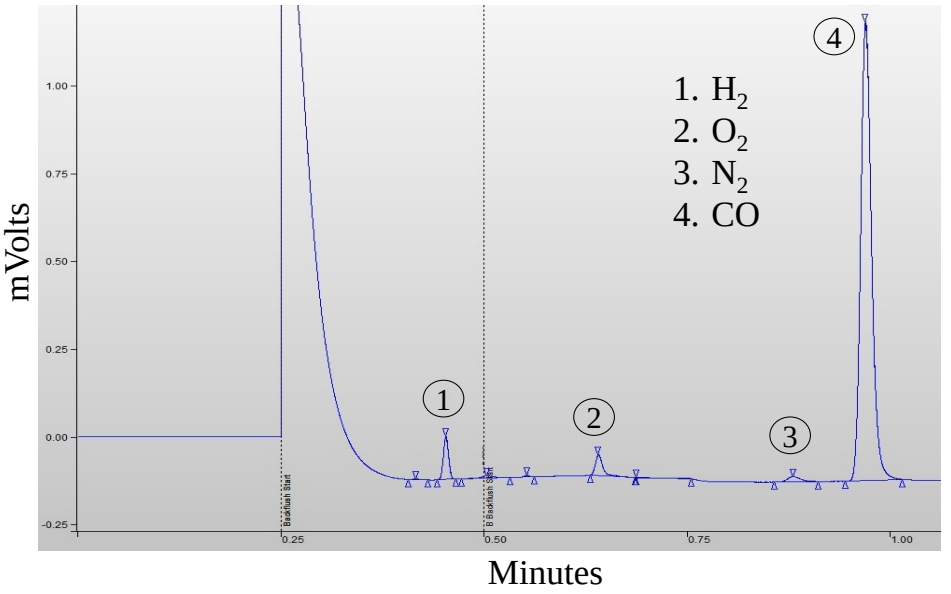

Figure 2.5: Typical chromatogram of the molecular sieve (MS-5) column of the micro-GC Varian CP-490.

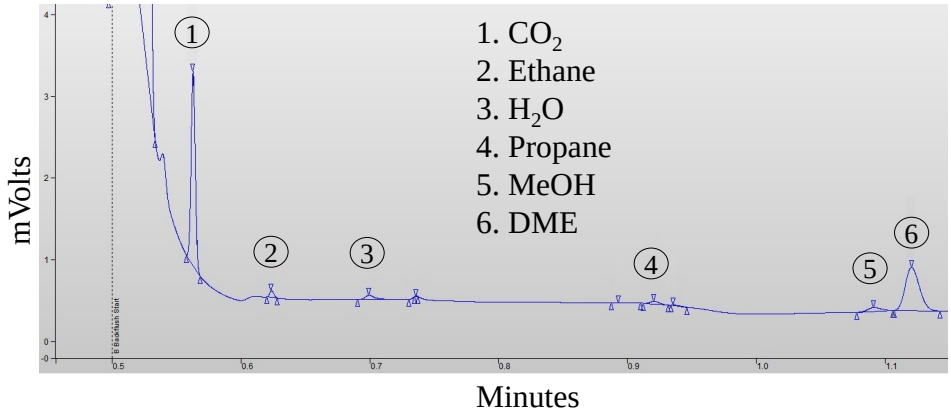

Figure 2.6: Typical chromatogram of the PPQ column of the micro-GC Varian CP-490

Moreover, in Table 2.1 the analysis conditions corresponding to modules previously described are related.

Table 2.1: Analysis conditions of the micro-GC Varian CP-490 modules.

	MS-5	PPQ
Column temperature (°C)	95	120
Injector temperature (°C)	110	110
Injection time (ms)	3	20
Backflush (ms)	15	30
Sample time (s)	10	10
Analysis time (s)	150	150
Pressure (psi)	20	20

Both analytic modules, MS-5 and PPQ, are equipped with a micro-injector with backflush, being able to inject different gas volumes. This automatic system allows the programming of flows as well as the flow reverse of each column, in order to

avoid the entrance of non-desirable compounds.

In order to identify and quantify properly the reaction products from both the reaction and permeate sections, a micro-GC calibration has been performed using a pattern compounds bottle and gas mixtures of know composition. The area of each chromatographic peak is proportional to the molar quantity of the compound present in the sample, taking into account the calibrated specific response factors of the area of each compound (Table 2.2).

Table 2.2: Calibration factors of the micro-GC Varian CP-490.

Column	Compound	Retention (min)	Reaction Factor	Permeate Factor
MS-5	H_2	0.50	360	300
	N_2	0.58	5.64	5.12
	CO	0.68	5.46	3.87
PPQ	Methane	0.52	1.13	1.40
	CO_2	0.55	1.00	1.00
	Ethane	0.62	1.17	1.25
	H_2O	0.69	2.39	2.54
	Propane	0.93	0.93	0.98
	MeOH	1.08	1.32	2.01
	DME	1.11	1.13	1.19

The acquisition and processing of the data is carried out by the Star Toolbar software, which allows the chromatographic areas to be integrated using a previously defined method. The product between the factor of each compound and its integrated surface allows the molar fraction of the sample to be known, being able to calculate the reaction indexes that will be described in Section 2.1.5.

2.1.5 Reaction indexes

The results have been quantified by the reaction indexes described as follows: 1) yield of each product; 2) CO_2 conversion; 3) CO_x conversion, and; 4) selectivity of each product. In this sense, the yield of each i product (Y_i) is defined by the ratio between its molar flow rate and the molar flow rate of CO_x in the feed:

$$Y_i = \frac{nC_i F_i}{F^0_{CO_x}} 100 \tag{2.1}$$

being nC_i the number of carbon atoms of each i product, respectively. F_i, the molar flow rate of the i product at the reactor outlet and $F^0_{CO_x}$ the molar flow rate of CO_x in the feed, respectively. It has to be considered that at the outlet of a PBMR two different flows are analyzed (reaction and permeate sections). Therefore, both reaction (R) and permeate (P) yields of products are added in order to define a total yield:.

$$Y_i = Y_i^R + Y_i^P \tag{2.2}$$

being Y_i^R and Y_i^P calculated from Eq. 2.1.

With regard to the conversion of CO_2, it is defined by the expression:

$$X_{CO_2} = \frac{F^0_{CO_2} - F_{CO_2}}{F^0_{CO_2}} 100 \tag{2.3}$$

where F_{CO_2} is the molar flow rate of CO_2 at the reactor outlet. This conversion is directly related with the capability of valorizing CO_2 of each reactor configuration.

Moreover, the conversion of CO_x (X_{CO_x}) is defined by the ratio between the moles of CO and CO_2 in the feed that have been converted (Eq. 2.4):

$$X_{CO_x} = \frac{F^0_{CO_x} - F_{CO_x}}{F^0_{CO_x}} 100 \tag{2.4}$$

being F_{CO_x} the molar flow ($CO + CO_2$) at the outlet of the reactor.

And finally, the selectivity (S_i) represents the ratio between the molar flow of each compound (i) in the product flow (F_i) and the total molar flow of the products (organic compounds, DME, methanol and paraffins), based on C units:

$$S_i = \frac{n_i F_i}{\sum_i (n_i F_i)} 100 \tag{2.5}$$

Like in the yield calculation (Eq. 2.2), both reaction and permeate selectivities of products are added in order to define a total selectivity:

$$S_i = S_i^R + S_i^P \tag{2.6}$$

The hydrocarbons present in the product flow are mostly paraffins and are differentiated into methane, ethane and propane. Therefore, the carbon quantity within the hydrocarbons fraction is defined as:

$$n_{HC} = n_{HC_4} + 2 \cdot n_{C_2H_6} + 3 \cdot n_{C_3H_8} \tag{2.7}$$

2.2 Catalyst synthesis

By the synthesis of DME a bifunctional (hybrid) catalyst was employed. This catalyst is made of a metallic phase, responsible for methanol synthesis, and an acid function that enables the dehydration of methanol towards DME (Sierra et al., 2010).

2.2.1 Metallic Function Preparation

The metallic function of the catalyst was synthesized following an adaptation of the procedure described by Ereña (1996).

a) *Preparation of the Solutions*

First, acid solutions of cupper (Panreac), zinc (Panreac) and zirconium (Panreac) nitrates with a total concentration of nitrates equals to 1 M were prepared. These three solutions were mixed having an atomic ratio of Cu:Zn:Zr = 2:1:1.5.

At the same time, a basic solution of sodium carbonate (Panreac) with a concentration of 1 M was prepared.

b) *Coprecipitation of the Metals*

The acid solution (nitrates solution) and the basic one (sodium carbonate) were simultaneously added over deionized water while stirring under controlled conditions (constant temperature of 70 °C and pH interval of 6.8 - 7.2). Afterwards, the precipitate was aged under stirring for 1 hour maintaining these conditions constant, in order to complete the coprecipitation of the metals. During this period of time, small volumes of the acid solution were added to maintain the pH constant.

c) *Separation of the Metallic Carbonates*

Once the co-precipitation is completed, the heating and stirring were removed and the water was separated from the solid precipitate for its subsequent centrifugation, filtering and washing with deionized water. The aim of this step is the elimination of sodium ions (Na^+) in the solution, which decrease the activity of the catalyst for the ($CO + CO_2$) hydrogenation to methanol (Jun et al., 1998). The presence of the residual sodium has been checked by the brucine test.

d) *Dry and Calcination of the Metallic Phase*

The precipitate was then dried in two steps. Firstly, under atmospheric conditions for 12 h and, secondly, dehumidified at 110 °C for the same time. In order to activate the metallic phase, the carbonates were transformed in oxides calcining the catalyst in air at 300 °C for 10 hours.

In this Thesis, the metallic function CuO-ZnO-ZrO_2 is shortened as CZZr.

2.2.2 Acid function preparation

SAPO-11 was synthesized as the acid function of the catalyst, active for methanol dehydration to DME. SAPOs (silica-aluminophosphates) are medium pore size molecular sieves with no-crossing channels, 10-atoms one-dimensional ring chains and orthorhombic structure, as shown in Figure 1.10. They are composed of tetrahedral Si, Al and P oxides groups and exhibit high thermal and hydrothermal stability. The preparation of the acid function was carried out in different steps described as follows, using the reactants detailed in Table 2.3.

Table 2.3: Quantities of the reactants employed for SAPO-11 synthesis.

Reactants	Quantity (g)	Purpose
Boehmite ($Al(OH)_3 \cdot H_2O$)	30.83	Source of Al
Silica (SiO_2) (40 %)	17.85	Source of Si
Phosphoric acid (H_3PO_4) (85 %)	45.66	Source of P
N-dipropylamine ($C_6H_{15}N$)	20.00	Organic Template
Deionized water (H_2O)	186.10	-

a) *Precursor precipitation*

For the synthesis of SAPO-11, the following formulation was prepared: boehmite and phosphoric acid were slowly added to stirring deionized water, homogenizing the solution for 1 h. Next, the addition of the silica and N-dipropilamina was followed by mixing the components with a beater forming the gel precursor.

b) *Crystallization*

In the autoclave (*HighPreactor BR300, Berghoff*), the mixture was then stirred at 195 °C for 24 hours to achieve the crystallization of SAPO-11.

c) *Precursor separation*

Once the synthesis was completed, the suspension was centrifuged, washed with deionized water at 80°C and finally filtered, separating the solid precursor by decantation.

d) *Drying and calcination of the acid function*

The drying of the catalyst was performed in two steps. First, it was dried in air for 12 h at room temperature and then in an oven at 110 °C for the same

time. Afterwards, the precursor was calcined in a furnace at 575 °C for 8 hours, activating the acid function SAPO-11.

2.2.3 Bifunctional catalyst preparation

The bifunctional catalyst was prepared by dry physical mixture of the metallic and acid phases. Sánchez-Contador et al. (2018b) have determined that the optimal mass ratio between these two functions is 1 / 2, respectively. The obtained catalyst (in powder form) has been finely powdered, pelletized, crushed and sieved to the desired particle size (125-500 μm).

The designation of the bifunctional catalyst is identified by the used metallic phase, formed by three different metals (copper, zinc and zirconium), followed by the acid phase (SAPO-11): CZZr / S-11.

Prior to the experimental reactions, an in-situ activation step of the catalyst in the reactor has been carried out. It consists of a reduction with a H_2 flow (diluted in N_2), at the optimal reduction temperature determined by TPR analysis. The objective of this step is the reduction of CuO of the metallic function towards Cu^0 and Cu^+, which are the active oxidation states for the hydrogenation of CO_x to methanol (Fierro et al., 1996; Liu et al., 2003).

2.3 Catalyst characterization techniques

The catalysts have been characterized by different techniques: 1) determination of morphological and physical properties; 2) analysis of structural and chemical properties; 3) study of acid properties; and, 4) determination of metallic properties.

2.3.1 Morphological and physical properties

The techniques employed to determine micro and mesoporous properties (N_2 adsorption−desorption isotherms) and the morphology (SEM) of the catalysts used in the process are detailed below.

2.3.1.1 Micro and mesoporous structure

Micromeritics ASAP 2010 has been used to determine the physical properties of the catalysts. BET specific surface area determination is based on the quantification of the amount of gas adsorbed forming a monolayer on the solid surface. Likewise, microporous and mesoporous volume and porous volume distribution are determined.

Specific surface area (S_{BET}) has been estimated from BET equation, t-method has been used for calculating the micropore volume (V_{micro}) and BJH method has been applied to determine the mean pore diameter (d_p). The mesopore volume (V_{meso}) has been computed by the difference between the total adsorbed volume and V_{micro}.

The experimental procedure consisted of the degasification of the sample at 150 °C for 8 h under vacuum (10^{-3} mmHg), in order to eliminate possible impurities

adsorbed in the catalyst, followed by a N_2 adsorption-desorption in multiple stages at liquid N_2 cryogenic temperature until the complete saturation of the sample.

2.3.1.2 Morphology

The morphology of the individual functions and the bifunctional catalyst has been characterized by Scanning Electron Microscopy (SEM). This technique allows obtaining images with a higher resolution than optical microscope, due to its shorter electron beam wavelength. The analyses have been carried out in the *Electronic Microscopy and Material Microanalysis Service (SGIker)* at the University of the Basque Country (UPB/EHU), using a JEOL/JSM-7000F instrument equipped with a W filament. Detection of secondary and backscattered electrons, energy dispersive X-ray spectroscopy (EDX) (Oxford), as well as acceleration voltages of 133 eV are applied.

2.3.2 Chemical and structural properties

Inductively Coupled Plasma Optical Emission Spectroscopy (ICP-OES) has been performed to quantitatively determine the composition of the metallic phase, and thus ascertaining the correct coprecipitation of the metals. Catalyst structural properties were analyzed by X-ray Diffraction (XRD).

2.3.2.1 Chemical composition

In order to quantitatively determine the composition of the synthesized metallic functions and to ensure the complete coprecipitation of the metals during the preparation, ICP-OES analysis has been performed in a PerkinElmer Optimal

8300. Through this technique, Cu, Zn and Zr contents have been analyzed.

Sample dissolution is achieved by the disgregation of the solid. For the first acid attack on the sample (50 mg), HNO_3 and H_2SO_4 (1:2 ratio) are added maintaining the temperature at 190 °C for 24 h in a closed Teflon container, followed by the complete evaporation of the solution. Concentrated HNO_3 is added on the obtained solid residue for its subsequent dilution.

2.3.2.2 Structural properties

X-ray diffraction (XRD) has been used to analyze the structural properties of the catalysts. This technology allows the qualitative identification of the different phases and the crystalline structure of the zeolites. XRD-patterns were collected on a Bruker D8 Advance diffractometer equipped with a Ge primary monochromator, with Bragg-Brentano geometry and a Kα wavelength of 1.5406 Å.

2.3.3 Metallic properties

The reducible metallic species present in the catalyst and the temperature, at which the reduction takes place, have been determined by temperature programmed reduction (TPR), while the metallic specific surface area has been analyzed by N_2O selective chemisorption. Both analyses have been combined to reduce the required sample amount for the characterization of the metallic properties of the catalyst.

2.3.3.1 Reducibility

Temperature-programmed reduction (TPR) is a thermal analysis technique performed to qualitatively study the metallic oxides in the catalyst, using a Micromerit-

ics Autochem 2920 equipment. Furthermore, the required temperature to ensure the complete reduction of CuO in the metallic functions into Cu^0 is determined. To carry out this procedure, the sample was loaded into a U-shaped quartz reactor, and subjected to the following analysis steps: 1) sweeping with He to eliminate possible impurities at 200 °C for 2 h; 2) stabilization of the sample at room temperature (15 min) in a diluted H_2 stream (10 % of H_2 diluted in Ar); 3) sample heating with a temperature ramp of 2 °C min^{-1} up to 260 °C (for 2 h) for its complete reduction, obtaining Cu^0 species.

2.3.3.2 Metallic surface and dispersion

The active metallic surface is assumed as the superficial metallic atoms available for the adsorption of the reactants, distinguishing between the specific metallic surface and the total metallic surface. The first one is defined as the occupied surface by metallic sites per metal mass unit ($m^2_{Cu}\ g^{-1}_{metal}$), whereas the second one is established per catalyst mass unit ($m^2_{Cu}\ g^{-1}_{cat}$).

This analysis has been performed by N_2O selective chemisorption on the catalyst metallic surface, calculating Cu surface by N_2O adsorption:

$$N_2O\,(g) + 2\,Cu\,(s) \longleftrightarrow Cu_2O\,(s) + N_2\,(g) \tag{2.8}$$

Chemisorbed N_2O quantity has been measured by mass spectrometry, calculated as the difference between the injected gas volume and the desorbed gas volume. Thus, once the reacted gas volume is determined, the active Cu surface is calculated (Evans et al., 1983).

2.3.3.3 Combined analysis: TPR + N_2O chemisorption

TPR and N_2O analyses have been performed in a Micromeritics Autochem 2920 RS232 Status, coupled to a mass spectrometer (Pfeiffer-Vacuum OmniStar).

The experimental procedure is described as follows:

- Step 1: Sweep with He to eliminate possible impurities.
- Step 2: Catalyst reduction with a 10 % H_2 + Ar stream at 260 °C for 2 h. The objective is that copper is presented as Cu^0, in order to be oxidized with N_2O.
- Step 3: Adsorption at 60 °C with a N_2O flow diluted in He (10 % of N_2O). It has been carried out in multiple steps (20 injections) until the complete saturation of the sample. The unreacted N_2O and formed N_2 signals have been recorded in a mass spectrometer, enabling therefore the direct correlation of the latter with the active Cu area, described in Section 2.3.3.2.

2.3.4 Acid properties

Total acidity and acid strength distribution study of the synthesized SAPO-11 acid function and the bifunctional catalyst have been determined through the monitoring of NH_3 adsorption-desorption, by means of combining thermogravimetry and calorimetry of NH_3 adsorption. This was followed by the desorption at programmed temperature of the adsorbed base (TPD-NH_3), quantified by a mass spectrometer. These techniques provide quantitative information on the acid sites amount per catalyst mass unit and, additionally, of the strength distribution of these sites. Both are calculated from the released heat per adsorbed base unit mass and the temperature at which NH_3 desorption takes place.

2.3.4.1 Total acidity and acid strength distribution

Figure 2.7 shows the analysis results of NH_3 adsorption-desorption of the SAPO-11 acid function.

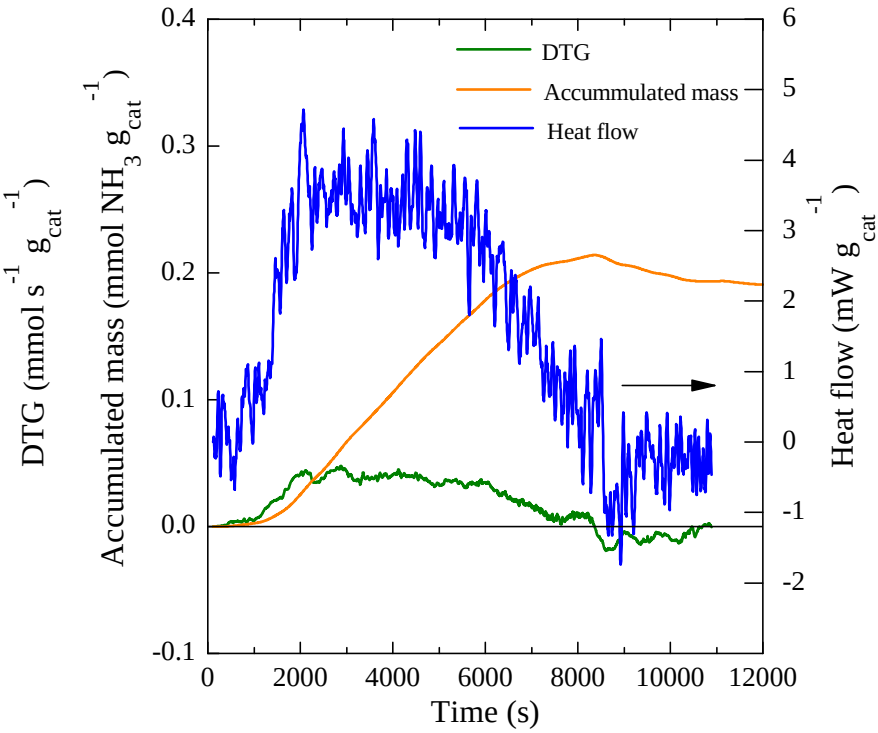

Figure 2.7: Results of NH_3 adsorption at 150 °C for SAPO-11 acid function.

Heat flow monitoring together with the variation of NH_3 adsorbed mass have been carried out using a Setaram TG-DSC 111 calorimeter. This method allows directly relating both signals, thereby providing the released heat amount per adsorbed base mass unit. Moreover, the total amount of NH_3 chemically adsorbed corresponds to the total acidity, quantified by catalyst mass unit. The procedure to carry out the diferential calorimetry of NH_3 adsorption involves the following steps: 1) sample pre-treatment to eliminate possible impurities through He sweep (60 cm^3 min^{-1},

30 min) at 550 °C; 2) sample stabilizing at 150 °C with a He flow of 20 cm^3; 3) sample complete saturation by means of NH_3 continuous injection (50 μL min^{-1} at 150 °C; 4) elimination of the base physisorbed on the sample with He sweeping (20 cm^3 min^{-1}) at 150 °C.

The signals exhibit the evolution with time of: 1) acumulated mass; 2) derived mass, DTG (Derived Thermo-Gravimetry); and, 3) heat flow obtained from DTA (Differential Thermal Analysis) signal, where it can be observed the NH_3 adsorption exothermic peak, and the desorption endothermic peak of the NH_3 physisorbed on the sample. From the temperature programmed NH_3 desorption (TPD) the acid strength distribution can be determined, since the presence of desorption peaks, the corresponding temperature at the maximum of each peak and its intensity, allow determining the acid strength and the amount of acid sites.

To obtain the TPD curve, the sample is saturated with NH_3 at 150 °C, following by the desorption through sample heating up to 550 °C with a He flow. Simultaneously, the intensity signals, corresponding to the used base mass, is monitored in the mass spectrometer. In this experimental procedure, m/e = 15 (8 % of the predominant signal) is recorded, since both NH_3 predominant signal (17) and the equivalent signal to m/e = 16 (20 % of the predominant signal) can cause masking issues in the presence of H_2O in the desorption flow. Using a moderate temperature sequence, clearly permits the differentiation of weak acid sites (desorbed at lower temperature) and the strong acid sites (desorbed at higher temperature).

2.3.5 Coke content analysis

The content and strength of coke deposited on deactivated catalysts have been characterized by temperature programmed oxidation (TPO).

Usually, the deposited coke measurement on the catalyst is determined by the difference between the initial and final sample mass during TPO experiment. Nonetheless, this method is unfeasible for samples that increase their mass during combustion. The metals of these type of catalysts react with oxygen giving rise to oxides, in parallel to the combustion of coke, as in the case of the metallic and bifunctional catalysts used in this Thesis.

Therefore, an alternative method, consisting of a TA Instruments TGA Q5000 thermobalance connected on line to a Thermostar mass spectrometer (Balzers Instruments), has been used to measure the deposited coke content on the catalysts. For that purpose, the signals of the compounds resulting from the combustion are recorded in the mass spectrometer. In this analysis procedure a pattern ($CaCO_3$), which is decomposed at higher temperature (700 °C) than the catalyst compounds, is added to the sample, in order to be enable the quantitative measure of CO_2 concentration in the combustion gases.

Through this technique, where air is used as oxidizing agent (Gayubo et al., 2014), the mass signals 14, 18 ,28 and 44 corresponding to N_2, H_2O, CO and CO_2, respectively, have been recorded in the mass spectrometer during the combustion. Being the CO_2 signal the only one taken into account for the measurement of the total coke content, it has been calculated by the following equation (Gayubo et al., 2014):

$$C_C(\%) = \frac{\dot{M}_{CO_2} \cdot 12}{\dot{M}_{cat}} 100 \tag{2.9}$$

For TPO analysis, the catalyst sample along with a known amount of $CaCO_3$ pattern are loaded in the thermobalance. Then the sample is heated up to 815 °C

(7 $^{\circ}$C min^{-1}) with pure He and air streams, achieving an oxygen partial pressure of 0.10 atm and the complete combustion of coke. During the whole process CO_2 signal is monitored in the mass spectrometer, relating each obtained signal point with the combustion temperature. In this manner, the different types of coke are determined by their combustion ease and each coke type quantity is established, obtaining the total coke content of the sample.

2.4 Membrane preparation

Four types of microporous zeolite membranes (LTA, MOR, SOD and LTX) have been synthesized and crystallized on stainless steel support (Figure 2.4), in order to compare them in the selective synthesis of DME. Table 2.4 shows the syntheses temperatures and times of the different membranes.

Table 2.4: Hydrothermal conditions for the synthesis of the different membranes.

Zeolite Membrane	Temperature (°C)	Time (h)
Linde Type A (LTA)	110	12
Mordenite (MOR)	180	48
Linde Type X (FAU)	90	8
Sodalite (SOD)	130	48

2.4.1 LTA

LTA zeolite has been prepared adding a silicate solution into an aluminate solution (Table 2.5) under stirring at room temperature following the methodology established by (Thompson and Huber, 1982). After a homogeneous solution with a molar ratio of $3.165\,Na_2O : Al_2O_3 : 1.926\,SiO_2 : 128\,H_2O$ was formed, it was placed together with the stainless steel support in a horizontal Teflon-lined stainless steel autoclave (*HighPreactor BR300, Berghoff*) for the hydrothermal synthesis. Once the LTA zeolite was crystallized on the support, the membrane was washed with deonized water for several times, and then dried in air for 24 h for the characterization.

Table 2.5: Quantities of the reactants for the preparation of LTA membrane.

Reactants	Quantity (g)	Purpose
Sodium hydroxide (NaOH)	3.25	Source of Al
Deionized water (H_2O)	360.00	
Sodium aluminate ($NaAlO_2$)	74.32	
Sodium hydroxide (NaOH)	3.25	Source of Si
Deionized water (H_2O)	360.00	
Sodium metasilicate (Na_2SiO_3)	139.32	

2.4.2 MOR

The hydrothermal synthesis to prepare the MOR membrane, using the recipe described by Kim and Ahn (1991), consists of an aluminate solution (NaOH, deionized H_2O and sodium aluminate) and a silicate solution (Ludox HS-40 and deionized H_2O) (Table 2.6).

Table 2.6: Quantities of the reactants for preparation of MOR membrane.

Reactants	Quantity (g)	Purpose
Sodium hydroxide (NaOH)	12.67	Source of Al
Deionized water (H_2O)	26.67	
Sodium aluminate ($NaAlO_2$)	9.53	
Ludox HS-40	150.25	Source of Si
Deionized water (H_2O)	340.22	

The silicate solution was gradually added to the aluminate solution under stirring at room temperature forming the gel precursor ($6\,Na_2O : Al_2O_3 : 30\,SiO_2 : 780\,H_2O$). The MOR membrane was finally synthesized following the previously described (Section 2.4.1) steps.

2.4.3 LTX

In order to prepare the LTX membrane, the synthesis solution was obtained by mixing aluminate and silicate solutions (Table 2.7) following the recipe reported by Lechert and Kacirek (1991).

Table 2.7: Quantities of the reactants for the preparation of LTX membrane.

Reactants	Quantity (g)	Purpose
Sodium hydroxide (NaOH)	39.78	Source of Al
Deionized water (H_2O)	178.00	
Aluminate trihydrate (Al_2O_3)	24.38	
Sodium hydroxide (NaOH)	14.78	Source of Si
Deionized water (H_2O)	153.00	
Sodium silicate (Na_2SiO_3)	54.93	

The aluminate solution was gradually added to the silicate solution under stirring. Subsequently, the resulting mixture was stirred producing a homogeneous clear solution. Finally, the molar ratio of the resulting synthesis solution was $NaAlO_2 : 4\,SiO_2 : 16\,NaOH : 325\,H_2O$. The LTX membrane was finally synthesized following the aforementioned (Section 2.4.1) steps.

2.4.4 SOD

SOD zeolite is prepared adding a silicate solution into an aluminate solution (Table 2.8) under stirring at 60°C, according to the recipe reported by Wang et al. (2015b).

After a homogeneous solution with a molar ratio of $50\,Na_2O : Al_2O_3 : 5\,SiO_2 : 100\,H_2O$ was obtained, the SOD membrane was finally synthesized following the previously described (Section 2.4.1) steps.

Table 2.8: Quantities of the reactants for the preparation of SOD membrane.

Reactants	Quantity (g)	Purpose
Sodium hydroxide (NaOH)	55.55	Source of Al
Deionized water (H_2O)	125.00	
Aluminium powder	0.75	
Deionized water (H_2O)	118.75	Source of Si
Ludox HS-40	10.40	

2.5 Membrane characterization techniques

The characterization of the synthesized membranes has pursued to determine the following properties: 1) physical, structural and morphological; 2) pervaporation and vapor permeation performances; 3) permeation of different gases, and; 4) thermal stability.

2.5.1 Structural, physical and morphological properties

In this section is described the membranes characterization techniques used to determine the phase purity, crystallinity and chemical composition (X-ray diffraction (XRD)); micropore volume, diameter and surface area (CO_2 adsorption isotherms); and, external morphology (Scanning Electron Microscopy (SEM)).

2.5.1.1 Structural properties

The crystallinity and phase purity of the synthesized zeolites have been studied by X-ray diffraction (XRD) measurements, using a PAN analytical Xpert PRO diffractometer equipped with CuKα radiation of 1.5418 Å. The XRD diffractograms have been recorded using a 2 Θ step of 0.026° in the 4 – 60° range and, subsequently, they have been analyzed with the peak-fit option of the WinPLOTR program without structural model. The obtained diffractogram has been compared with patterns of the Bruker-binary V3 database.

2.5.1.2 Physical properties

The determination of the physical properties of the membranes has been carried out by CO_2 physisorption using a Micromeritics ASAP 2020 apparatus (*Servicios Centrales de Apoyo a la Investigación SCAI, Universidad de Málaga*). The main textural parameters have been determined from CO_2 adsorption isotherm, using the Dubinin-Radushkevich equation for estimating the narrow micropore volume (VDR) and area (SDR). The average pore diameter of the zeolite has been also calculated from CO_2 adsorption isotherm by the Horvath-Kawazoe method.

The experimental procedure consists firstly of the degasification of the sample at 150 °C under vacuum (10^{-3} mmHg) for 8 h, in order to eliminate potential impurities. Afterwards, the adsorption of CO_2 takes place in multiple equilibrium stages until the saturation of the sample at 0 °C.

2.5.1.3 Morphological properties

As previously described in Section 2.3.1.2, the morphology of the different prepared membranes has been analyzed by Scanning Electron Microscopy (SEM), in a JEOL/JSM-7000f with a W filament (resolution of 3.5 eV), attached to an energy dispersive X-ray analyzer (EDX) (Oxford) (resolution of 133 eV).

2.5.2 Permeation performance

The permeation characterization of the zeolite membranes (carried out at the Yamaguchi University in Japan) is focused on the analysis and study of their permeability and permselectivity (or separation factor (α)) through three main experiments: pervaporation (PV) measurement, vapor permeation (VP) and single gas permeation techniques (GP).

2.5.2.1 Pervaporation measurement

The hydrophilicity and permselectivity of synthesized membranes have been tested trough PV experiments. Membranes have been sealed with heated fluorinated ethylene propylene on both ends. Two different solutions have been prepared ($EtOH / H_2O$ = 90 / 10 wt% and $MeOH / H_2O$ = 90 / 10 wt%) at 75 °C and 60 °C, respectively, in order to be fed on the outer side of the membrane (feed side), meanwhile on the inner side the permeate has been evacuated with a vacuum pump and collected within liquid nitrogen cooled trap tubes. These trapped tubes had been weighed empty before the experiment and after it with the trapped permeate, which has been finally analyzed on a gas chromatograph. The separation factor (α) of a binary mixture ($EtOH / H_2O$ or $MeOH / H_2O$) is defined as the quotient between the molar fractions of both components in the permeate (Y) and the molar fractions of both components in the retentate (X):

$$\alpha_{H_2O/EtOH} = \frac{Y_{H_2O} / Y_{EtOH}}{X_{H_2O} / X_{EtOH}} \tag{2.10}$$

$$\alpha_{H_2O/MeOH} = \frac{Y_{H_2O} / Y_{MeOH}}{X_{H_2O} / X_{MeOH}} \tag{2.11}$$

Furthermore, the flux (Q) is calculated as follows:

$$Q = \frac{M}{A \cdot t} \tag{2.12}$$

being M the total weight of the permeate in kg, A is the membrane surface in m^2 and t the collecting time in h.

2.5.2.2 Vapor permeation measurement

Additionally to PV experiments, vapor permeation (VP) measurements have been performed on the prepared membranes feeding a vaporized solution of EtOH / H_2O = 90 / 10 wt% at 125 °C in a permeation cell preheated at 100 °C, in order to avoid any condensation in the feed. The experimental procedure for VP has been analogous to PV measurement (Section 2.5.2.1).

2.5.2.3 Single gas permeation technique

The analysis of gas permeation (GP) behaviors of gases through the synthesized membranes shows both their membrane pore size and adsorption properties. He, H_2, CO_2, O_2, N_2, CH_4 and SF_6 permeances through the membranes have been determined, whose kinetic diameters is shown in Table 2.9.

Table 2.9: Kinetic diameters of the different gases used for GP experiments.

Gas compound	Kinetic Diameter (Å)
He	2.60
H_2	2.89
CO_2	3.30
O_2	3.46
N_2	3.64
CH_4	3.80
SF_6	5.50

Prior to the GP experiments, the membranes had been sealed in a permeation module with silicone O-rings. The temperature within the cell have been increasing from 35 °C to 200 °C and the pressure difference between the feed and permeate sides has been kept under 0.01 MPa, setting the permeation side under atmospheric pressure.

2.5.3 Thermal stability

Thermal resistance of the synthesized membranes has been tested, due to the high temperature it should withstand in DME synthesis (275 °C - 325 °C). PV, VP and GP experiments have been performed before and after the calcination at 300 °C of the membranes, in order to analyze the effect of the temperature on them.

III

3

KINETIC MODELING

3 | Kinetic Modeling

The overall trend of the works in the literature on the kinetic modeling and fixed bed reactor design for DME synthesis (De Falco et al., 2016; Hadipour and Sohrabi, 2008; Lu et al., 2004; Moradi et al., 2008; Ng et al., 1999; Ravaghi-Ardebili and Manenti, 2015), has been based on the utilization of well established kinetic equations for each individual reaction steps (methanol synthesis and its dehydration towards DME). Although these kinetic equations have been obtained in the literature with prepared monofunctional catalysts and used in suitable conditions for each individual reaction. However, these reaction conditions differ from the optimum for DME synthesis. Hence, DME synthesis is carried out under lower pressure and at higher temperature than methanol synthesis, and under greater pressure than methanol dehydration towards DME. On the kinetic studies of the individual reactions, consequently, the thermodynamic equilibrium conditions also differ from the ones when the two reactions are integrated within the same reactor and, additionally, between the two separate reactions the synergy is not developed as in the direct synthesis of DME. Moreover, while the catalysts used originally for the direct synthesis of DME were physical mixtures of a CZA catalyst (common in methanol synthesis) and γ-Al_2O_3 (in methanol dehydration), the progress of the knowledge leads to the design of specific bifunctional catalysts to enhance the

synergy of the reactions. Factors like the mass ratio between the metallic and acid functions and the design of each function have been taken into consideration, in order to avoid a negative interference between each other. Also noteworthy is the lack of literature concerning deactivation kinetic models for both the direct synthesis of DME and the individual reactions. This scarcity requires the development of a kinetic modeling of the direct synthesis of DME, considering the particular circumstances of this reaction and the deactivation of the catalyst.

3.1 Catalyst properties

The results of the catalyst kinetic performance in DME synthesis are determined by its properties. Thus, the characterization of the synthesized catalyst has been carried out, as well as of the individual metallic and acid functions. The preparation conditions of the individual functions and the catalyst have been described in Section 2.2. The composition of the metallic and acid functions is optimal for each reaction step (Sánchez-Contador et al., 2018a,c).

3.1.1 Morphological and physical properties

The porous texture was studied by means of N_2 adsorption - desorption isotherms, following the experimental procedure described in Section 2.3.1. Figure 3.1 shows N_2 adsorption-desorption isotherms of the synthesized CZZr metallic function, SAPO-11 acid function and the bifunctional catalyst (CZZr / S-11).

The isotherms present at high relative pressure values (> 0.4) a steep hysteresis curve, which is characteristic of mesoporous materials. Moreover, on SAPO-11 and CZZr / S-11 isotherms (Figures 3.1b and 3.1c), at relative pressure values

lower than 0.3, can be observed a step indicative of the presence of microporous materials (SAPO-11) (Yoo et al., 2007).

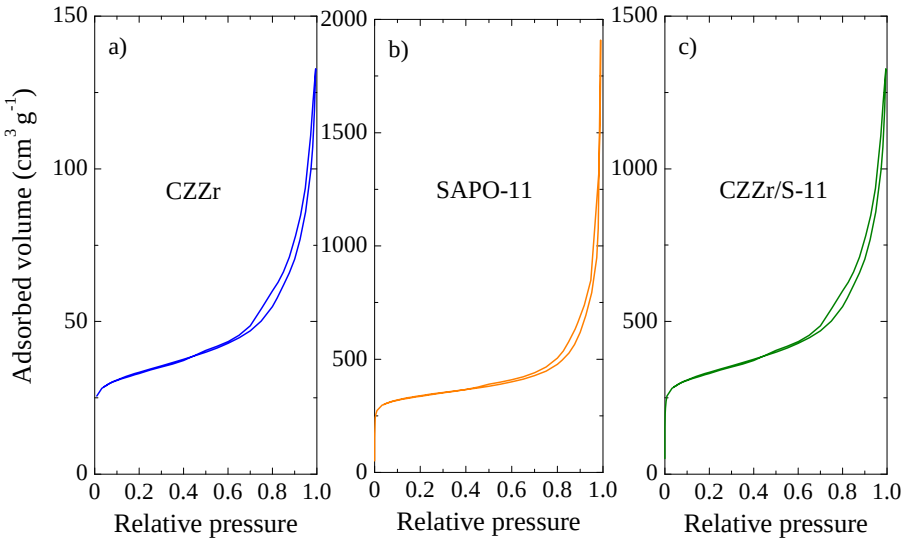

Figure 3.1: N_2 adsorption-desorption isotherms of the CZZr metallic function (a), SAPO-11 acid function (b) and CZZr / S-11 bifunctional catalyst (c).

The main physical parameters calculated from N_2 adsorption-desorption of the metallic function, acid function and bifunctional catalyst are displayed in Table 3.1.

Table 3.1: Physical properties of CZZr metallic function, SAPO-11 acid function and CZZr / S-11 bifunctional catalyst.

	S_{BET} (m^2g^{-1})	V_{micro} (cm^3g^{-1})	V_{meso} (cm^3g^{-1})	d_p (Å)
CZZr	109	0.003	0.267	87.30
SAPO-11	126	0.037	0.214	178.62
CZZr / S-11	122	0.029	0.170	97.91

As can observed in Table 3.1, the bifunctional catalyst exhibits a S_{BET} of 122 m^2g^{-1} and a predominantly mesoporous texture, with values of V_{micro} and V_{meso} of 0.03 and 0.17 cm^3g^{-1}, respectively. The decrease of V_{meso} of the catalyst, with respect to the corresponding of the individual functions, should be attributed to the SAPO-11 mesopores blockade by the metallic function particles in the pelletization step.

Figure 3.2 displays the SEM images of CZZr metallic function (Figure 3.2a) and SAPO-11 acid function (Figure 3.2b).

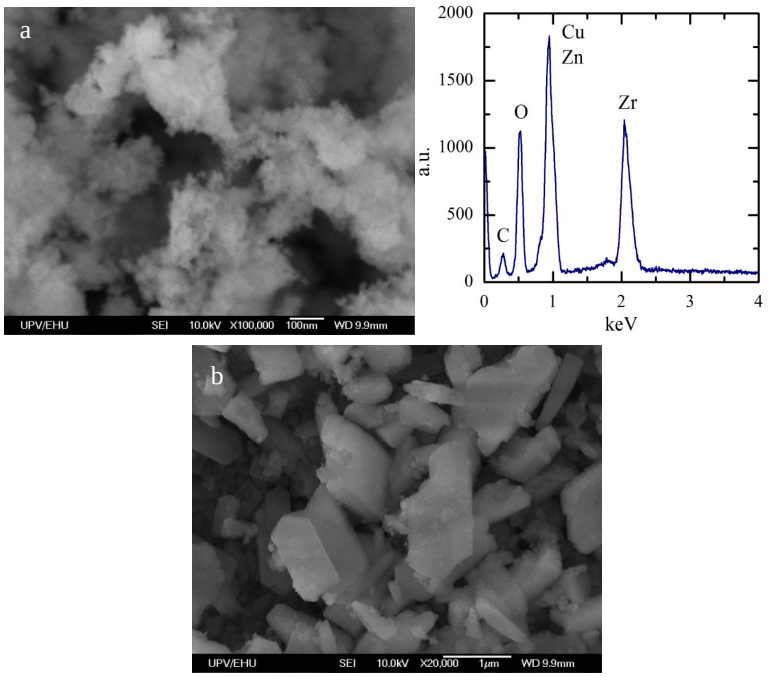

Figure 3.2: SEM/EDX image of the CZZr metallic function (a) and SEM image of the SAPO-11 acid function (b).

On one side, the image of CZZr suggests that the metallic function is composed by agglomerates of small particles with a size smaller than 100 nm. On the other side, the SEM image of SAPO-11 shows that the crystals have a diameter of ~ 1

μm and present a characteristic polyhedral form of monoclinic crystal system.

3.1.2 Chemical and structural properties

Through Inductively Coupled Plasma Optical Emission Spectrometry (ICP-OES) the metallic content (Cu, Zn and Zr) of the CZZr metallic function has been analyzed, as previously detailed (Section 2.3.2.1). Table 3.2 summarizes the metallic ratio of the catalyst along with the nominal value. The obtained values are close the theoretical ratio ($\pm$ 4 % error), demonstrating the adequate co-precipitation of the synthesized metallic function.

Table 3.2: Atomic ratios determined by ICP-OES between the metals of the synthesized catalyst.

Catalyst	Nominal	Cu	Zn	Zr
CZZr	2:1:1.5	2	0.75	1.21

Normalized XRD patterns of the CZZr metallic function and the SAPO-11 acid function are depicted in Figure 3.3. It can be observed that at 32.0 and 56.7 $^\circ$ Zn oxides are presented, at 35.7 and 39.0 $^\circ$ Cu oxide and at 35.7 CuO and ZnO structures can be found. Different authors (Agrell et al., 2003; Li et al., 2015) have demonstrated that increasing Zr content in the metallic phase causes the reduction of the crystal size, as well as changes in the crystalline structure. Therefore, the characteristic peaks of CZZr (Figure 3.3a) are less intense and, consequently, more difficult to identify. Figure 3.3b shows the SAPO-11 XRD pattern with its characteristic peaks between 15 - 20 $^\circ$ and 20 - 25 $^\circ$.

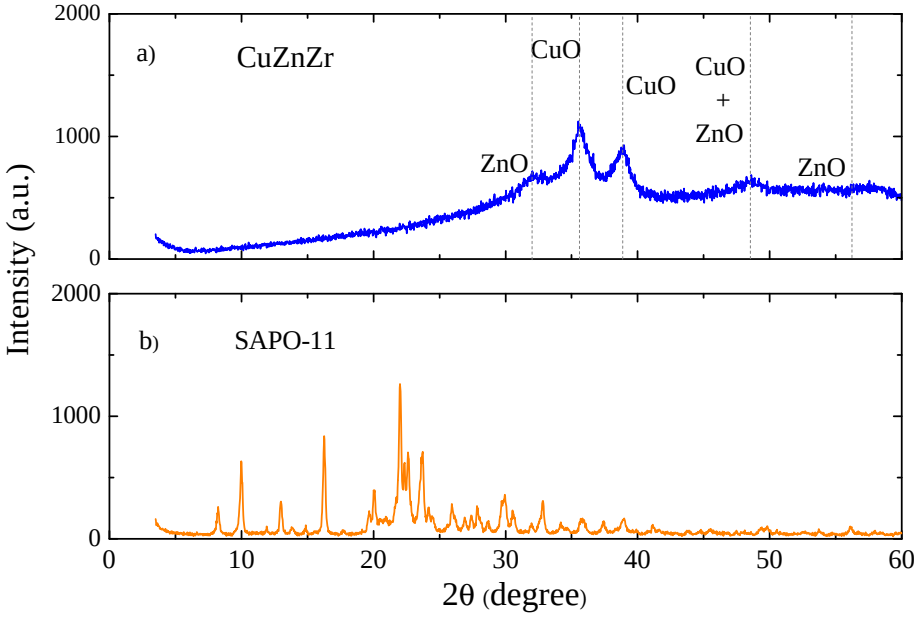

Figure 3.3: XRD patterns of CZZr metallic function (a) and SAPO-11 acid function (b).

3.1.3 Metallic properties

Normalized TPR profiles (per gram of Cu and per gram of catalyst) of the CZZr metallic function and the bifunctional catalyst are depicted in Figure 3.4. The results have highlighted that 250 °C is a sufficient temperature to reduce the catalyst. These TPR profiles display CuO reducibility since Zn and Zr metals are not reducible at these conditions. On the two samples the total reduction of the catalyst is achieved below 200 °C, being the reduction temperature of CZZr / S-11 the highest one. CZZr metallic phase presents a unique reduction peak at 132 °C whereas the bifunctional catalyst exhibits a peak at 148 °C and a shoulder (159 °C). The presence of a peak and a shoulder on CZZr / S-11 might be assigned to different Cu reduction stages from Cu^{2+} to Cu^{+} and/or Cu^{0}, while the metallic phase produces

a unique peak due to the homogeneous dispersion of CuO.

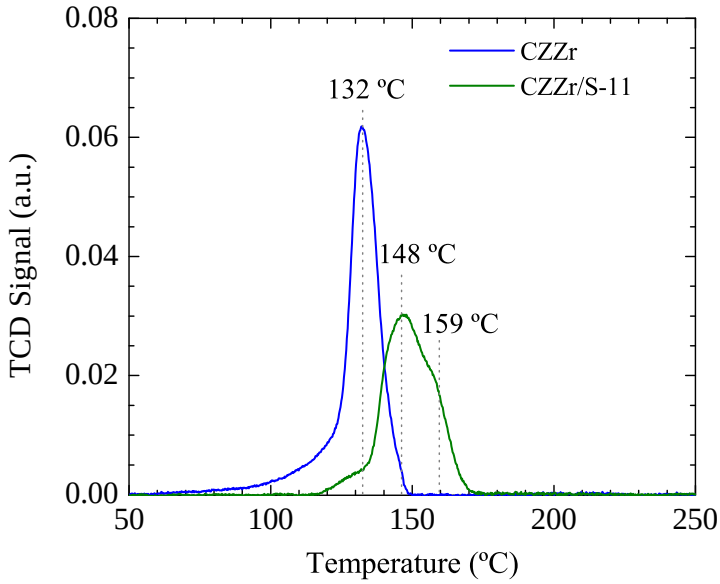

Figure 3.4: TPR profiles of CZZr metallic function and CZZr / S-11 bifunctional catalyst.

Through N_2O chemisorption Cu surface (S_{Cu}) and the Cu dispersion of the CZZr metallic function and CZZr / S-11 bifunctional catalyst have been determined. Table 3.3 summarizes the metallic properties of the two samples.

Table 3.3: Metallic properties of CZZr metallic function and CZZr / S-11 bifunctional catalyst.

	CZZr	CZZr / S-11
S_{Cu} ($m^2\ g_{Cu}^{-1}$)	17.1	53.5
S'_{Cu} ($m^2\ g_{cat}^{-1}$)	5.9	6.3
Cu dispersion (%)	2.6	8.2

CZZr possesses a Cu surface of around 17.1 $m^2\ g_{Cu}^{-1}$ whereas in the case of CZZr / S-11 its Cu surface reaches 53.5 $m^2\ g_{Cu}^{-1}$. Concerning the metallic dispersion, for CZZr a 2.6 % was obtained and, on the other hand, a 8.2 % was reached for the bifunctional catalyst, evidencing that a higher Cu dispersion is produced incorporating the acid phase.

3.1.4 Acid properties

In methanol dehydration the different acid properties of the catalyst (total acidity and acid strength distribution) are determining for both the activity and selectivity (Alharbi et al., 2015), and these depend, concerning zeolites and SAPOs, of SiO_2/Al_2O_3 ratio of the acid function. Furthermore, this ratio is proportional to the hidrophobicity of the catalyst, improving the removal of H_2O (Corma, 1995) and, consequently, favoring methanol adsorption on the acid sites and enhancing the catalyst dehydration activity.

The catalyst properties, moreover, have an impact on the formation of byproducts, such a paraffins, olefins or aromatics (Spivey, 1991), as well as on coke formation, which is responsible for the deactivation of the catalyst.

Figure 3.5 displays the results of the temperature programmed desorption of NH_3 (Figure 3.5a) and the acid strength distribution (Figure 3.5b) of SAPO-11 acid function and CZZr / S-11 bifunctional catalyst. The quantity of adsorbed NH_3 (surface under the curve in those profiles) determines the total acidity whereas the distribution of the acid strength is related to the peaks desorption temperature ranges. Thus, strong acid sites require a higher temperature for the base desorption (300 - 550 °C), meanwhile weak basic sites correspond the temperature range between 150 and 300 °C.

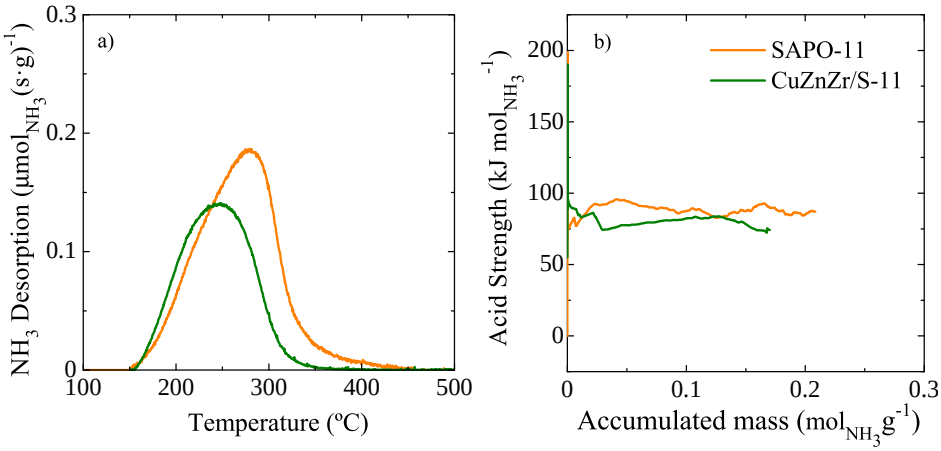

Figure 3.5: NH_3-TPD profile and acid strength distribution of SAPO-11 acid function (a) and CZZr / S-11 (b).

In Figure 3.5b is shown the acid strength distribution, which has been quantitatively determined by the simultaneous monitoring of the released heat and the adsorbed mass in NH_3 differential adsorption, described in Section 2.3.4.1.

SAPO-11 performs an uniform acidity, showing an unique peak at 282 °C (Figure 3.5a) that demonstrates the weak character of the present sites, which is characteristic of this material (Zhang et al., 2007). On the other hand, the surface of the bifunctional catalyst TPD curve is narrower and displaced to a lower temperature (peak at 250 °C) in comparison with the acid function, which shows a decrease in both the total acidity and its acid strength. In Figure 3.5b can be observed a great homogeneity of the acid strength, and that the mean acid strength (about 75 $kJ\,mol^{-1}_{NH_3}$ is slightly lower for the catalyst than for SAPO-11, attributable to the pelletizing step.

Table 3.4 summarizes the results of the acid properties of SAPO-11 and CZZr / S-11 bifunctional catalyst.

Table 3.4: Summary of the acid properties of SAPO-11 and CZZr / S-11 bifunctional catalyst.

Catalyst	Acid strength (kJ $mol^{-1}_{NH_3}$)	Total acidity ($mmol_{NH_3}$ g^{-1})
SAPO-11	98	0.19
CZZr / S-11	85	0.17

3.2 Backgrounds for the individual reactions in DME synthesis

The major advances in the studies on the mechanism and kinetic modeling of the three individual reactions are described in the following.

3.2.1 Methanol synthesis

Sánchez-Contador (2017) has reviewed the literature of the methanol synthesis kinetics, differentiating the periods in which the reaction was initially studied under high pressure and afterward under moderate pressure. In the pioneer work of Natta (1955) for the synthesis under high pressure, a Langmuir-Hinshelwood-Hougen-Watson (LHHW) expression type was established, taking into consideration that CO_2 is practically inactive and with a term in the denominator that considers the occupation of active sites by CO, H_2 and methanol adsorption. For methanol synthesis under less pressure, it has been considered different actives sites for CO and CO_2 hydrogenation, and WGS reaction. Furthermore, that methanol is formed by successive hydrogenations of CO and CO_2 adsorbed in a specific type of sites, while H_2 and H_2O are adsorbed in another type of sites (Graaf et al., 1990, 1988). Mochalin et al. (1984) and Malinovskaya et al. (1988) have compared kinetic models from the literature, proposed in base of these considerations. van den Bussche and Froment (1996) have developed a kinetic model with a transcendental role of CO_2, based on the formation of carbonate species as first active compound and the hydrogenation of formate towards formaldehyde as rate determining step. Lim et al. (2009), nevertheless, have minimized the importance of CO_2 after proving its low reactivity in comparison with that of CO. These authors have established a mechanism that differentiates the key components in methanol synthesis (methoxy

species from CO and formate species from CO_2 and in WGS reaction). Yang et al. (2013) have contributed to clarify the relative importance of CO and CO_2 reactivity and the controversies in that regard. A mechanism is proposed formed by three routes, whose relative importance depend on the reaction conditions and their key intermediates are formal species (with CO as reactant), formates (from CO_2), and carboxylates (formed from CO and CO_2 through two different routes), in whose formation H_2O in the reaction medium plays a relevant role .

3.2.2 WGS reaction

de la Osa et al. (2011) have differentiated 4 different mechanisms among those proposed in the literature: 1) redox (Ovesen et al., 1996); 2) with formate species as intermediates (Burch et al., 2011); 3) with carbonate species as intermediates (Ma and Lund, 2003) and; 4) through CO associative mechanism with OH adsorbed groups (Rhodes et al., 1995). It should be pointed out, nevertheless, that the attention of this reaction is focused in the literature on the intensification of H_2 production by reforming (of methane principally), which is carried out over 350 °C, with Fe catalysts and under reduced pressure. Hence, the information is only partially valid for this reaction in methanol or DME synthesis, whose limit temperature is 300 °C, as to avoid Cu sintering in conventional catalysts. Additionally, as has been indicated, the higher reactivity of CO in methanol synthesis requires the study of this reaction from the perspective of enhancing the reverse WGS (rWGS), favoring the conversion of CO_2 towards CO.

3.2.3 Methanol dehydration

The mechanism of this reaction has received considerable attention mainly because it is the first step in methanol conversion towards hydrocarbons, giving rise to the development of MTG, MTO, MTP and MTA processes for the selective formation of gasoline, olefins, propylene and aromatics, respectively. These reactions are carried out under low pressure and with zeolite HZSM-5 or silicoaluminophosphates (SAPOs, -34 or -18) catalysts. Methanol dehydration has also gained attention for being the first step in the MTP process of Lurgi, where methanol is dehydrated on a γ-Al_2O_3 catalyst to obtain a mixture of DME, methanol and H_2O in thermodynamic equilibrium. This mixture is afterwards selectively converted into propylene in a second reactor on a zeolite HZSM-5 catalyst. Even though Langmuir-Hinshelwood (Gates and Johanson, 1969) and Eley-Rideal (Kiviranta-Pääkkönen et al., 1998) mechanisms and also empirical kinetic models (Schmitz, 1978) have been proposed, the first ones become more accepted, considering methanol adsorption in two adjacent acid sites. The differences arise as a result of the identification of the steps that determine the kinetics, which for some authors is the adsorption of methanol (Beranek et al., 1972), of methanol and H_2O (Bercic and Levec, 1992, 1993; Ha et al., 2011; Hosseininejad et al., 2012; Lu et al., 2004) or of methanol, DME and H_2O (An et al., 2004).

3.2.4 Deactivation

The pioneer studies of the kinetics of the catalyst deactivation in DME synthesis have used CuO-ZnO-Al_2O_3/γ-Al_2O_3 as catalyst and synthesis gas as feed Sierra et al. (2009) and later on, Ereña et al. (2011) assessed deactivation on DME synthesis from $CO_2 + H_2$. Previously, it had been established that the main cause

of deactivation is the coke deposition (Aguayo et al., 2005), whose origin is the degradation of methoxy species adsorbed in the metallic sites, forming aromatic structures that partially block these Cu-Zn sites. The evolution of coke condensed structures gives rise to the growing deposition of coke in the inert Al_2O_3 external to the metallic sites, and the presence of γ-Al_2O_3 acid sites activates the coke condensation reactions. In like manner, although at a lower rate, it is also considered that the adsorbed methoxy species adsorbed in γ-Al_2O_3 acid sites generate the coke deposition and the partial block of acid sites. However, this deposition does not impact on the catalyst deactivation due to its preparation with an excess of acid function (in order to achieve the conversion of the synthesized methanol in the metallic function). These hypotheses have been formulated from the TPO results of coke and are consistent with the attenuation effect of coke deposition by the increase of H_2O concentration in the reaction medium, which is attributed to the decrement of adsorbed methoxy species concentration (Sierra et al., 2011).

3.3 Data analysis methodology

The methodology applied in this Thesis regarding the kinetic modeling is similar the one used by Sánchez-Contador (2017) and Ateka (2014) for DME synthesis with other catalysts, and also to the methodology described for other catalytic processes with complex reaction schemes and product fractions (lumps) (Epelde et al., 2014; Gayubo et al., 2010, 2011; Mier et al., 2011). Toch et al. (2015) have described the main steps for the kinetic modeling of these processes, without considering the deactivation. Recently Cordero-Lanzac et al. (2018) have performed an update of this methodology, considering n-pentane cracking as model reaction and with the significant improvement of adjusting the results at zero time on stream together with those considering deactivation.

3.3.1 Calculation steps

The gas flow used experimentally in the fixed bed reactor has been considered ideal, without any radial concentration gradients. Also that the bed is isothermal, because the temperature differences between different radial and longitudinal positions are less than 1 °C. Consequently, the basic equation for the calculation of mass conservation of each i component, at zero time on stream (fresh catalyst) is:

$$r_{i,0} = \frac{dy_i}{d(W/F_0)} \tag{3.1}$$

where the concentration of each component, y_i, is the molar fraction in the case of inorganic compounds, and the contained carbon fraction in the case of organic compounds, referring to the total carbon moles (constant in the reaction). W is the catalyst mass and F_0, the carbon molar flow fed in form of CO and CO_2, in

contained C units.

The formation velocity of each i component is calculated considering the different reaction steps in which it is involved:

$$r_{i,0} = \sum_{j=1}^{n_j} (\upsilon_i)_j \, r_j \tag{3.2}$$

where $(\upsilon_i)_j$ is the stoichiometric coefficient of the i component in the j reaction of the kinetic scheme, r_j is the reaction rate of j step and n_j is the number of reactions in the scheme.

Eq. 3.2 has been formulated assuming the reaction steps to be elementary. In the reaction steps where deactivation is considered, the reaction rate at t time is:

$$r_j = r_{j,0} \, a \tag{3.3}$$

The application of Eq. 3.3 requires a kinetic equation of deactivation that relates the activity with the time, temperature and composition in the reaction medium. A general expression of the deactivation kinetics is:

$$-\frac{da}{dt} = \Psi \, (T, p_i) \, a^d \tag{3.4}$$

where Ψ (T,p_i) is a deactivation function, which is dependent on the temperature and the concentration of the components in the reaction medium, p_i, and whose role is to act as precursors or inhibitors of coke.

Therefore, the kinetics of the formation of each i component at t time are calculated as follows:

$$r_i = \frac{dy_i}{d(W/F_0)} = (r_{i,0})\,a = \sum_{j=1}^{n_j} (\upsilon_i)_j\,(r_{j,0})\,a \tag{3.5}$$

The kinetic parameters for each proposed kinetic model has been calculated by multivariable non-linear regression adjusting of the experimental results of concentration with the calculated by resolution of the mass balance of each component, minimizing an objective function. This objective function has been defined as a vector with two components, regarding the error of adjusting the kinetics at zero time (first term) and the error of adjusting at different reaction times, that is, related to the deactivation kinetics. This proposal enables to perform the fitting of the reaction and deactivation data simultaneously.

$$O.F. = \begin{pmatrix} \sum_{i=1}^{n_l} \omega_i \sum_{j=1}^{n_{e,0}} \frac{R_j}{n_{e,0}} \left((\bar{y}^*_{i,j})_0 - (y_{i,j})_0\right)^2 \\ \sum_{i=1}^{n_l} \omega_i \sum_{j=1}^{n_{e,d}} \frac{R_j}{n_{e,d}} \left((\bar{y}^*_{i,j})_d - (y_{i,j})_d\right)^2 \end{pmatrix} \tag{3.6}$$

where ω_i is the weight factor for each component of the kinetic scheme; $(\bar{y}^*_{i,j})_0$ and $(\bar{y}^*_{i,j})_d$ are the average experimental values of the molar fraction of each component (at zero time and at t reaction time), determined in R_j repeated experiments for the experimental condition j; $(y_{i,j})_0$ and $(y_{i,j})_d$ the corresponding calculated values with model; $n_{e,0}$ and $n_{e,d}$ represent the number of experimental data used in the first and second term of the objective error function (Eq. 3.6).

The parameters to be optimized are the kinetic constants of each j reaction, which are related with the temperature through the Arrhenius equation. In order to reduce the correlation between the pre-exponential factor and the activation energy, this equation is reparametrized, expressing the kinetic constant as a function of its

corresponding value, k_j^*, at a reference temperature, T* (275 °C).

$$k_j = k_j^* \exp\left[-\frac{E_j}{R}\left(\frac{1}{T}-\frac{1}{T^*}\right)\right] \tag{3.7}$$

In like manner, the relation between the adsorption constants (of the components that limit the kinetic with its adsorption) and the temperature are reparametrized:

$$K_{ad,i} = K_{ad,i}^* \exp\left[-\frac{\Delta H_{ad,i}^0}{R}\left(\frac{1}{T}-\frac{1}{T^*}\right)\right] \tag{3.8}$$

With this reparametrization the kinetic parameters to be calculated are the kinetic constants, k_j^*, and the adsorption equilibrium constants $K_{ad,i}^*$, at the reference temperature and their corresponding activation energies, E_j, or adsorption enthalpies, $\Delta H_{ad,i}^0$.

To integrate the kinetic equations (mass balances) and the multiple non-linear regression, a calculation program written in MATLAB® has been developed, whose block diagram is described in Figure 3.6. The main program reads the experimental data of the components in the kinetic scheme and assigns initial values to the parameters to be estimated, to afterwards call the calculation routine of the multivariable non-lineal regression. The standard procedure for the determination of the optimal values for the parameters consisted of a first approach to the optimum through a genetic algorithm (ga) subroutine (that imitates the biological evolution as a strategy to solve problems (Coley, 1999); followed by a second search of the optimum with the own MATLAB® subroutine *fminsearch*; and finishes calling to the *aju_mul* subroutine, developed by the user (based on the Levenberg-Marquardt method) for the calculation of the confidence intervals of the parameters to be optimized.

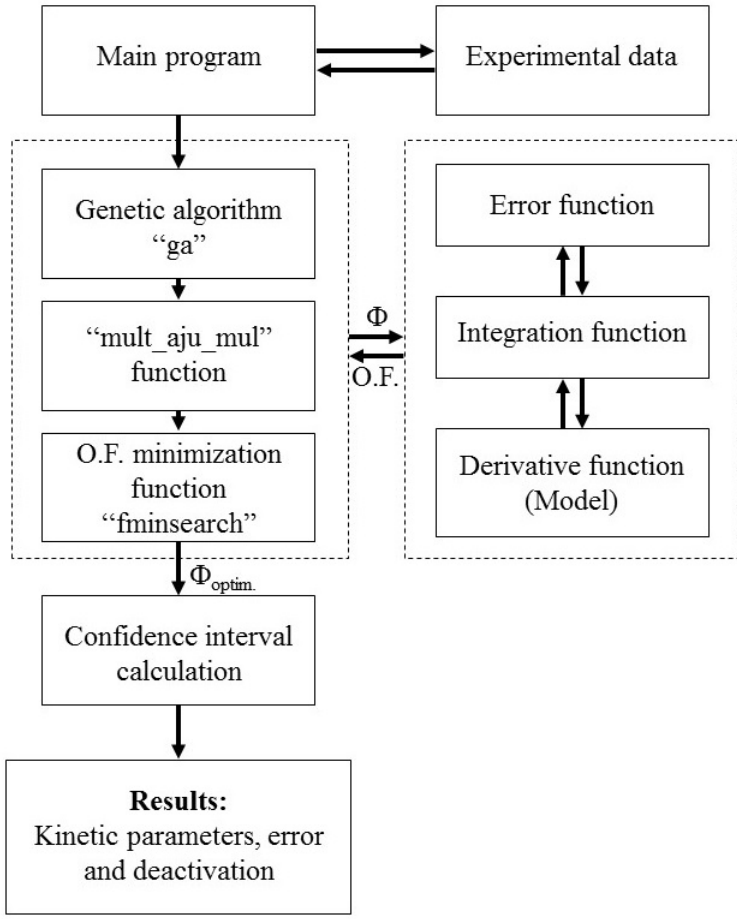

Figure 3.6: Steps of the calculation program of the kinetic model, where Φ represents the vector of the kinetic parameters to be adjusted.

These subroutines call additionally to the integration subroutine to calculate the compositions and activity (equal to 1 in the case of the calculation of the parameters at zero time on stream) at different experimental conditions in each of the points in the mesh and the subroutine to minimize the error objective function (Eq. 3.6). The subroutine "Integration function" integrates the differential equations system defined in the subroutine "Derivative function", and also calculates the equilibrium constants as a function of the temperature. For that purpose, it ap-

plies the equation described by Aguayo et al. (2007) for the reaction of methanol formation from CO (Eq. 3.12; while the methanol formation from CO_2 is calculated as the product of the constants K of Eqs. 3.12 and 3.14 for being linear combination of themselves) and the described by Iliuta et al. (2010) for the reactions of methanol dehydration towards DME (Eq. 3.15) and WGS (Eq. 3.14).

3.3.2 Significance and validity of the model

The significance of the kinetic model has been verified by a variances analysis, Fisher test, considering that the kinetic model fits well to the experimental data, if the following criterion is fulfilled:

$$F = \frac{s_{aj}^2}{s_{exp}^2} < F_{1-\alpha}\left(\nu_{aj}, \nu_{exp}\right) \tag{3.9}$$

where s_{aj}^2 is the variance for the lack of fitting and s_{exp}^2 is the variance of the experimental error.

With this criterion can be estimated that the lack of fitting of the model is similar to the experimental error. The critical value has been calculated with the MATLAB® function *fin(1-*α*.* ν_{aj}*,* ν_{exp}*)* for a value α = 0.05 (confidence interval of 95 %, from the degrees of freedom ν_{aj} and ν_{exp}.

As different models have been tested, for the selection of the most suitable one the significance of each enhancement has been quantified (greater complexity of the model), substituting the model a by the b one. In this sense, if the degrees of freedom of both models are (ν_a, ν_b), being $s_a^2 > s_b^2$ and the sum of square errors $SSE_a > SSE_b$, the improvement of the model b in comparison with the a one is

significant if the following is fulfilled:

$$F_{a-b} = \frac{(SSE_a - SSE_b)/SSE_b}{(\nu_a - \nu_b)/\nu_b} > F_{1-\alpha}\left((\nu_a - \nu_b), \nu_b\right) \tag{3.10}$$

When $\nu_a = \nu_b$ the criterion (Eq. 3.10) can not be applied and the variances analysis is carried out consisted of comparing model b with model a. If $s_a^2 > s_b^2$, the improvement of the fitting with model b is significant if the following is fulfilled:

$$F_{a-b} = \frac{SSE_a/\nu_a}{SSE_b/\nu_b} = \frac{s_a^2}{s_b^2} > F_{1-\alpha}\left(\nu_a - \nu_b\right) \tag{3.11}$$

If this criterion is not satisfied, the enhancement is not significant and, consequently, previous model a is selected.

3.4 Proposed kinetic model

The proposed model is based on the experience of the PhD Thesis of Sánchez-Contador (2017) for a catalyst with similar composition as the one used in this Thesis, but with a core-shell configuration in his case. The reactions involved in the reaction scheme are the following:

Methanol synthesis

$$CO + 2\,H_2 \longleftrightarrow CH_3OH \tag{3.12}$$

$$CO_2 + 3\,H_2 \longleftrightarrow CH_3OH + H_2O \tag{3.13}$$

Reverse water gas shift (rWGS)

$$CO_2 + H_2 \longleftrightarrow CO + H_2O \tag{3.14}$$

Methanol dehydration towards DME

$$2\,CH_3OH \longleftrightarrow CH_3OCH_3 + H_2O \tag{3.15}$$

Paraffins formation secondary reaction (mainly methane)

$$n\,CO + (2\,n + 1)\,H_2 \longleftrightarrow C_nH_{2n+2} + n\,H_2O \quad (n = 1 - 3) \tag{3.16}$$

For the kinetic study, the experiments have been carried out within the temperature range of 250 - 350 °C, under 10 - 40 bar, feeding H_2 + CO + CO_2 and H_2 + CO_2, with a space time of 5 and 10 $g_{cat}\,h\,(mol_C)^{-1}$, and a time on stream of 5 h.

3.4.1 Kinetic equations of the reaction and deactivation steps

The selected kinetic equations based on its fitting, attending to the fitting and significance criteria aforementioned, are the following:

Methanol synthesis through hydrogenation of CO (Eq. 3.12) and CO_2 (Eq. 3.13):

$$r_{MeOH} = \left[k_1 \left(f_{CO}\, f_{H_2}^2 - \frac{f_{CH_3OH}}{K_1} \right) + \right. \\ \left. + k_4 \left(f_{CO_2}\, f_{H_2}^3 - \frac{f_{CH_3OH}\, f_{H_2O}}{K_1} \right) \right] \frac{1}{1 + K_{ad,H_2O}\, f_{H_2O}} \tag{3.17}$$

Methanol dehydration towards DME (Eq. 3.15):

$$r_{DME} = k_2 \left[f_{CH_3OH}^2 \; - \; \frac{f_{CH_3OCH_3}\, f_{H_2O}}{K_2} \right] \tag{3.18}$$

WGS reaction (CO_2 formation) (reverse of Eq. 3.14):

$$r_{CO_2} = \left(k_3\, f_{CO}\, f_{H_2O} - \frac{f_{CO_2}\, f_{H_2}}{K_3} \right) \frac{1}{1 + K_{ad,CO_2}\, f_{CO_2}} \tag{3.19}$$

Hydrocarbons synthesis (C_1-C_4 paraffins) (Eq. 3.16):

$$r_{HC} = \beta_1 \; + \; \beta_2(T) \; + \; k_5 \left(f_{CO}\, f_{H_2}^3\, f_{CO} - \frac{f_{HC}\, f_{H_2O}}{K_5} \right) \; \approx \beta \tag{3.20}$$

In the expressions of Eqs. 3.17 - 3.20, the reactions have been considered to be elemental and the adopted hydrocarbons formation (Eq. 3.20) corresponding to the formation of CH_4 (main hydrocarbon).

The preliminary study of the individual reactions significance has allowed to establish that the reaction rate in Eq. 3.20 has little impact on the total carbon balance due to the low CH_4 concentration, as a constant β.

On the other hand, the model incorporates in the kinetics of methanol synthesis (Eq. 3.17) and WGS reaction (Eq. 3.19) attenuation terms that, according to Langmuir-Hinshelwood (L-M) competitive adsorption assumptions, limit the reaction rate by H_2O and CO_2 adsorption in the metallic sites. The attenuation is quantified with the adsorption equilibrium constants K_{H_2O} and K_{CO_2} in Eqs. 1.17 and 1.19, respectively. These terms have been maintained in the kinetics after the significance study, demonstrating the absence of improvements in the fitting considering the adsorption of other components in each case. The reaction rate of methanol dehydration (Eq. 3.18) might be attenuated, predictably, by H_2O adsorption in the acid sites of SAPO-11. However, this will not affect the reaction rate because the catalyst has been prepared with an excess of acid function, being the limiting step, in DME synthesis, the methanol synthesis and the key role on DME yield corresponds to the metallic function.

Attending to the aforementioned deactivation backgrounds and based on the preliminary studies, where other alternatives have been discarded, a deactivation kinetic equation has been proposed (Eq. 3.21. This equation is dependent on the product oxygenates concentration (methanol and DME), given the capacity of both (DME one is higher) to generate methoxy ions through adsorption in the metallic sites. Considering therefore that the coke formation mechanism takes place by adsorption of the oxygenates in the metallic sites, two limiting terms of this adsorption and hence of the deactivation have been accounted. It considers the limitation of the oxygenates adsorption rates by the competition of adsorption between CO_2 and H_2O in the metallic sites. Thus, the proposed deactivation kinetic equation is:

$$-\frac{da}{dt} = \frac{k_d(f_{MeOH} + f_{DME})}{1 + K^d_{ad,H_2O}\, f_{H_2O} + K^d_{ad,CO_2}\, f_{CO_2}}\, a \tag{3.21}$$

3.4.2 Kinetic parameters

In Table 3.5 the kinetic parameters of best fit calculated for the proposed kinetic model have been gathered, with the methodology described in Section 3.3.

The sum of squared errors, the degrees of freedom, the variance of both the experimental error and of the lack of fitting of the kinetic model, as well as the Fisher critical value F are shown in Table 3.6.

The results demonstrate that the model satisfies the required significance test, since the error associated to the lack of fit is similar to the experimental error. The values of the kinetic parameters (Table 3.5) exhibit that the kinetic constant of methanol dehydration (k_2^*) is significantly higher than the WGS reaction one (k_3^*) and this is greater than the kinetic constant of methanol synthesis, from both CO and CO_2 (k_1^* and k_4^*, respectively). This latter (methanol synthesis) is the slowest step and it is considered the controlling step of the reaction progress. The paraffins formation constant (β) is even slower, which however is important in the catalyst deactivation by coke. Furthermore, methanol synthesis has a higher activation energy than the rest of the reactions, consistent with the greater effect with temperature.

At the same time, it is significant the attenuating role of methanol synthesis and WGS reactions through the competitive adsorption of H_2O and CO_2 in the metallic sites, being more important the first one, attending to the values of the adsorption constants.

Table 3.5: Calculated kinetic parameters and fitting magnitudes to the experimental results.

Kinetic parameters	Units	Value
k_1^*	$mol_{MeOH}\ g^{-1}\ h^{-1}\ bar^{-3}$	5.89 E-06
k_2^*	$mol_{DME}\ g^{-1}\ h^{-1}\ bar^{-2}$	2.86 E+00
k_3^*	$mol\ g^{-1}\ h^{-1}\ bar^{-2}$	2.57 E-02
k_4^*	$mol_{MeOH}\ g^{-1}\ h^{-1}\ bar^{-4}$	4.45 E-07
E_1	$kcal\ mol^{-1}$	2.04 E+01
E_2	$kcal\ mol^{-1}$	1.21 E+01
E_3	$kcal\ mol^{-1}$	1.32 E+01
E_4	$kcal\ mol^{-1}$	1.30 E+01
β	$mol_{HC}\ g^{-1}\ h^{-1}\ bar^{-1}$	4.24 E-07
K^*_{ads,H_2O}	bar^{-1}	3.40 E+00
K^*_{ads,CO_2}	bar^{-1}	2.63 E-01
$\Delta H_{ads,H_2O}$	$kcal\ mol^{-1}$	2.22 E-02
$\Delta H_{ads,CO_2}$	$kcal\ mol^{-1}$	1.95 E-02
k_d^*	$h^{-1}\ bar^{-1}$	1.31 E-01
E_d	$kcal\ mol^{-1}$	6.55 E-01
K^{*d}_{dads,CO_2}	bar^{-1}	1.32 E-02
K^{*d}_{ads,H_2O}	bar^{-1}	1.27 E-02
$\Delta H^d_{ads,CO_2}$	$kcal\ mol^{-1}$	1.28 E-01
$\Delta H^d_{ads,H_2O}$	$kcal\ mol^{-1}$	3.24 E-01
Error		3.74 E-03
Residual variance		3.76 E-05

Table 3.6: Significance test parameters of the kinetic model.

Parameters	Value
SSE_{exp}	1.36 E-03
ν_j	18
s_j^2	1.36 E-03
s_i^2	1.03 E-03
s_i^2 / s_j^2	0.76
$F_{1-\alpha}\ (\nu_i, \nu_j)$	1.93
Significance test	Valid

It should be pointed out that the activation energy of the deactivation is small. This can be explained because it is an apparent value influenced by the values of H_2O and CO_2 adsorption in the metallic sites. Attending to the values of these adsorption constants, the adsorption effect of H_2O and CO_2 are similar in the attenuation of the deactivation.

In Figure 3.7 is depicted, in a parity diagram, the fitting of the calculated results with the model and the experimental ones, of the molar fraction of each component in the reaction scheme.

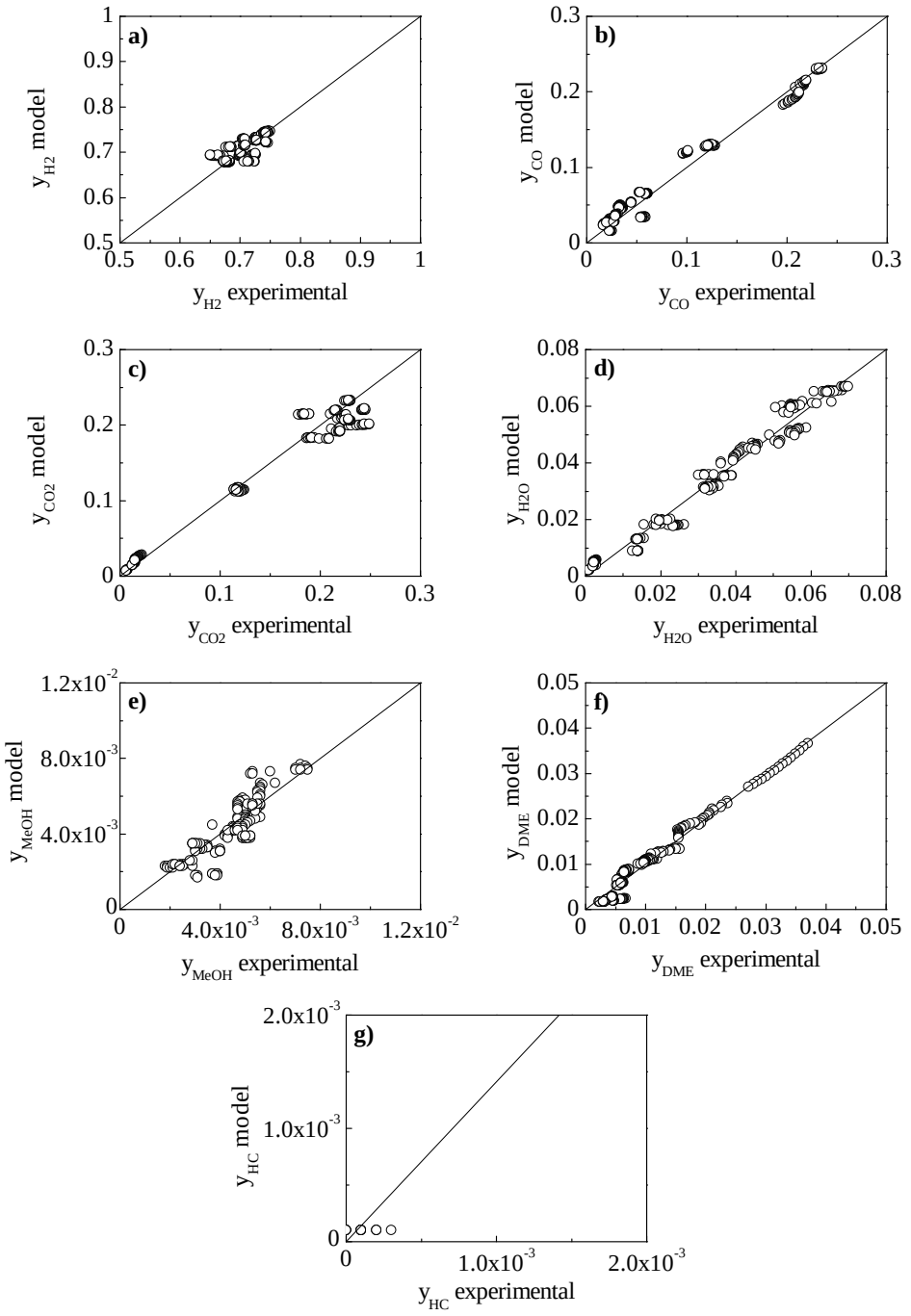

Figure 3.7: Fitting of the experimental values of the components molar fractions to those calculated with the model. H_2 (a), CO (b), CO_2 (c), H_2O (d), MeOH (e), DME (f), HC (g).

3.5 Effect of the operating variables

3.5.1 Products yield

The experimental and calculated (with the model) results of the components yields in reaction medium are shown below and have been calculated as described in Eq. 2.1. These results have been selected to illustrate the effect of each operating variables and, simultaneously, to show the reactor simulation capacity of the reactor with the kinetic model described in Section 3.4.

3.5.1.1 Temperature

In Figure 3.8 the evolution with time on stream of the yields of the components in the reaction medium is shown, comparing both the experimental results (dots) and those calculated with the model (lines). These results correspond to three different temperatures (one in each graph), 30 bar and syngas as feed, with $H_2 / CO_x = 3$. In the first place, a suitable fitting between the calculated and the experimental results can be observed, being a general comment for the results shown in this Section 3.5.

For each temperature it is shown that CO yield ("apparent" since it is a reactant) slightly enhances with time on stream, due to the deactivation. This deactivation is exposed more clearly in the decrease of product DME yield and barely in methanol yield. The slight decrease of CO_2 yield is a consequence of the catalyst deactivation for WGS reaction. Increasing the temperature, DME yield is significantly higher as a result of that the reaction is controlled by the methanol synthesis step, achieving an initial DME yield higher than 24 % at 325 °C (Figure 3.8c). The deactivation, nevertheless, is more prominent increasing the temperature, funda-

mentally because at 325 °C leads to Cu sintering along with the main cause, which is the coke deposition (Sánchez-Contador, 2017). These products yields trends, varying the temperature, are consistent with the results with other catalysts in the literature (Ateka et al., 2016a,b) and also with the process thermodynamics (Ateka et al., 2017b).

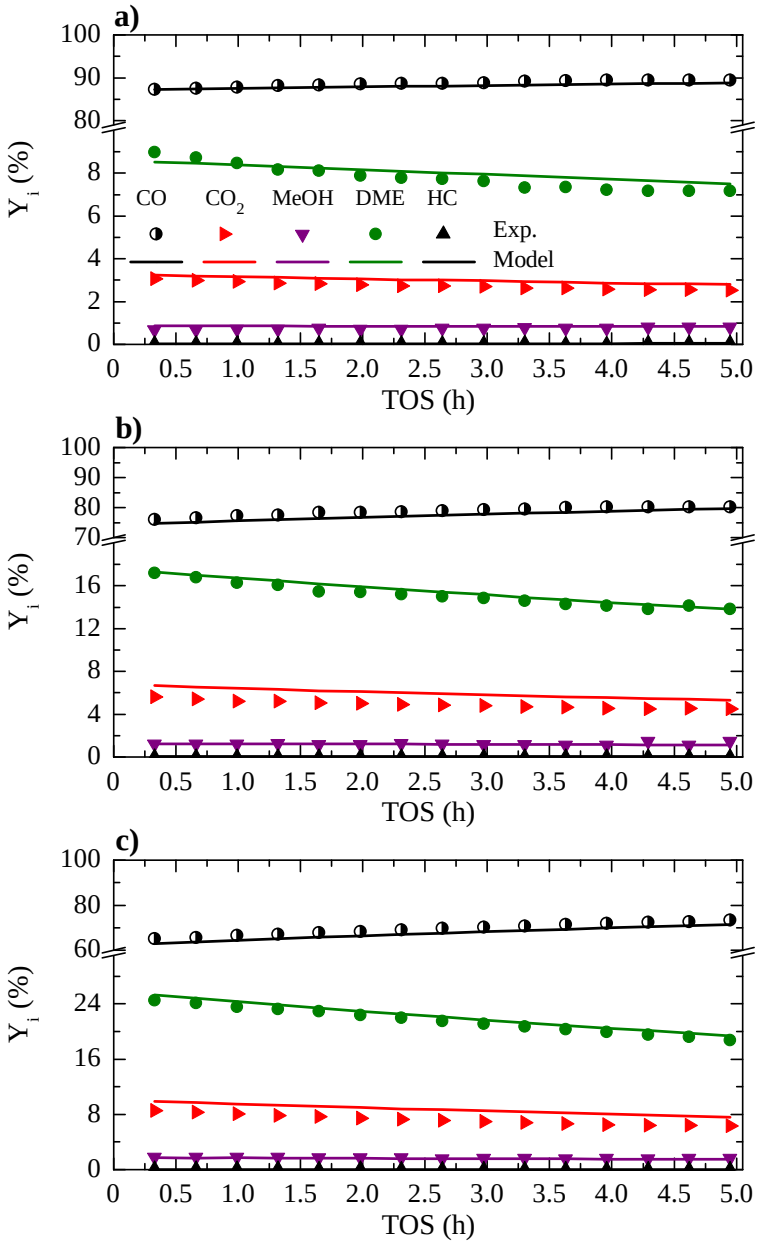

Figure 3.8: Comparison of the evolution with time on stream of the experimental values of products yields (dots) and those calculated (lines) for the PBR, at 275 °C (a), 300 °C (b) and 325 °C (c). Reaction conditions: feed, H_2 + CO; 30 bar; 5 g_{cat} h $(mol_C)^{-1}$; H_2 / CO_x, 3; CO_2 / CO_x, 0.

The results depicted in Figure 3.9 correspond to CO_2 co-feeding with a CO_2 / CO_x ratio = 0.5. DME and methanol yields are significantly lower than the observed in Figure 3.8 for synthesis gas conversion, as a result of the minor reactivity of CO_2.

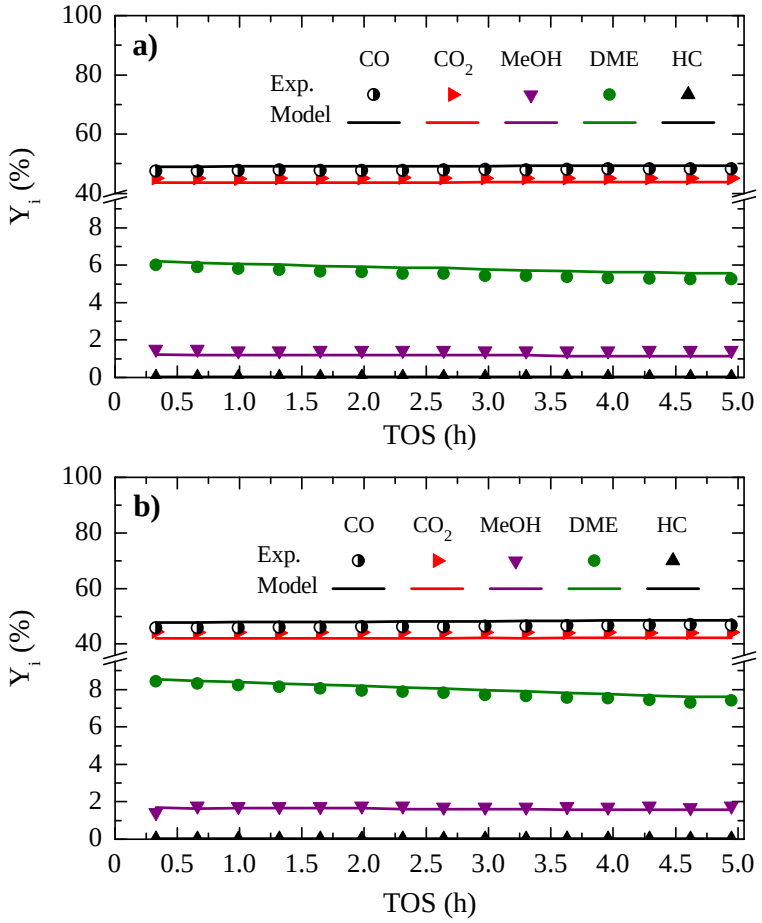

Figure 3.9: Comparison of the evolution with time on stream of the experimental values of products yields (dots) and those calculated (lines) for the PBR, at 275 °C (a) and 300 °C (b). Reaction conditions: feed, $H_2 + CO + CO_2$; 30 bar; 5 $g_{cat}\,h\,(mol_C)^{-1}$; H_2 / CO_x, 3; CO_2 / CO_x, 0.5.

Increasing the temperature from 275 °C (Figure 3.9a) to 300 °C (Figure 3.9b), DME yield is greater enhanced than of methanol. It is remarkable that the decreasing rate of DME yield with time on stream is lower than in synthesis gas conversion, due to the well established effect of attenuation of both the initial conversion and coke deposition rising the H_2O content in the reaction medium (Sierra et al., 2011). In like manner, the effect of temperature and CO_2 co-feeding follows the trends previously observed in the literature (Ateka et al., 2017a; Ereña et al., 2011) and are consistent with the thermodynamics (Ateka et al., 2017b).

3.5.1.2 Pressure

The experimental (dots) and the calculated (lines) results in Figure 3.10 correspond to a feed of CO_2 and H_2 (CO_2 / CO_x = 1), at 300 °C. The graphs a, b and c depict the pressures of 20, 30 and 40 bar, respectively. The results in Figure 3.11 have been obtained at 275 °C with the double space time, 10 g_{cat} h $(mol_C)^{-1}$, maintaining the rest of the operating conditions as in Figure 3.10.

At 300 °C (Figure 3.10) CO_2 conversion is limited by the thermodynamics and DME yield is enhanced increasing the pressure. At 40 bar achieves a yield of 8 %. It is also clear the higher deactivation (attending to the decrease with time on stream of DME yield), increasing the pressure, particularly between 30 and 40 bar. It should be pointed out that the general trend of the pressure effect on the products distribution is similar to the one obtained in the literature with other catalysts (Ateka et al., 2017a, 2016a,b,b; Sánchez-Contador et al., 2019; Saravanan et al., 2017).

Attending to the previous results, 30 bar of pressure can be considered as suitable since it allows to achieve a considerable DME yield with a slow deactivation.

Likewise, 275 °C is an appropriate temperature in order to avoid thermodynamic limitations and to be able to work with a slight catalyst deactivation.

The enhance in DME yield achieved increasing the space time from 5 g_{cat} h $(mol_C)^{-1}$ to 10 g_{cat} h $(mol_C)^{-1}$ at 275 °C is relatively small, from 4.5 % to 6 % under 30 bar, since it is close to the thermodynamic equilibrium.

It is also noteworthy that although DME yield can be considered low in one step reaction, this performance is also characteristic of methanol synthesis from syngas and, even more notable, from CO_2, where its conversion is lower than by the synthesis of DME. Consequently, as well as by the industrial methanol synthesis, DME synthesis requires the recirculation of CO, CO_2 and H_2 after the separation of this gas flow from DME, methanol and H_2O, which are condensed at the reactor outlet. It should be also pointed out the high CO yield in the one step reaction that has been studied in the preceding figures.

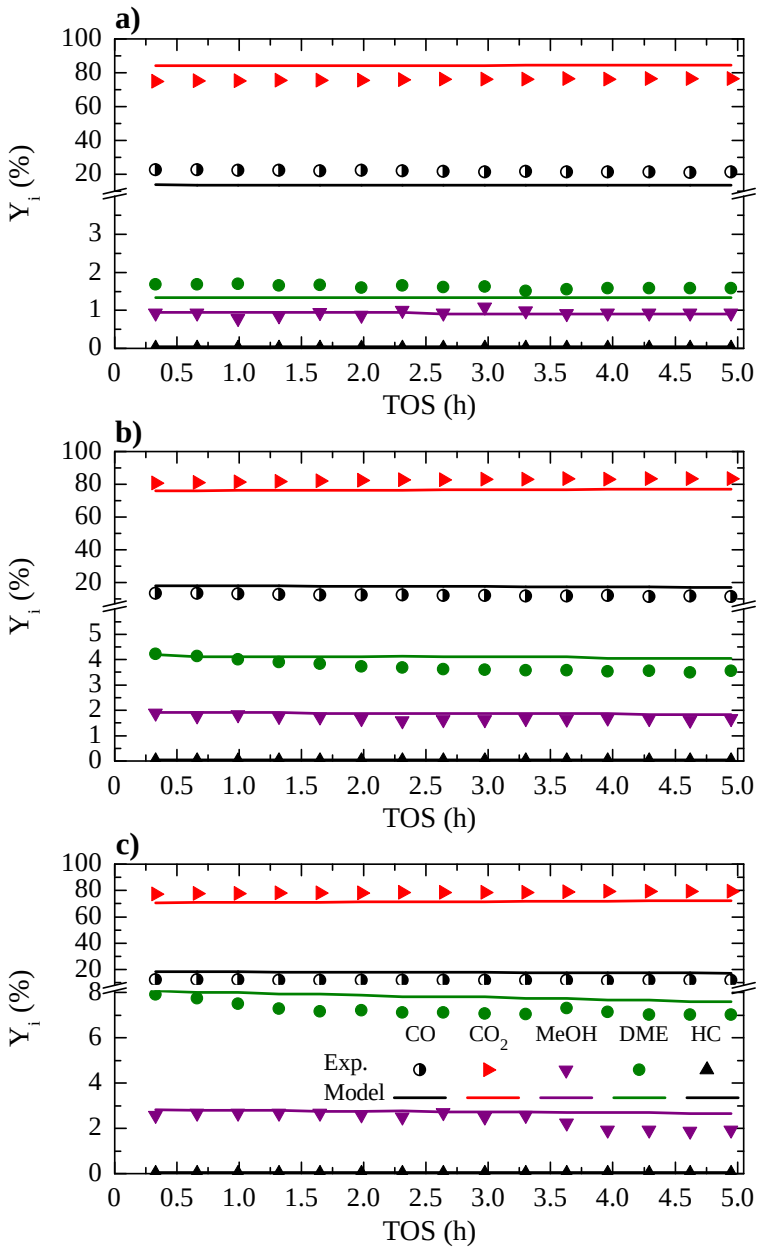

Figure 3.10: Comparison of the evolution with time on stream of the experimental values of products yields (dots) and those calculated (lines) for the PBR, under 20 bar (a), 30 bar (b) and 40 bar (c). Reaction conditions: feed, H_2 + CO_2; 300 °C; 5 g_{cat} h $(mol_C)^{-1}$; H_2 / CO_x, 3; CO_2 / CO_x, 1.

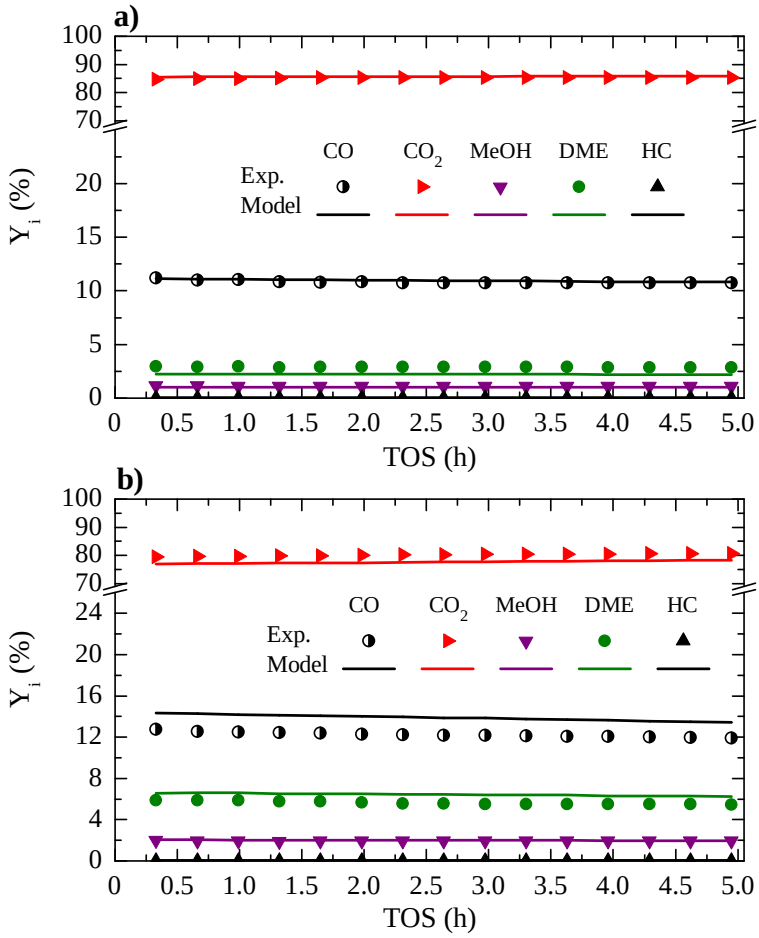

Figure 3.11: Comparison of the evolution with time on stream of the experimental values of products yields (dots) and those calculated (lines) for the PBR, under 20 bar (a) and 30 bar (b). Reaction conditions: feed, $H_2 + CO_2$; 275 °C; 10 $g_{cat}\,h\,(mol_C)^{-1}$; $H_2\,/\,CO_x$, 3; $CO_2\,/\,CO_x$, 1.

3.5.1.3 Space time

The aforementioned thermodynamic limitation at 300 °C is predicted by the model in Figure 3.12, where the results are depicted for two space time values, 10 $g_{cat}\,h\,(mol_C)^{-1}$ (a) and 5 $g_{cat}\,h\,(mol_C)^{-1}$ (b), at 325 °C.

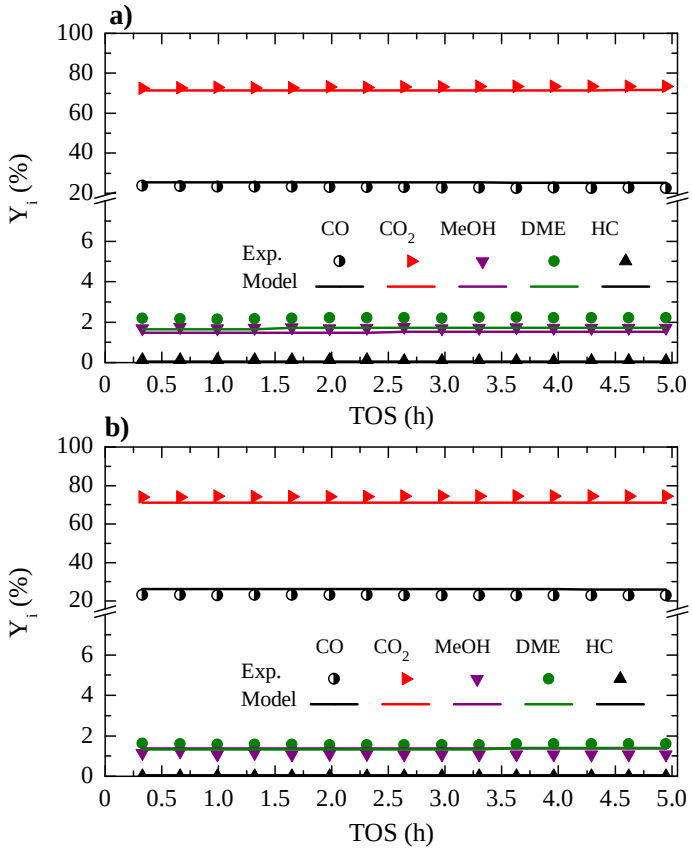

Figure 3.12: Comparison of the evolution with time on stream of the experimental values of products yields (dots) and those calculated (lines) for the PBR, for 10 (a) and 5 (b) $g_{cat}\,h\,(mol_C)^{-1}$. Reaction conditions: feed, $H_2 + CO_2$; 325 °C; 30 bar; $H_2\,/\,CO_x$, 3; $CO_2\,/\,CO_x$, 1.

The kinetic model has also adequately foreseen that the deactivation ("apparent" for being close to the thermodynamic equilibrium and hence with an excess of catalyst) is negligible at these conditions.

3.5.1.4 CO_2 content in the feed

Figure 3.13 indicates the effect of CO_2 concentration in the feed. The evolutions with time on stream on the products yields are compared, for a CO_2 and H_2 feed (a) and CO_2 co-fed with synthesis gas with the same current flow as CO (b).

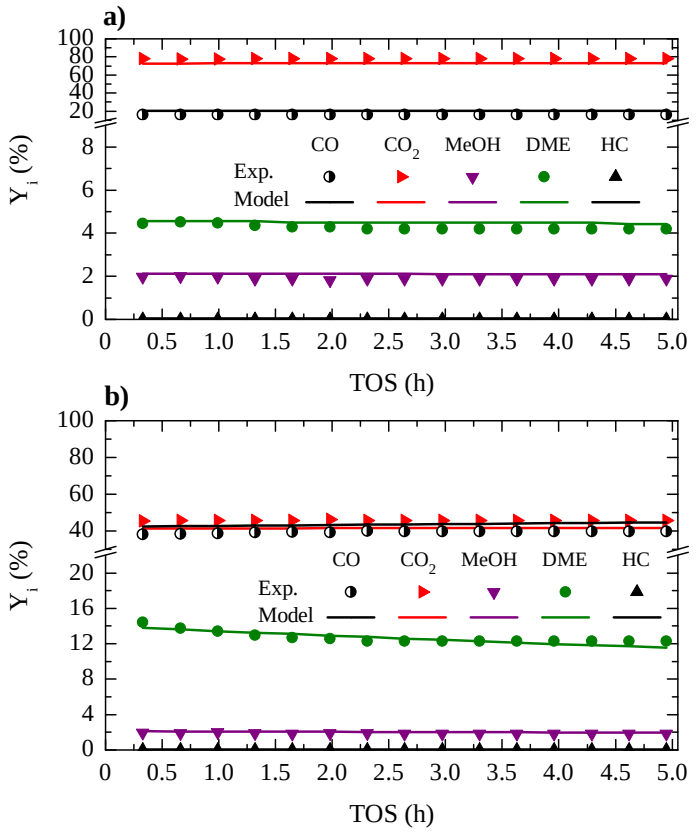

Figure 3.13: Comparison of the evolution with time on stream of the experimental values of products yields (dots) and those calculated (lines) for the PBR, for $H_2 + CO_2$ feed (a) and $H_2 + CO + CO_2$ feed with CO_2 / CO_x, 0.5 (b). Reaction conditions: 300 °C; 30 bar; 10 g_{cat} h $(mol_C)^{-1}$; H_2 / CO_x, 3.

The low DME yield and also the insignificant deactivation can be noted with $H_2 + CO_2$ feed (Figure 3.13a), while at these conditions the deactivation is noteworthy in Figure 3.13b.

3.5.2 Oxygenates yields and CO_2 conversion

The availability of the kinetic model enables the calculation, by simulation of the isothermal fixed bed reactor, of the values of possible pursued targets such as DME or oxygenates (methanol and DME) yield, due to their commercial interest as fuel or raw materials, or CO_2 conversion if the goal is the reduction of this greenhouse effect gas. It is worth noting that from the perspective of emission taxes saving, this conversion will have an economic connotation to be evaluated. Presumably, it will be required a commitment between the commercial and environmental objectives towards the process economy.

As an example of the capability of the simulation program and the kinetic model for the described objectives, Figures 3.14 - 3.17 show the effect of temperature and pressure on the yields (Eq. 2.1) at 1 h time on stream of DME (Figures 3.14a and 3.16a) and methanol (Figures 3.14b and 3.16b), carbon feed conversion ($CO + CO_2$) (Eq. 2.4) (Figures 3.15a and 3.17a) and CO_2 conversion (Eq. 2.3) (Figures 3.15b and 3.17b). Figures 3.14 and 3.15 corresponds to a $H_2 + CO + CO_2$ feed with $CO_2 / CO_x = 0.5$ and Figures 3.16 and 3.17 to a $H_2 + CO_2$ feed, being the rest of the conditions similar in all cases.

It can be observed in Figure 3.14 the enhancement of DME and methanol yields (whose values are remarkably lower) increasing the pressure and temperature. DME yield (Figure 3.14a) achieves its utmost value (slightly pronounced) for each pressure at around 300 °C, while methanol yield (Figure 3.14b) reaches a theoretical maximum above 325 °C, which is a limiting condition by the presumably Cu sintering in the catalyst.

$CO + CO_2$ conversion (Figure 3.15a) is greater increasing the pressure and at 310 °C achieves a peak, which is more pronounced rising the pressure. The dependence

of CO_2 conversion with temperature and pressure (Figure 3.15) is qualitatively similar, however the maximum of the conversion can only be observed over 40 bar and also at around 310 °C.

The evolution of DME yield with pressure and temperature feeding CO_2 with H_2 (Figures 3.16 and 3.17) exhibits a notable effect of CO_2 concentration in the reaction medium on the oxygenates yield and CO_2 conversion. Thus, DME yield (Figure 3.16a), besides being lower when increasing CO_2 concentration, it is little dependent on the temperature under moderate pressures. Although this reaches a peak, it is evident that this maximum is displaced at lower temperatures, within the range 250 - 275 °C, increasing the pressure between 20 and 50 bar. Furthermore, methanol yield (Figure 3.16b), similar to the one obtained with lower CO_2 concentration in the feed (Figure 3.14b), achieves in this case a maximum at around 300 °C, more pronounced increasing the pressure, but it remains at this temperature.

The effect of increasing the pressure is higher than the temperature influence to promote CO_x conversion (Figure 3.17a), and a peak is presented at a temperature that decreases in the range of 275 - 290 °C increasing the pressure between 20 and 50 bar. Comparing the Figures 3.15b and 3.17b, is remarkable the upgrade of CO_2 conversion increasing its concentration in the feed. The overall effect of increasing temperature and pressure are similar, nevertheless the maximum in this case is displaced at limiting temperatures, above 325 °C.

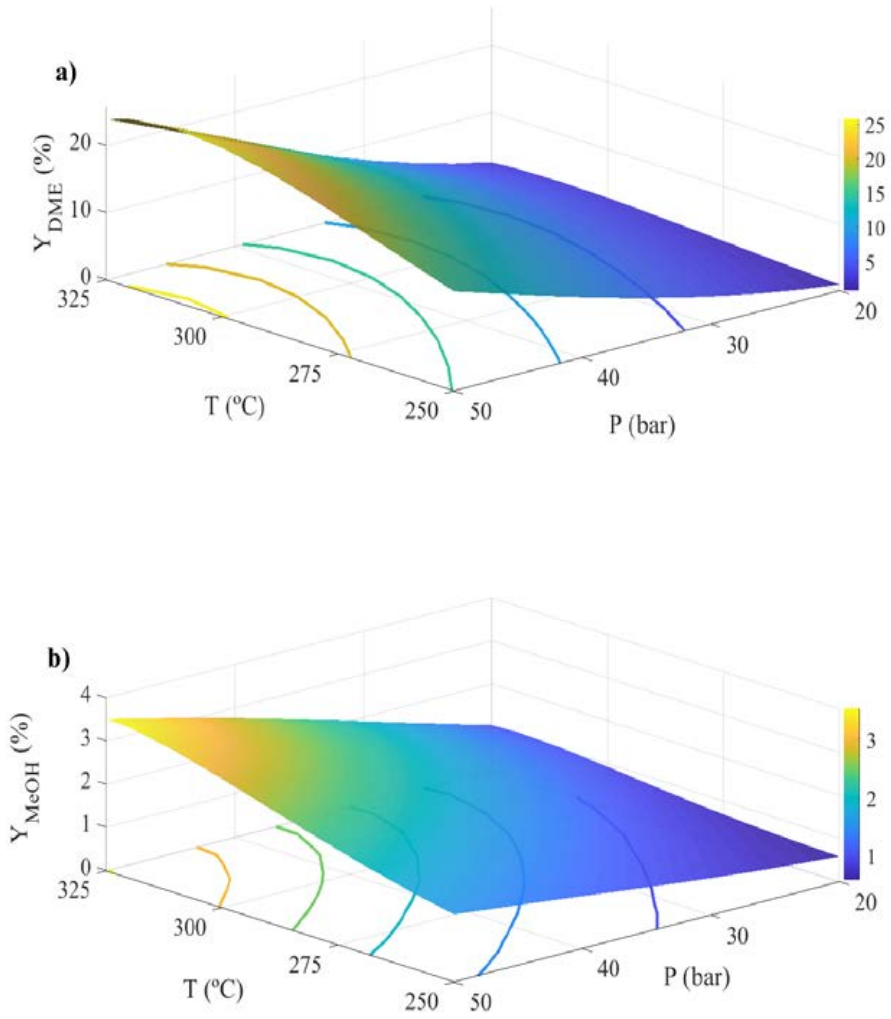

Figure 3.14: Evolution with temperature and pressure of DME yield (a) and MeOH yield (b). Reaction conditions: feed, $H_2 + CO + CO_2$; 5 $g_{cat}\,h\,(mol_C)^{-1}$; $H_2\,/\,CO_x$, 3; $CO_2\,/\,CO_x$, 0.5.

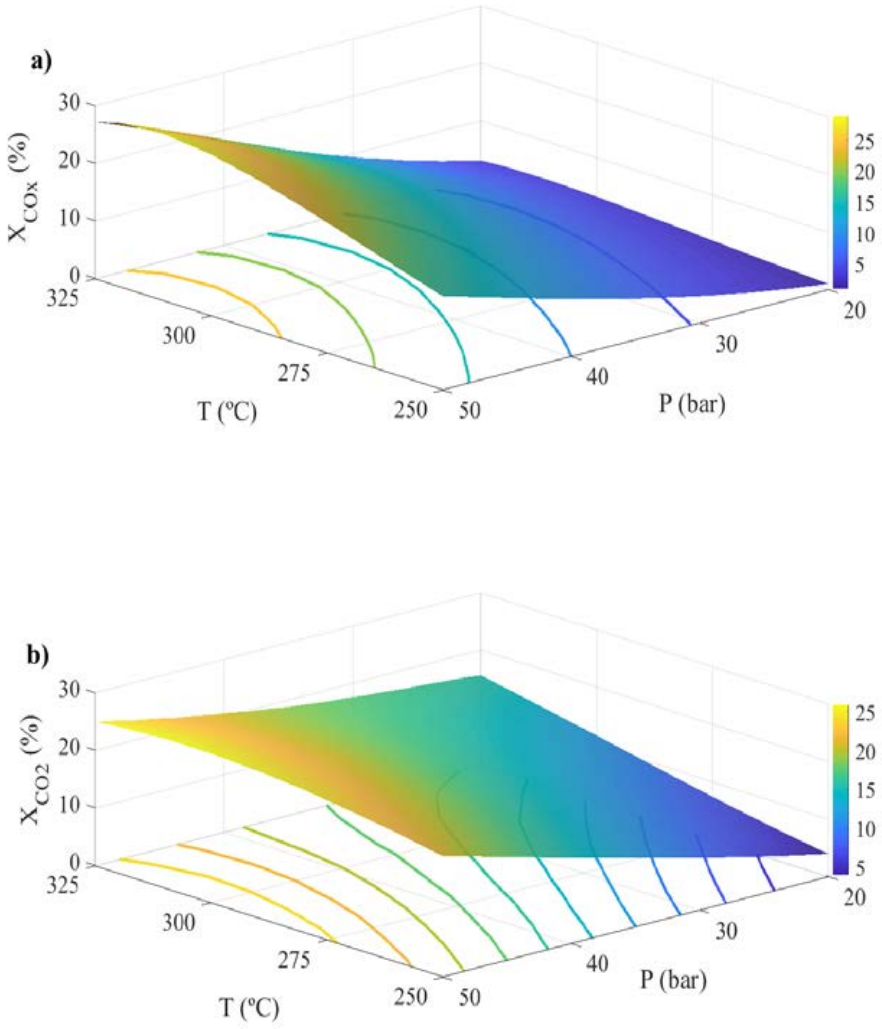

Figure 3.15: Evolution with temperature and pressure of CO_x conversion (a) and CO_2 conversion (b). Reaction conditions: feed, $H_2 + CO + CO_2$; 5 g_{cat} h $(mol_C)^{-1}$; H_2 / CO_x, 3; CO_2 / CO_x, 0.5.

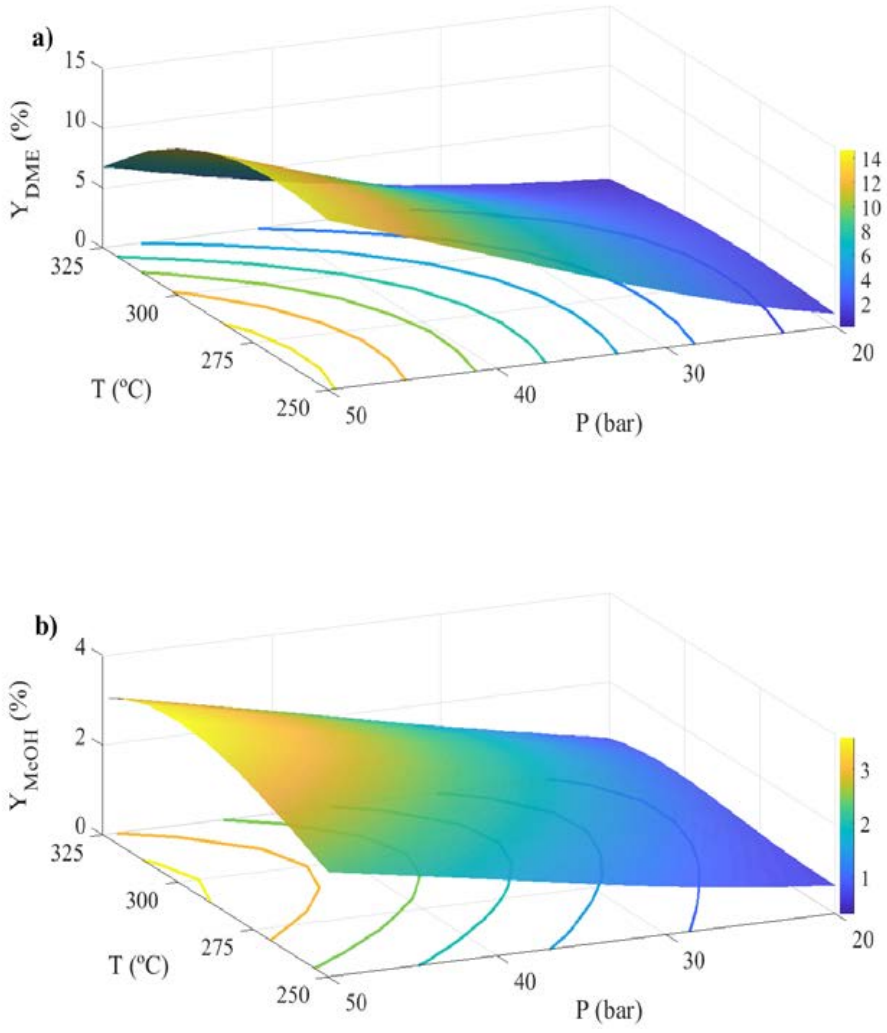

Figure 3.16: Evolution with temperature and pressure of DME yield (a), MeOH yield (b). Reaction conditions: feed, $H_2 + CO_2$; 5 $g_{cat}\,h\,(mol_C)^{-1}$; $H_2\,/\,CO_x$, 3; $CO_2\,/\,CO_x$, 1.

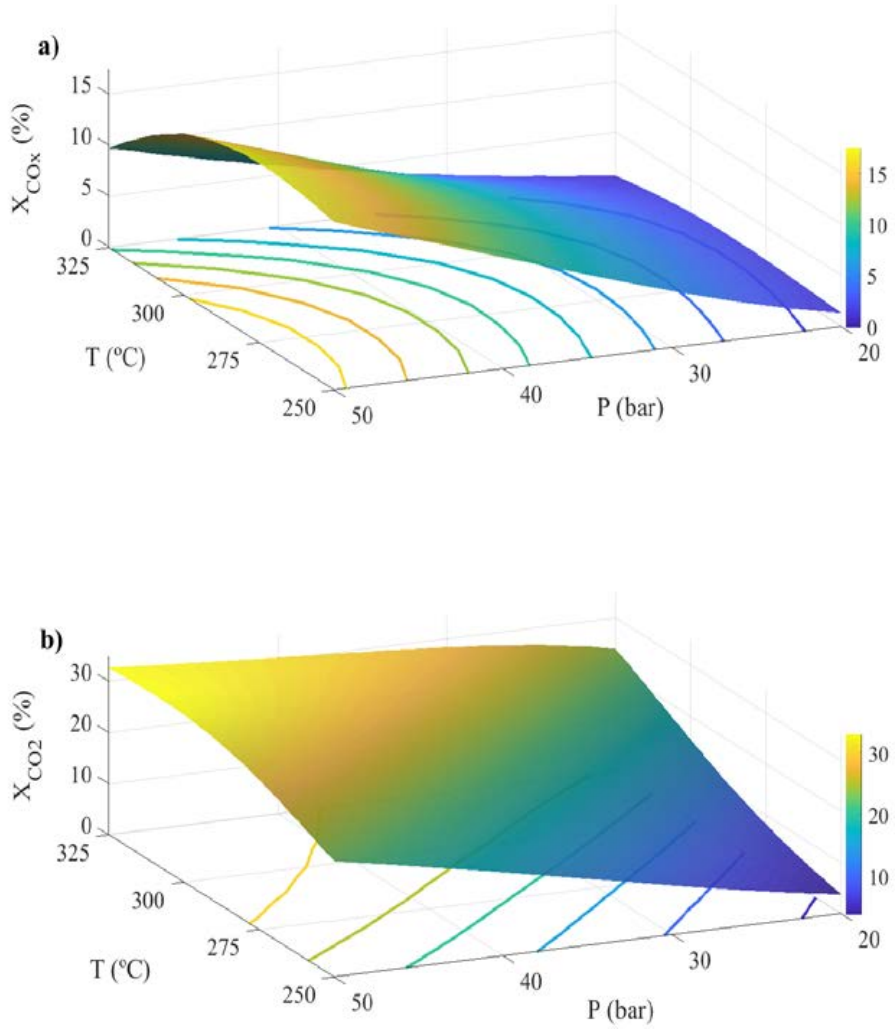

Figure 3.17: Evolution with temperature and pressure of CO_x conversion (a) and CO_2 conversion (b). Reaction conditions: feed, $H_2 + CO_2$; 5 $g_{cat}\,h\,(mol_C)^{-1}$; $H_2\,/\,CO_x$, 3; $CO_2\,/\,CO_x$, 1.

In Figure 3.18 is depicted the comparison of the evolution of temperature and pressure of the two possible pursued targets (commercial and environmental), thus DME yield and CO_2 conversion. Hence, these results provide interesting information in order to pursue a commitment between both objectives. To give another complementary perspective of the simulation results, the axes have been reversed with regard to Figures 3.14, 3.15, 3.16 and 3.17.

The results of DME yield and CO_2 conversion have a qualitatively similar trend, as shown in Figure 3.18a, corresponding to a $H_2 + CO + CO_2$ feed. Both values are enhanced increasing temperature and pressure, observing the before described maximum (less pronounced) with the temperature on DME yield under 20 bar and CO_2 conversion under 50 bar. Moreover, it can be observed that the effect of each of the variables (temperature and pressure) is quantitatively different according with the value of the other variable. Thus, at low pressure the influence of increasing the temperature is higher on CO_2 conversion than on DME yield and, conversely, is lower under high pressure. On the other hand, the effect of increasing the pressure is greater on CO_2 conversion in comparison with DME yield and the difference becomes wider increasing the temperature.

CO_2 concentration in the feed has a relevant influence, as depicted on the response surface of Figure 3.18b, corresponding to $H_2 + CO_2$ feed. These surfaces possess different trends, in a manner that the effect of temperature and pressure variables is remarkably pronounced on CO_2 conversion, and the influence on DME yield is significantly smaller. The maximum for different intermediate temperatures of DME yield and CO_2 conversion are the causes for which CO_2 conversion is overall enhanced with the temperature until 325 °C, while DME yield reaches its peak in the range of 275 - 290 °C. As a result of these effects, consequence of the complexity of the reaction scheme, the response surfaces in Figure 3.16 achieve

their greatest difference at high temperature and under high pressure, conditions that maximize CO_2 conversion , but are excessive for DME production.

Taking into consideration the aforementioned results, it can be concluded that within the interval of studied conditions remarkable values of DME yield and CO_2 conversion are obtained. In both cases around 25 % has been achieved, for a co-feeding of CO_2 with CO and H_2, as shown in Figure 3.18a, which enables the integration of the commercial and environmental objectives. These co-feeding conditions are also suitable for corresponding the optimal values of both objectives to similar conditions. It is also noteworthy that at moderate temperatures and pressures results close to the optimum ones are obtained, avoiding the associated costs increasing the pressure and the problems of Cu sintering in the catalyst at high temperature. In this sense, a pressure around 30 bar and a temperature within the range of 275 -290 °C, provide attractive results in comparison with the alternative processes for the production of fuels from CO_2 valorization. One of them is the methanol synthesis, whose yields are lower and also operates industrially with recirculation in order to mitigate the small per pass conversion.

Additionally, it is clear that the increase of CO_2 content in the feed favors greatly the conversion of CO_2 (up to 33 % in Figure 3.18b). Nevertheless, a lower DME yield is obtained (18 % at the most suitable conditions for this objective), emphasizing that the optimal conditions for both objectives differ substantially.

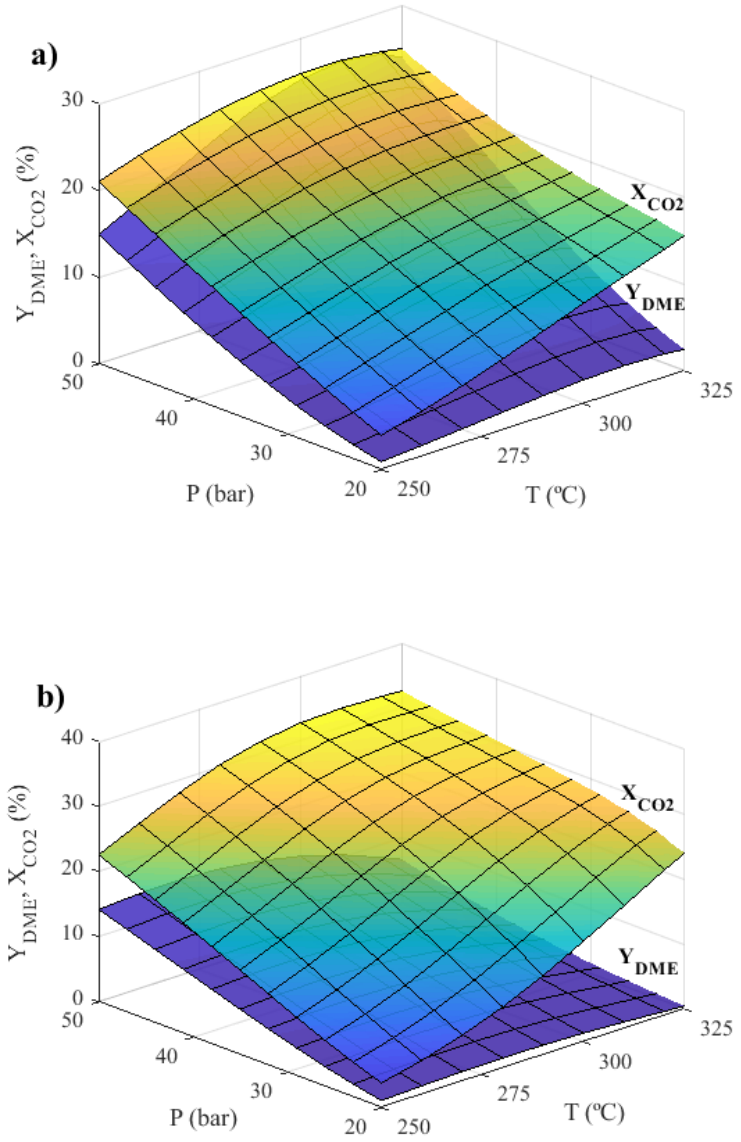

Figure 3.18: Comparison of the evolution with temperature and pressure of DME yield and CO_2 conversion for H_2 + CO + CO_2 feed. Reaction conditions: 30 bar; 5 g_{cat} h $(mol_C)^{-1}$; H_2 / CO_x, 3; CO_2 / CO_x, 0.5 (a) and 1 (b).

IV

4

RESULTS

4 | Experimental Results with the Packed Bed Membrane Reactor (PBMR)

In this chapter a background of the applications of H_2O permselective membranes in DME synthesis reactions steps has been firstly described (Section 4.1). Next, the properties of the different studied membranes have been compared and LTA membrane is analyzed in more detail (Section 4.2), as it has been selected for the reactor configuration. Subsequently, in Section 4.3 the effect of the reaction conditions in the membrane reactor (PBMR) has been studied for $H_2 + CO / CO_2$ and $H_2 + CO_2$ feeds, focusing on DME yield and CO_2 conversion. In Section 4.4 the advantages of the PBMR have been compared with the results obtained in the PBR.

4.1 Backgrounds

The incorporation of the membrane in the reactor for DME direct synthesis from CO_2 and synthesis gas is a paradigm of the application of this technology for

processes intensification. Its main objective is the reduction of both energy consumption and the production costs of fuels and chemical products from sustainable sources, minimizing the environmental impact (Tian et al., 2018).

Concerning CO_2 capture, significant progresses have been achieved in the development of different alternative technologies (absorption, adsorption, carbonation, membranes, cryogenics, chemical looping combustion, biofixation, etc.), and also of hybrid technologies in order to reduce the energetic requirements (Song et al., 2019, 2018). The membrane reactor proposal undertakes an important role in CO_2 valorization on a large scale through technologies entitled power to fuel (PTF). These are aimed, on one hand, to synthesize hydrocarbonated and oxygenated fuels (methanol, ethanol and other alcohols and DME), and, on the other hand, to collectively valorize synthesis gas produced from sources alternative to fossil fuels, either abundant fossil sources (carbon or natural gas) or renewable sources (biomass or consumer society residues). H_2 production from renewable electricity (via electrolysis) (Schemme et al., 2018) will play an important role in the industrial implementation of these initiatives.

As described in the introduction of this Thesis (Section 1.2.3), the interest in the direct synthesis of DME for CO_2 valorization (Leonzio, 2018) is motivated by different reasons: 1) interest in DME as economical biofuel and suitable for reducing polluting emissions, as well as energy carrier for substituting and improving the so-called methanol economy; 2) less stoichiometric requirement of H_2 in comparison with other processes; 3) relative ease to have the expertise on the technology of methanol synthesis and its dehydration towards DME, corresponding to established industrial processes, and specially for; 4) the good perspectives that the developments in the design of new catalysts and reactors are providing, avoiding the main process limitations (Alavi et al., 2018; Catizzone et al., 2017c).

Hereafter will be described the main progresses in the membrane reactors development for the individual steps of synthesis and dehydration of methanol, and subsequently for DME synthesis. These initiatives emerge to solve a common problem, which is the presence of water in the reaction medium (higher co-feeding CO_2). Thus, the separation of water through selective hydrophilic membranes contributes to a greatest progress of the involved reactions (methanol synthesis, WGS and methanol dehydration), displacing its thermodynamic equilibrium and attenuating the catalyst activity (due to the water molecules competition in their adsorption in the active sites). The severe reaction conditions (high pressure and temperature) require the use of inorganic membranes with high hydrothermal stability at these conditions.

Inorganic membranes (ceramic, or based on carbon, silica and zeolites) have been generally used in water treatments and desalination due to their chemical and hydrothermal stability (Kayvani Fard et al., 2018). Currently, the improvements in synthesis, diffusion and permeability measurements and application of different zeolitic membrane processes are remarkable (Bedard and Liu, 2018), highlighting the progresses in active membranes, like FAU zeolites (Kumakiri et al., 2018). Nevertheless, the application of this type of membranes in methanol and DME synthesis is still at the experimental stage.

4.1.1 Membranes for methanol synthesis

The interest in the incorporation of membranes in the fixed bed reactor for methanol synthesis is justified because it is the most used reactor in the industry (Bozzano and Manenti, 2016). Thus, Lurgi process consists of a multi-tubular reactor with single vertical fixed bed reactors (around 3000 units with 7 m of length and $3.8{\cdot}10^{-2}$ m of diameter), externally cooled by water, which is evaporated by the

transmitted heat from the external walls of the catalytic beds. Rahimpour and Ghader (2003) have proven by simulation the advantages of using a Pd / Ag membrane (typically also used in methane reforming) to longitudinally distribute H_2 feed. Galluci et al.(Gallucci et al., 2004) have emphasized on the increase of CO_2 conversion, co-fed with synthesis gas, using this membrane.

Farsi and Jahanmiri (2014) have simulated a dual-membrane rector for methanol synthesis by an unidimensional simulation model, non-isothermal and, moreover, catalyst deactivation is considered. The reaction system is composed by three concentric cylinders (the external one is the reactor metallic wall). The two membranes are, on the one side, a Pd / Ag one (intermediate cylinder) for H_2 permeation and, on the other side, a silica / alumina membrane (inner cylinder) to remove water from the reaction zone. These authors have compared the simulation results with the ones of an industrial plant with a conventional reactor. This comparison shows a higher conversion of the co-fed CO_2, an increase in methanol production and a decreased catalyst deactivation.

Responding to the necessity of zeolitic membranes for this purpose, Gorbe et al. (2018) have studied the properties of zeolite A to selectively separate water and methanol. The experiments have been carried out through the permeation measurement of a H_2, CO_2 and water mixture, within the range of interest for methanol synthesis (160 - 240 °C, 100 - 270 kPa), obtaining the highest separation factor at 240 °C.

4.1.2 Membranes for methanol dehydration

Fedosov et al. (2015) have experimentally studied methanol dehydration using a packed bed reactor, with γ-Al_2O_3 as catalyst (also industrially used) and an inert

membrane, permeable to water, based on NaA zeolite synthesized on a metall-ceramic support. Water / methanol separation factor obtained within the temperature range 150 - 250 °C was from 22 to 5, and a permeate flux of 0.6 kg h^{-1} m^{-2}. The effect of the reaction conditions (temperature, pressure and sweep flow) has been also studied, achieving a maximal conversion of 88 %, considerably higher than in a conventional reactor (8 %) at the same conditions.

A dual-layer FAU-LTA sandwich zeolite membrane deposited on alumina has been applied for methanol dehydration by Zhou et al. (2016a). Methanol is dehydrated towards DME on the H-FAU layer (moderate acidity) and water is eliminated through the LTA zeolite. The methanol conversion is around 90 % at 310 °C with a DME selectivity of 100 %. It should be emphasized that the deactivation of FAU zeolite is avoided due to the removal of water.

4.1.3 Membranes for the direct synthesis of DME

Iliuta et al. (2010) have studied by simulation the potential of removing water from the reaction medium using a hydrophilic membrane. Co-feeding CO_2, methanol yield and DME selectivity increase enhancing the water permeability of the membrane, attributed by the authors to the fact that the removal of water attenuates the inhibition of methanol dehydration. These authors have also analyzed by simulation the strategy of water adsorption in order to increase methanol and DME yields. It was determined that the adsorption is more effective increasing CO_2 concentration in the feed, because a considerably great amount of water is formed in the reaction medium and, therefore, the displacement of WGS reaction is higher (Iliuta et al., 2011).

Water separation technologies of interest have been reviewed by Diban et al. (2013),

focusing the attention on the utilization of membrane reactors in processes related to food, pharmacy and petrochemical sectors (catalytic processes for the formation of ethers, methanol, DME, linear paraffins, oxygenated additives of fuels, etc.), where the formation of water as byproduct inhibits the advance of the reaction, due to thermodynamic limitations. These authors have emphasized that the application of membrane reactors in processes of the petrochemical industry, requires hydrothermally stable membranes by the presence of water vapor at high temperature (200 - 300 °C) and under high pressure (1 - 4 MPa).

By simulation, Diban et al. (2013) have proposed a mathematical model to simulate a packed bed membrane reactor system, in order to determine the transport characteristics of the most suitable membrane for the direct synthesis of DME, co-feeding CO_2 together with CO and H_2. In this model an unidirectional current of the feed and the sweep gas in counter-current mode are considered. Other assumptions in the model are: 1) isothermal regime; 2) negligible catalyst deactivation; 3) plug flow in the reactor without any axial or radial dispersion; 4) reaction control of the different steps in the reaction scheme, being negligible the mass transport limitations in the catalyst particles; 5) the components are considered ideal gases, and; 6) use of the kinetic of the reaction steps previously established in the literature for a CuO-ZnO-Al_2O_3 / γ-Al_2O_3 catalyst (Aguayo et al., 2007). Water permeability and H_2O / H_2 selectivity data of zeolitic membranes (ZSM-5, MOR, SIL) used in the literature for FT synthesis are values within the range 0.5 - 4.0·10^{-7} mol Pa^{-1} m^{-2} s^{-1} and 0.5 - 20, respectively. The implementation of these parameters by Diban et al. (2013) has allowed to establish that due to a high loss of methanol through these membranes, DME yield decreases with regards to the conventional reactor (7.0 % instead of 14.8 %). Nonetheless, the simulation results with ideal membranes and water permeability lower than 1.2·10^{-7} mol Pa^{-1} m^{-2} s^{-1} have

revealed the advantages of the membrane reactor, achieving a maximal yield of 16.7 % at conditions where an equilibrium between water production and its permeation is reached.

In another further study, Diban et al. (2014) have developed the same simulation model to study the operation conditions effect, like the sweep flow and its recirculation, given the difficulty of having available an ideal membrane at that time with the hydrothermal stability and permeability properties required in this reaction. Controlling adequately the recirculation of the sweep flow, CO_2 conversion increases in about 85 %, with a sweep flow higher than 0.60 mol CO_x h^{-1}. Moreover, this flow recirculation reduces methanol permeation through the membrane, enhancing DME yield in about 30 % over a conventional reactor, for a high recirculation velocity. The authors have pointed out on the necessity of considering the required energetic costs for the refrigeration, heating and compression of the sweep flow, as well as on the importance of improving the catalyst to decrease the hydrocarbons yield (up to 4 % at some studied conditions).

Farsi et al. (2016) have compared, by a simulation program of a non-isothermal unidimensional reactor, the performance for the direct synthesis of DME of a double membrane reactor (hydrogen-water), previously proposed for methanol synthesis (Farsi and Jahanmiri, 2014), with respect to reactors with hydrophilic membranes, hydrogen selective membranes and without membrane. The corresponding DME productions are 8910.44, 8592.9, 8221.1 and 7604 kmol day^{-1}, revealing the interest of these innovations in the reactor design, implementing membranes with adequate properties (considered in the simulation). As background to this study, Farsi and Jahanmiri (2011) had simulated a fluidized bed reactor, with a water selective membrane, for DME synthesis. Furthermore, the reactor (fluidized bed in this case) with a H_2 selective membrane had been previously also simulated by

Mardanpour et al. (2012) for DME synthesis with synthesis gas as feed, demonstrating the enhance in CO conversion and DME yield.

The negative effect on methanol and DME yield co-feeding CO_2 with CO and H_2 has been evaluated by De Falco et al. (2016). It has been proven by simulation the advantages of two alternative reaction systems, like a zeolite membrane reactor and two series units, consisted of a packed bed reactor and a water separation module. In addition, it was determined by an unidimensional simulation model that to be able to efficiently operate a membrane reactor, a stable and selective membrane with a water permeability of 10^{-7} mol Pa^{-1} m^{-2} s^{-1} and a H_2O / H_2 selectivity of 10 is required.

Subsequently, these authors (De Falco et al., 2017a) have studied the effect of the operation conditions (CO_2 / CO_x and H_2 / CO_x ratios in the feed, temperature, pressure, space time) on CO_2 conversion and DME yield, at industrial scale conditions with a non-isothermal model in the simulation of the membrane reactor. Among the simulation results, it should be highlighted the achievement of a DME yield of 75 % (57 % in the conventional reactor), a DME selectivity close to 100 % and CO_x and CO_2 conversions of 75 % and 69 %, respectively, enhancing in 15.4 % and 30.2 % the results in the conventional reactor.

Additionally, the membrane reactor results have been improved by these authors (De Falco et al., 2017b), with an operation strategy called Double Recycling Loop DME (DRL-DME). This design consists of the utilization of a pure CO_2 stream as sweep gas in the permeation section and a recirculation flow to the reactor, which is composed by the flow mixture of the unreacted reactants and the outlet gases from the permeation section.

4.2 Membrane properties

4.2.1 Comparison of membranes

The discrimination study of the different synthesized membranes, described in Section 2.4, has consisted of the comparison of their properties to select the most suitable for the direct synthesis of DME. Consequently, the membranes have been characterized by their structural, physical and morphological properties, pervaporation, vapor permeation and single gas permeation performance and, finally, their thermal stability.

First of all, a leakage test has been carried out by soaking the membranes in ethanol and passing a N_2 flow through them under 2 bar. This procedure allows to detect immediately leaks on the membranes if bubbles are observed in the liquid. It should be noted that after having tested all the membranes for leakage, MOR membrane was the only one that leaked, being discarded from this discrimination analysis and the further characterization. On the other hand, LTA, LTX and SOD membranes successfully passed the leakage test, meaning that the crystallization of the zeolites on the support has been correctly performed.

The pervaporation (PV) of the different membranes membranes have been evaluated as described in Section 2.5.2.1. The separation factors (Eqs. 2.10 and 2.11) and fluxes (Eq. 2.12) of the PV experiments have been calculated for EtOH / H_2O and MeOH / H_2O mixtures at 75 °C and 60 °C, respectively. In Table 4.1 the PV performances of the synthesized membranes are summarized.

The best PV performance achieved has been through LTA membrane with a separation factor (α) for EtOH / H_2O and MeOH / H_2O mixtures higher than 9000

and 1400, respectively. LTA membrane has shown a great H_2O permselectivity towards EtOH and MeOH. Its hydrophilicity is key in our process, in order to be able to remove only H_2O from the reaction medium. Conversely, LTX and SOD membranes have shown a low selectivity toward both mixtures, being α below 10.

According to these PV results described in Table 4.1, LTX and SOD membranes have been discarded for further characterization techniques. Moreover, the great reproducibility of the LTA membrane preparation method is to be highlighted, using a relatively simple method described in Section 2.4.1.

Table 4.1: Pervaporation of H_2O from EtOH / H_2O and MeOH / H_2O mixtures through the different membranes at 75 °C and 60 °C, respectively.

Membrane	Composition	Feed (wt%)	Permeate (wt%)	Q ($kg\,m^{-2}\,h^{-1}$)	α
LTA	EtOH H_2O	90.0 10.0	0.15 99.8	1.59	9329
LTA	MeOH H_2O	90.0 10.0	0.45 99.5	0.92	1486
LTX	EtOH H_2O	90.0 10.0	55.4 44.6	2.40	7.9
LTX	MeOH H_2O	90.0 10.0	69.4 30.6	2.00	2.9
SOD	EtOH H_2O	90.0 10.0	89.7 10.3	0.80	1.1

4.2.2 LTA membrane

4.2.2.1 Vapor permeation

Vapor permeation (VP) performance of LTA membrane, determined following the instructions presented in Section 2.5.2.2, for an EtOH / H_2O mixture at 125 °C is summarized in Table 4.2.

LTA membrane keeps its high selectivity with α = 7778, despite the increase in the temperature. Nevertheless, the flux through it decreases (Q = 1.01 kg $m^{-2}h^{-1}$) in comparison with its value at 75 °C (1.59 kg $m^{-2}h^{-1}$).

Table 4.2: Vapor permeation from EtOH / H_2O mixtures through LTA membrane at 125 °C.

Composition	Feed (wt%)	Permeate (wt%)	Q (kg $m^{-2}h^{-1}$)	α
EtOH	90.0	0.17	1.01	7778
H_2O	10.0	99.8		

4.2.2.2 Single gas permeation

For our process is fundamental that the reactants involved in the DME synthesis (H_2, CO and CO_2) do not permeate through the membrane. Therefore, a low gas permeance through the membrane is required.

The permeances and ideal selectivities for different gas mixtures (Table 4.3) through LTA membrane at 35 °C and under 0.01 MPa have been calculated, as described in Section 2.5.2.3.

Table 4.3: Single gas permeances through LTA membrane at 35 °C (in 10^{-9} mol m^{-2} s^{-1} Pa^{-1}).

He	H_2	CO_2	N_2	CH_4	SF_6
1.31	1.20	0.41	0.62	0.45	0.22

Furthermore, in Table 4.4 the ideal selectivities for different gas mixtures at 35 °C through LTA membrane are summarized.

Table 4.4: Ideal selectivities for different gas mixtures through LTA membrane at 35 °C.

H_2/N_2	H_2/CH_4	CO_2/N_2	CO_2/CH_4	He/SF_6	H_2/SF_6
2.1	2.7	0.7	0.9	6.0	5.5

Attending to these results, LTA membrane possesses a low GP performance at 35 °C, as shown in Table 4.3. Increasing the kinetic diameter of the gases used in the experiment, their permeances decrease considerably, as it can be concluded from the results listed in Table 4.4

4.2.2.3 Thermal stability

The thermal stability of LTA membrane has been analyzed through its calcination at 300 °C for 5 h and, subsequently, evaluating its PV, VP and GP performances.

Pervaporation

The PV properties of LTA membrane after its calcination are shown in Table 4.5.

Table 4.5: Pervaporation from EtOH / H_2O and MeOH / H_2O mixtures through calcined LTA membrane at 75 °C and 60 °C, respectively.

Composition	Feed (wt%)	Permeate (wt%)	Q ($kg\,m^{-2}h^{-1}$)	α
EtOH	90.0	0.47	1.70	2905
H_2O	10.0	99.5		
MeOH	90.0	0.75	1.05	1011
H_2O	10.0	99.2		

The separation factors (α) of LTA membrane, both for EtOH / H_2O and MeOH / H_2O mixtures, decrease after the calcination (2905 and 1011 respectively). Neverthe-

less, it maintains its hydrophilicity towards both mixtures. Concerning the fluxes (Q) through the membrane of the two feed compositions, these values slightly raise from 1.59 to 1.70 kg/m^{2}h for EtOH / H_2O ($\sim$ 6 %) and from 0.92 to 1.01 kg $m^{-2}h^{-1}$ for MeOH / H_2O ($\sim$ 14 %).

Vapor permeation

VP performance of LTA membrane after its calcination is summarized in Table 4.6.

Table 4.6: Vapor permeation from EtOH / H_2O mixture through calcined LTA membrane at 125 °C.

Composition	Feed (wt%)	Permeate (wt%)	Q (kg $m^{-2}h^{-1}$)	α
EtOH	90.0	0.19	1.32	3232
H_2O	10.0	99.8		

LTA membrane water permselectivity remains after its calcination (α higher than 3000) and the vapor flux through it raises up to 1.32 kg $m^{-2}h^{-1}$.

Single gas permeation

The permeances for different gases at different temperatures (100, 150 and 200 °C) through the calcined LTA membrane are shown in Table 4.7.

Table 4.7: Gas permeances through the calcined LTA membrane at 100, 150 and 200 °C (in 10^{-9} mol m^{-2} s^{-1} Pa^{-1}).

Temperature (°C)	He	H_2	CO_2	N_2	CH_4	SF_6
100	2.39	2.90	0.56	0.78	0.93	0.31
150	3.47	4.60	0.94	1.24	1.61	0.55
200	9.24	13.2	3.18	3.61	4.34	1.66

Moreover, in Table 4.8 the ideal selectivities of different gas mixtures at 100, 150 and 200 °C through the calcined LTA membrane are gathered. Increasing the temperature up to 200 °C, a slight increment in the gas permeances through the calcined LTA membrane can be observed. In spite of this permeance increase, this analysis demonstrates that even at high temperatures LTA membrane has a low gas permeability and, therefore, is able to operate at temperatures near to those required in DME synthesis.

Table 4.8: Ideal selectivities for different gas mixtures through calcined LTA membrane at 100, 150 and 200 °C.

Temperature (°C)	H_2/N_2	H_2/CH_4	CO_2/N_2	CO_2/CH_4	He/SF_6	H_2/SF_6
100	3.7	3.1	0.3	0.2	10	11
150	3.7	2.8	0.8	0.6	6	8
200	3.7	3.0	0.9	0.7	6	8

4.2.2.4 Structural properties

XRD pattern of LTA membrane has been obtained (Figure 4.1) in order to confirm, on one hand, if the zeolite has been appropriately synthesized and, on the other hand, its crystallization on the stainless steel support (fundamental step within the membrane reactor configuration).

Neat and well-defined peaks can observed on the synthesized LTA zeolite, indicating an absence of amorphous phase in the material. According to the database, the most intense peaks on the diffractogram, which can be clearly identified in Figure 4.1, suggests that a crystalline phase with high purity supported on stainless-steel can be achieved through this preparation method. On the other hand, XRD pattern

of steel consists of three peaks at higher values of 2Θ angles (56.5, 67.1 and 79.5 degrees). The XRD diffractogram of the prepared membrane (Figure 4.1) also shows these peaks attributed to the metallic support of the membranes.

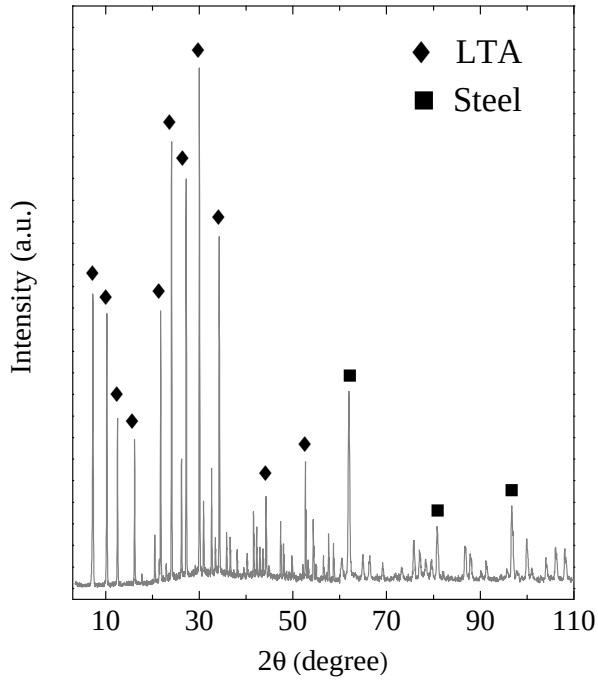

Figure 4.1: XRD pattern of synthesized LTA zeolite crystallized on stainless-steel support.

4.2.2.5 Physical and morphological properties

The porous texture of LTA zeolite powder has been characterized by CO_2 adsorption at 0 °C (Figure 4.2). To carry out the analysis, LTA has been prepared following the same procedure described in Section 2.4.1, without introducing the metallic support in the autoclave.

Well-defined CO_2 adsorption isotherm has been obtained with a practically satu-

rated shape in the range of low relative pressure. Pore width and micropore surface of LTA zeolite, calculated using the Dubinin-Radushkevich equation and by Horvath-Kawazoe method, is summarized in Table 4.9. These results suggest that the crystalline zeolite presents narrow micropores (3.98 Å).

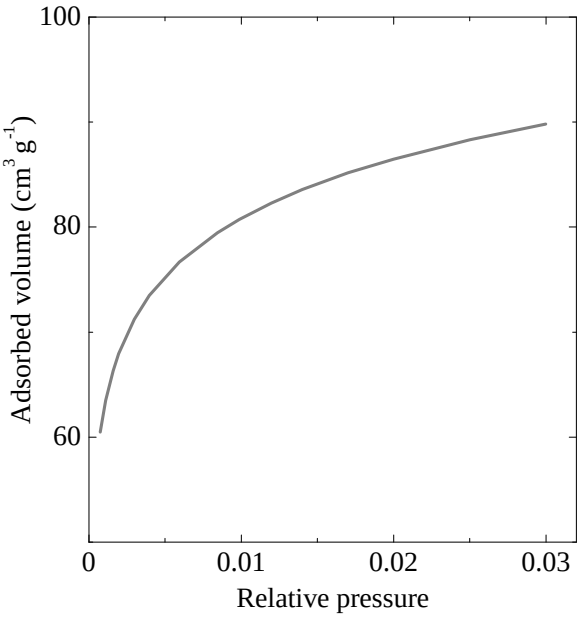

Figure 4.2: CO_2 adsorption isotherm of synthesized LTA zeolite powder at 0 °C.

Table 4.9: Pore diameter and micropore surface of synthesized LTA zeolite powder.

Zeolite	Pore width (Å)	Micropore surface ($m^2\ g^{-1}$)
LTA	3.98	458

The morphology of the zeolite membranes has been analyzed by SEM technology using the equipment described in Section 2.3.1.2. Figure 4.3 shows the porous stainless steel support sample where LTA zeolite has been crystallized on for evaluation.

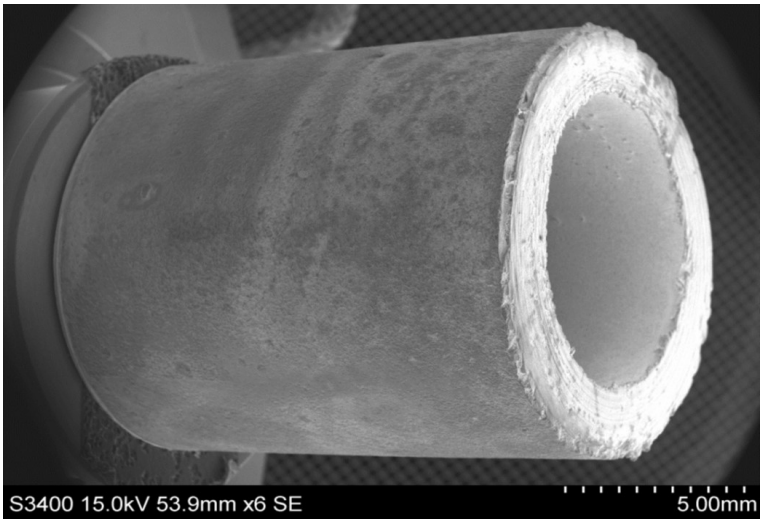

Figure 4.3: SEM image of the porous stainless steel support.

SEM micrograph of the synthesized LTA zeolite crystallized on the stainless steel support is depicted in Figure 4.4.

At the front view of the membrane cross-section (Figure 4.4a) both phases (zeolite and support) can be clearly differentiated. A constant thickness of the zeolite layer has been obtained deposited on the surface of the non-polished stainless steel support. The homogeneous texture of the LTA membrane (Figure 4.4b) suggests a high effectiveness of the preparation method for the purpose of achieving a complete covering of the support with zeolite crystals. It can be observed in Figure 4.4c that the morphology of LTA zeolite consists of cubic aggregates.

SEM characterization has demonstrated the correct synthesis method of LTA membranes, highlighting the formation of uniform thickness zeolite layer and the homogeneous distribution of it on the support surface.

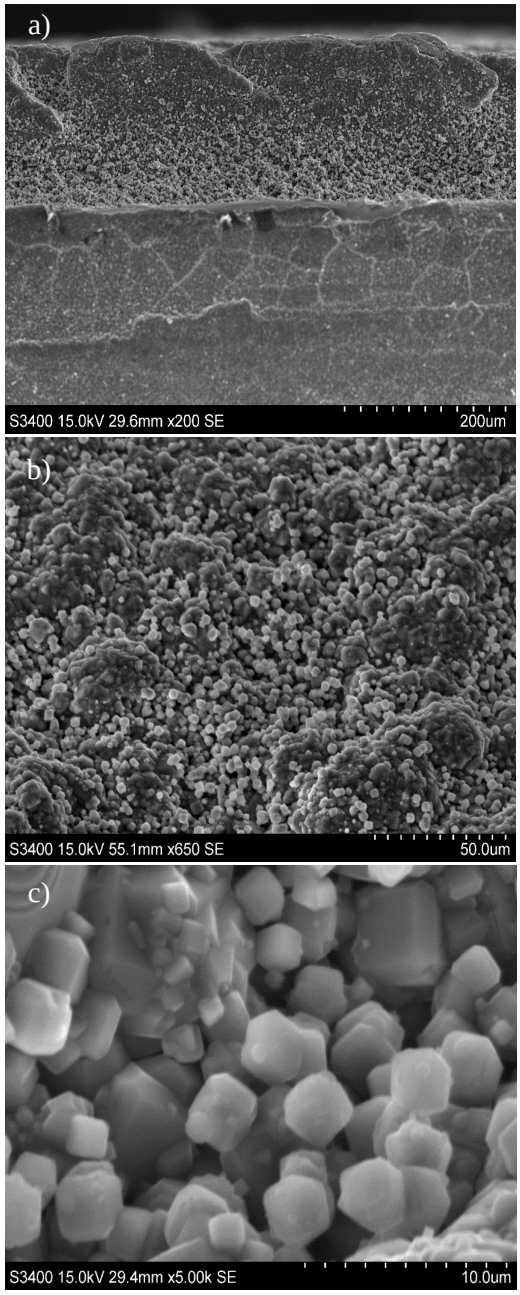

Figure 4.4: SEM images of the cross-section (a), top view (b) and detailed surface view (c) of LTA zeolite membrane.

4.3 Parametric study of DME synthesis in PBMR

In this section the experimental results obtained with the original PBMR are illustrated. First of all, in Section 4.3.1 is shown an example of the evolution with time on stream of the components molar fractions both in the reaction and permeate sections. Subsequently, the results of the effect of the reaction conditions (temperature in Section 4.3.2 and pressure in Section 4.3.3) on the reaction indexes (described in Section 2.1.5) and on the evolution with time on stream of these indexes, feeding $H_2 + CO / CO_2$ and $H_2 + CO_2$.

It should be emphasized that being this the first study with this experimental reactor, the same sweep strategy has been maintained for the whole set of experiments. Hence, the sweep gas in the permeate section has been fed with the same partial pressure as that of the feed to the reaction section.

4.3.1 Example of the experimental results

The incorporation of the LTA membrane in the synthesis of DME has contributed to the elimination of H_2O from the reaction medium, which promotes the incorporation of CO_2 in the feed (Ateka, 2014; De Falco et al., 2017a,b; Diban et al., 2013, 2014; Iliuta et al., 2010). Thus, through the hydrogenation of CO_2 Figures 4.5 and 4.6 show the evolution with TOS of the molar fractions of the reaction products (DME, MeOH, H_2O) at the reactor outlet, both in the reaction section (RS) and the permeate section (PS), at 275 °C, under 10 and 40 bar, respectively. These results are shown as an example of the information that has been provided by the chromatographic analysis, monitoring the composition of the flows in both reactor sections.

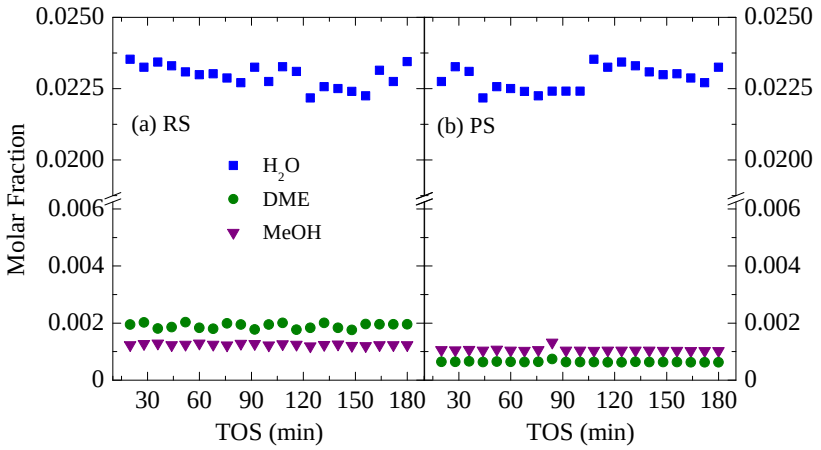

Figure 4.5: Comparison of the evolution of DME, MeOH and HC molar fractions with time on stream (TOS) in the reaction section (a) and the permeate section (b). Reaction conditions: 275 °C; 10 bar; 10 $g_{cat}h(mol_C)^{-1}$; H_2 / CO_x, 3; CO_2 / CO_x, 1.

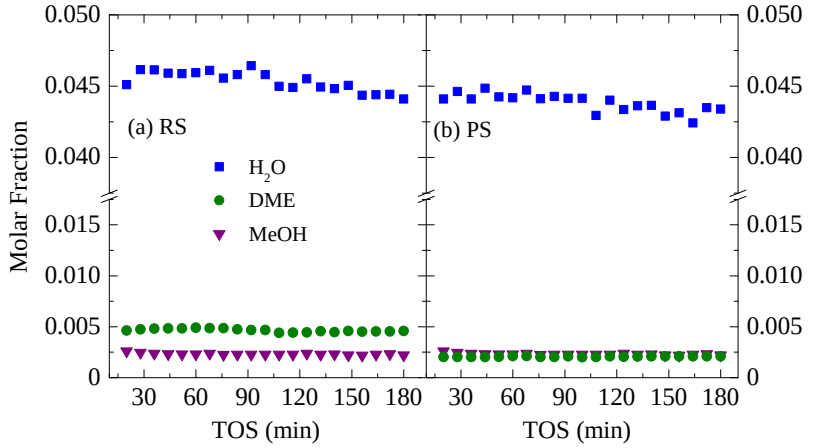

Figure 4.6: Comparison of the evolution of DME, MeOH and HC molar fractions with time on stream (TOS) in the reaction section (a) and the permeate section (b). Reaction conditions: 275 °C; 40 bar; 10 $g_{cat}h(mol_C)^{-1}$; H_2 / CO_x, 3; CO_2 / CO_x, 1.

The similar concentration of H_2O in the reaction and permeate sections is due to the hydrophilic nature of LTA membrane, which is water perm-selective toward other molecules, such as ethanol or methanol (Table 4.1). This LTA membrane se-

lectivity can also be confirmed by the difference of DME concentrations between PS and RS, being higher in this latter zone. However, the permeability of all compounds becomes higher at high reaction temperatures (Table 4.7). For this reason, DME and methanol molecules (kinetic diameter of ca. 4.3 Å and 3.8 Å, respectively) partially permeate through the membrane, as can be observed in Figures 4.5b and 4.6b.

4.3.2 Temperature

The usual temperature range in which DME synthesis is studied in literature is 250 - 300 °C, since the upper temperature is limited by the thermodynamic equilibrium (Ateka et al., 2017b) and also to preserve the hydrothermal stability of Cu in the catalyst. Nevertheless, the utilization of the membrane reactor (PBMR) diminishes the thermodynamic limitation due to the less H_2O concentration in the reaction medium, allowing the displacement of the thermodynamic equilibrium of H_2O formation reactions (methanol synthesis, reverse WGS and methanol dehydration). Consequently, it allows to operate at higher temperatures achieving a greater conversion. Attending to this advantage (analyzed in Section 4.4.1), in the following sections the studied temperature range has been widened to 275 - 325 °C. Furthermore, the knowledge acquired in previous works (Sánchez-Contador et al., 2018a,c) has been applied to be able to work at 325 °C with an acceptable hydrothermal stability of the catalyst. The fact that H_2O concentration in the reaction medium is lower than in the conventional reactor (PBR) is, *a priori*, another advantage of the PBMR, in which a lower Cu sintering is expected (dependent on temperature and reaction medium composition).

4.3.2.1 $H_2 + CO / CO_2$ feed

Figure 4.7 shows the effect of temperature on both CO_2 and CO_x conversion and DME, MeOH and paraffins yields at zero time on stream feeding $H_2 + CO / CO_2$.

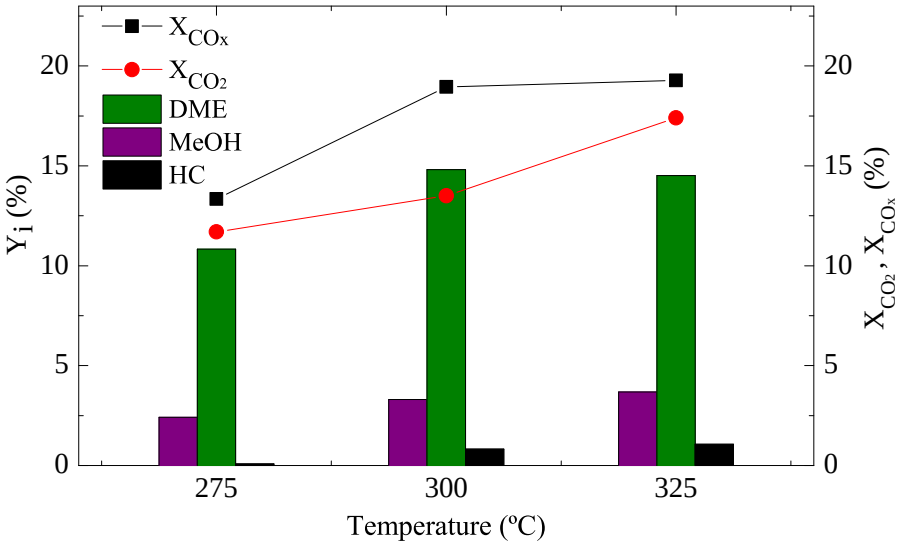

Figure 4.7: Temperature effect on DME, MeOH and hydrocarbons yield, and CO_2 and CO_x conversion. Reaction conditions: 30 bar; 10 $g_{cat}h(mol_C)^{-1}$; H_2 / CO_x, 3; CO_2 / CO_x, 0.5.

It shows that temperature has a great importance on CO_x conversion, improving from 13.34 % at 275 °C to 19.27 % operating at 325 °C. DME yield enhances from 275 °C until 300 °C, achieving a maximum of $\sim$ 14.81 % at this temperature. Increasing this temperature, a slight decay can be observed due to, predictably, the thermodynamic limitation. On the other hand, MeOH and paraffins yields continue to rise with a maximum of 3.68 % and 1.07 %, respectively, at 325 °C.

As a consequence of the evolution of the individual yields with temperature, DME selectivity drops increasing the temperature from 275 to 300 °C, remaining quasi

constant at higher temperature, while paraffins selectivity should be pointed out since it rises up to 5.55 % at 325 °C (Figure 4.8). At this temperature, paraffins formation mechanisms are promoted, either from DME and methanol through the hydrocarbon pool mechanism (activated by the acid function) or through methanation mechanisms or Fischer-Tropsch from CO and CO_2 on the metallic function.

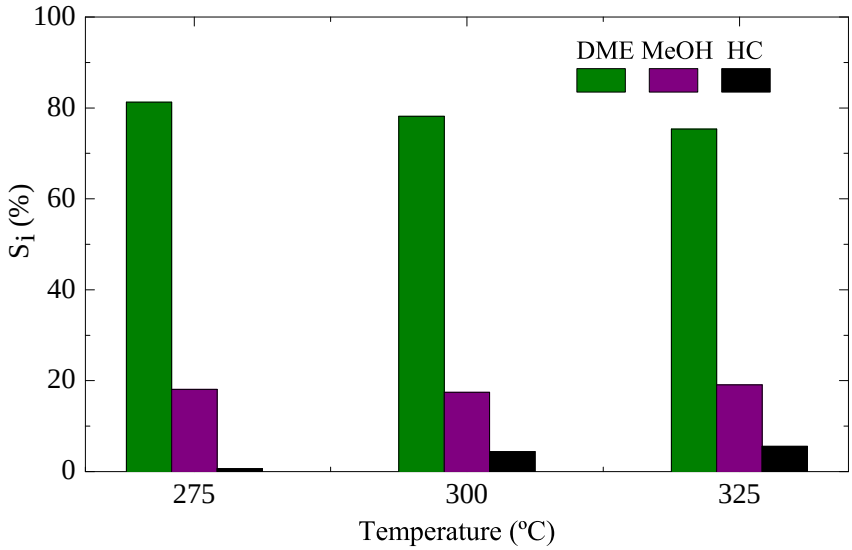

Figure 4.8: Temperature effect on DME, MeOH and hydrocarbons selectivity. Reaction conditions: 30 bar; 10 $g_{cat}h(mol_C)^{-1}$; H_2 / CO_x, 3; CO_2 / CO_x, 0.5.

The formation of hydrocarbons constitutes a great disadvantage in the process due to their stability and, therefore, facing the impossibility of their recirculation in the feed. The deactivation by coke, moreover, is related with the reactivity of these hydrocarbons or their intermediates to form aromatics, which condensate to coke.

The effect of temperature on the evolution with time on stream (TOS) of DME yield is depicted in Figure 4.9. It demonstrates how temperature affects the catalyst stability, which is lower the higher is the temperature within the range of 275 - 300 °C. The observed catalyst stability at 325 °C, although DME yield is lower,

is similar to that at 300 °C, which indicates that the catalyst sintering is not significant. The less DME yield, at zero time on stream, at 300 °C than at 325 °C has as its favorable counterpart a less deactivation. It also should be pointed out that the deactivation at 275 °C is significantly slow.

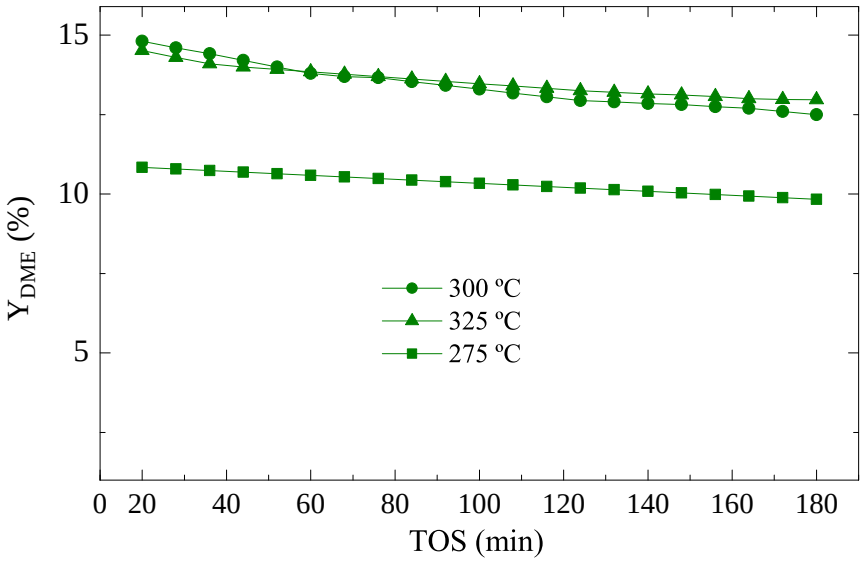

Figure 4.9: Temperature effect on TOS evolution of DME yield. Reaction conditions: 30 bar; 10 $g_{cat}h(mol_C)^{-1}$; H_2 / CO_x, 3; CO_2 / CO_x, 0.5.

4.3.2.2 $H_2 + CO_2$ feed

The experiments with $H_2 + CO_2$ as feed gas have been conducted under the same reaction conditions indicated in previous Section 4.3.2. DME, MeOH and paraffins yields together with CO_x and CO_2 conversions at zero time on stream are shown in Figure 4.10.

In contrast to $H_2 + CO$ / CO_2 feed (Figure 4.7), the maximum CO_x conversion corresponds to lowest studied temperature (275 °C) (X_{CO_x} = 15.93 %), and decreases at higher temperatures. With regard to CO_2 conversion, on the contrary, it is en-

hanced increasing the temperature, achieving a value of 34.03 % at 325 °C.

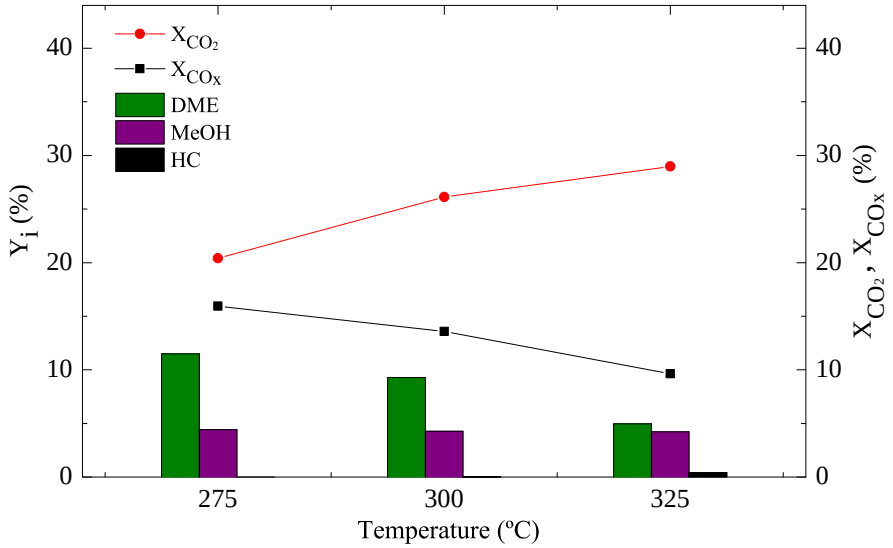

Figure 4.10: Temperature effect on DME, MeOH and hydrocarbons yield and CO_2, CO_x conversion. Reaction conditions: 40 bar; 10 $g_{cat}h(mol_C)^{-1}$; H_2/CO_x, 3; CO_2/CO_x, 1.

This improvement in CO_2 conversion with temperature is due to the key role the rWGS reaction (Eq. 1.8) plays, where CO_2 is converted to CO, more reactive in methanol synthesis. This effect, remarkably, is very important on the process thermodynamics. Moreover, the greatest DME yield is obtained at 275 °C (Y_{DME} = 10.45 %), while the formation of methanol remains quasi-constant within the studied temperature range ($Y_{MeOH} \approx 4.3$ %) (Figure 4.10). In contrast, paraffins yield rises with temperature, occurring the same effect as feeding $H_2 + CO/CO_2$ (described in Section 4.3.2.1), reaching a peak of 0.43 % at 325 °C.

The effect of the reaction temperature on the products selectivity is presented in Figure 4.11. Within the studied temperature range DME selectivity decreases from its maximum (70.21 % at 275 °C) to 51.61 % at 325 °C whereas that of MeOH rises by about 46 %. It should be emphasized that methanol is the main byproduct.

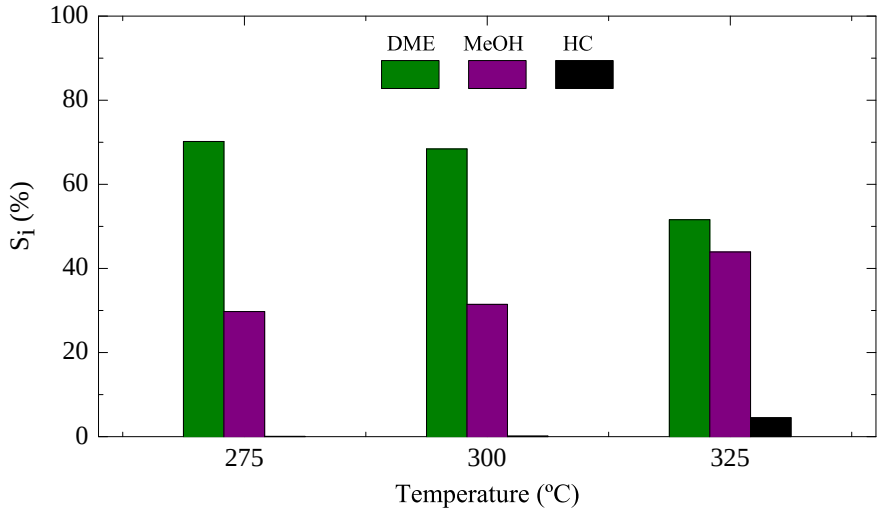

Figure 4.11: Effect of temperature on DME, MeOH and hydrocarbons selectivity. Reaction conditions: 40 bar; 10 $g_{cat}h(mol_C)^{-1}$; H_2 / CO_x, 3; CO_2 / CO_x, 1.

This formed methanol is a minor issue for the industrial process scale-up, since it is a product of commercial interest, it can be dehydrated towards DME under atmospheric pressure with a well known technology in an independent reactor (Sierra et al., 2013). Significantly, paraffins selectivity increases from barely detectable at 275 °C to its maximum (S_{HC} = 4.46 %) at 325 °C, which indicates, as aforementioned described, that at this temperature paraffins formation mechanisms are activated.

The tendency of the evolution with TOS of DME yield (Figure 4.12) at different temperatures (275 - 325 °C) indicates that feeding CO_2 the deactivation of the catalyst seems to be imperceptible within this temperature range for $H_2 + CO_2$ feed.

In addition to the advantages in the results regarding PBR, which will be explained in Section 4.4, the aforementioned results in PBMR reveal the capacity of this reactor for CO_2 conversion and also the significant effect of CO_2 content in the feed on the CO_x conversion and products yield. Firstly, comparing Figures 4.7 and 4.10

it is remarkable the lower CO_x conversion, DME yield and selectivity obtained feeding $H_2 + CO_2$, what evidences the effect of the increase of CO_2 content at the reactor inlet.

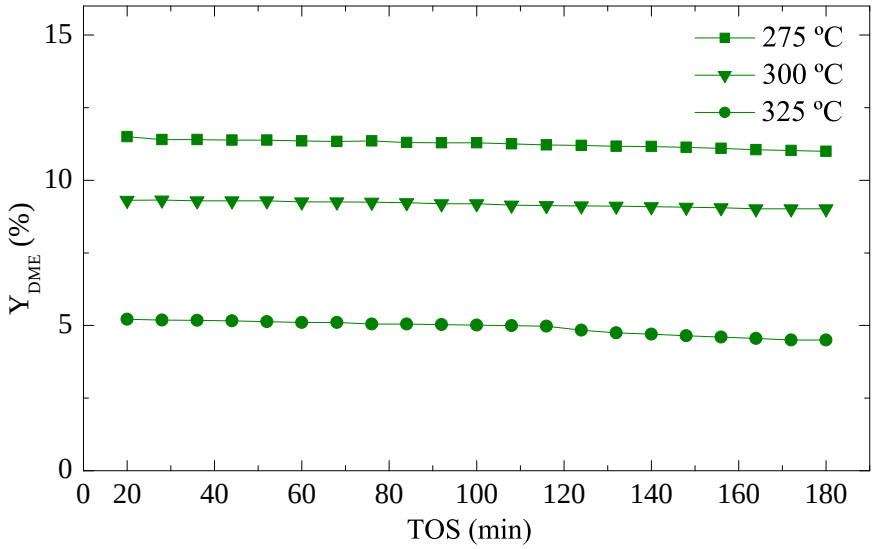

Figure 4.12: Temperature effect on TOS evolution of DME yield. Reaction conditions: 40 bar; 10 $g_{cat}h(mol_C)^{-1}$; H_2/CO_x, 3; CO_2/CO_x, 1.

Moreover, for $H_2 + CO/CO_2$ feed (Figure 4.7) CO_2 and CO_x and conversions are higher increasing the temperature, while DME yield achieves its maximum at 300 °C. Feeding $H_2 + CO_2$ (Figure 4.10), nevertheless, these indexes diminish increasing the temperature, being relevant the enhance in CO_2 conversion, whose meaning is the valorization of this compound. In this sense, a CO_2 conversion of 45 % in a one-step reaction, achieved feeding $H_2 + CO_2$ at 325 °C is an excellent result. On the other hand, although DME selectivity is lower for this feed, it must be pointed out that paraffins selectivity is inferior and that the higher methanol selectivity does not represent a major economic problem.

As it has also been indicated, the catalyst deactivation is lower incrementing CO_2

content in the feed, which is attributable to the fact that higher H_2O concentration in the reaction medium, generated by WGS reaction, favors the attenuation of coke formation. This comparison, accordingly, indicates that PBMR is particularly attractive for feeds with high CO_2 concentration.

4.3.3 Pressure

Similarly to the study of the temperature effect, the results for $H_2 + CO / CO_2$ and $H_2 + CO_2$ feeds under different pressures are shown.

4.3.3.1 $H_2 + CO / CO_2$ feed

The experiments have been conducted at 300 °C (temperature established as suitable in Section 4.3.2.1, at which DME yield is maximal). In Figure 4.13 the effect of pressure on the products yield is depicted.

The operating pressure has been found to have a notable effect on CO_x conversion at zero time on stream, rising paraffins, MeOH and DME yields practically linearly, which is due to the favorable effect of pressure on reactions with a reduction in the number of moles. Hence, increasing the pressure from 20 to 30 bar enhances CO_x conversion from 8.77 to 17.91 % and DME yield from 7.01 to 13.7 %. In spite of the positive effect of pressure on these reaction indexes, further experiments with higher pressures have not been carried out due to their asymptotic increase tendency over 40 bar (Azizi et al., 2014; Behrens et al., 2012; Ereña et al., 2005; Jia et al., 2006; Khoshbin and Haghighi, 2013) and that operational issues may be presented increasing the pressure.

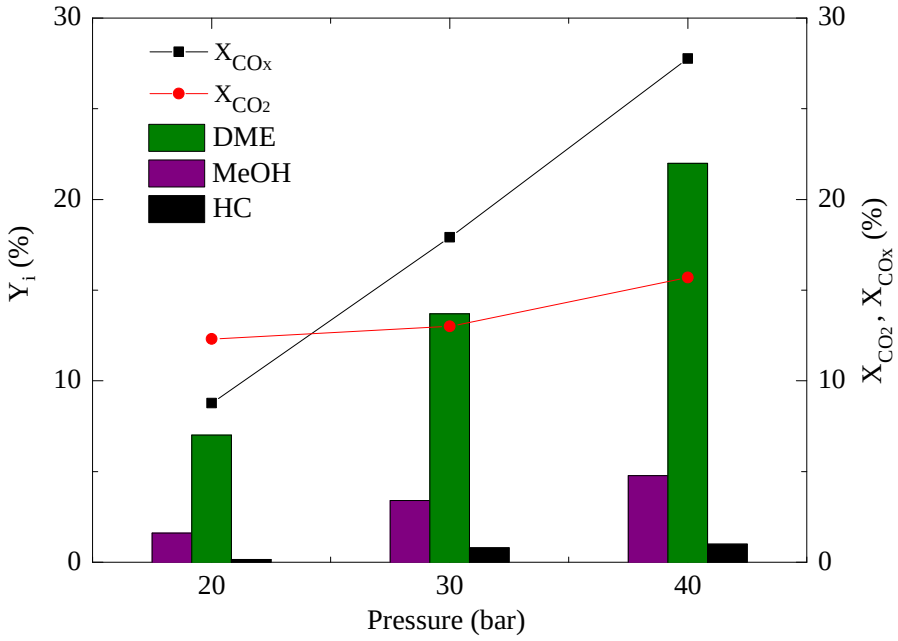

Figure 4.13: Effect of pressure on products yield and CO_2, CO_x conversion. Reaction conditions: 300 °C; 10 $g_{cat}h(mol_C)^{-1}$; H_2 / CO_x, 3; CO_2 / CO_x, 0.5.

As a result of the enhancement in all products yields, DME and MeOH selectivities remain constant within the studied pressure range ($S_{DME} \approx 78$ % and $S_{MeOH} \approx 19$ %) (Figure 4.14). Concerning paraffins selectivity, it rises (from 1.82 to 4.47 %) with pressure.

Figure 4.15 displays the role that plays operating pressure in the catalyst stability. It can be observed that under not severe conditions (20 bar), the evolution of DME yield with TOS is practically horizontal in 3 h. Increasing the operating pressure the catalyst deactivation becomes more significant, being the most rapid one at 40 bar and specially during the first hour of reaction.

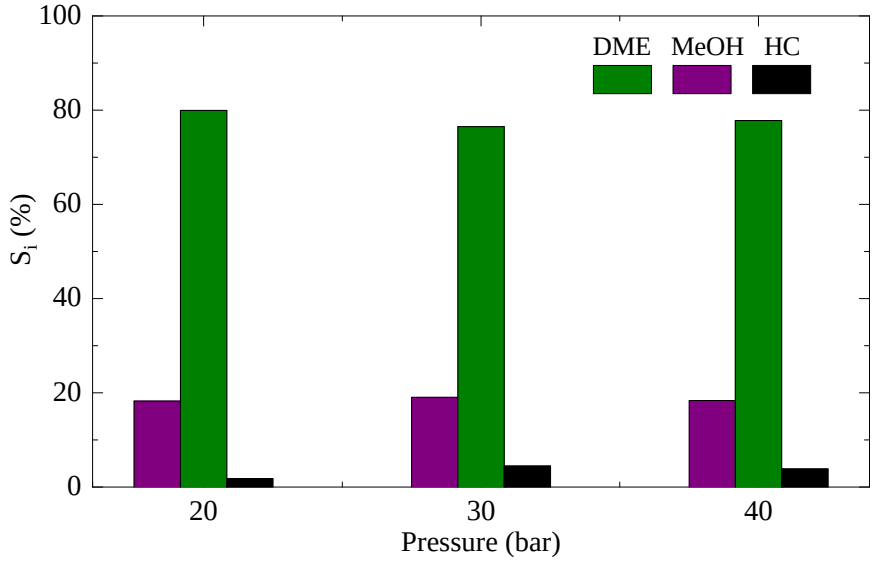

Figure 4.14: Effect of pressure on DME, MeOH and hydrocarbons selectivity. Reaction conditions: 300 °C; 10 $g_{cat}h(mol_C)^{-1}$; H_2/CO_x, 3; CO_2/CO_x, 0.5.

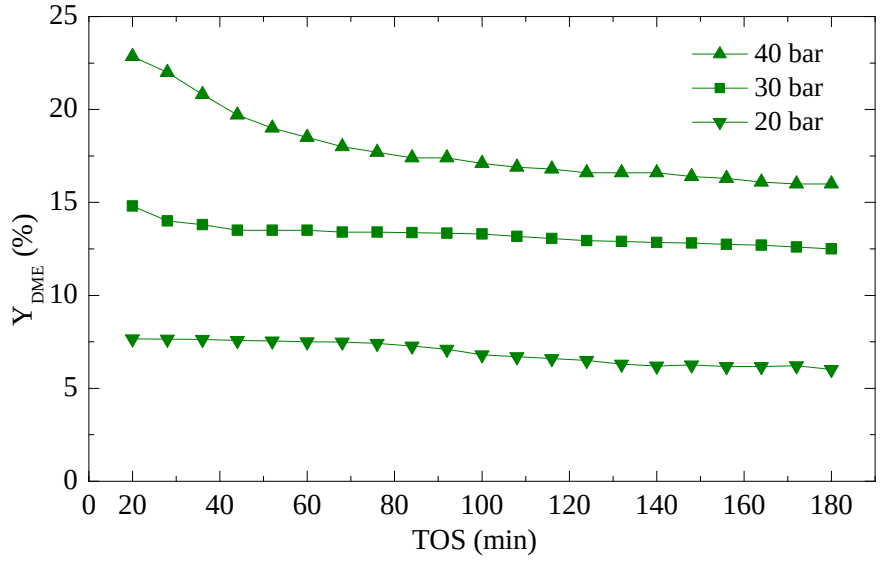

Figure 4.15: Effect of pressure on TOS evolution of DME yield. Reaction conditions: 300 °C; 10 $g_{cat}h(mol_C)^{-1}$; H_2/CO_x, 3; CO_2/CO_x, 0.5.

4.3.3.2 $H_2 + CO_2$ feed

The effect of pressure on the reaction indexes at zero time on stream, feeding $H_2 + CO_2$ at 275 °C (Figure 4.16), is qualitatively similar to the described in Section 4.3.3.1 for $H_2 + CO / CO_2$ feed at 300 °C. The temperature of 275 °C has been determined in Section 4.3.2.2 to be the most appropriate to achieve DME maximum yield.

The increase of the operating pressure favors the linear rise of both CO_x conversion (from 3.03 to 14.89 %) and CO_2 conversion (from 9.38 to 25.04 %) within 10 - 40 bar range. Concerning DME and MeOH yields, the enhancement with pressure can be clearly observed whereas paraffins formation remains quasi-negligible achieving a a maximum of 0.01 % under 40 bar.

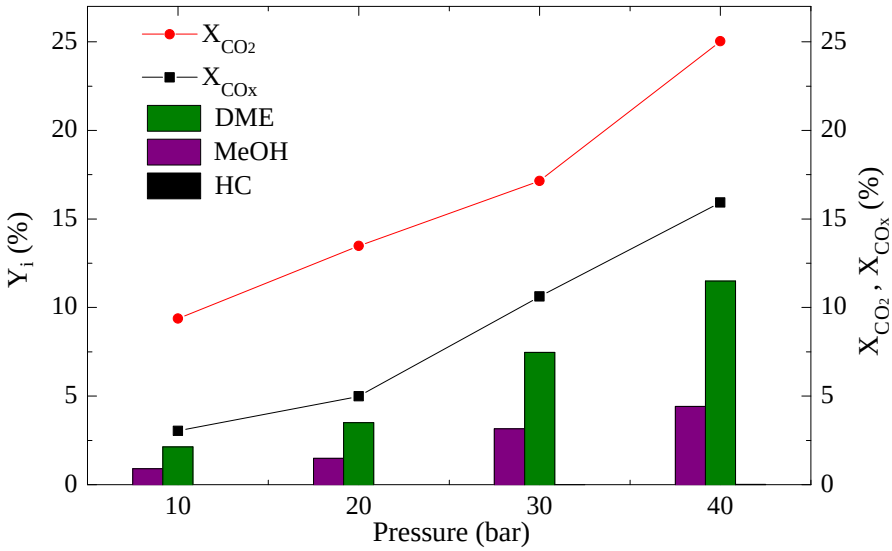

Figure 4.16: Effect of pressure on products yield, CO_2 and CO_x conversion. Reaction conditions: 275 °C; 10 $g_{cat}h(mol_C)^{-1}$; H_2 / CO_x, 3; CO_2 / CO_x, 1.

Due to the constant rise of the products yield in the studied pressure range, MeOH and DME selectivity (Figure 4.17) are barely affected by the increase of the oper-

ating pressure (from 24.34 to 20.02 % and from 76.05 to 79.96 %, respectively).

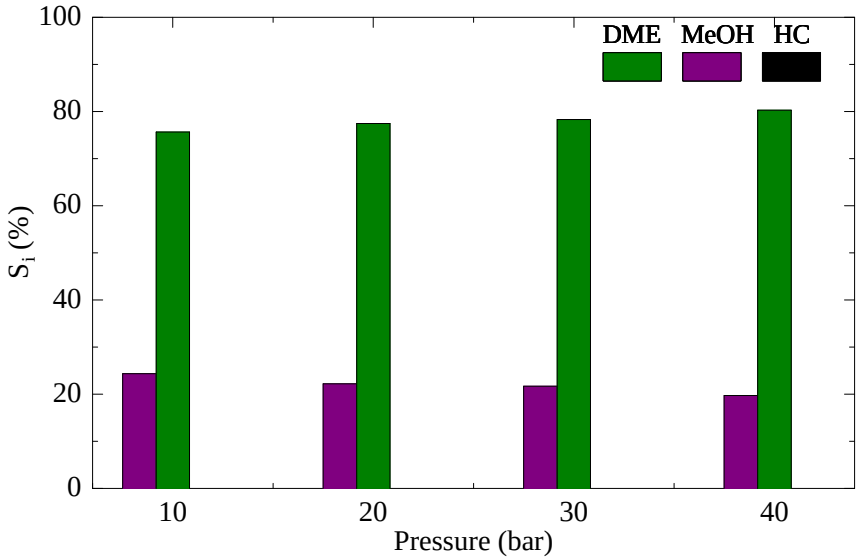

Figure 4.17: Effect of pressure on products selectivity. Reaction conditions: 275 °C; 10 $g_{cat}h(mol_C)^{-1}$; H_2/CO_x, 3; CO_2/CO_x, 1.

Figure 4.18 displays the deactivation of the catalyst with the time on stream. It demonstrates that, at this temperature and feeding $H_2 + CO_2$, the deactivation of the catalyst is practically negligible in 3 h of reaction throughout the studied pressure range.

Attending to these results under different pressures, even though the temperature is different for the two feeds, the effect of pressure on DME yields and selectivities and on CO_2 conversion for $H_2 + CO/CO_2$ and $H_2 + CO_2$ feeds can be compared. First of all, the effect of pressure is qualitatively similar. The drop of DME yield decreasing the pressure (interesting for reducing operating costs) is proportionally similar for both feeds, as well as the drop of CO_x conversion. Regarding DME selectivity, it is constant with pressure in both cases. Nonetheless, feeding $CO + CO_2$, a pressure decrease implies a rise of paraffins selectivity to the detri-

ment of methanol one (being favored CH_4 synthesis and Fischer-Tropsch reactions with respect to methanol synthesis). Feeding CO_2 at 275 °C, on the contrary, paraffins formation is insignificant even under 10 bar. It is also remarkable that the catalyst deactivation is slightly favored by the increase of pressure for $CO + CO_2$ feed at 325 °C, and very slow for $H_2 + CO_2$ feed at 275 °C.

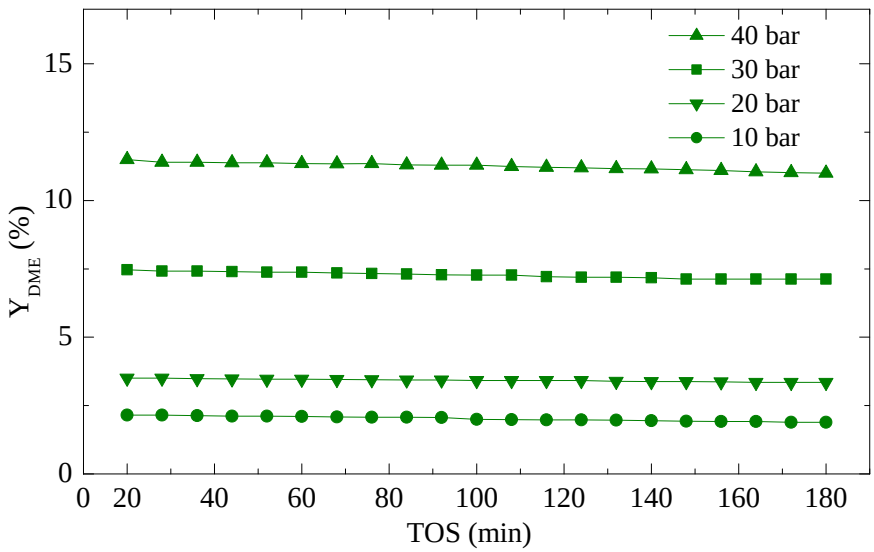

Figure 4.18: Effect of pressure on TOS evolution of DME yield. Reaction conditions: 275 °C; 10 $g_{cat}h(mol_C)^{-1}$; H_2 / CO_x, 3; CO_2 / CO_x, 1.

4.4 Comparison between PBMR and PBR

In this section the influence of incorporating a membrane (PBMR) is compared to the conventional packed bed reactor (PBR), concerning oxygenates (MeOH and DME) yield and CO_2 conversion. As previously described, according to the thermodynamic study (Ateka et al., 2017b), when CO_2 concentration in the feed increases, the thermodynamic limitations of the reaction are raised, due to the increment of H_2O concentration in the reaction medium (formed by methanol synthesis from CO_2 (Eq. 1.69) and rWGS (Eq. 1.70) reactions). H_2O is adsorbed, on one side, on the acid sites of the catalyst reducing its capacity to dehydrate methanol (Jun et al., 2002) and, on the other side, on the metallic sites limiting the methanol synthesis rate (Dadgar et al., 2016).

4.4.1 Thermodynamic considerations

Figure 4.19 shows the oxygenates yield (MeOH + DME) obtained for certain operating conditions at different temperatures. These results aim to verify how the removal of H_2O from the reaction medium enables the overtaking of the process thermodynamic equilibrium. It can be observed that increasing the temperature, up to 325 °C, the upgrade of oxygenates yield using a membrane compared with the process thermodynamic equilibrium becomes more significant.

Obviously, reactions with higher space time could have been carried out, achieving a greater enhancement with respect to the thermodynamic equilibrium shown in Figure 4.19.

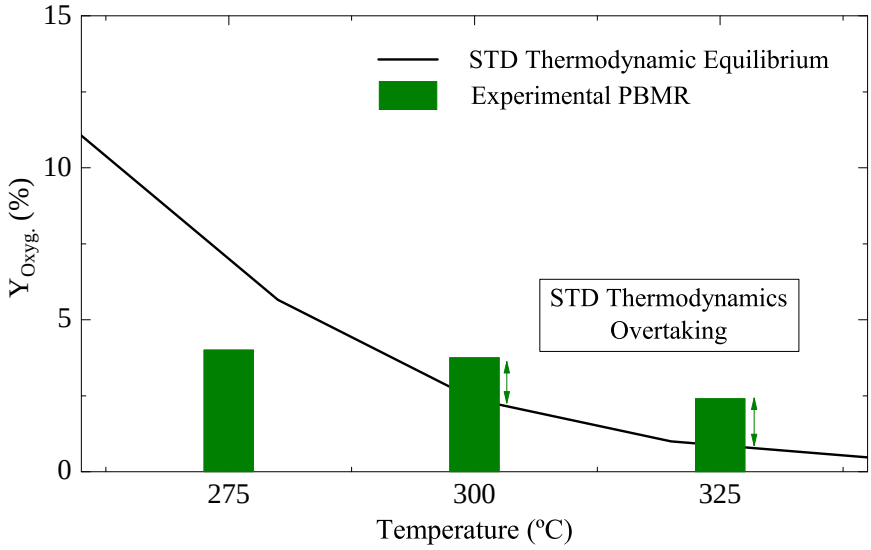

Figure 4.19: Evolution with temperature of experimental oxygenates yield using a PBMR and oxygenates yield at STD thermodynamic equilibrium. Reaction conditions: 20 bar; 10 $g_{cat}h(mol_C)^{-1}$; H_2 / CO_x, 3; CO_2 / CO_x, 1.

4.4.2 Oxygenates yield

The comparison between the evolution of oxygenates yield with temperature for the PBR and PBMR is depicted in Figure 4.20. In all the cases, within the temperature range (275 - 325 °C), using the PBMR oxygenates yield is enhanced over that obtained in the PBR. This improvement is greater increasing the temperature, from 2.80 to 6.57 % at 325 °C.

Moreover, Figure 4.21 shows the effect on oxygenates yield of the variation of CO_2 / CO_x ratio content in the feed (from 0 to 1) at 325 °C and under 30 bar. The rise of oxygenates yield using the PBMR can be observed for all the different CO_2 contents in the feed. Most remarkable is the greatest enhancement achieved with the highest CO_2 content in the feed, improving oxygenates yield by $\sim$ 135 % feeding $H_2 + CO_2$.

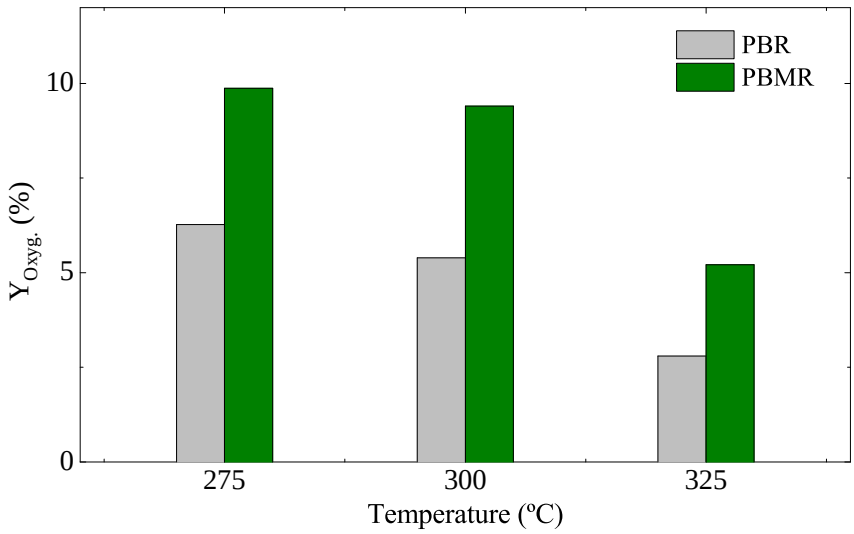

Figure 4.20: Comparison of the evolution with temperature of oxygenates (DME and MeOH) yield with temperature for PBR and PBMR. Reaction conditions: 30 bar; 10 $g_{cat}h(mol_C)^{-1}$; H_2 / CO_x, 3; CO_2 / CO_x, 1.

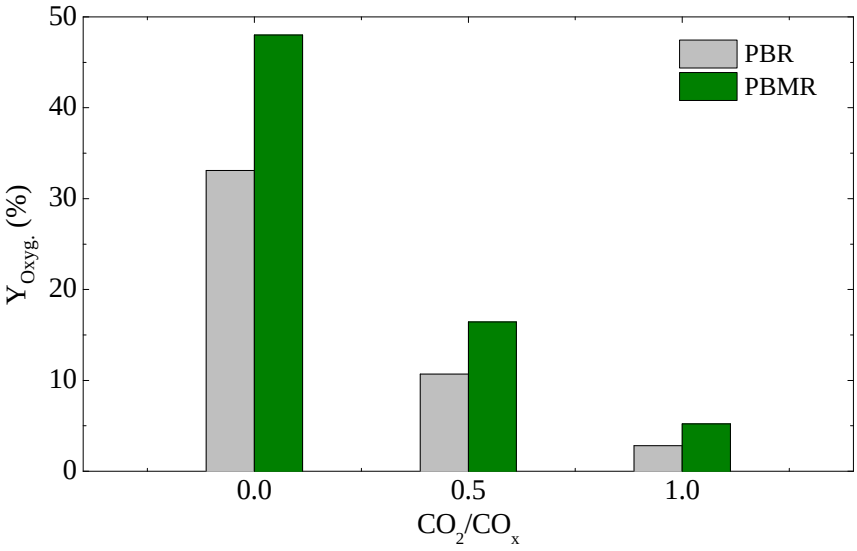

Figure 4.21: Comparison of the evolution of oxygenates (DME and MeOH) yield between PBR and PBMR with different CO_2 / CO_x ratios in the feed. Reaction conditions: 325 ºC; 30 bar; 10 $g_{cat}h(mol_C)^{-1}$; H_2 / CO_x, 3; CO_2 / CO_x, 0 - 1.

4.4.3 CO_2 conversion

The effect of the operating temperature (275 - 325 °C) on CO_2 conversion has been studied in both PBR and PBMR (Figure 4.22). The conversion of CO_2 is greater in PBMR within the studied temperature range, observing the highest enhancement (37 %) at 275 °C.

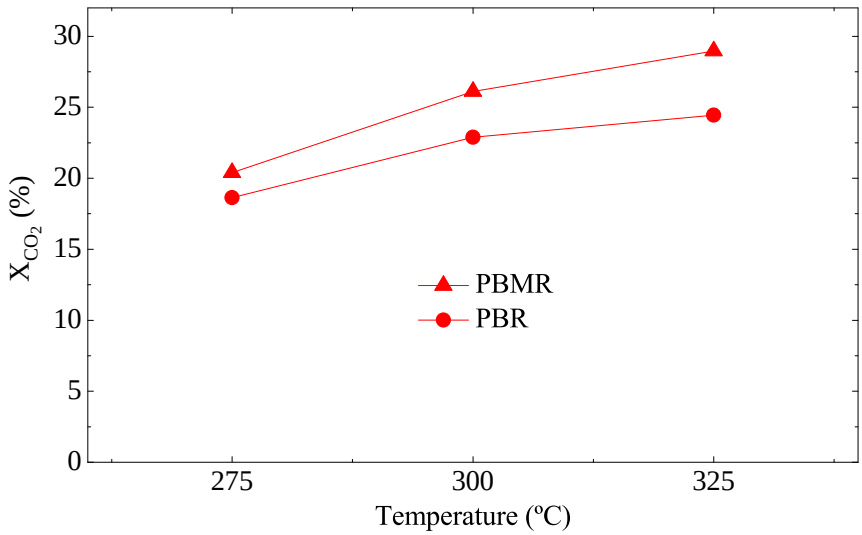

Figure 4.22: Comparison of the evolution with temperature of CO_2 conversion between PBR and PBMR. Reaction conditions: 30 bar; 10 $g_{cat}h(mol_C)^{-1}$; H_2 / CO_x, 3; CO_2 / CO_x, 1.

4.4.4 Coke deposition

The deposition of coke has been identified as the main cause of CZZr / S-11 catalyst deactivation. The total coke content, typology and location have been studied in this section following the procedure described in Section 2.3.5. The primary interest of this deactivation study is to compare the catalyst coke content using a PBMR regarding the results obtained by Sánchez-Contador et al. (2019) with a PBR.

The presence of H_2O in the reaction medium attenuates the deposition of coke on the catalyst surface, since it prevents the evolution of coke precursors (Gayubo et al., 1999). In our case, as a PBMR is used to synthesize DME, removing H_2O from the reaction zone and thus, theoretically, greater amount of coke is expected on the deactivated catalyst.

In TPO analysis (Figure 4.23) the measurement of coke combustion is based on the released CO_2. Furthermore, the temperature sequence of the thermogravimetric analysis has been followed until 815 °C in order to determine, in addition to coke combustion (completed at 600 °C), $CaCO_3$ decomposition, which has been used as reference pattern, enabling the quantitative measurement of the CO_2 amount and, hence, the burned coke.

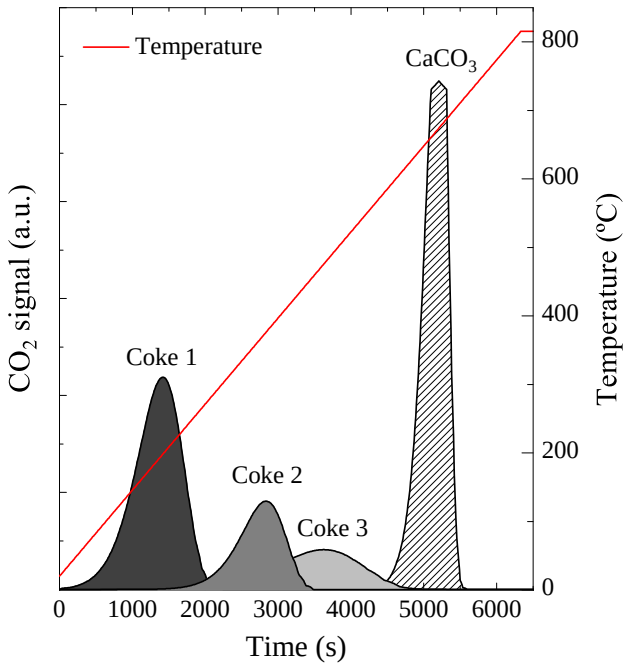

Figure 4.23: TPO curve of the combustion of coke deposited on the deactivated CZZr / S-11 bifunctional catalyst.

The TPO curves of the deactivated catalysts have three well defined peaks that have to be taken into consideration, with maxima at 200, 350 and 475 °C. These different combustion temperatures of the coke deposited on the catalyst indicate the temperature at which each fraction is being burned. The low combustion temperature of the first peak (coke type 1) can be explained because its combustion is catalyzed by the metallic function of the catalyst (mesoporous structure), where it is deposited (Abu-Dahrieh et al., 2012; Ereña et al., 2008). The presence of coke type 2 (second peak) can be observed when the concentration of coke is high, as in our case, and it can be considered that it is located between the metallic and acid functions. The combustion temperature of the third peak (coke type 3) is characteristic of the non-catalyzed combustion of coke retained in microporous structures, like the one of SAPO-11 used as acid function.

At the reaction conditions taken as an example in Table 4.10, the total coke content on the deactivated catalyst, comparing a PBR (Sánchez-Contador et al., 2018a,c) and a PBMR, rises from 0.32 to 0.61 wt%, respectively. As it was described (Gayubo et al., 1999), the removal of H_2O promotes the evolution of coke precursors on the catalyst surface. Thus, based on these results, it can be experimentally verified that using a PBMR the coke content on the deactivated catalyst rises considerably.

Table 4.10: Total coke content in deactivated CZZr / S-11 catalyst. Reaction conditions: 300 °C; 10 $g_{cat}h(mol_C)^{-1}$; H_2 / CO, 3; CO_2 / CO_x, 0.5.

Catalyst	Reactor type	Coke content (wt%)
CZZr / S-11	PBR	0.32
	PBMR	0.61

V

5

MODELING OF THE PBMR

5 | Modeling of the PBMR

In contrast to the modeling of the isothermal fixed-bed reactor, where the components formation rate was based on the mass conservation equation (in carbon atoms) (Section 3.3), in the isothermal PBMR the permeance of the components from the reaction to the permeate section (and vice versa) needs to be taken into account. In this configuration some components will diffuse through the LTA membrane from the reaction to the permeate section, thus disappearing from the reactive flow rate. Therefore, the kinetic modeling and simulation of the tubular membrane reactor are based on the resolution of the convection-diffusion equations for each component of the reaction medium.

The methodology is described in Section 5.1. Subsequently, in Section 5.2, the simulation model of the PBMR is applied to determine the membrane transport parameters. In Section 5.3 the validation of the model is performed, comparing the experimental and simulated results of the components concentration at the reactor outlet, as well as DME yield and CO_2 conversion. The kinetic model and the membrane transport parameters in the simulation of the PBMR are used in Section 5.4 to compare the results with the PBR simulation. Moreover, a scale-up study of the process is performed, simulating a PBMR with greater dimensions and space time.

5.1 Description of the methodology

The flow geometry of the catalytic bed of the reactor is depicted in Fig. 5.1, where two concentric tubes are observed parallel to the z coordinate. The interphase between the tubes represents the LTA membrane, through which the compounds diffuse.

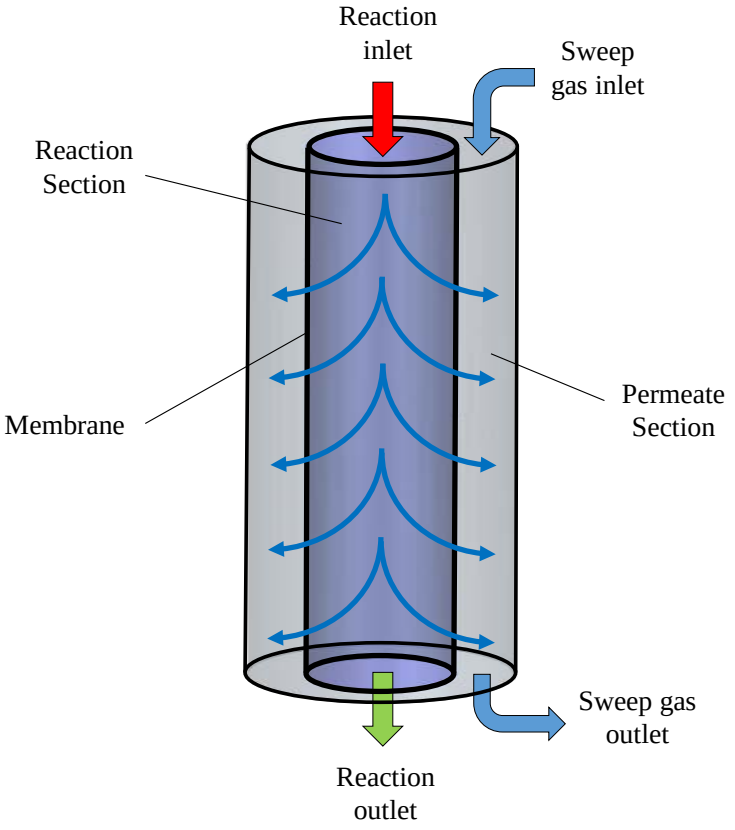

Figure 5.1: Schematic geometry of the catalytic bed.

The convection-diffusion equation for the concentration of each component (expressed in terms of partial pressure) in a porous catalytic bed can be written as:

$$\varepsilon_b \frac{\partial (P y_i)}{\partial t} = -\nabla \cdot (\nu P y_i) + \nabla \cdot [De_i \nabla (P y_i)] + s_i \tag{5.1}$$

where ε_b is the bed porosity, P is the total pressure, y_i is the molar fraction of each i compound, ν is the linear velocity, De_i is the effective diffusion coefficient of each i compound and s_i is the source term of each i compound. In a first approximation, the linear velocity can be assumed to be a function of the drop of pressure in the porous bed according to the Kozeny-Carman equation:

$$\nu = k \frac{\partial P}{\partial l} \tag{5.2}$$

being k a constant related to the permeability of the fluid within the porous bed and l the longitudinal position in the catalytic bed. Given the configuration of the reactor, unidirectional flow in the z axis is assumed. Accordingly, simplifying Eq. 5.1 in a system of parabolic differential equations (PDEs):

$$\varepsilon_b \frac{\partial (P y_i)}{\partial t} = \frac{\partial}{\partial l} \left[-kP \left(\frac{\partial P}{\partial l} \right) y_i + De_i \left(\frac{\partial y_i}{\partial l} \right) P \right] + s_i \tag{5.3}$$

This equation is solved for each i compound in both reaction (the inner tube with the catalytic bed) and permeate sections (the outer tube) of the membrane reactor. In the reaction section, the source term is defined with two different components: a first one associated with the generation by chemical reaction and a second one related to the diffusion of compounds through the membrane.

$$s_i = RT \left(r_i \rho_b - \frac{4}{D} p_i \Delta P_i \right) \tag{5.4}$$

where R is the universal gas constant, T is the temperature, r_i is the formation rate of each i compound, ρ_b is the catalytic bed density, D is the diameter of the inner tube of the reactor, p_i is the permeance constant of each i compound and ΔP_i is the

difference between the partial pressures of each i compound in the reaction and in the permeate sections.

As to the source term in the permeate section regards, it only considers the diffusion of the compounds from the reaction section of the reactor through the LTA membrane:

$$s_i = RT\,\frac{4}{D}\,p_i\,\Delta P_i \tag{5.5}$$

All in all, as has been previously reported (Cordero-Lanzac et al., 2018), a vector form of Eq. 5.3 allows for simultaneously modeling the chemical reaction and the deactivation of the catalyst. Thereby, Eq. 5.3 can be rewritten as follows for the reaction section:

$$\begin{aligned}\varepsilon_b\left(P^r\frac{\partial \mathbf{u}^r}{\partial t}+\mathbf{u}^r\frac{\partial P^r}{\partial t}\right) = \frac{\partial}{\partial l}\left[-kP^r\left(\frac{\partial P}{\partial l}\right)\mathbf{u}^r+\mathbf{De}\otimes\left(\frac{\partial \mathbf{u}^r}{\partial l}\right)P^r\right]+\\ +\underbrace{RT\left(\mathbf{r_L}\,\rho_b-\frac{4}{D}\mathbf{p}\otimes\Delta\mathbf{P}\right)}_{s^r}\end{aligned} \tag{5.6}$$

For the permeate section:

$$\begin{aligned}\left(P^p\frac{\partial \mathbf{u}^p}{\partial t}+\mathbf{u}^p\frac{\partial P^p}{\partial t}\right) = \frac{\partial}{\partial l}\left[-kP^p\left(\frac{\partial P}{\partial l}\right)\mathbf{u}^p+\mathbf{De}\otimes\left(\frac{\partial \mathbf{u}^p}{\partial l}\right)P^p\right]+\\ +\underbrace{RT\frac{4}{D}\mathbf{p}\otimes\Delta\mathbf{P}}_{s^p}\end{aligned} \tag{5.7}$$

In this sense, with the superscript r, $\mathbf{u}^r$ is defined as a vector of dependent variables in the reaction section, which contains a vector y_i of the molar fractions of each i compound and the activity of the catalyst (a) in its last position; while $\mathbf{u}^p$ comprises those for the permeate section. In like manner, P^r and P^p are the values of the pressure in each section. **De** and **s** are the vectors of effective diffusion coefficients and source terms for each i compound, respectively. Note that the symbol

$\otimes$ denotes the "element-by-element" multiplication of each element of the vectors. Furthermore, in the last position of the vectors, the convective and diffusion terms are null, being the source term the deactivation rate of the catalyst. Finally, since the total pressure varies with time and along the catalytic bed length, the total mass balance (in both reaction and permeate sections) given by the general Eq. 5.8 is also necessary for computing:

$$\varepsilon_b \frac{\partial P}{\partial t} = \frac{\partial}{\partial l}\left[-kP \frac{\partial P}{\partial l} \right] + \sum_i s_i \tag{5.8}$$

The matrix-based calculation method for solving the system of PDEs (each row corresponds to a compound, being the last two ones referred to the catalyst activity and the total pressure) consists of their transformation into a system of ordinary differential equations (ODEs) as shown in Eqs. 5.9 and 5.10.

The finite differential method proposed by Skeel and Berzins (1990) has been used, and the resulting ODEs have been integrated by means of an implicit Runge-Kutta method based on the numerical differentiation formulas of orders 1 – 5, specific for solving this kind of stiff equations.

For the reaction section:

$$\left(\begin{array}{ccccc:c}
\varepsilon_b P^r & 0 & 0 & \dots & 0 & \varepsilon_b y^r_{H_2} \\
0 & \varepsilon_b P^r & 0 & & 0 & \varepsilon_b y^r_{CO} \\
0 & 0 & \varepsilon_b P^r & & 0 & \varepsilon_b y^r_{CO_2} \\
\vdots & & & \ddots & \vdots & \vdots \\
\hdashline
0 & 0 & 0 & \dots & 1 & 0 \\
\hdashline
0 & 0 & 0 & \dots & 0 & \varepsilon_b
\end{array}\right)
\left(\begin{array}{c}
\dfrac{\partial y^r_{H_2}}{\partial t} \\
\dfrac{\partial y^r_{CO}}{\partial t} \\
\dfrac{\partial y^r_{CO_2}}{\partial t} \\
\vdots \\
\dfrac{\partial a}{\partial t} \\
\dfrac{\partial P^r}{\partial t}
\end{array}\right) =$$

$$= \left(\begin{array}{c}
-kP\left(\dfrac{\partial P^r}{\partial l}\right) y^r_{H_2} + De_{H_2}\left(\dfrac{\partial y^r_{H_2}}{\partial l}\right) P + RT\rho_b r_{H_2} - RT\dfrac{4}{D} p_{H_2}\Delta P_{H_2} \\
-kP\left(\dfrac{\partial P^r}{\partial l}\right) y^r_{CO} + De_{CO}\left(\dfrac{\partial y^r_{CO}}{\partial l}\right) P + RT\rho_b r_{CO} - RT\dfrac{4}{D} p_{CO}\Delta P_{CO} \\
-kP\left(\dfrac{\partial P^r}{\partial l}\right) y^r_{CO_2} + De_{CO_2}\left(\dfrac{\partial y^r_{CO_2}}{\partial l}\right) P + RT\rho_b r_{CO_2} - RT\dfrac{4}{D} p_{CO_2}\Delta P_{CO_2} \\
\vdots \\
r_d \\
-kP\dfrac{\partial P^r}{\partial l} + RT\rho_b \sum_i r_i - RT\dfrac{4}{D}\sum_i p_i \Delta P_i
\end{array}\right) \tag{5.9}$$

For the permeate section:

$$\left(\begin{array}{cccc:c:c} P^p & 0 & 0 & \dots & 0 & y^p_{H_2} \\ 0 & P^p & 0 & & 0 & y^p_{CO} \\ 0 & 0 & P^p & & 0 & y^p_{CO_2} \\ \vdots & & & \ddots & \vdots & \vdots \\ \hdashline 0 & 0 & 0 & \dots & 1 & 0 \\ \hdashline 0 & 0 & 0 & \dots & 0 & 1 \end{array}\right) \left(\begin{array}{c} \frac{\partial y^p_{H_2}}{\partial t} \\ \frac{\partial y^p_{CO}}{\partial t} \\ \frac{\partial y^p_{CO_2}}{\partial t} \\ \vdots \\ 0 \\ \frac{\partial P^p}{\partial t} \end{array}\right) =$$

$$= \left(\begin{array}{c} -kP^p\left(\frac{\partial P^p}{\partial l}\right)y^p_{H_2} + De_{H_2}\left(\frac{\partial y^p_{H_2}}{\partial l}\right)P^p + RT\frac{4}{D}p_{H_2}\Delta P_{H_2} \\ -kP^p\left(\frac{\partial P^p}{\partial l}\right)y^p_{CO} + De_{CO}\left(\frac{\partial y^p_{CO}}{\partial l}\right)P^p + RT\frac{4}{D}p_{CO}\Delta P_{CO} \\ -kP^p\left(\frac{\partial P^p}{\partial l}\right)y^p_{CO_2} + De_{CO_2}\left(\frac{\partial y^p_{CO_2}}{\partial l}\right)P + RT\frac{4}{D}p_{CO_2}\Delta P_{CO_2} \\ \vdots \\ 0 \\ -kP^p\frac{\partial P^p}{\partial l} + RT\frac{4}{D}\sum_i p_i\Delta P_i \end{array}\right) \tag{5.10}$$

The initial condition of molar fractions and total pressure used (in each section) in order to solve the system of ODEs are:

$$\mathbf{y}_i\,(t=0,l) = \mathbf{y}_{i,0} \tag{5.11}$$

$$P\,(t=0,l) = P_{in} - \alpha\, l \tag{5.12}$$

where $\mathrm{y}_{i,0}$ is the vector of molar fractions of each i compound at zero time on

stream, P_{in} is the pressure at the inlet of the reactor and α is defined as a function of the pressure drop (Δ P) along the total length of catalytic bed (L):

$$\alpha = \frac{\Delta P}{L} \tag{5.13}$$

When the dependent variable is referred to the activity of the catalyst, the initial condition is 1 (deactivation not observed at the initial time) in the reaction section. On the other hand, the activity value is always 0 in the permeate section due to the absence of catalyst in this region of the membrane reactor:

$$a_r\,(t=0,l)=1 \tag{5.14}$$

$$a_p\,(t,l)=0 \tag{5.15}$$

As the molar fraction of each i compound ($y_{i,in}$) and the total pressure at the inlet of the reactor are known, Robin and Dirichelet boundary conditions have been respectively used for each variable respect to the bed length:

$$y_i\,(t,l=0)=y_{i,in}-\left(\frac{\mathbf{De}}{\mathbf{v}_{in}}\right)\otimes\left(\frac{\partial \mathbf{y}_i}{\partial l}\right) \tag{5.16}$$

$$P\,(t,l=0)=P_{in} \tag{5.17}$$

$$P\,(t,l=L)=P_{in}-\Delta P \tag{5.18}$$

being v_{in} the gas linear velocity at the inlet of the reaction section. Regarding the source term previously introduced in Eq. 5.4, in order to calculate together the kinetic parameters of the reaction and deactivation steps, the formation rate of each i compound (r_i) and the catalyst deactivation rate (r_d) can be expressed as a vector $\mathbf{r}_L$ (Cordero-Lanzac et al., 2018):

$$\mathbf{r}_L = \begin{bmatrix} \mathbf{r}_i \\ r_d \end{bmatrix} \tag{5.19}$$

where r_i is the vector that contains the formation rate of each i compound. The values of these formation rates have been calculated from the reaction rates of each j step of the kinetic scheme for the DME synthesis process. Thus, the vector of reaction rates is transformed into the vector of formation rates through a coefficient matrix A.

$$\mathbf{r}_L = \mathbf{A}\,\mathbf{r} \tag{5.20}$$

where $\mathbf{r}$ contains the vector of the reaction rates of each j steps of the kinetic scheme and the catalyst deactivation rate (r_d):

$$\mathbf{r} = \begin{bmatrix} \mathbf{r}_j \\ r_d \end{bmatrix} \tag{5.21}$$

In our case of study, as introduced in Section 3.4, the reaction scheme implies the following five steps: 1) formation of methanol from synthesis gas (Eq. 3.12); 2) formation of methanol from CO_2 (Eq. 3.13); 3) water-gas shift (WGS) reaction (Eq. 3.14); 4) dehydration of methanol towards DME (Eq. 3.15), and; 5) formation of paraffins (mainly CH_4) from synthesis gas (Eq. 3.16). This reaction network for the synthesis of DME from $CO\,/\,CO_2$ and H_2 has been deeply studied (Ateka et al., 2018b; Farsi et al., 2016; Hadipour and Sohrabi, 2008; Iliuta et al., 2010; Ng et al., 1999; Sierra et al., 2010), however a great number of authors do not take into account the formation of hydrocarbons as byproducts, which is considered in this Thesis.

Taking into consideration the reaction steps stoichiometry:

$$\mathbf{r}_L = \begin{pmatrix} r_{H_2} \\ r_{CO} \\ r_{CO_2} \\ r_{H_2O} \\ r_{CH_3OH} \\ r_{DME} \\ r_{HC} \\ r_{N_2} \\ r_d \end{pmatrix} = \underbrace{\begin{pmatrix} -2 & 0 & 1 & -3 & -3 & 0 \\ -1 & 0 & -1 & 0 & -1 & 0 \\ 0 & 0 & 1 & -1 & 0 & 0 \\ 0 & 1 & -1 & 1 & 1 & 0 \\ 1 & -2 & 0 & 1 & 0 & 0 \\ 0 & 1 & 0 & 0 & 0 & 0 \\ 0 & 0 & 0 & 0 & 1 & 0 \\ 0 & 0 & 0 & 0 & 0 & 0 \\ 0 & 0 & 0 & 0 & 0 & 1 \end{pmatrix}}_{A} \underbrace{\begin{pmatrix} r_1 \\ r_2 \\ r_3 \\ r_4 \\ r_5 \\ r_d \end{pmatrix}}_{r}$$

$$= \begin{pmatrix} -2r_1 + r_3 - 3r_4 - 3r_5 \\ -r_1 - r_3 - r_5 \\ r_3 - r_4 \\ r_2 - r_3 + r_4 + r_5 \\ r_1 - 2r_2 + r_4 \\ r_2 \\ r_5 \\ 0 \\ r_d \end{pmatrix} \tag{5.22}$$

According to the proposed kinetic scheme and the above detailed methodology, the expressions of vector $\mathbf{r}_j$ are the ones described in Eqs. 3.17-3.19, applied in terms of partial pressure. Each reaction rate is a function of the partial pressure of reactants and products involved in the reaction step, both related by the thermodynamic equilibrium constant of the reaction. It is known that the lower concentration of H_2O in the medium (in this case due to the permeation through the membrane)

may lead to higher CH_4 formation, since the inhibiting effect of H_2O on this step (Ateka et al., 2018a; Sierra et al., 2012) will be reduced. However, taking into consideration the low paraffins formation experimentally detected, a constant β (as detailed in Eq. 3.20) has been considered for hydrocarbons formation.

Furthermore, in Eq. 5.21, the catalyst deactivation rate is assumed to be directly dependent on the oxygenates content in the medium, according to the expression of Eq. 3.21.

Following the methodology described in Section 3.3.1, all kinetic constants and adsorption equilibrium constants have been reparameterized. Hence, k vector can be expressed as a function of the vectors **k*** (kinetic constants at the reference temperature, 275 °C) and $\mathbf{E}_j$ (activation energy of each j step) (Eq. 3.7). In like manner, the adsorption equilibrium constants have been also reparameterized (Eq. 3.8) and K* and ΔH_{ads} are the vectors gathering the values of the adsorption constant at the reference temperature and the apparent adsorption heats of each adsorption process, respectively. Conversely, the values of the equilibrium constants of the different individual reactions have been estimated from empirical equations, as explained in Section 3.3.1.

5.2 Obtention of the membrane transport parameters

In the literature there is scarce information on the permeance and perm-selectivity characteristics of the membranes, given the low reproducibility of commercial zeolite membranes synthesis, which is still a major drawback for the implementation of membrane reactors (Diban et al., 2013; Gascon et al., 2012) and, moreover, the issues to conduct tests at the experimental conditions of interest for this application. An exception is the study of Gorbe et al. (2018) of the permeance of a H_2, CO_2 and H_2O mixture, through a zeolite A membrane, with the perspective of its future application in methanol synthesis. Accordingly, to overcome this gap of experimentally supported data, determining the permeance and permselectivity values of the used membrane is a key feature for the future kinetic modeling of the PBMR. Bearing this in mind, unlike the general approach in the literature where wide H_2O permeability ranges are assumed for conducting simulation studies, or only H_2O and H_2 permeabilities are considered (Diban et al., 2013; Farsi et al., 2016; Iliuta et al., 2010), in this Thesis the individual permeances of each i compound present in the reaction medium have been determined from real experimental values.

The experiments have been conducted using an inert SiC bed in the PBMR (that is, without catalyst) and the LTA membrane. The tests have been performed using N_2 as sweeping gas in the permeate section while feeding the following compound mixtures in the same total flow rate (of 60 $cm^3\ min^{-1}$): 1) H_2 (66 vol%), CO (17 vol%) and CO_2 (17 vol%); 2) H_2O (1 vol%), MeOH (9 vol%) and N_2 (90 vol%); 3) DME (78 vol%) and N_2 (22 vol%). The compositions of each section (reaction and permeate) have been analyzed in a gas-chromatograph as described in detail in Section 2.1. Carrying out the experiments at different temperatures (125, 275, 300

and 325 °C under a constant pressure of 1.5 bar) has allowed studying the effect of temperature on the individual permeances.

In contrast to the aforementioned approach for establishing the kinetic parameters, in this case, the source term in Eq. 5.4 simplifies to the diffusion of the components through the LTA membrane, being the reaction rate of all components null, as introduced in Eq. 5.5. This diffusion model has also been computed using the same vectorized LM-based algorithm, and therefore a vector of permeances (p) of each i compound has been defined. These permeances are also assumed to fit an exponential tendency with temperature, similar to that described for the kinetic and adsorption constants (Eqs. 3.7 and 3.8):

$$\mathbf{p} = \mathbf{p}^* \otimes exp\left[-\frac{\Delta \mathbf{H}_{diff}}{R} \left(\frac{1}{T^*} - \frac{1}{T} \right) \right] \tag{5.23}$$

where $\mathbf{p}^*$ and $\Delta \mathbf{H}_{diff}$ are the permeance vectors at the reference temperature and of the apparent diffusion heats of each i compound, respectively.

Because of the absence of catalyst and the negligible LTA membrane deactivation, constant values of molar fractions have been observed at different times on stream in the collected experimental data. For this reason, the objective function (Eq. 3.6) defined for minimizing the errors between experimental data $\bar{y}^{r*}_{i,j}$ and $\bar{y}^{p*}_{i,j}$, molar fractions in the reaction and permeate section, respectively) and those calculated integrating the diffusion model ($y^{r}_{i,j}$ and $y^{p}_{i,j}$) only presents a single scalar term, simplifying to:

$$O.F._2 = \sum_{i=1}^{n_l} \omega_i \sum_{j=1}^{n_e} \frac{R_j}{n_e} \left[\left(\bar{y}^{r*}_{i,j} - y^{r}_{i,j} \right)^2 + \left(\bar{y}^{p*}_{i,j} - y^{p}_{i,j} \right)^2 \right] 6 \tag{5.24}$$

From this experimental analysis, the individual permeance and adsorption heat values at the reference temperature have been determined, and the values of best

fit are gathered in Table 5.1.

Table 5.1: Estimated individual permeances and adsorption heats.

Component (i)	Individual permeance ($mol\,m^{-2}\,s^{-1}\,Pa^{-1}$)	ΔH_{diff} ($J\,mol^{-1}$)
H_2	3.99 E-08	1.68 E+03
CO	3.98 E-08	1.56 E+03
CO_2	4.04 E-08	2.38 E+03
H_2O	4.63 E-08	1.83 E+03
MeOH	4.71 E-08	3.64 E+03
DME	2.85 E-08	7.46 E+03
HC	4.00 E-08	5.00 E+03
N_2	4.00 E-08	5.00 E+03

The H_2O permeance value determined experimentally ($4.63{\cdot}10^{-8}$ $mol\,m^{-2}\,s^{-1}\,Pa^{-1}$), is close to the lowest limit of the preferred permeability range (5 - $12{\cdot}10^{-8}$ $mol\,m^{-2}\ s^{-1}\,Pa^{-1}$) reported in the literature by Diban et al. (2013) for the synthesis of DME. According to these authors, low H_2O permeability and $H_2O\,/\,H_2$ permselectivity values are preferred to achieve a commitment between optimal DME and remarkable CO_2 conversion at the described operating conditions. In contrast to the study of Rohde et al. (2008) for Fischer-Tropsch synthesis, where high $H_2O\,/\,H_2$ permselectivity is required for achieving high CO_x conversion. Regarding DME permselectivity ($H_2O\,/\,DME$), it is 40 % higher than those of $H_2O\,/\,H_2$ or $H_2O\,/\,CO$. However, the low $H_2O\,/\,i$ permselectivity values achieved, explained by the high temperature, reveal the importance of further improving this key property of the membrane. On the other hand, it must be pointed out that the high

permeability of methanol was expected, since, asides from being a molecule larger than H_2, its polarity favors the adsorption onto the zeolite membranes as reported by Salomón et al. (2000) using zeolite membranes in the synthesis of MTBE.

The accuracy of the model for fitting the experimental values in the reactor (circles) and permeate (crosses) sides of the reactor can be observed in Figure 5.2, where each graph corresponds to a component of the medium.

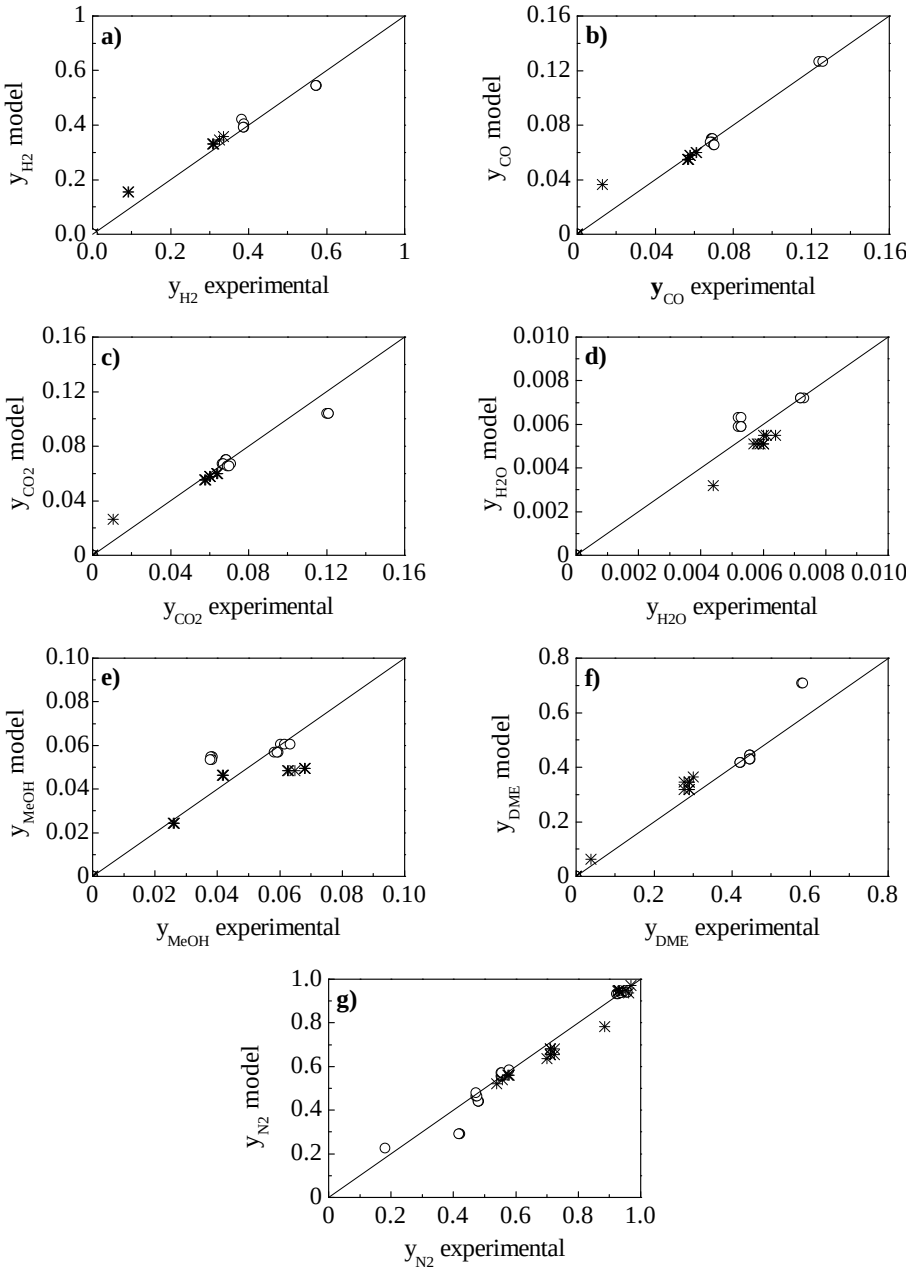

Figure 5.2: Fitting of the experimental values of the molar fractions of the compounds to those calculated with the membrane transport model. H_2 (a), CO (b), CO_2 (c), H_2O (d), MeOH (e), DME (f), N_2 (g).

5.3 Validation of the model

5.3.1 Concentration of the components

In Figures 5.3 - 5.8 the obtained fitting with the PBMR simulation model can be qualitatively observed, using the values of the transport and kinetic parameters summarized in Tables 5.1 and 3.5, respectively. In this case, in contrast to Figure 3.7 for the PBR, for each experimental condition in the PBMR two graphs are depicted, corresponding to the reaction and permeate sections. Thus, Figure 5.3 shows the parity diagrams for each component in the reaction section whereas Figure 5.4 displays the data in the permeate section. Considering these figures, it can be concluded that the simulation model for the PBMR fits appropriately the experimental results, taking into account the experimental complexity as well as the estimation of the parameters above indicated. Both the reaction (Figure 5.3) and the permeate (Figure 5.4) sections are acceptably described with the proposed model. This means that not only the catalyst activity, but also the permeability parameters, determined in Section 5.2, are acceptable to describe the process performance with the PBMR within a wide range of conditions. The highest relative deviation is observed by the hydrocarbons (Figures 5.3g and 5.4g), nonetheless considering its value, the importance of these compounds in regards to the rest is relatively small.

As an example, in Figures 5.6 - 5.8 the evolution with time on stream of the experimental results (dots) of the components molar fractions and those calculated with the PBMR model (lines) are compared at the reaction section (left) and permeate section (right). The analysis of the effect of the reaction conditions is omitted in this case due to its qualitative similarity to the described in Section 3.5.

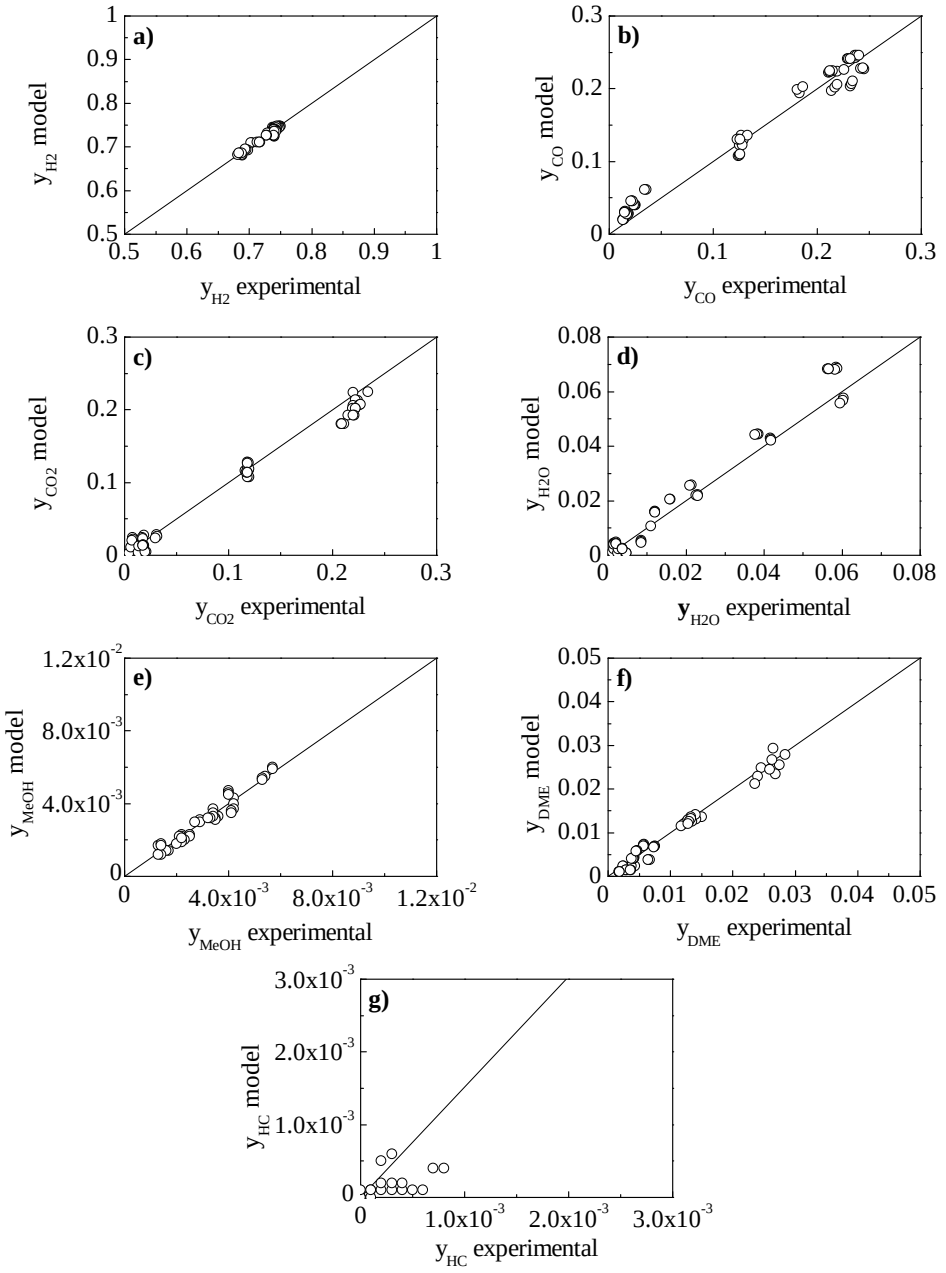

Figure 5.3: Fitting of the experimental values of products molar fractions to those calculated with the PBMR model in the reaction section (RS). H_2 (a), CO (b), CO_2 (c), H_2O (d), MeOH (e), DME (f), HC (g).

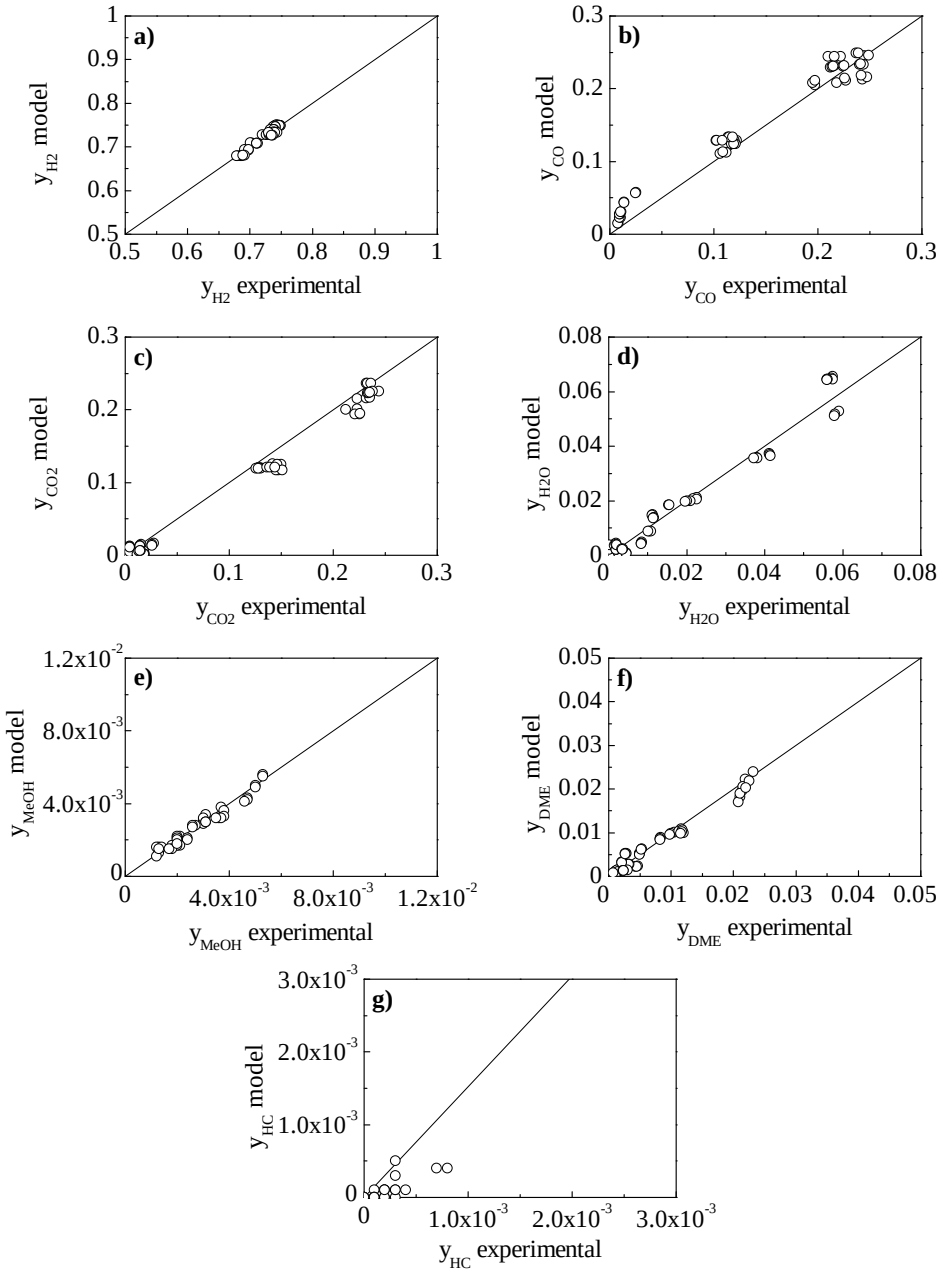

Figure 5.4: Fitting of the experimental values of products molar fractions to those calculated with the PBMR model in the permeate section (PS). H_2 (a), CO (b), CO_2 (c), H_2O (d), MeOH (e), DME (f), HC (g).

The results in Figures 5.6 and 5.5 correspond to ternary feeds of $H_2 + CO + CO_2$ feed (CO_2 / CO_x = 0.5) for different operating conditions. The higher is the temperature and pressure, it means at the most severe reaction conditions in which DME production is maximized, the greater is the water content. Analyzing individually each graph (a, b, c) in Figure 5.6, it can be observed that H_2O is the compound that permeates the most, and that their molar fractions in the reaction section (left squares) are similar to those monitored in the permeate section (right squares). This indicates that with this strategy almost the half of the generated water is removed at these conditions.

In Figures 5.7a and 5.7b, feeding $H_2 + CO_2$ at 20 and 30 bar respectively, H_2O concentration in the reaction section is 30 and 20 % less, respectively, than in the PBR at the same reaction conditions (results not shown). As can be predicted from the determined individual values for permeability and adsorption heats in Section 5.2 (Table 5.1), the rest of the components also permeate through the membrane, although to a minor extent, being DME the compound that least permeates through the membrane.

In the results in Figure 5.8 remarkable attenuating effect of deactivation by the formed water can be observed, feeding $H_2 + CO_2$ (Figures 5.8a and 5.8b, under 20 and 40 bar, respectively). Nonetheless, feeding $H_2 + CO$ (Figure 5.8c) the concentration of methanol and DME decreases notably with the time on stream, as consequence of the catalyst deactivation by coke.

Comparing the overall results of Figures 5.6 - 5.8, it is evident that the most influential parameter in the formation of water is the CO_2 / CO_x ratio in the feed. With CO_2-rich feeds the production of H_2O is greater through the rWGS reaction, whose kinetic constant is four orders of magnitude superior than the formation of

methanol. At these conditions (CO_2 / CO_x = 1), the PBMR model also predicts successfully the production of water and its permeation through the membrane, as can be observed in Figures 5.7, 5.8a and 5.8b.

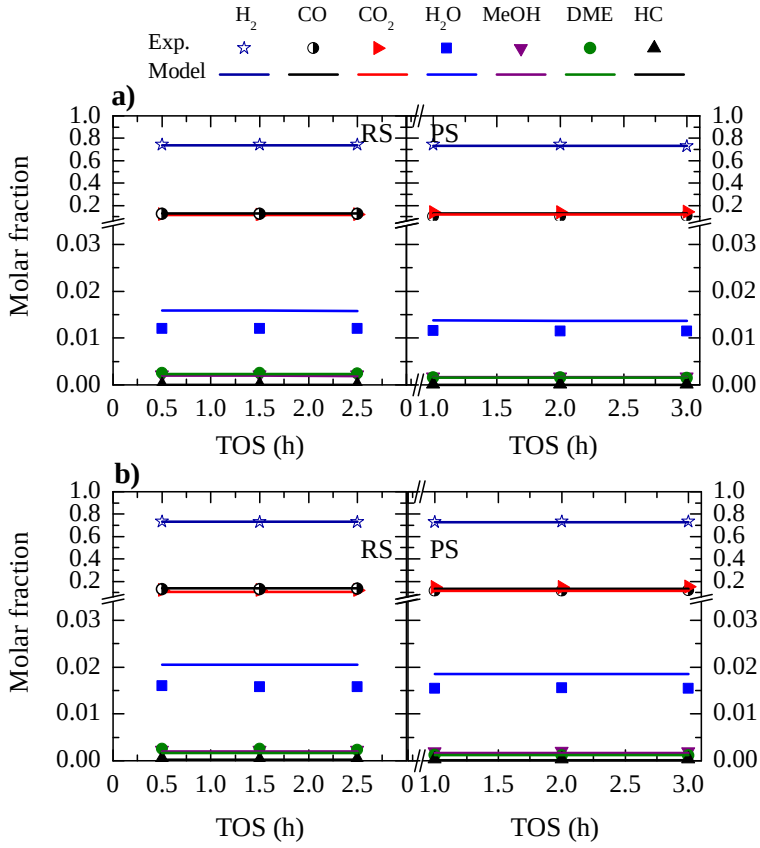

Figure 5.5: Comparison of the evolution with time on stream (TOS) of the experimental values of products yields (dots) and those calculated using the PBMR model (lines), in the reaction (left) and in the permeate section (right), at 300 °C (a) and 325 °C (b). Reaction conditions: feed, H_2 + CO + CO_2; 20 bar; 10 g_{cat} h $(mol_C)^{-1}$; H_2 / CO_x, 3; CO_2 / CO_x, 0.5.

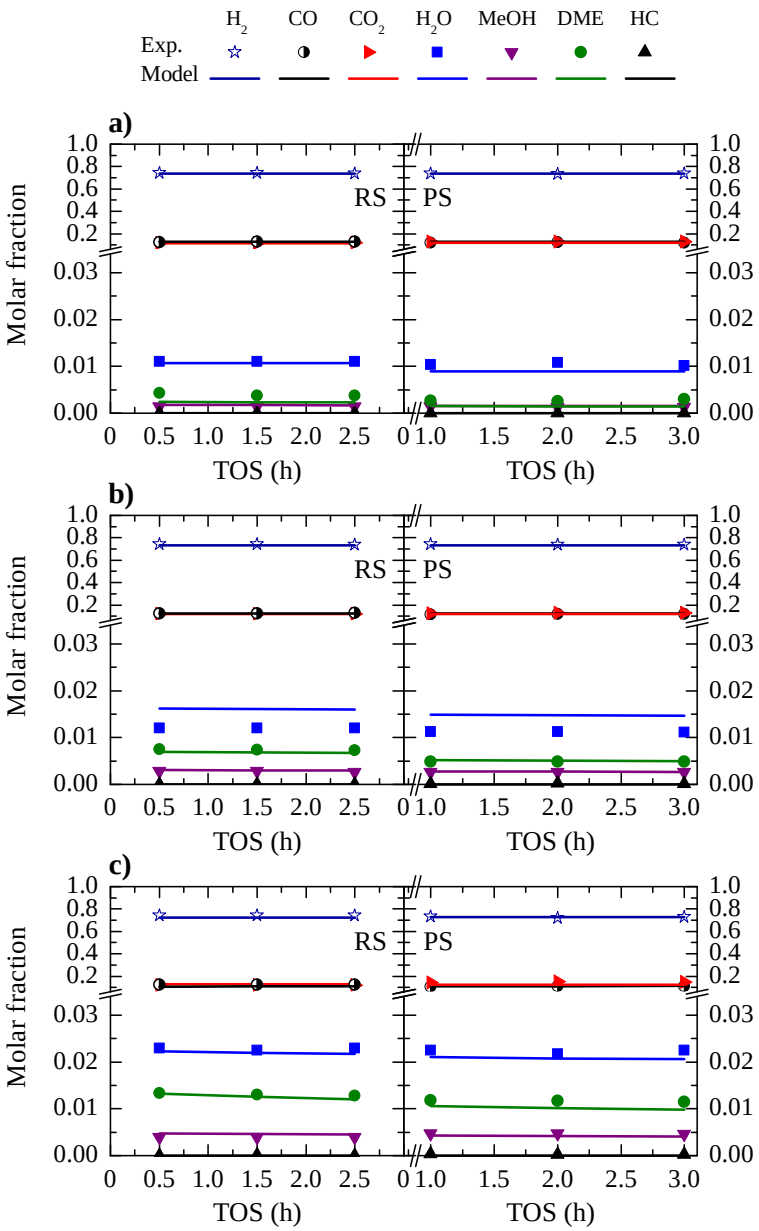

Figure 5.6: Comparison of the evolution with time on stream (TOS) of the experimental values of products yields (dots) and those calculated using the PBMR model (lines), in the reaction (left) and in the permeate section (right), under 20 bar (a), 30 bar (b) and 40 bar (c). Reaction conditions: feed, H_2 + CO + CO_2; 275 °C; 10 g_{cat} h $(mol_C)^{-1}$; H_2 / CO_x, 3; CO_2 / CO_x, 0.5.

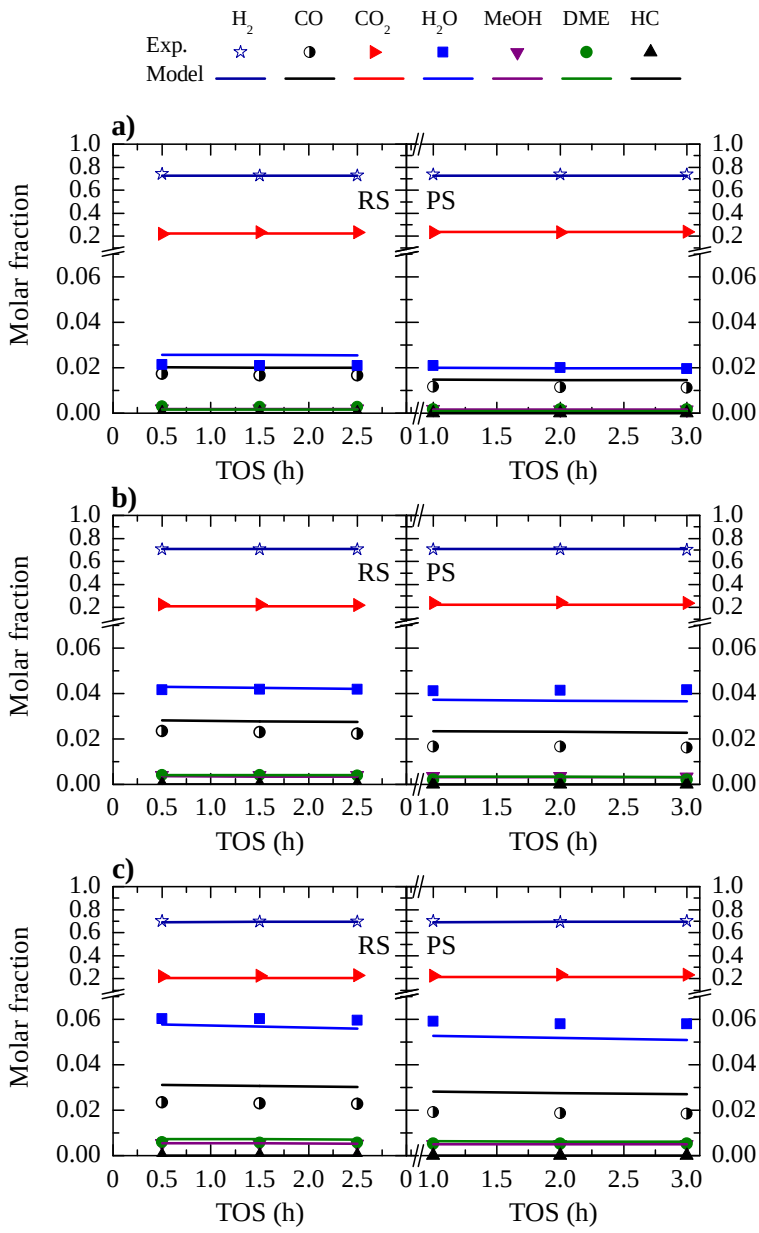

Figure 5.7: Comparison of the evolution with time on stream (TOS) of the experimental values of products yields (dots) and those calculated using the PBMR model (lines), in the reaction (left) and in the permeate section (right), under 20 bar (a), 30 bar (b) and 40 bar (c). Reaction conditions: feed, H_2 + CO_2; 275 °C; 10 g_{cat} h $(mol_C)^{-1}$; H_2 / CO_x, 3; CO_2 / CO_x, 1.

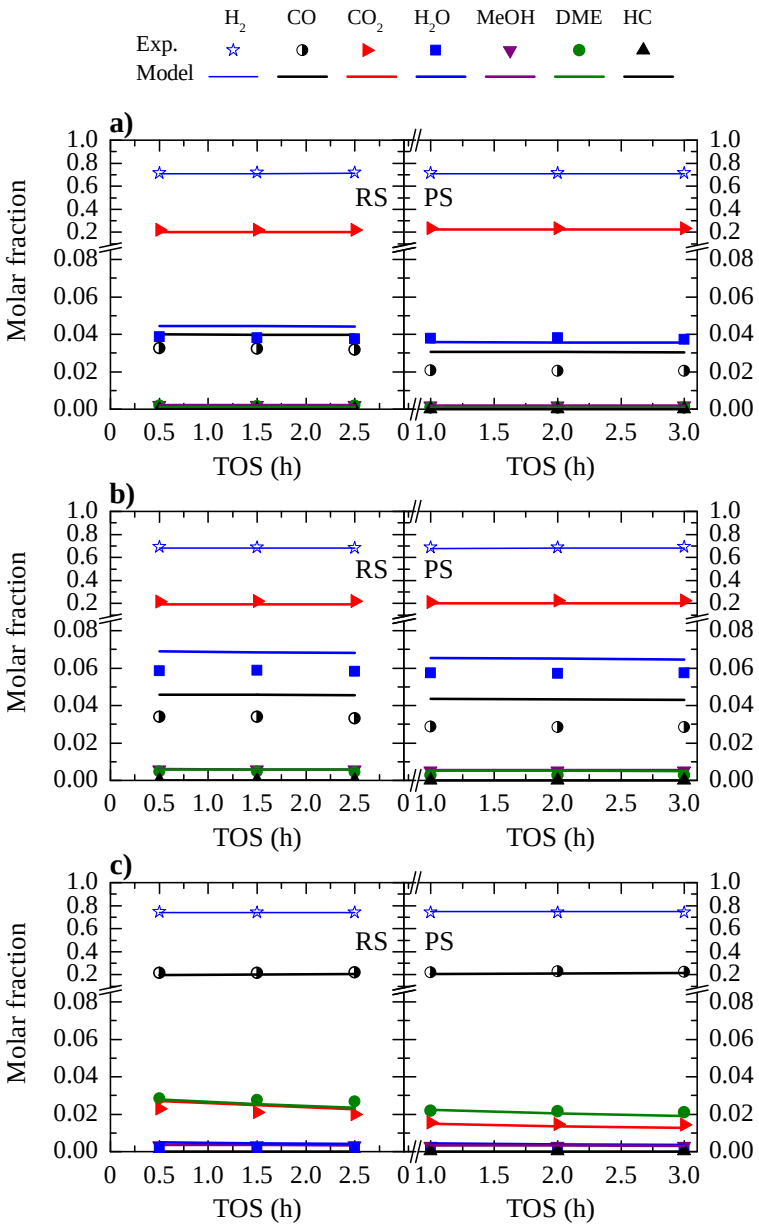

Figure 5.8: Comparison of the evolution with time on stream (TOS) of the experimental values of products yields (dots) and those calculated using the PBMR model (lines), in the reaction (left) and in the permeate section (right), for CO_2 / CO_x, 1 under 20 bar (a) and 40 bar (b); and for CO_2 / CO_x, 0 under 40 bar (c). Reaction conditions: feed, H_2 + CO + CO_2; 300 °C; 10 g_{cat} h $(mol_C)^{-1}$; H_2 / CO_x, 3

5.3.2 DME yield and CO_2 conversion

While in Section 5.3.1 the capacity of the PMBR model to predict the reaction components of the complex reaction scheme is demonstrated, from the application perspective it is more interesting its capacity to predict the macroscopic results such as DME yield or CO_2 conversion. In Figure 5.9 the DME yield evolutions with temperature that is predicted by the model (continuous lines) are compared with the experimental values (symbols).

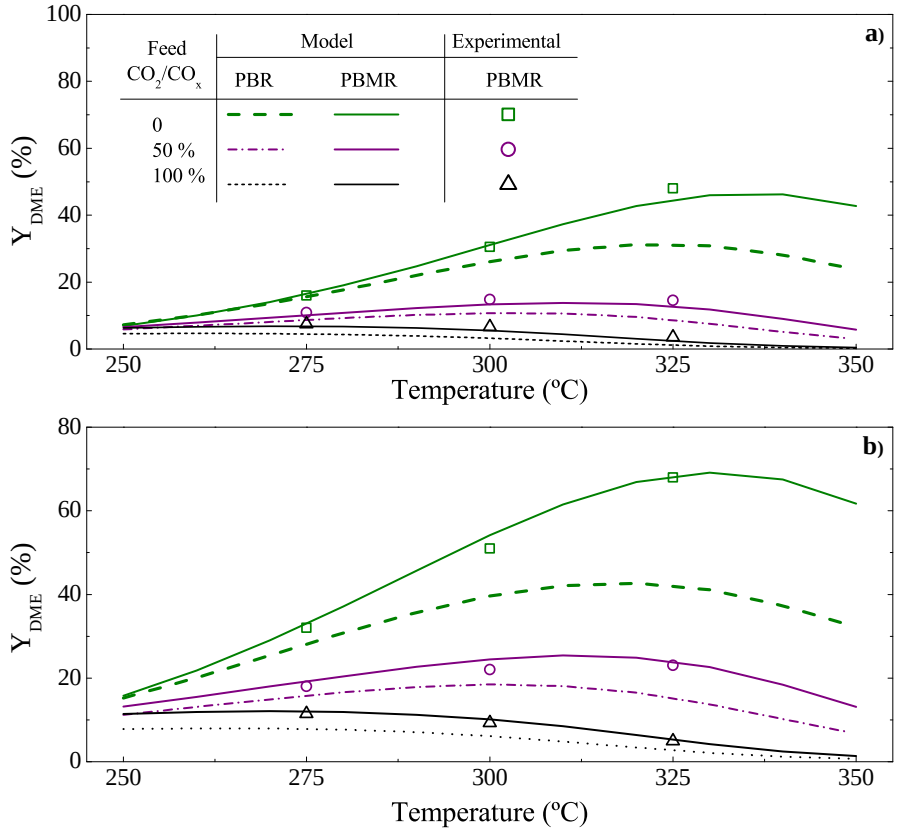

Figure 5.9: Evolution of DME yield with the reaction temperature estimated by the model (lines) for the PBR (dashed) and PBMR (continuous), and the experimental values (symbols) obtained with the PBMR, under 30 bar (a) and 40 bar (b). Reaction conditions: space time, 10 g_{cat} h $(mol_C)^{-1}$; H_2 / CO_x, 3; CO_2 / CO_x, 0 - 1.

These results correspond to 30 bar (Figure 5.9a) and 40 bar (Figure 5.9b) and in both cases to CO_2 / CO_x ratios in the feed of 0, 0.5 and 1. Additionally, on the same graphs the results of the PBR simulation are depicted (dashed lines), which serve as reference for assessing the advantage of using the PBMR.

The calculated and simulated results of the evolution of CO_2 conversion with the reaction temperature are compared in Figure 5.10, for a CO_2 / CO_x ratio of 0.5 in the feed. Similarly to Figure 5.9, the results correspond to a space time of 10 $g_{cat}\,h\,(mol_C)^{-1}$.

The suitable fitting between the calculated and experimental results demonstrates that the model is appropriate to represent the performance of the PBMR, and hence it has been applied in the simulation studies of the next section.

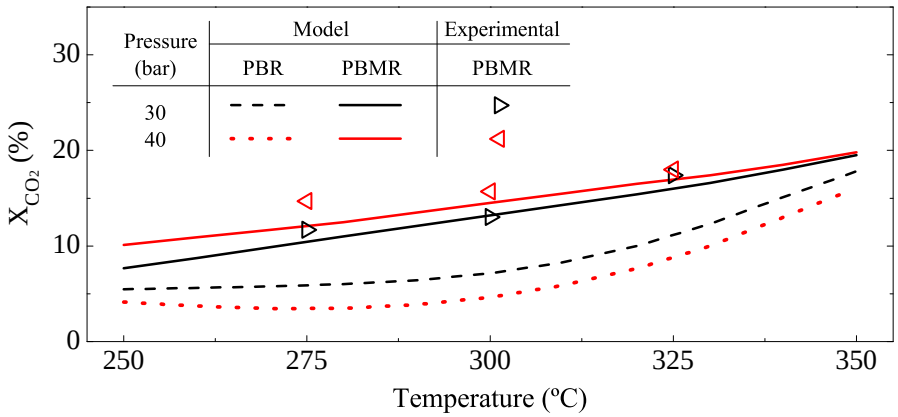

Figure 5.10: Evolution of CO_2 conversion with the reaction temperature estimated by the model (lines) for the PBR (dashed) and PBMR (continuous), and the experimental values (symbols) obtained with the PBMR. Reaction conditions: space time, 10 $g_{cat}\,h\,(mol_C)^{-1}$; H_2 / CO_x, 3; CO_2 / CO_x, 0.5.

5.4 Simulation of the PBMR

The advantages of the PBMR in comparison to the PBR are quantified in Section 5.4.1, comparing the simulation results of both reactors for the production of DME, methanol and the sum of both oxygenates, respectively. The criteria used is the valuation of the advantage using a permeate zone, comparing the results with and without permeate section. The results have been obtained by the simulation of both reactors with the simulation programs described in Sections 3.4 and 5.1. Subsequently, the capacity of the simulation program to perform scale-up studies is detailed in Section 5.4.2, with the knowledge of the composition profiles both in the reaction and permeate sections.

5.4.1 Comparison between PBMR and PBR

The results of DME, methanol and oxygenates (methanol and DME) yields for both the PBMR and PBR are compared in Figures 5.11 - 5.13 as an example of the simulation results. On graphs a), the effect of the variables temperature (within the range 250 - 350 °C) and CO_2 / CO_x ratio (0 - 100 %) for both reactors is depicted. Meanwhile, on graphs b) and c) the projection of the results (operation maps) for the PBMR and PBR are shown, respectively, allowing to analyze the results with the perspective of optimizing the corresponding yield. The results correspond to a feed of $H_2 + CO + CO_2$ and experimental conditions (30 bar; space time, 5 $g_{cat}\,h\,(mol_C)^{-1}$; H_2 / CO_x ratio, 3; time on stream, 1 h) taken as an example.

5.4.1.1 DME yield

A yield maximum can be observed in Figure 5.11a at an intermediate temperature, which is lower increasing CO_2 / CO_x ratio in the feed. Comparing the results of both reactors, DME yield is greater in the PBMR at each of the reaction conditions. Although the scale does not allow to identify the relative difference, it can indeed be observed that the improvement is more remarkable above 275 °C.

Comparing the contour maps for the PBMR and PBR the difference of DME yields in both reactors can be more clearly appreciated. Thus, at 300 °C and feeding $H_2 + CO_2$ DME yield (remarkably low with this feed) is about 5 % in the PBMR (Figure 5.11b) and 3 % in the PBR (Figure 5.11c). Furthermore, DME yield is greater in the PBMR at the conditions where DME yield is maximal (high temperature) and $H_2 + CO$ feed (H_2 / CO_x = 0). DME yield at these conditions achieves a 30 % in the PBMR and 22 % in the PBR. A slight difference can be observed on the temperature corresponding to DME maximal yield that is within 340 - 350 °C range in the PBMR and 330 - 340 °C in the PBR.

5.4.1.2 Methanol yield

The production of methanol as byproduct is very important for the process economy, either due to its commercial interest or for being valorized through dehydration towards DME. As shown in Figure 5.12 methanol yield is significantly low, but it is higher in the PBMR (practically double than in the PBR) within the whole studied range of conditions. The maximal methanol yield is achieved at a determined temperature and CO_2 / CO_x ratio, which are around 340 °C and a CO_2 / CO_x ratio = 30 % for the PBMR (Figure 5.12b), and 330 °C and 30 % for the PBR. The values of these methanol yields peaks are 3 % and 1.8 %, respectively.

5.4.1.3 Oxygenates yield

Figure 5.13 shows the comparison of the oxygenates (methanol + DME) yield and encompasses what was previously described in Figures 5.11 and 5.12, being the optimal conditions those previously established for maximizing DME yield (high temperature and feed without CO_2), with values of 34 % for the PBMR (Figure 5.13b) and 24 % of oxygenates yield for the PBR (Figure 5.13c).

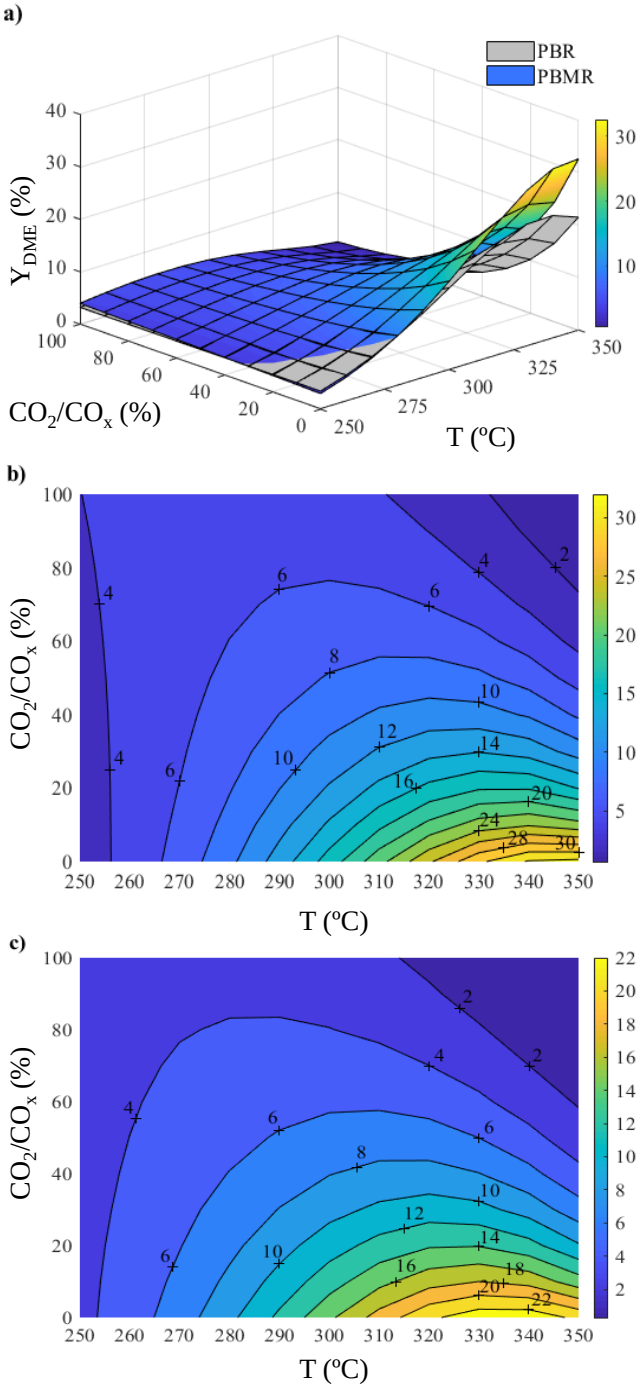

Figure 5.11: DME yield for PBR vs PBMR (a) and contour maps for PBMR (b), and PBR (c). Reaction conditions: feed, $H_2 + CO + CO_2$; 30 bar, space time, 5 $g_{cat}\,h\,(mol_C)^{-1}$; $H_2\,/\,CO_x$, 3; time on stream, 1 h.

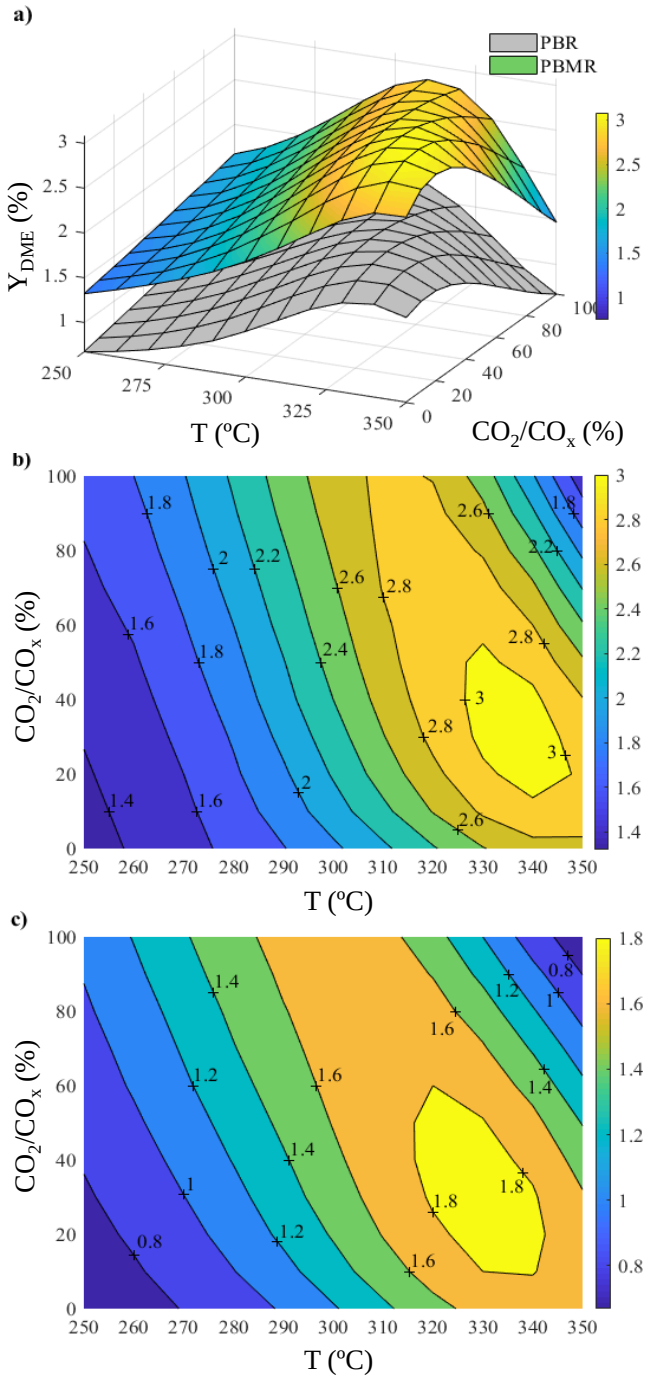

Figure 5.12: Methanol yield for PBR vs PBMR (a) and contour maps for PBMR (b), and PBR (c). Reaction conditions: feed, $H_2 + CO + CO_2$; 30 bar, space time, 5 g_{cat} h $(mol_C)^{-1}$; H_2 / CO_x, 3; time on stream, 1 h.

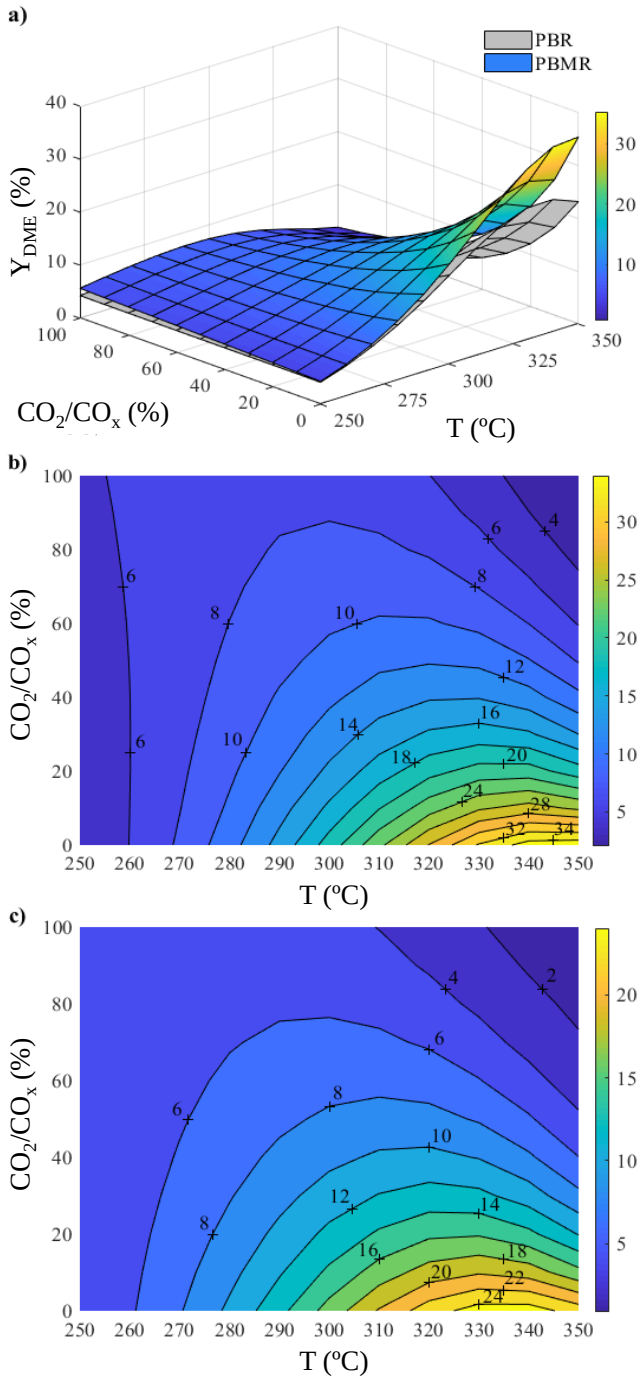

Figure 5.13: Oxygenates (methanol + DME) yield for PBR vs PBMR (a) and contour maps for PBMR (b), and PBR (c). Reaction conditions: feed, $H_2 + CO + CO_2$; 30 bar, space time, 5 g_{cat} h $(mol_C)^{-1}$; H_2 / CO_x, 3; time on stream, 1 h.

5.4.2 Scale-up study

The effect of two factors, like the reactor geometry and space time, is analyzed as a previous study of the possibilities that the simulation model for the scale-up offers, as well as the perspectives provided by this sizing. In addition, the capacity of the model to quantify the concentration of each component in the reaction medium is illustrated.

5.4.2.1 Concentration profiles

As an example of the PBMR simulation model capacity, its performance has been studied for greater dimensions than the experimental system: L = 1 m and D = 4 cm, and at the following reaction conditions: 30 bar; 275 °C; space time, 100 $g_{cat}\,h\,(mol_C)^{-1}$; feed, $H_2 + CO + CO_2$; $CO_2\,/\,CO_x$, 0.5; sweep strategy, same concentration as the feed and co-current mode; time on stream, 1 h. It should be pointed out that besides being greater the reactor dimensions and the L / D ratio in the example, the space time is also notably higher than the one used in the experiments in the lab-scale reactor and simulation.

The longitudinal profiles of the molar concentration (in %) of the components in the reaction and permeate sections are depicted in Figure 5.14, on their way downwards through the reactor. H_2 excess can be observed in the permeate, as well as its consumption with the reaction proceeding downward. CO, in excess in the permeate section, is remarkably consumed in the reaction zone, where CO_2 and H_2O concentrations rise with the longitudinal position of the reactor.

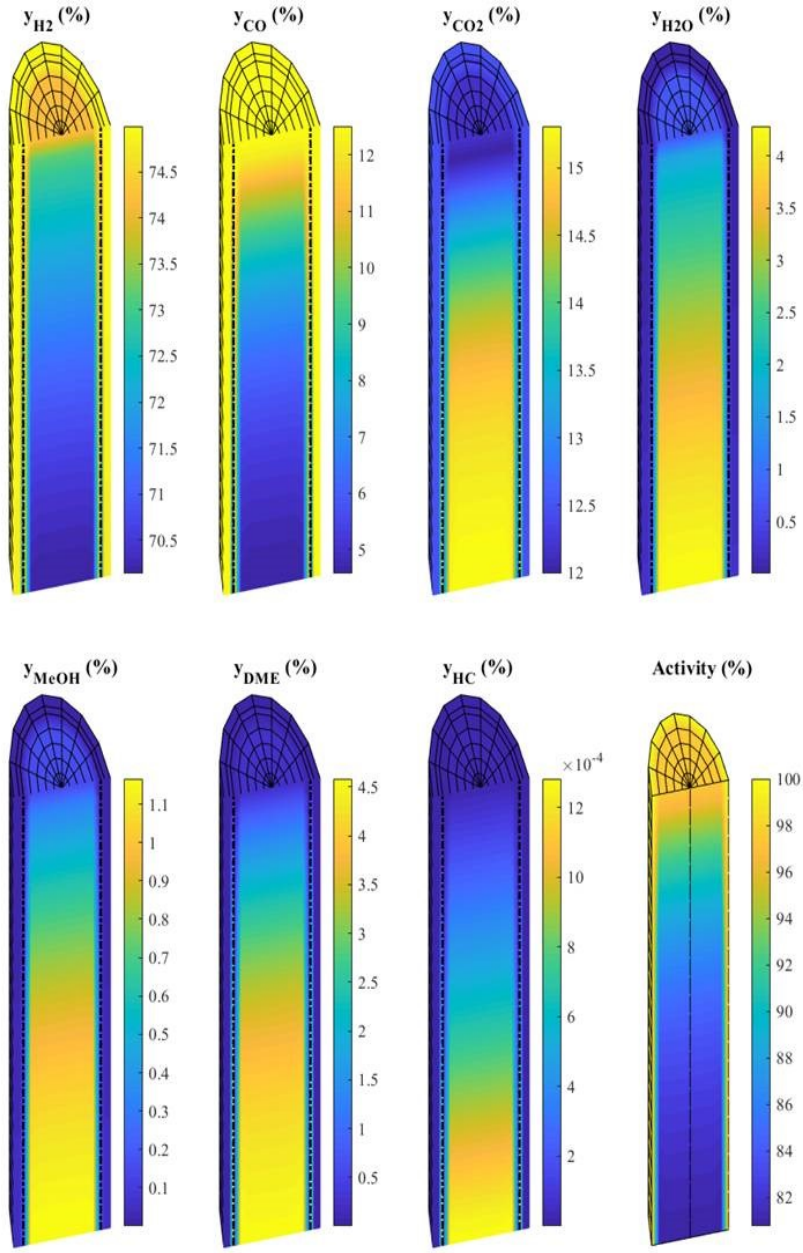

Figure 5.14: Evolution of the concentrations of the components (%) of the reaction medium with the longitudinal position (on their way downwards to the reactor outlet) in the reaction and permeate sections, for a PBMR and at the following conditions: feed, $H_2 + CO + CO_2$; 275 °C; 30 bar, space time, 100 g_{cat} h $(mol_C)^{-1}$; H_2 / CO_x, 3; CO_2 / CO_x, 0.5; TOS, 1 h.

In Figure 5.14 (bottom profiles) are shown the progressive increment with the longitudinal position of methanol, DME and hydrocarbons concentrations. The activity profile predicted by the model decreases towards the reactor outlet as the concentration of coke precursors in the kinetic model (methanol and DME) increases, according to the established hypothesis of coke formation being dependent on the oxygenates in the reaction medium (Section 3.4.1)

Attending to these results depicted in Figure 5.14, CO_2 concentration at the reactor outlet will be higher than in the inlet. Therefore, these conditions are not suitable for a CO_2 negative balance, being its concentration in the feed of 12.5 % (H_2 / CO_x ratio is 3 and CO_2 / CO_x ratio 0.5 in this simulation) and 15.5 % at the outlet. The model allows to establish the conditions for CO_2 conversion (although at the expense of a diminishing oxygenates yield). Thus, Figure 5.15 shows, with the same reactor dimensions, the longitudinal profiles of CO_2 composition at different experimental conditions. In Figure 5.15a it is depicted the profile corresponding to a lower space time (10 g_{cat} h $(mol_C)^{-1}$) and for the same CO_2 / CO_x ratio in the feed as in Figure 5.14 (thus, 0.5). In this case, a different evolution of the concentration can be observed. In the first half of the reactor CO_2 concentration decreases and, conversely, it rises when approching the outlet. Despite this increment at the reactor exit, globally analyzing CO_2 concentration (around 12.4 %) at the reactor outlet, it is slightly less than at the inlet, resulting CO_2 conversion, albeit being small, positive.

Figure 5.15b shows the evolution of CO_2 conversion with the same space time as in Figure 5.14, but feeding a higher CO_2 / CO_x ratio (equal to 1), knowing that this parameter is key in CO_2 conversion. Comparing both profiles, with the higher CO_2 concentration in the feed (Figure 5.15b), a descending longitudinal profile through the reactor is shown. It decreases from the fed 25 % to 20 % at the reactor outlet,

resulting in values remarkably higher of CO_2 conversion than with the strategy in Figure 5.14 or even in Figure 5.15a. Theses comparisons seek to demonstrate the sensibility of the simulation against the operation conditions, such as CO_2 concentration in the feed, which influence on products distribution, hence on oxygenates yields and the final value of CO_2 conversion.

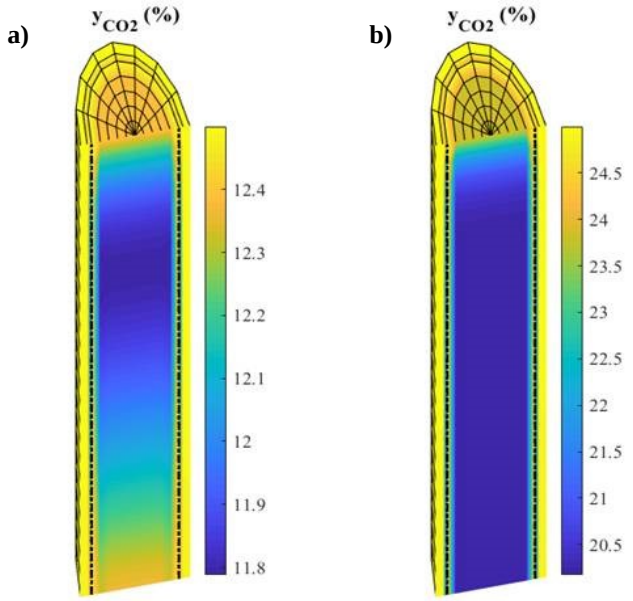

Figure 5.15: Evolution of CO_2 concentration with the longitudinal position (on their way downwards to the reactor outlet) in the reaction and permeate sections, for a PBMR and at the conditions of Figure 5.14, and space time of 10 $g_{cat}\,h\,(mol_C)^{-1}$ (a); and $CO_2\,/\,CO_x$, 1 (b).

5.4.2.2 DME yield and CO_2 conversion

As an example of the possibilities of the PBMR model to progress towards an optimal development of the PBMR technology, the effect of space time on DME yield (Figure 5.16a) and on CO_2 conversion (Figure 5.16b) has been also applied, maintaining in this case the geometry (L / D ratio) of the experimental reactor. It shows

how the increase in space time, regarding the highest value used in the experiments (10 $g_{cat}\,h\,(mol_C)^{-1}$), allows rising notably DME yield, for different values of $CO_2\,/\,CO_x$ ratio (Figure 5.16a). Furthermore, it is remarkable that increasing the space time the advantage of PBMR (continuous lines) with respect of PBR (dashed lines) is greater.

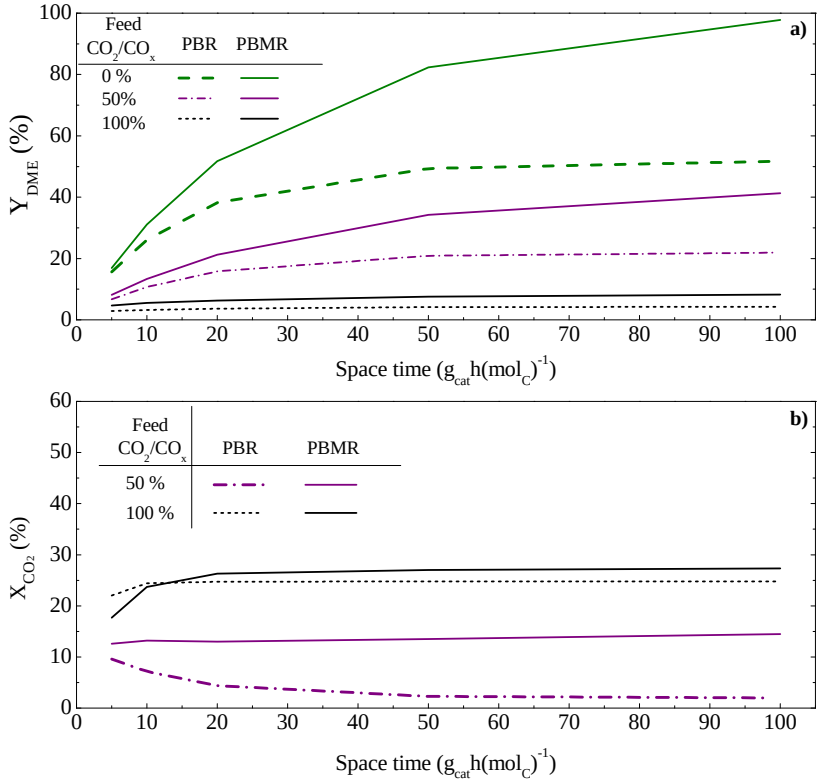

Figure 5.16: Evolution of DME yield (a) and CO_2 conversion (b) with space time calculated by simulation for the PBMR and PBR, for different values of $CO_2\,/\,CO_x$ ratio. Reaction conditions: 330 °C; 30 bar; $H_2\,/\,CO_x$, 3.

The enhancement in DME yield that is predicted by the model is a consequence of the alteration of the thermodynamic equilibrium that leads to a pseudo-equilibrium state, which will be characteristic of the applied membrane. This greater "per

pass" DME yield with a higher space time has a significant impact on the reaction economy, since it will allow to reduce the recirculation of the unreacted gases until achieving an optimal DME yield.

Nevertheless, the increase of space time above 10 g_{cat} h $(mol_C)^{-1}$ enhances slightly CO_2 conversion for CO_2 / CO_x feeds ratios of 0.5 and 1 (Figure 5.16b).

VI

6

CONCLUSIONS

6 | Conclusions

As a result of this thesis the following conclusions can be extracted, selected for their contribution to the knowledge and technological development of the DME direct synthesis process, or for their interest in the future evolution of the research line.

Membrane selection and its implementation in the reactor

Linde Type A (LTA) zeolite shows favorable conditions for the physical configuration of the membrane reactor, considering that it can be crystallized, in a reproducible manner and with a relatively simple procedure, on a metallic support at the established conditions. Employing this method, the membrane acquires the required mechanical resistance for its use at high reaction pressure and temperature. The hydrophilicity of LTA justifies its H_2O permselectivity, considerably higher than of the other alternative zeolites (LTX and SOD). H_2O permeation at 275 °C is 4.63 $\mathrm{mol\,m^{-2}\,s^{-1}\,Pa^{-1}}$ and the perm-selectivity of H_2O / DME is 40 % greater than of H_2O / H_2 and H_2O / CO.

Membrane reactor performance

The thermodynamic advantages of the membrane reactor enable achieving higher

conversions than those predicted by the thermodynamic equilibrium for a PBR, corresponding to a pseudo-equilibrium state, whose conversion also diminishes increasing the temperature. This alteration of the equilibrium (established for PBR) allows achieving a DME yield of 14.8 % at 300 °C, co-feeding CO_2 with synthesis gas (CO_2 / CO_x ratio = 0.5), under not severe conditions (30 bar; space time, 10 $g_{cat}h(mol_C)^{-1}$; H_2 / ($CO + CO_2$), 3) and a slow deactivation. Furthermore, CO_2 conversion at these conditions is about 14 %. For a relatively low temperature, 275 °C, are remarkable the DME yield and CO_2 conversion (11 and 12 %, respectively), the negligible paraffins formation and the very slow deactivation.

The temperature of 275 °C is also suitable for $H_2 + CO_2$ feeds obtaining under 40 bar and a space time of 10 $g_{cat}h(mol_C)^{-1}$, a DME yield of 12 % and a CO_2 conversion of around 20 %, without the formation of paraffins and a great catalyst stability. At this temperature, the increase of the pressure in the 10 - 40 bar range, gives rise to a practically linear increment of DME yield and CO_2 conversion, both for $H_2 + CO + CO_2$ and $H_2 + CO_2$ feeds. For this latter, it is more relevant the conversion of CO_2 and it is, at the same time, remarkable the stability of the catalyst within the whole range of pressures.

Kinetic modeling

The hybrid catalyst formed by the functions CuO-ZnO-ZrO_2 and SAPO-11 has been proven to be active, selective towards DME formation and stable. Its performance has been quantified with a kinetic model that fits the experimental results in a wide temperature range (250 - 350 °C), pressures (until 40 bar), CO_2 / CO_x ratios in the feed and with time on stream. The model considers the kinetic equations of the individual reaction steps and the effect of CO_2 and H_2O adsorption in order to attenuate the rate of WGS and methanol synthesis reactions, respectively. The de-

activation kinetics is quantified by a expression dependent on methanol and DME concentration in the reaction medium, being this kinetics also attenuated by CO_2 and H_2O adsorption.

Membrane reactor modeling

The proposed original model design for the PBMR, combining both the equations of components transport from the reaction medium to the permeate section and the kinetic model, and employing the experimentally determined transport and kinetic parameters, enables to predict the compositions of both the reaction and permeate sections and their evolution with time within a wide range of conditions. Additionally, allows calculating the effect of the parameters required in scale-up studies, such as space time or the reactor dimensions (that affect the membrane surface per reactor unite volume).

The advantages of the membrane reactor and optimal conditions

The PBMR allows obtaining a great DME yield at higher temperature and space time than in the PBR, due to the less restrictive thermodynamic limitations.

Within the range of conditions that have been experimentally proven, with a space time up to 10 $g_{cat}h(mol_C)^{-1}$, the simulation program predicts a greater DME yield with the PBMR. The enhancement varies from a 66 % (3 % with the PBR and 5 % with the PBMR), at conditions where DME yield is relatively low (300 °C and CO_2/CO_x ratio = 1), to a 36 % (22 % and 30 % respectively) under conditions where DME yield is high (325 - 350 °C and CO_2/CO_x ratio = 0). Similarly, methanol yield is greater with the PBMR (approximately the double under all the conditions), with a maximal value of 3 % at 330 °C and CO_2/CO_x ratio = 0.3.

The simulation predicts a notable rise in the oxygenates yield increasing the space

time above the experimentally studied one, and also a greater difference of this yield with respect to the PBR. The highest DME yield obtained in one-pass will lead to a remarkable economical advantage, being required a less intensive recirculation of non-reacting gases.

Recommendations for future works

Although the performance of an inorganic membrane at temperatures up to 350 °C, and additionally for a reaction system with oxygenates and water, is an important milestone of this Thesis, it should be assumed that the improvements achieved by the membrane reactor are limited by the properties of the membrane. Consequently, the first enhancement initiative should be the preparation of new zeolite membranes with higher H_2O perm-selectivity.

Moreover, it will be interesting to study different sweep alternatives in the permeate section, as well as the simulation of the recirculation, in order to enhance the oxygenates yield or the conversion of CO_2.

On the other hand, the alteration of the thermodynamic equilibrium with the membrane reactor rises the limit working temperature of DME synthesis. The results of this work emphasizes the potential interest of a catalyst without sintering issues at 350 °C and even higher temperatures. Consequently, it requires to continue improving in the synthesis of new catalysts, prepared with a metallic function (for methanol synthesis) without Cu in its composition.

NOMENCLATURE

Nomenclature

a	Activity
C / H, C / O	Molar ratio of carbon / hydrogen and carbon / hydrogen
CO_2 / CO_x	Ratio between CO_2 and ($CO + CO_2$) in the feed
D	Reactor diameter
D_e	Diffusion of effective coefficient, $m^2 s^{-1}$
d_p	Mean pore diameter
E_j	Activation energy of j step, kJ mol^{-1}
F, $F_{1-\alpha}$	Fisher distribution and critical value
f_i	Fugacity of i component, atm
H_2 / CO_x	Ratio between H_2 and ($CO + CO_2$) in the feed
H / O	Molar ratio of hydrogen / oxygen
$K_{ad,i}$, $K^*_{ad,i}$	Adsorption equilibrium constant of i component and corresponding value at reference temperature
K_i	Equilibrium constant of j reaction step
K	Constant in the Kozeny-Carman equation
k_j, k^*_j	Kinetic constant of j step and corresponding value at reference temperature
L	Length of the catalytic bed, m
l	Longitudinal position in the reactor, m

$n_{e,0}$, $n_{e,d}$	Number of experimental data used in the first and second term of the objective error function
O.F.	Objective function
P, P^r, P^p	Pressure, and pressure in the reaction and permeate sections, respectively
p_i	Partial pressure of i component in the rection medium
Q	Permeate flux of the membrane, $kg\,m^{-2}\,h^{-1}$
R	Universal constant of gases, $KJ\,(mol\,K)^{-1}$
r_d	Deactivation rate
r_i, $r_{i,0}$	Formation rate of i component at t time and zero time, $(mol_i)_C\,(g_{cat}h)^{-1}$
r_j	Reaction rate of j step, $(mol_i)_C\,(g_{cat}h)^{-1}$
$\mathbf{r}_L$	Vector of the formation velocities
s^2_{aj}, s^2_{exp}	Variance for the lack of fitting and the experimental error
S_i	Selectivity of i component
S_{BET}	BET specific surface, m^2g^{-1}
SSE	Sum of the square errors
S_i	Source term of i component
T, T^*	Temperature and reference temperature, K
t	Time, h
V_{micro}, V_{meso}	Micropores and mesopores volume, cm^3g^{-1}
v	Gas linear velocity, $m\,s^{-1}$
W	Mass of the catalyst, g
X_{CO_2}, X_{CO_x}	Conversion of CO_2 and CO_x
Y_i	Yield of i component
y_i	Molar fraction of i component
$(y_{i,j})_0$, $(y_{i,j})_d$	Values of the molar fraction of i component with the model zero and t time

$(\bar{y}^*_{i,j})_0$, $(\bar{y}^*_{i,j})_d$	Average experimental values of the molar fraction of i component at zero and t time, at reference temperature
$(\bar{y}_{i,j})_0$, $(\bar{y}_{i,j})_d$	Average experimental values of the molar fraction of i component at zero and t time

Greek letters

α	Separation factor of the membrane
β	Reaction rate of the formation of hydrocarbons
$\Delta \mathbf{H}^0_{ad,i}$	Adsorption enthalpy of i component
ΔP	Pressure drop, bar
ε_b	Bed porosity
ν_{aj},ν_{exp}	Degrees of freedom of the fitting and the experimental error
ν_a, ν_b	Degrees of freedom of a and b models
ω_i	Weight factor of i component
Ψ	Deactivation function
ρ_b	Bed density, kg m^{-3}
$(\upsilon_i)_j$	Stoichiometric coefficient of i component in j step of the kinetic scheme

Acronyms and Abbreviations

ATR	Autothermal reforming of methane
BET	Brunauer, Emmett and Teller
BTX	Benzene, toluene and xylenes
CCS	Carbon capture and storage technologies
CCU	Carbon capture and utilization technologies
CCUS	Carbon capture, utilization and storage technologies
CTM	Carbon to methanol
DME	Dimethyl ether
DRM	Dry reforming of methane

DSC	Differential scanning calorimetry
DTG, DTO	Dimethyl ether to gasoline (and derivative thermogravimetry), and dimethyl ether to olefins
EDX	Energy dispersive X-ray analysis
GC / MS	Gas chromatography / Mass spectrometry
GTM	Natural gas to methanol
HC	Hydrocarbons and heteropolyacids
HC	Hydrocarbons
ICP-OES	Inductively coupled plasma optical emission spectroscopy
LPG	Liquified petroleum gas
LTA	Linde Type A zeolite
LTX	Linde Type X zeolite
MeOH	Methanol
Micro-GC	Gas micro-chromatograph
MOR	Mordenite zeolite
MTD	Methanol to DME
MTG	Methanol to gasoline
MTO	Methanol to olefins
MTP	Methanol to propylene
PBMR	Packed bed membrane reactor
PBR	Packed bed reactor
POM	Partial oxidation of methane
PS	Permeate section
RS	Reaction section
rWGS, WGS	Reverse water gas shift and water gas shift reaction
SEM	Scanning electron microscopy
SOD	Sodalite zeolite

SRM	Steam reforming of methane
STD	DME direct synthesis from synthesis gas
TGA	Thermogravimetric analysis
TOS	Time on stream
TPD	Temperature programmed desorption
TPO	Temperature programmed oxidation
TPR	Temperature programmed reduction
XRD	X-ray Diffraction

REFERENCES

References

Abashar, M. E. E. and Al-Rabiah, A. A. (2018). Investigation of the efficiency of sorption-enhanced methanol synthesis process in circulating fast fluidized bed reactors. *Fuel Processing Technology*, 179:387–398.

Abu-Dahrieh, J., Rooney, D., Goguet, A., and Saih, Y. (2012). Activity and deactivation studies for direct dimethyl ether synthesis using CuO–ZnO–Al_2O_3 with NH_4ZSM-5, HZSM-5 or γ-Al_2O_3. *Chemical Engineering Journal*, 203:201–211.

Agrell, J., Birgersson, H., Boutonnet, M., Melián-Cabrera, I., Navarro, R. M., and Fierro, J. L. G. (2003). Production of hydrogen from methanol over Cu/ZnO catalysts promoted by ZrO_2 and Al_2O_3. *Journal of Catalysis*, 219(2):389–403.

Aguayo, A. T., Ereña, J., Mier, D., Arandes, J. M., Olazar, M., and Bilbao, J. (2007). Kinetic modeling of dimethyl ether synthesis in a single step on a CuO-ZnO-Al_2O_3/γ-Al_2O_3 catalyst. *Industrial & Engineering Chemistry Research*, 46(17):5522–5530.

Aguayo, A. T., Ereña, J., Sierra, I., Olazar, M., and Bilbao, J. (2005). Deactivation and regeneration of hybrid catalysts in the single-step synthesis of dimethyl ether from syngas and CO_2. *Catalysis Today*, 106(1-4):265–270.

Al-Dughaither, A. S. and de Lasa, H. (2014). Neat dimethyl ether conversion to olefins (DTO) over HZSM-5: Effect of SiO_2/Al_2O_3 on porosity, surface chemistry, and reactivity. *Fuel*, 138:52–64.

Alavi, M., Hamedi, N., and Rahimpour, M. R. (2018). Modeling of the dimethyl ether production reactors. In *Methanol*, pages 573 – 591.

Alharbi, W., Kozhevnikova, E., and Kozhevnikov, I. (2015). Dehydration of methanol to dimethyl ether over heteropoly acid catalysts: The relationship between reaction rate and catalyst acid strength. *ACS Catalysis*, 5(12):7186–7193.

Alper, E. and Orhan, O. Y. (2017). CO_2 utilization: Developments in conversion processes. *Petroleum*, 3(1):109–126.

An, W., Chuang, K. T., and Sanger, A. R. (2004). Dehydration of methanol to dimethyl ether by catalytic distillation. *The Canadian Journal of Chemical Engineering*, 82(5):948–955.

An, X., Zuo, Y. Z., Zhang, Q., Wang, D. Z., and Wang, J. F. (2008). Dimethyl ether synthesis from CO_2 hydrogenation on a $CuO-ZnO-Al_2O_3-ZrO_2$/HZSM-5 bifunctional catalyst. *Industrial & Engineering Chemistry Research*, 47(17):6547–6554.

Arcoumanis, C., Bae, C., Crookes, R., and Kinoshita, E. (2008). The potential of dimethyl ether (DME) as an alternative fuel for compression-ignition engines: A review. *Fuel*, 87(7):1014–1030.

Arena, F., Barbera, K., Italiano, G., Bonura, G., Spadaro, L., and Frusteri, F. (2007). Synthesis, characterization and activity pattern of Cu–ZnO/ZrO_2 catalysts in the hydrogenation of carbon dioxide to methanol. *Journal of Catalysis*, 249(2):185–194.

Arena, F., Italiano, G., Barbera, K., Bonura, G., Spadaro, L., and Frusteri, F. (2009). Basic evidences for methanol-synthesis catalyst design. *Catalysis Today*, 143(1):80–85.

Arena, F., Italiano, G., Barbera, K., Bordiga, S., Bonura, G., Spadaro, L., and Frusteri, F. (2008). Solid-state interactions, adsorption sites and functionality of Cu-ZnO/ZrO_2 catalysts in the CO_2 hydrogenation to CH_3OH. *Applied Catalysis A: General*, 350(1):16–23.

Aresta, M., Dibenedetto, A., and Pastore, C. (2005). Biotechnology to develop innovative syntheses using CO_2. *Environmental Chemistry Letters*, 3(3):113–117.

Aresta, M., Dibenedetto, A., and Quaranta, E. (2016). Carbon dioxide conversion in high temperature reactions. In *Reaction Mechanisms in Carbon Dioxide Conversion*, pages 237–310.

Ateka, A. (2014). *Innovaciones en el proceso de síntesis de dimetil éter en una etapa con secuestro de CO_2*. PhD thesis, University of the Basque Country, UPV/EHU, Bilbao.

Ateka, A., Ereña, J., Bilbao, J., and Aguayo, A. T. (2018a). Kinetic modeling of the direct synthesis of dimethyl ether over a CuO-ZnO-MnO/SAPO-18 catalyst and assessment of the CO_2 conversion. *Fuel Processing Technology*, 181:233–243.

Ateka, A., Ereña, J., Pérez-Uriarte, P., Aguayo, A. T., and Bilbao, J. (2017a). Effect of the content of CO_2 and H_2 in the feed on the conversion of CO2 in the direct synthesis of dimethyl ether over a CuOZnOAl_2O_3/SAPO-18 catalyst. *International Journal of Hydrogen Energy*, 42(44):27130–27138.

Ateka, A., Ereña, J., Sánchez-Contador, M., Pérez-Uriarte, P., Bilbao, J., and Aguayo, A. T. (2018b). Capability of the direct dimethyl ether synthesis process for the conversion of carbon dioxide. *Applied Sciences*, 8(5):677.

Ateka, A., Pérez-Uriarte, P., Gamero, M., Ereña, J., Aguayo, A. T., and Bilbao, J. (2017b). A comparative thermodynamic study on the CO_2 conversion in the synthesis of methanol and of DME. *Energy*, 120:796–804.

Ateka, A., Pérez-Uriarte, P., Sánchez-Contador, M., Ereña, J., Aguayo, A. T., and Bilbao, J. (2016a). Direct synthesis of dimethyl ether from syngas on CuO-ZnO-MnO/SAPO-18 bifunctional catalyst. *International Journal of Hydrogen Energy*, 41(40):18015–18026.

Ateka, A., Sierra, I., Ereña, J., Bilbao, J., and Aguayo, A. T. (2016b). Performance of CuO-ZnO-ZrO_2 and CuO-ZnO-MnO as metallic functions and SAPO-18 as

acid function of the catalyst for the synthesis of DME co-feeding CO_2. *Fuel Processing Technology*, 152:34–45.

Awayssa, O., Al-Yassir, N., Aitani, A., and Al-Khattaf, S. (2014). Modified HZSM-5 as FCC additive for enhancing light olefins yield from catalytic cracking of VGO. *Applied Catalysis A: General*, 477:172 – 183.

Azizi, Z., Rezaeimanesh, M., Tohidian, T., and Rahimpour, M. R. (2014). Dimethyl ether: A review of technologies and production challenges. *Chemical Engineering and Processing: Process Intensification*, 82:150–172.

Badmaev, S. D., Volkova, G. G., Belyaev, V. D., and Sobyanin, V. A. (2007). Steam reforming of dimethyl ether to hydrogen-rich gas. *Reaction Kinetics and Catalysis Letters*, 90(1):205–211.

Bae, J. W., Potdar, H. S., Kang, S. H., and Jun, K. W. (2008). Coproduction of Methanol and Dimethyl Ether from Biomass-Derived Syngas on a $Cu-ZnO-Al_2O_3/\gamma$-Al_2O_3 Hybrid Catalyst. *Energy & Fuels*, 22(1):223–230.

Ballivet-Tkatchenko, D., dos Santos, J. H. Z., Philippot, K., and Vasireddy, S. (2011). Carbon dioxide conversion to dimethyl carbonate: The effect of silica as support for SnO_2 and ZrO_2 catalysts. *Comptes Rendus Chimie*, 14(7–8):780–785.

Ban, H., Li, C., Asami, K., and Fujimoto, K. (2014). Influence of rare-earth elements (La, Ce, Nd and Pr) on the performance of Cu/Zn/Zr catalyst for CH_3OH synthesis from CO_2. *Catalysis Communications*, 54:50–54.

Bayat, M., Dehghani, Z., and Rahimpour, M. R. (2014). Membrane/sorption-enhanced methanol synthesis process: Dynamic simulation and optimization. *Journal of Industrial and Engineering Chemistry*, 20(5):3256–3269.

Bedard, R. and Liu, C. (2018). Recent Advances in zeolitic membranes. *Annual Review of Materials Research*, 48(1):83–110.

Behrens, M., Studt, F., Kasatkin, I., Kühl, S., Hävecker, M., Abild-Pedersen, F., Zander, S., Girgsdies, F., Kurr, P., and Kniep, B. L. (2012). The active

site of methanol synthesis over $Cu/ZnO/Al_2O_3$ industrial catalysts. *Science*, 336(6083):893–897.

Beranek, L., Setínek, K., and Kraus, M. (1972). Kinetics and adsorption on acid catalysts. III. Structure effects in reesterification of esters with alcohols. *Collection of Czechoslovak Chemical Communications*, 37(7):2265–2268.

Bercic, G. and Levec, J. (1992). Intrinsic and global reaction rate of methanol dehydration over γ-Al_2O_3 pellets. *Industrial & Engineering Chemistry Research*, 31(4):1035–1040.

Bercic, G. and Levec, J. (1993). Catalytic dehydration of methanol to dimethyl ether. Kinetic investigation and reactor simulation. *Industrial & engineering chemistry research*, 32(11):2478–2484.

Bhattacharya, S., Kabir, K. B., and Hein, K. (2013). Dimethyl ether synthesis from Victorian brown coal through gasification - Current status, and research and development needs. *Progress in Energy and Combustion Science*, 39(6):577–605.

Bjørgen, M., Olsbye, U., Petersen, D., and Kolboe, S. (2004). The methanol-to-hydrocarbons reaction: insight into the reaction mechanism from [12C]benzene and [13C]methanol co-reactions over zeolite H-beta. *Journal of Catalysis*, 221(1):1–10.

Bonura, G., Arena, F., Mezzatesta, G., Cannilla, C., Spadaro, L., and Frusteri, F. (2011). Role of the ceria promoter and carrier on the functionality of Cu-based catalysts in the CO_2-to-methanol hydrogenation reaction. *Catalysis Today*, 171(1):251–256.

Bonura, G., Frusteri, F., Cannilla, C., Ferrante, G. D., Aloise, A., Catizzone, E., Migliori, M., and Giordano, G. (2016). Catalytic features of CuZnZr–zeolite hybrid systems for the direct CO_2-to-DME hydrogenation reaction. *Catalysis Today*, 277:48–54.

Bozzano, G. and Manenti, F. (2016). Efficient methanol synthesis: Perspectives, technologies and optimization strategies. *Progress in energy and combustion science*, 56:71 – 105.

Bradford, M. C. J. and Vannice, M. A. (1999). CO_2 reforming of CH_4. *Catalysis Reviews*, 41(1):1–42.

Burch, R., Goguet, A., and Meunier, F. C. (2011). A critical analysis of the experimental evidence for and against a formate mechanism for high activity water-gas shift catalysts. *Applied Catalysis A: General*, 409:3–12.

Burri, D. R., Choi, K. M., Lee, J. H., Han, D. S., and Park, S. E. (2007). Influence of SBA-15 support on CeO_2–ZrO_2 catalyst for the dehydrogenation of ethylbenzene to styrene with CO_2. *Catalysis Communications*, 8(1):43–48.

Cai, M., Palčić, A., Subramanian, V., Moldovan, S., Ersen, O., Valtchev, V., Ordomsky, V. V., and Khodakov, A. Y. (2016). Direct dimethyl ether synthesis from syngas on copper-zeolite hybrid catalysts with a wide range of zeolite particle sizes. *Journal of Catalysis*, 338:227–238.

Carlos Colmenares, J. (2010). Novel trends in the utilization of CO_2 as a reagent and mild oxidant in the CC Coupling Reactions. *Current Organic Synthesis*, 7(6):533–542.

Castro, A., Soares, J., Josue Filho, M., Oliveira, A., Campos, A., and Milet, E. (2013). Oxidative dehydrogenation of ethylbenzene with CO_2 for styrene production over porous iron-based catalysts. *Fuel*, 108:740–748.

Catizzone, E., Aloise, A., Migliori, M., and Giordano, G. (2017a). From 1-D to 3-D zeolite structures: performance assessment in catalysis of vapour-phase methanol dehydration to DME. *Microporous and Mesoporous Materials*, 243:102–111.

Catizzone, E., Aloise, A., Migliori, M., and Giordano, G. (2017b). The effect of FER zeolite acid sites in methanol-to-dimethyl-ether catalytic dehydration. *Journal of Energy Chemistry*, 26(3):406–415.

Catizzone, E., Bonura, G., Migliori, M., Frusteri, F., and Giordano, G. (2017c). CO_2 recycling to dimethyl ether: State-of-the-art and perspectives. *Molecules*, 23(1):31.

Chang, T., Rousseau, R. W., and Kilpatrick, P. K. (1986). Methanol synthesis reactions: calculations of equilibrium conversions using equations of state. *Industrial & Engineering Chemistry Process Design and Development*, 25(2):477–481.

Chen, C. S., Wu, J. H., and Lai, T. W. (2010). Carbon dioxide hydrogenation on Cu nanoparticles. *The Journal of Physical Chemistry C*, 114(35):15021–15028.

Chen, H. J., Fan, C. W., and Yu, C. S. (2013). Analysis, synthesis, and design of a one-step dimethyl ether production via a thermodynamic approach. *Applied Energy*, 101:449–456.

Chen, P., Gupta, P., Dudukovic, M. P., and Toseland, B. A. (2006). Hydrodynamics of slurry bubble column during dimethyl ether (DME) synthesis: Gas–liquid recirculation model and radioactive tracer studies. *Chemical Engineering Science*, 61(19):6553–6570.

Chen, Q., Lu, M., Tang, Z., Wang, H., Wei, W., and Sun, Y. (2016a). Opportunities of integrated systems with CO_2 utilization technologies for green fuel & chemicals production in a carbon-constrained society. *Journal of CO_2 Utilization*, 14:1–9.

Chen, W. H., Hsu, C. L., and Wang, X. D. (2016b). Thermodynamic approach and comparison of two-step and single step DME (dimethyl ether) syntheses with carbon dioxide utilization. *Energy*, 109:326–340.

Chen, Z., Li, X., Xu, Y., Dong, Y., Lai, W., Fang, W., and Yi, X. (2018). Fabrication of nano-sized SAPO-11 crystals with enhanced dehydration of methanol to dimethyl ether. *Catalysis Communications*, 103:1–4.

Coley, D. A. (1999). *An introduction to genetic algorithms for scientists and engineers*. World Scientific Publishing Company.

Cordero-Lanzac, T., Aguayo, A. T., Gayubo, A. G., Castaño, P., and Bilbao, J. (2018). Simultaneous modeling of the kinetics for n-pentane cracking and the deactivation of a HZSM-5 based catalyst. *Chemical Engineering Journal*, 331:818–830.

Corma, A. (1995). Inorganic solid acids and their use in acid-catalyzed hydrocarbon reactions. *Chemical Reviews*, 95(3):559–614.

Corma, A., Fornés, V., Guil, J. M., Pergher, S., Maesen, T. L. M., and Buglass, J. G. (2000). Preparation, characterisation and catalytic activity of ITQ-2, a delaminated zeolite. *Microporous and Mesoporous Materials*, 38(2):301–309.

Dadgar, F., Myrstad, R., Pfeifer, P., Holmen, A., and Venvik, H. J. (2016). Direct dimethyl ether synthesis from synthesis gas: The influence of methanol dehydration on methanol synthesis reaction. *Catalysis Today*, 270:76–84.

Dahl, I. M. and Kolboe, S. (1993). On the reaction mechanism for propene formation in the MTO reaction over SAPO-34. *Catalysis Letters*, 20(3):329–336.

Dahl, I. M. and Kolboe, S. (1994). On the Reaction Mechanism for Hydrocarbon Formation from Methanol over SAPO-34: I. Isotopic Labeling Studies of the Co-Reaction of Ethene and Methanol. *Journal of Catalysis*, 149(2):458 – 464.

Dai, W., Kong, W., Wu, G., Li, N., Li, L., and Guan, N. (2011). Catalytic dehydration of methanol to dimethyl ether over aluminophosphate and silicoaluminophosphate molecular sieves. *Catalysis Communications*, 12(6):535–538.

Dai, Z., Middleton, R., Viswanathan, H., Fessenden-Rahn, J., Bauman, J., Pawar, R., Lee, S. Y., and McPherson, B. (2013). An integrated framework for optimizing CO_2 sequestration and enhanced oil recovery. *Environmental Science & Technology Letters*, 1(1):49–54.

De Falco, M., Capocelli, M., and Basile, A. (2017a). Selective membrane application for the industrial one-step DME production process fed by CO_2 rich streams: Modeling and simulation. *International Journal of Hydrogen Energy*, 42(10):6771–6786.

De Falco, M., Capocelli, M., and Centi, G. (2016). Dimethyl ether production from CO_2 rich feedstocks in a one-step process: Thermodynamic evaluation and reactor simulation. *Chemical Engineering Journal*, 294:400–409.

De Falco, M., Capocelli, M., and Giannattasio, A. (2017b). Membrane Reactor for one-step DME synthesis process: Industrial plant simulation and optimization. *Journal of CO_2 Utilization*, 22:33–43.

de la Osa, A. R., de Lucas, A., Romero, A., Valverde, J. L., and Sánchez, P. (2011). Kinetic models discrimination for the high pressure WGS reaction over a commercial CoMo catalyst. *International Journal of Hydrogen Energy*, 36(16):9673–9684.

Diban, N., Urtiaga, A. M., Ortiz, I., Ereña, J., Bilbao, J., and Aguayo, A. T. (2013). Influence of the membrane properties on the catalytic production of dimethyl ether with in situ water removal for the successful capture of CO_2. *Chemical Engineering Journal*, 234:140–148.

Diban, N., Urtiaga, A. M., Ortiz, I., Ereña, J., Bilbao, J., and Aguayo, A. T. (2014). Improved performance of a PBM reactor for simultaneous CO_2 capture and DME synthesis. *Industrial & Engineering Chemistry Research*, 53(50):19479–19487.

Dutta, A., Farooq, S., Karimi, I. A., and Khan, S. A. (2017). Assesing the potential of CO_2 utilization with an integrated framework for producing power and chemicals. *Journal of CO_2 Utilization*, 19:49–57.

Epelde, E., Aguayo, A. T., Olazar, M., Bilbao, J., and Gayubo, A. G. (2014). Kinetic model for the transformation of 1-butene on a K-modified HZSM-5 catalyst. *Industrial & Engineering Chemistry Research*, 53(26):10599–10607.

Ereña, J. (1996). *Conversión de gas de síntesis a gasolina sobre catalizadores bifuncionales. Condiciones de operación y modelado cinético*. PhD thesis, University of the Basque Country, UPV/EHU, Bilbao.

Ereña, J., Garoña, R., Arandes, J. M., Aguayo, A. T., and Bilbao, J. (2005). Effect of operating conditions on the synthesis of dimethyl ether over a CuO-ZnO-Al_2O_3/NaHZSM-5 bifunctional catalyst. *Catalysis Today*, 107:467–473.

Ereña, J., Sierra, I., Aguayo, A. T., Ateka, A., Olazar, M., and Bilbao, J. (2011). Kinetic modelling of dimethyl ether synthesis from (H2 + CO_2) by considering catalyst deactivation. *Chemical Engineering Journal*, 174(2):660–667.

Ereña, J., Sierra, I., Olazar, M., Gayubo, A. G., and Aguayo, A. T. (2008). Deactivation of a $CuO-ZnO-Al_2O_3/\gamma$-Al_2O_3 catalyst in the synthesis of dimethyl ether. *Industrial & Engineering Chemistry Research*, 47(7):2238–2247.

Ereña, J., Vicente, J., Aguayo, A. T., Gayubo, A. G., Olazar, M., and Bilbao, J. (2013a). Effect of combining metallic and acid functions in CZA/HZSM-5 desilicated zeolite catalysts on the DME steam reforming in a fluidized bed. *International Journal of Hydrogen Energy*, 38(24):10019–10028.

Ereña, J., Vicente, J., Aguayo, A. T., Olazar, M., Bilbao, J., and Gayubo, A. G. (2013b). Kinetic behaviour of catalysts with different CuO-ZnO-Al_2O_3 metallic function compositions in DME steam reforming in a fluidized bed. *Applied Catalysis B: Environmental*, 142:315–322.

Espinoza, R., du Toit, E., Santamaria, J., Menendez, M., Coronas, J., and Irusta, S. (1999). Production of hydrocarbons. *PCT patent WO*, 99:64380.

Espinoza, R. L., du Toit, E., Santamaria, J., Menendez, M., Coronas, J., and Irusta, S. (2000). Use of membranes in Fischer-Tropsch reactors. volume 130 of *Studies in Surface Science and Catalysis*, pages 389–394.

Espinoza, R. L., Santamaria, J. M., Menendez, M. A., Coronas, J., and Irusta, S. (2002). Production of hydrocarbons.

Evans, J. W., Wainwright, M. S., Bridgewater, A. J., and Young, D. J. (1983). On the determination of copper surface area by reaction with nitrous oxide. *Applied Catalysis*, 7(1):75–83.

Farsi, M. and Jahanmiri, A. (2011). Enhancement of DME production in an optimized membrane isothermal fixed-bed reactor. *International Journal of Chemical Reactor Engineering*, 9(1).

Farsi, M. and Jahanmiri, A. (2012). Dynamic modeling of a H_2O-permselective membrane reactor to enhance methanol synthesis from syngas considering catalyst deactivation. *Journal of Natural Gas Chemistry*, 21(4):407–414.

Farsi, M. and Jahanmiri, A. (2014). Dynamic modeling and operability analysis of a dual-membrane fixed bed reactor to produce methanol considering catalyst

deactivation. *Journal of Industrial and Engineering Chemistry*, 20(5):2927 – 2933.

Farsi, M., Sani, A. H., and Riasatian, P. (2016). Modeling and operability of DME production from syngas in a dual membrane reactor. *Chemical Engineering Research and Design*, 112:190–198.

Faungnawakij, K., Fukunaga, T., Kikuchi, R., and Eguchi, K. (2008a). Deactivation and regeneration behaviors of copper spinel-alumina composite catalysts in steam reforming of dimethyl ether. *Journal of Catalysis*, 256(1):37–44.

Faungnawakij, K., Shimoda, N., Fukunaga, T., Kikuchi, R., and Eguchi, K. (2008b). Cu-based spinel catalysts CuB_2O_4 (B = Fe, Mn, Cr, Ga, Al, $Fe_{0.75}Mn_{0.25}$) for steam reforming of dimethyl ether. *Applied Catalysis A: General*, 341(1-2):139–145.

Faungnawakij, K., Shimoda, N., Viriya-Empikul, N., Kikuchi, R., and Eguchi, K. (2010). Limiting mechanisms in catalytic steam reforming of dimethyl ether. *Applied Catalysis B: Environmental*, 97(1-2):21–27.

Faungnawakij, K., Tanaka, Y., Shimoda, N., Fukunaga, T., Kikuchi, R., and Eguchi, K. (2007). Hydrogen production from dimethyl ether steam reforming over composite catalysts of copper ferrite spinel and alumina. *Applied Catalysis B: Environmental*, 74(1-2):144–151.

Fedosov, D. A., Smirnov, A. V., Shkirskiy, V. V., Voskoboynikov, T., and Ivanova, I. I. (2015). Methanol dehydration in NaA zeolite membrane reactor. *Journal of Membrane Science*, 486:189–194.

Feng, D., Wang, Y., Wang, D., and Wang, J. (2009). Steam reforming of dimethyl ether over CuO-ZnO-Al_2O_3-ZrO_2 + ZSM-5: A kinetic study. *Chemical Engineering Journal*, 146(3):477–485.

Fierro, J. L. G., Jacono, M. L., Inversi, M., Porta, P., Cioci, F., and Lavecchia, R. (1996). Study of the reducibility of copper in CuO-ZnO catalysts by temperature-programmed reduction. *Applied Catalysis A: General*, 137(2):327–348.

Fleisch, T. H., Basu, A., and Sills, R. A. (2012). Introduction and advancement of a new clean global fuel: The status of DME developments in China and beyond. *Journal of Natural Gas Science and Engineering*, 9:94–107.

Frusteri, F., Bonura, G., Cannilla, C., Ferrante, G. D., Aloise, A., Catizzone, E., Migliori, M., and Giordano, G. (2015). Stepwise tuning of metal-oxide and acid sites of CuZnZr-MFI hybrid catalysts for the direct DME synthesis by CO_2 hydrogenation. *Applied Catalysis B: Environmental*, 176-177:522–531.

Frusteri, F., Migliori, M., Cannilla, C., Frusteri, L., Catizzone, E., Aloise, A., Giordano, G., and Bonura, G. (2017). Direct CO_2-to-DME hydrogenation reaction: New evidences of a superior behaviour of FER-based hybrid systems to obtain high DME yield. *Journal of CO_2 Utilization*, 18:353–361.

Gallucci, F., Paturzo, L., and Basile, A. (2004). An experimental study of CO_2 hydrogenation into methanol involving a zeolite membrane reactor. *Chemical Engineering and Processing: Process Intensification*, 43(8):1029–1036.

Gao, Z., Huang, W., Yin, L., and Xie, K. (2009). Liquid-phase preparation of catalysts used in slurry reactors to synthesize dimethyl ether from syngas: Effect of heat-treatment atmosphere. *Fuel Processing Technology*, 90(12):1442–1446.

García-García, I., Izquierdo, U., Barrio, V. L., Arias, P. L., and Cambra, J. F. (2016). Power-to-Gas: Storing surplus electrical energy. Study of Al_2O_3 support modification. *International Journal of Hydrogen Energy*, 41(43):19587–19594.

García-Trenco, A. and Martínez, A. (2012). Direct synthesis of DME from syngas on hybrid CuZnAl/ZSM-5 catalysts: New insights into the role of zeolite acidity. *Applied Catalysis A: General*, 411:170–179.

García-Trenco, A. and Martínez, A. (2014). The influence of zeolite surface-aluminum species on the deactivation of CuZnAl/zeolite hybrid catalysts for the direct DME synthesis. *Catalysis Today*, 227:144–153.

García-Trenco, A., Vidal-Moya, A., and Martínez, A. (2012). Study of the interaction between components in hybrid CuZnAl/HZSM-5 catalysts and its impact in the syngas-to-DME reaction. *Catalysis Today*, 179(1):43–51.

Gascon, J., Kapteijn, F., Zornoza, B., Sebastian, V., Casado, C., and Coronas, J. (2012). Practical approach to zeolitic membranes and coatings: state of the art, opportunities, barriers, and future perspectives. *Chemistry of Materials*, 24(15):2829–2844.

Gates, B. C. and Johanson, L. N. (1969). The dehydration of methanol and ethanol catalyzed by polystyrene sulfonate resins. *Journal of Catalysis*, 14(1):69–76.

Gayubo, A. G., Aguayo, A. T., del Campo, A. E. S., Benito, P. L., and Bilbao, J. (1999). The role of water on the attenuation of coke deactivation of a SAPO-34 catalyst in the transformation of methanol into olefins. In *Studies in Surface Science and Catalysis*, volume 126, pages 129–136.

Gayubo, A. G., Alonso, A., Valle, B., Aguayo, A. T., and Bilbao, J. (2010). Kinetic model for the transformation of bioethanol into olefins over a HZSM-5 zeolite treated with alkali. *Industrial & Engineering Chemistry Research*, 49(21):10836–10844.

Gayubo, A. G., Alonso, A., Valle, B., Aguayo, A. T., Olazar, M., and Bilbao, J. (2011). Kinetic modelling for the transformation of bioethanol into olefins on a hydrothermally stable Ni–HZSM-5 catalyst considering the deactivation by coke. *Chemical Engineering Journal*, 167(1):262–277.

Gayubo, A. G., Vicente, J., Ereña, J., Oar-Arteta, L., Azkoiti, M. J., Olazar, M., and Bilbao, J. (2014). Causes of deactivation of bifunctional catalysts made up of CuO-ZnO-Al_2O_3 and desilicated HZSM-5 zeolite in DME steam reforming. *Applied Catalysis A: General*, 483:76–84.

Gorbe, J., Lasobras, J., Francés, E., Herguido, J., Menéndez, M., Kumakiri, I., and Kita, H. (2018). Preliminary study on the feasibility of using a zeolite A membrane in a membrane reactor for methanol production. *Separation and Purification Technology*, 200:164–168.

Graaf, G. H., Scholtens, H., Stamhuis, E. J., and Beenackers, A. A. C. M. (1990). Intra-particle diffusion limitations in low-pressure methanol synthesis. *Chemical Engineering Science*, 45(4):773–783.

Graaf, G. H., Stamhuis, E. J., and Beenackers, A. A. C. M. (1988). Kinetics of low-pressure methanol synthesis. *Chemical Engineering Science*, 43(12):3185–3195.

Gu, M. and Cheng, Z. (2015). Carboxylation of aromatics by CO_2 under "Si/Al based frustrated Lewis Pairs" catalytic system. *Journal of Materials Science and Chemical Engineering*, 3(01):103.

Ha, K. S., Lee, Y. J., Bae, J. W., Kim, Y. W., Woo, M. H., Kim, H. S., Park, M. J., and Jun, K. W. (2011). New reaction pathways and kinetic parameter estimation for methanol dehydration over modified ZSM-5 catalysts. *Applied Catalysis A: General*, 395(1-2):95–106.

Hadipour, A. and Sohrabi, M. (2008). Synthesis of some bifunctional catalysts and determination of kinetic parameters for direct conversion of syngas to dimethyl ether. *Chemical Engineering Journal*, 137(2):294–301.

Han, Y., Zhang, H., Ying, W., and Fang, D. (2009). Modeling and simulation of production process on dimethyl ether synthesized from coal-based syngas by one-step method. *Chinese Journal of Chemical Engineering*, 17(1):108–112.

Hočevar, S. and Summers, W. (2008). Hydrogen production. In *Hydrogen Technology*, pages 15–79.

Homs, N., Toyir, J., and de la Piscina, P. R. (2013). Catalytic processes for activation of CO_2. *New and Future Developments in Catalysis: Activation of Carbon Dioxide*, pages 1–23.

Hosseininejad, S., Afacan, A., and Hayes, R. E. (2012). Catalytic and kinetic study of methanol dehydration to dimethyl ether. *Chemical Engineering Research and Design*, 90(6):825–833.

Hou, Z., Chen, P., Fang, H., Zheng, X., and Yashima, T. (2006). Production of synthesis gas via methane reforming with CO_2 on noble metals and small amount of noble-(Rh-) promoted Ni catalysts. *International Journal of Hydrogen Energy*, 31(5):555–561.

Hu, Y., Nie, Z., and Fang, D. (2008). Simulation and model design of pipe-shell reactor for the direct synthesis of dimethyl ether from syngas. *Journal of Natural Gas Chemistry*, 17(2):195–200.

Huang, Z., Jiang, H., F., H., Chen, D., Wei, G., Zhao, K., Zheng, A., Feng, Y., Zhao, Z., and Li, H. (2016). Evaluation of multi-cycle performance of chemical looping dry reforming using CO_2 as an oxidant with Fe–Ni bimetallic oxides. *Journal of Energy Chemistry*, 25(1):62–70.

Ilias, S. and Bhan, A. (2013). Mechanism of the Catalytic Conversion of Methanol to Hydrocarbons. *ACS Catalysis*, 3(1):18–31.

Iliuta, I., Iliuta, M. C., and Larachi, F. (2011). Sorption-enhanced dimethyl ether synthesis—multiscale reactor modeling. *Chemical Engineering Science*, 66(10):2241–2251.

Iliuta, I., Larachi, F., and Fongarland, P. (2010). Dimethyl ether synthesis with in situ H_2O removal in fixed-bed membrane reactor: model and simulations. *Industrial & Engineering Chemistry Research*, 49(15):6870–6877.

Iyer, S. S., Renganathan, T., Pushpavanam, S., Kumar, M. V., and Kaisare, N. (2015). Generalized thermodynamic analysis of methanol synthesis: Effect of feed composition. *Journal of CO_2 Utilization*, 10:95–104.

Jang, J. G., Kim, G. M., Kim, H. J., and Lee, H. K. (2016). Review on recent advances in CO_2 utilization and sequestration technologies in cement-based materials. *Construction and Building Materials*, 127:762–773.

Jhong, M., Ma, S., and Kenis, P. J. (2013). Electrochemical conversion of CO_2 to useful chemicals: current status, remaining challenges, and future opportunities. *Current Opinion in Chemical Engineering*, 2:191–9.

Jia, G., Tan, Y., and Han, Y. (2006). A comparative study on the thermodynamics of dimethyl ether synthesis from CO hydrogenation and CO_2 hydrogenation. *Industrial & Engineering Chemistry Research*, 45(3):1152–1159.

Jun, K. W., Lee, H. S., Roh, H. S., and Park, S. E. (2002). Catalytic dehydration of methanol to dimethyl ether (DME) over solid-acid catalysts. *Bulletin of the Korean Chemical Society*, 23(6):803–806.

Jun, K. W., Shen, W. J., Rao, K. S. R., and Lee, K. W. (1998). Residual sodium effect on the catalytic activity of Cu-ZnO-Al_2O_3 in methanol synthesis from CO_2 hydrogenation. *Applied Catalysis A: General*, 174(1):231–238.

Jutz, F., Grunwaldt, J. D., and Baiker, A. (2009). In situ XAS study of the Mn (III)(salen) Br catalyzed synthesis of cyclic organic carbonates from epoxides and CO_2. *Journal of Molecular Catalysis A: Chemical*, 297(2):63–72.

Kabir, K. B., Hein, K., and Bhattacharya, S. (2013). Process modelling of dimethyl ether production from Victorian brown coal—Integrating coal drying, gasification and synthesis processes. *Computers & Chemical Engineering*, 48:96–104.

Kawabata, T., Matsuoka, H., Shishido, T., Li, D., Tian, Y., Sano, T., and Takehira, K. (2006). Steam reforming of dimethyl ether over ZSM-5 coupled with Cu/ZnO/Al_2O_3 catalyst prepared by homogeneous precipitation. *Applied Catalysis A: General*, 308:82–90.

Kayvani Fard, A., McKay, G., Buekenhoudt, A., Al Sulaiti, H., Motmans, F., Khraisheh, M., and Atieh, M. (2018). Inorganic membranes: Preparation and application for water treatment and desalination. *Materials*, 11(1).

Khadzhiev, S. N., Kolesnichenko, N. V., and Ezhova, N. N. (2008). Manufacturing of lower olefins from natural gas through methanol and its derivatives (review). *Petroleum Chemistry*, 48(5):325–334.

Khoshbin, R. and Haghighi, M. (2013). Direct syngas to DME as a clean fuel: the beneficial use of ultrasound for the preparation of CuO–ZnO–Al_2O_3/HZSM-5 nanocatalyst. *Chemical Engineering Research and Design*, 91(6):1111–1122.

Kim, G. J. and Ahn, W. S. (1991). Direct synthesis and characterization of high-SiO_2-content mordenites. *Zeolites*, 11(7):745–750.

Kim, M. Y., Yoon, S. H., Ryu, B. W., and Lee, C. S. (2008). Combustion and emission characteristics of DME as an alternative fuel for compression ignition engines with a high pressure injection system. *Fuel*, 87(12):2779–2786.

Kim, S. D., Baek, S. C., Lee, Y. J., Jun, K. W., Kim, M. J., and Yoo, I. S. (2006). Effect of γ-alumina content on catalytic performance of modified ZSM-5 for dehydration of crude methanol to dimethyl ether. *Applied Catalysis A: General*, 309(1):139–143.

Kiviranta-Pääkkönen, P. K., Struckmann, L. K., Linnekoski, J. A., and Krause, A. O. I. (1998). Dehydration of the alcohol in the etherification of isoamylenes with methanol and ethanol. *Industrial & Engineering Chemistry Research*, 37(1):18–24.

Kortlever, R., Shen, J., Schouten, K. J. P., Calle-Vallejo, F., and Koper, M. T. M. (2015). Catalysts and reaction pathways for the electrochemical reduction of carbon dioxide. *The Journal of Physical Chemistry Letters*, 6(20):4073–4082.

Kumakiri, I., Sasaki, Y., Shimidzu, W., Hashimoto, K., Kita, H., Yamaguchi, T., and Nakao, S. I. (2018). Micro-structure change of polycrystalline fau zeolite membranes during a hydrothermal synthesis in a dilute solution. *Microporous and Mesoporous Materials*, 272:53 – 60.

Kumar, M. and Srivastava, V. C. (2010). Simulation of a fluidized-bed reactor for dimethyl ether synthesis. *Chemical Engineering & Technology*, 33(12):1967–1978.

Ladera, R. M., Fierro, J. L. G., Ojeda, M., and Rojas, S. (2014). TiO_2-supported heteropoly acids for low-temperature synthesis of dimethyl ether from methanol. *Journal of Catalysis*, 312:195–203.

Lechert, H. and Kacirek, H. (1991). Investigations on the crystallization of X-type zeolites. *Zeolites*, 11(7):720–728.

Lee, S., Oh, S., and Choi, Y. (2009). Performance and emission characteristics of an SI engine operated with DME blended LPG fuel. *Fuel*, 88(6):1009–1015.

Lee, S. B., Cho, W., Park, D. K., and Yoon, E. S. (2006). Simulation of fixed bed reactor for dimethyl ether synthesis. *Korean Journal of Chemical Engineering*, 23(4):522–530.

Leonzio, G. (2018). State of art and perspectives about the production of methanol, dimethyl ether and syngas by carbon dioxide hydrogenation. *Journal of CO_2 Utilization*, 27:326–354.

Li, L., Mao, D., Yu, J., and Guo, X. (2015). Highly selective hydrogenation of CO_2 to methanol over CuO–ZnO–ZrO_2 catalysts prepared by a surfactant-assisted co-precipitation method. *Journal of Power Sources*, 279:394–404.

Li, M. M. J., Zeng, Z., Liao, F., Hong, X., and Tsang, S. C. E. (2016). Enhanced CO_2 hydrogenation to methanol over CuZn nanoalloy in Ga modified Cu/ZnO catalysts. *Journal of Catalysis*, 343:157–167.

Li, Z., Li, J., Dai, M., Liu, Y., Han, D., and Wu, J. (2014a). The effect of preparation method of the Cu–La_2O_3–ZrO_2/γ-Al_2O_3 hybrid catalysts on one-step synthesis of dimethyl ether from syngas. *Fuel*, 121:173–177.

Li, Z., Mo, L., Kathiraser, Y., and Kawi, S. (2014b). Yolk–Satellite–Shell Structured Ni–Yolk@Ni@SiO_2 nanocomposite: Superb catalyst toward methane CO_2 reforming reaction. *ACS Catalysis*, 4(5):1526–1536.

Lim, H. W., Park, M. J., Kang, S. H., Chae, H. J., Bae, J. W., and Jun, K. W. (2009). Modeling of the kinetics for methanol synthesis using Cu/ZnO/Al_2O_3/ZrO_2 catalyst: Influence of carbon dioxide during hydrogenation. *Industrial & Engineering Chemistry Research*, 48(23):10448–10455.

Liu, X. M., Lu, G. Q., Yan, Z. F., and Beltramini, J. (2003). Recent advances in catalysts for methanol synthesis via hydrogenation of CO and CO_2. *Industrial & Engineering Chemistry Research*, 42(25):6518–6530.

Liu, Y., Zhang, Y., Wang, T., and Tsubaki, N. (2007). Efficient conversion of carbon dioxide to methanol using copper catalyst by a new low-temperature hydrogenation process. *Chemistry Letters*, 36(9):1182–1183.

Liu, Y. M., Cao, Y., Yi, N., Feng, W. L., Dai, W. L., Yan, S. R., He, H. Y., and Fan, K. N. (2004). Vanadium oxide supported on mesoporous SBA-15 as highly selective catalysts in the oxidative dehydrogenation of propane. *Journal of Catalysis*, 224(2):417–428.

Liu, Z. W., Wang, C., Fan, W. B., Liu, Z. T., Hao, Q. Q., Long, X., Lu, J., Wang, J. G., Qin, Z. F., and Su, D. S. (2011). $V_2O_5/Ce_{0.6}Zr_{0.4}O_2$-$Al_2O_3$ as an Efficient Catalyst for the Oxidative Dehydrogenation of Ethylbenzene with Carbon Dioxide. *ChemSusChem*, 4(3):341–345.

Lok, B. M., Messina, C. A., Patton, R. L., Gajek, R. T., Cannan, T. R., and Flanigen, E. M. (1984). Silicoaluminophosphate molecular sieves: another new class of microporous crystalline inorganic solids. *Journal of the American Chemical Society*, 106(20):6092–6093.

Lu, W. Z., Teng, L. H., and Xiao, W. D. (2004). Simulation and experiment study of dimethyl ether synthesis from syngas in a fluidized-bed reactor. *Chemical Engineering Science*, 59(22):5455–5464.

Luu, M. T., Milani, D., Sharma, M., Zeaiter, J., and Abbas, A. (2016). Model-based analysis of CO_2 revalorization for dimethyl ether synthesis driven by solar catalytic reforming. *Applied Energy*, 177:863–878.

Ma, D. and Lund, C. R. F. (2003). Assessing high-temperature water-gas shift membrane reactors. *Industrial & engineering chemistry research*, 42(4):711–717.

Malinovskaya, O. A., Rozovskii, A. Y., Zolotarskii, I. A., Lender, Y. V., Lin, G. I., Matros, Y. S., Dubovich, G. V., Popova, N. A., and Savostina, N. V. (1988). Kinetic model of methanol synthesis over a catalyst containing copper. *Kinetics and Catalysis*, 28(4).

Mardanpour, M. M., Sadeghi, R., Ehsani, M. R., and Esfahany, M. N. (2012). Enhancement of dimethyl ether production with application of hydrogen-permselective Pd-based membrane in fluidized bed reactor. *Journal of Industrial and Engineering Chemistry*, 18(3):1157–1165.

Michorczyk, P., Pietrzyk, P., and Ogonowski, J. (2012). Preparation and characterization of SBA-1-supported chromium oxide catalysts for CO_2 assisted dehydrogenation of propane. *Microporous and Mesoporous Materials*, 161:56–66.

Mier, D., Gayubo, A. G., Aguayo, A. T., Olazar, M., and Bilbao, J. (2011). Olefin production by cofeeding methanol and n-butane: Kinetic modeling considering the deactivation of HZSM-5 zeolite. *AIChE Journal*, 57(10):2841–2853.

Migliori, M., Aloise, A., Catizzone, E., and Giordano, G. (2014). Kinetic analysis of methanol to dimethyl ether reaction over H-MFI catalyst. *Industrial & Engineering Chemistry Research*, 53(38):14885–14891.

Mo, L., Leong, K. K. M., and Kawi, S. (2014). A highly dispersed and anti-coking Ni–La_2O_3/SiO_2 catalyst for syngas production from dry carbon dioxide reforming of methane. *Catalysis Science & Technology*, 4:2107–2114.

Mochalin, V. P., Lin, G. I., and Rozovsky, A. Y. (1984). Kinetic-model of the process of methanol synthesis on the Snm-1 catalyst. *Khimicheskaya Promyshlennost*, (1):11–13.

Moradi, G. R., Ahmadpour, J., and Yaripour, F. (2008). Intrinsic kinetics study of LPDME process from syngas over bi-functional catalyst. *Chemical Engineering Journal*, 144(1):88–95.

Moradi, G. R., Ahmadpour, J., Yaripour, F., and Wang, J. (2011). Equilibrium calculations for direct synthesis of dimethyl ether from syngas. *The Canadian Journal of Chemical Engineering*, 89(1):108–115.

Moradi, G. R., Nosrati, S., and Yaripor, F. (2007). Effect of the hybrid catalysts preparation method upon direct synthesis of dimethyl ether from synthesis gas. *Catalysis Communications*, 8(3):598–606.

Naik, S., Goud, V., Rout, P., and Dalai, A. (2010). Production of first and second generation biofuels: a comprehensive review. *Renewable and Sustainable Energy Reviews*, 14(2):578–597.

Natta, G. (1955). Synthesis of methanol. *Catalysis*, 3:349–411.

Ng, K. L., Chadwick, D., and Toseland, B. A. (1999). Kinetics and modelling of dimethyl ether synthesis from synthesis gas. *Chemical Engineering Science*, 54(15):3587–3592.

Nie, R., Lei, H., Pan, S., Wang, L., Fei, J., and Hou, Z. (2012). Core–shell structured CuO–ZnO@H-ZSM-5 catalysts for CO hydrogenation to dimethyl ether. *Fuel*, 96:419–425.

Oar-Arteta, L., Aguayo, A. T., Remiro, A., Bilbao, J., and Gayubo, A. G. (2015a). Behavior of a $CuFe_2O_4/\gamma$-Al_2O_3 catalyst for the steam reforming of dimethyl ether in reaction-regeneration cycles. *Industrial & Engineering Chemistry Research*, 54(45):11285–11294.

Oar-Arteta, L., Remiro, A., Aguayo, A. T., Bilbao, J., and Gayubo, A. G. (2015b). Effect of operating conditions on dimethyl ether steam reforming over a $CuFe_2O_4/\gamma$-Al_2O_3 bifunctional catalyst. *Industrial & Engineering Chemistry Research*, 54(40):9722–9732.

Oar-Arteta, L., Remiro, A., Epron, F., Bion, N., Aguayo, A. T., Bilbao, J., and Gayubo, A. G. (2016). Comparison of noble metal-and copper-based catalysts for the step of methanol steam reforming in the dimethyl ether steam reforming process. *Industrial & Engineering Chemistry Research*, 55(12):3546–3555.

Oar-Arteta, L., Remiro, A., Vicente, J., Aguayo, A. T., Bilbao, J., and Gayubo, A. G. (2014). Stability of $CuZnOAl_2O_3$/HZSM-5 and $CuFe_2O_4$/HZSM-5 catalysts in dimethyl ether steam reforming operating in reaction-regeneration cycles. *Fuel Processing Technology*, 126:145–154.

Ohno, Y., Yagi, H., Inoue, N., Okuyama, K., and Aoki, S. (2007). Slurry phase DME direct synthesis technology - 100 tons/day demonstration plant operation and scale up study. *Surface Science and Catalysis*, 167:403–408.

Olah, G. A. (2005). Beyond oil and gas: the methanol economy. *Angewandte Chemie International Edition*, 44(18):2636–2639.

Olah, G. A., Goeppert, A., and Prakash, G. K. S. (2009). Chemical recycling of carbon dioxide to methanol and dimethyl Ether: From greenhouse gas to

renewable, environmentally carbon neutral fuels and synthetic hydrocarbons. *The Journal of Organic Chemistry*, 74(2):487–498.

Ovesen, C. V., Clausen, B. S., Hammershøi, B. S., Steffensen, G., Askgaard, T., Chorkendorff, I., Nørskov, J. K., Rasmussen, P. B., Stoltze, P., and Taylor, P. (1996). A microkinetic analysis of the water–gas shift reaction under industrial conditions. *Journal of Catalysis*, 158(1):170–180.

Oyola-Rivera, O., Baltanás, M., and Cardona-Martínez, N. (2015). CO_2 hydrogenation to methanol and dimethyl ether by Pd–Pd_2Ga catalysts supported over Ga_2O_3 polymorphs. *Journal of CO_2 Utilization*, 9:8–15.

Parkash, S. (2010). Petroleum Fuels Manufacturing Handbook. *McGraw Hill*.

Peng, X. D., Wang, A. W., Toseland, B. A., and Tijm, P. J. A. (1999). Single-step syngas-to-dimethyl ether processes for optimal productivity, minimal emissions, and natural gas-derived syngas. *Industrial & Engineering Chemistry Research*, 38(11):4381–4388.

Pérez-Uriarte, P., Ateka, A., Aguayo, A. T., and Bilbao, J. (2016a). Comparison of HZSM-5 zeolite and SAPO (-18 and-34) based catalysts for the production of light olefins from DME. *Catalysis Letters*, 146(10):1892–1902.

Pérez-Uriarte, P., Ateka, A., Aguayo, A. T., Gayubo, A. G., and Bilbao, J. (2016b). Kinetic model for the reaction of DME to olefins over a HZSM-5 zeolite catalyst. *Chemical Engineering Journal*, 302:801–810.

Pérez-Uriarte, P., Ateka, A., Gamero, M., Aguayo, A. T., and Bilbao, J. (2016c). Effect of the operating conditions in the transformation of DME to olefins over a HZSM-5 zeolite catalyst. *Industrial & Engineering Chemistry Research*, 55(23):6569–6578.

Pérez-Uriarte, P., Gamero, M., Ateka, A., Díaz, M., Aguayo, A. T., and Bilbao, J. (2016d). Effect of the acidity of HZSM-5 zeolite and the binder in the DME transformation to olefins. *Industrial & Engineering Chemistry Research*, 55(6):1513–1521.

Phienluphon, R., Pinkaew, K., Yang, G., Li, J., Wei, Q., Yoneyama, Y., Vitidsant, T., and Tsubaki, N. (2015a). Designing core ($Cu/ZnO/Al_2O_3$)-shell (SAPO-11) zeolite capsule catalyst with a facile physical way for dimethyl ether direct synthesis from syngas. *Chemical Engineering Journal*, 270:605–611.

Phienluphon, R., Pinkaew, K., Yang, G., Li, J., Wei, Q., Yoneyama, Y., Vitidsant, T., and Tsubaki, N. (2015b). Designing core ($Cu/ZnO/Al_2O_3$)–shell (SAPO-11) zeolite capsule catalyst with a facile physical way for dimethyl ether direct synthesis from syngas. *Chemical Engineering Journal*, 270:605–611.

Pinkaew, K., Yang, G., Vitidsant, T., Jin, Y., Zeng, C., Yoneyama, Y., and Tsubaki, N. (2013). A new core–shell-like capsule catalyst with SAPO-46 zeolite shell encapsulated Cr/ZnO for the controlled tandem synthesis of dimethyl ether from syngas. *Fuel*, 111:727–732.

Pontzen, F., Liebner, W., Gronemann, V., Rothaemel, M., and Ahlers, B. (2011). CO_2-based methanol and DME-Efficient technologies for industrial scale production. *Catalysis Today*, 171(1):242–250.

Qin, Z. Z., Zhou, X. H., Su, T. M., Jiang, Y. X., and Ji, H. B. (2016). Hydrogenation of CO_2 to dimethyl ether on La-, Ce-modified Cu-Fe/HZSM-5 catalysts. *Catalysis Communications*, 75:78–82.

Rafiee, A., Khalilpour, K. R., Milani, D., and Panahi, M. (2018). Trends in CO_2 conversion and utilization: A review from process systems perspective. *Journal of Environmental Chemical Engineering*.

Rahimpour, M. R. and Dehghani, Z. (2016). Membrane reactors for methanol synthesis from forest-derived feedstocks. In *Membrane Technologies for Biorefining*, pages 383–410. Elsevier.

Rahimpour, M. R. and Ghader, S. (2003). Theoretical investigation of a Pd-membrane reactor for methanol synthesis. *Chemical Engineering & Technology*, 26(8):902–907.

Ravaghi-Ardebili, Z. and Manenti, F. (2015). Unified modeling and feasibility study of novel green pathway of biomass to methanol/dimethylether. *Applied Energy*, 145:278–294.

Reddy, G. K., Boolchand, P., and Smirniotis, P. G. (2012). Unexpected Behavior of Copper in Modified Ferrites during High Temperature WGS Reaction Aspects of Fe^{3+} Fe^{2+} Redox Chemistry from Mössbuaer and XPS Studies. *The Journal of Physical Chemistry C*, 116(20):11019–11031.

Reddy, G. K. and Smirniotis, P. G. (2015). Mechanism and kinetics of the WGS reaction. *Water Gas Shift Reaction, Elsevier, Amsterdam*, pages 225–261.

Restrepo, G., Weckert, M., Brüggemann, R., Gerstmann, S., and Frank, H. (2008). Ranking of refrigerants. *Environmental Science & Technology*, 42(8):2925–2930.

Rezaei, M., Alavi, S. M., Sahebdelfar, S., and Yan, Z. F. (2006). Syngas Production by Methane Reforming with Carbon Dioxide on Noble Metal Catalysts. *Journal of Natural Gas Chemistry*, 15(4):327–334.

Rhodes, C., Hutchings, G. J., and Ward, A. M. (1995). Water-gas shift reaction: finding the mechanistic boundary. *Catalysis Today*, 23(1):43–58.

Rohde, M. P., Schaub, G., Khajavi, S., Jansen, J. C., and Kapteijn, F. (2008). Fischer–Tropsch synthesis with in situ H_2O removal – Directions of membrane development. *Microporous and Mesoporous Materials*, 115(1):123 – 136.

Rohde, M. P., Unruh, D., and Schaub, G. (2005). Membrane application in Fischer−Tropsch synthesis to enhance CO_2 Hydrogenation. *Industrial & Engineering Chemistry Research*, 44(25):9653–9658.

Rostrup-Nielsen, J. R. (1994). Aspects of CO_2-reforming of methane. In *Studies In Surface Science and Catalysis*, volume 81, pages 25–41.

Sadrameli, S. M. (2015). Thermal/catalytic cracking of hydrocarbons for the production of olefins: A state-of-the-art review I: Thermal cracking review. *Fuel*, 140:102 – 115.

Saito, M. and Murata, K. (2004). Development of high performance Cu/ZnO-based catalysts for methanol synthesis and the water-gas shift reaction. *Catalysis Surveys from Asia*, 8(4):285–294.

Salomón, M. A., Coronas, J., Menéndez, M., and Santamaría, J. (2000). Synthesis of MTBE in zeolite membrane reactors. *Applied Catalysis A: General*, 200(1-2):201–210.

Sánchez-Contador, M. (2017). *Diseño y comportamiento de un catalizador core-shell en la síntesis directa de dimetil éter con valorización de CO_2*. PhD thesis, University of the Basque Country, UPV/EHU, Bilbao.

Sánchez-Contador, M., Ateka, A., Aguayo, A. T., and Bilbao, J. (2018a). Behavior of SAPO-11 as acid function in the direct synthesis of dimethyl ether from syngas and CO_2. *Journal of Industrial and Engineering Chemistry*, 63:245–254.

Sánchez-Contador, M., Ateka, A., Aguayo, A. T., and Bilbao, J. (2018b). Direct synthesis of dimethyl ether from CO and CO_2 over a core-shell structured CuO-ZnO-ZrO_2@SAPO-11 catalyst. *Fuel Processing Technology*, 179:258–268.

Sánchez-Contador, M., Ateka, A., Ibáñez, M., Bilbao, J., and Aguayo, A. T. (2019). Influence of the operating conditions on the behavior and deactivation of a CuOZnOZrO_2@SAPO-11 core-shell-like catalyst in the direct synthesis of DME. *Renewable Energy*, 138:585–597.

Sánchez-Contador, M., Ateka, A., Rodriguez-Vega, P., Bilbao, J., and Aguayo, A. T. (2018c). Optimization of the Zr content in the CuO-ZnO-ZrO_2/SAPO-11 catalyst for the selective hydrogenation of CO + CO_2 mixtures in the direct synthesis of dimethyl ether. *Industrial & Engineering Chemistry Research*, 57(4):1169–1178.

Saravanan, K., Ham, H., Tsubaki, N., and Bae, J. W. (2017). Recent progress for direct synthesis of dimethyl ether from syngas on the heterogeneous bifunctional hybrid catalysts. *Applied Catalysis B: Environmental*, 217:494–522.

Schemme, S., Breuer, J. L., Samsun, R. C., Peters, R., and Stolten, D. (2018). Promising catalytic synthesis pathways towards higher alcohols as suitable transport fuels based on H_2 and CO_2. *Journal of CO_2 Utilization*, 27:223–237.

Schmitz, G. (1978). Déshydratation du methanol sur silice-alumine. *Journal de Chimie Physique*, 75:650–655.

Sciarra, J. J. and Sciarra, C. J. (2001). Aerosols. *Kirk-Othmer Encyclopedia of Chemical Technology. American Cancer Society*.

Sea, B. and Lee, K. H. (2006). Synthesis of dimethyl ether from methanol using alumina–silica membrane reactor. *Desalination*, 200(1):689 – 691.

Semelsberger, T. A., Borup, R. L., and Greene, H. L. (2006). Dimethyl ether (DME) as an alternative fuel. *Journal of Power Sources*, 156(2):497–511.

Shimoda, N., Muroyama, H., Matsui, T., Faungnawakij, K., Kikuchi, R., and Eguchi, K. (2011). Dimethyl ether steam reforming under daily start-up and shut-down (DSS)-like operation over $CuFe_2O_4$ spinel and alumina composite catalysts. *Applied Catalysis A: General*, 409:91–98.

Sierra, I., Ereña, J., Aguayo, A. T., Arandes, J. M., and Bilbao, J. (2010). Regeneration of CuO-ZnO-Al_2O_3/γ-Al_2O_3 catalyst in the direct synthesis of dimethyl ether (DME). *Applied Catalysis B: Environmental*, 94(1):108–116.

Sierra, I., Ereña, J., Aguayo, A. T., Ateka, A., and Bilbao, J. (2013). Kinetic modelling for the dehydration of methanol to dimethyl ether over γ-Al_2O_3. *Chemical Engineering*, 32.

Sierra, I., Ereña, J., Aguayo, A. T., Olazar, M., and Bilbao, J. (2009). Deactivation kinetics for direct dimethyl ether synthesis on a CuO-ZnO-Al_2O_3/γ-Al_2O_3 catalyst. *Industrial & Engineering Chemistry Research*, 49(2):481–489.

Sierra, I., Ereña, J., Ateka, A., Aguayo, A. T., Arandes, J. M., and Bilbao, J. (2012). Inhibiting effect of water on the deactivation of the metallic function in the syngas to dimethyl ether process. *CHISA 2012 - 20th International Congress of Chemical and Process Engineering and PRES 2012 - 15th Conference PRES*.

Sierra, I., Ereña, J., Aguayo, A. T., Arandes, J. M., Olazar, M., and Bilbao, J. (2011). Co-feeding water to attenuate deactivation of the catalyst metallic function (CuO–ZnO–Al_2O_3) by coke in the direct synthesis of dimethyl ether. *Applied Catalysis B: Environmental*, 106(1-2):167–173.

Sierra Gallego, G., Mondragón, F., Tatibouët, J. M., Barrault, J., and Batiot-Dupeyrat, C. (2008). Carbon dioxide reforming of methane over La_2NiO_4 as

catalyst precursor - Characterization of carbon deposition. *Catalysis Today*, 133-135:200–209.

Silva, V. M. T. M., Pereira, C. S. M., and Rodrigues, A. E. (2011). PermSMBR—A new hybrid technology: Application on green solvent and biofuel production. *AIChE Journal*, 57(7):1840–1851.

Skeel, R. D. and Berzins, M. (1990). A method for the spatial discretization of parabolic equations in one space variable. *SIAM journal on scientific and statistical computing*, 11(1):1–32.

Song, C., Liu, Q., Deng, S., Li, H., and Kitamura, Y. (2019). Cryogenic-based CO_2 capture technologies: State-of-the-art developments and current challenges. *Renewable and Sustainable Energy Reviews*, 101:265–278.

Song, C., Liu, Q., Ji, N., Deng, S., Zhao, J., Li, Y., Song, Y., and Li, H. (2018). Alternative pathways for efficient CO_2 capture by hybrid processes—A review. *Renewable and Sustainable Energy Reviews*, 82:215–231.

Song, C. and Pan, W. (2004). Tri-reforming of methane: A novel concept for catalytic production of industrially useful synthesis gas with desired H_2/CO ratios. *Catalysis Today*, 98(4):463–484.

Song, R., Li, K., Feng, Y., and Liu, S. (2009). Performance and emission characteristics of DME engine with high ratio of EGR. *Energy & Fuels*, 23(11):5460–5466.

Spivey, J. J. (1991). Dehydration catalysts for the methanol/dimethyl ether reaction. *Chemical Engineering Communications*, 110(1):123–142.

Struis, R. P. W. J. and Stucki, S. (2001). Verification of the membrane reactor concept for the methanol synthesis. *Applied Catalysis A: General*, 216(1):117–129.

Styring, P. and Armstrong, K. (2011). Catalytic carbon dioxide conversions to value-added chemicals. *Chimica Oggi-Chemistry Today*, 29:34–37.

Sun, J., Yang, G., Yoneyama, Y., and Tsubaki, N. (2014a). Catalysis Chemistry of dimethyl ether synthesis. *ACS Catalysis*, 4(10):3346–3356.

Sun, K., Lu, W., Wang, M., and Xu, X. (2004). Low-temperature synthesis of DME from CO_2/H_2 over Pd-modified CuO–ZnO–Al_2O_3–ZrO_2/HZSM-5 catalysts. *Catalysis Communications*, 5(7):367–370.

Sun, X., Mueller, S., Liu, Y., Shi, H., Haller, G. L., Sanchez-Sanchez, M., van Veen, A. C., and Lercher, J. A. (2014b). On reaction pathways in the conversion of methanol to hydrocarbons on HZSM-5. *Journal of Catalysis*, 317:185–197.

Sutthiumporn, K., Maneerung, T., Kathiraser, Y., and Kawi, S. (2012). CO_2 dry-reforming of methane over $La_{0.8}Sr_{0.2}Ni_{0.8}M_{0.2}O_3$ perovskite (M = Bi, Co, Cr, Cu, Fe): Roles of lattice oxygen on C–H activation and carbon suppression. *International Journal of Hydrogen Energy*, 37(15):11195–11207.

Thompson, R. W. and Huber, M. J. (1982). Analysis of the growth of molecular sieve zeolite NaA in a batch precipitation system. *Journal of Crystal Growth*, 56(3):711–722.

Tian, P., Wei, Y., Ye, M., and Liu, Z. (2015). Methanol to olefins (MTO): From fundamentals to commercialization. *ACS Catalysis*, 5(3):1922–1938.

Tian, Y., Demirel, S. E., Hasan, M. M. F., and Pistikopoulos, E. N. (2018). An overview of process systems engineering approaches for process intensification: state of the art. *Chemical Engineering and Processing-Process Intensification*.

Toch, K., Thybaut, J. W., and Marin, G. B. (2015). A systematic methodology for kinetic modeling of chemical reactions applied to n-hexane hydroisomerization. *AIChE Journal*, 61(3):880–892.

Toyir, J., de la Piscina, P. R., and Homs, N. (2015). Ga-promoted copper-based catalysts highly selective for methanol steam reforming to hydrogen; relation with the hydrogenation of CO_2 to methanol. *International Journal of Hydrogen Energy*, 40(34):11261–11266.

Trippe, F., Fröhling, M., Schultmann, F., Stahl, R., Henrich, E., and Dalai, A. (2013). Comprehensive techno-economic assessment of dimethyl ether (DME) synthesis and Fischer–Tropsch synthesis as alternative process steps within biomass-to-liquid production. *Fuel Processing Technology*, 106:577–586.

Uner, D. and Oymak, M. M. (2012). On the mechanism of photocatalytic CO_2 reduction with water in the gas phase. *Catalysis Today*, 181(1):82–88.

van Bennekom, J. G., Winkelman, J. G. M., Venderbosch, R. H., Nieland, S. D. G. B., and Heeres, H. J. (2012). Modeling and experimental studies on phase and chemical equilibria in high-pressure methanol synthesis. *Industrial and Engineering Chemistry Research*, 51(38):12233–12243.

van den Bussche, K. M. and Froment, G. F. (1996). A steady-state kinetic model for methanol synthesis and the water gas shift reaction on a commercial $Cu/ZnO/Al_2O_3$ catalyst. *Journal of Catalysis*, 161(1):1 – 10.

Vicente, J., Gayubo, A. G., Ereña, J., Aguayo, A. T., Olazar, M., and Bilbao, J. (2013). Improving the DME steam reforming catalyst by alkaline treatment of the HZSM-5 zeolite. *Applied Catalysis B: Environmental*, 130:73–83.

von der Assen, N., Sternberg, A., Kätelhön, A., and Bardow, A. (2015). Environmental potential of carbon dioxide utilization in the polyurethane supply chain. *Faraday Discussions*, 183:291–307.

Wang, C., Xu, J., Qi, G., Gong, Y., Wang, W., Gao, P., Wang, Q., Feng, N., Liu, X., and Deng, F. (2015a). Methylbenzene hydrocarbon pool in methanol-to-olefins conversion over zeolite H-ZSM-5. *Journal of Catalysis*, 332:127–137.

Wang, N., Liu, Y., Huang, A., and Caro, J. (2015b). Hydrophilic SOD and LTA membranes for membrane-supported methanol, dimethyl ether and dimethyl carbonate synthesis. *Microporous and Mesoporous Materials*, 207:33–38.

Wang, W., Wang, S., Ma, X., and Gong, J. (2011). Recent advances in catalytic hydrogenation of carbon dioxide. *Chemical Society Reviews*, 40:3703–3727.

Wang, W. L., Wang, Y., Chen, Y. X., Zhao, W. C., and Li, R. F. (2013a). Preparation of core-shell catalysts for one-step synthesis of dimethyl ether from syngas. *Journal of Fuel Chemistry and Technology*, 8:019.

Wang, X., Pan, X., Lin, R., Kou, S., Zou, W., and Ma, J. X. (2010). Steam reforming of dimethyl ether over Cu-Ni/γ-Al_2O_3 bifunctional catalyst prepared

by deposition–precipitation method. *International Journal of Hydrogen Energy*, 35(9):4060–4068.

Wang, Y., Wang, W., Chen, Y., Ma, J., and Li, R. (2014). Synthesis of dimethyl ether from syngas over core-shell structure catalyst CuO-ZnO-Al_2O_3@SiO_2-Al_2O_3. *Chemical Engineering Journal*, 250:248–256.

Wang, Y., Wang, W., Chen, Y., Ma, J., Zheng, J., and Li, R. (2013b). Core-shell catalyst CuO-ZnO-Al_2O_3@Al_2O_3 for dimethyl ether synthesis from syngas. *Chemistry Letters*, 42(4):335–337.

Wender, I. (1996). Reactions of synthesis gas. *Fuel Processing Technology*, 48(3):189–297. Reactions of synthesis gas.

Yang, G., Thongkam, M., Vitidsant, T., Yoneyama, Y., Tan, Y., and Tsubaki, N. (2011). A double-shell capsule catalyst with core-shell-like structure for one-step exactly controlled synthesis of dimethyl ether from CO_2 containing syngas. *Catalysis today*, 171(1):229–235.

Yang, Y., Mims, C. A., Mei, D. H., Peden, C. H. F., and Campbell, C. T. (2013). Mechanistic studies of methanol synthesis over Cu from CO/CO_2/H_2/H_2O mixtures: The source of C in methanol and the role of water. *Journal of Catalysis*, 298:10 – 17.

Yaripour, F., Shariatinia, Z., Sahebdelfar, S., and Irandoukht, A. (2015). The effects of synthesis operation conditions on the properties of modified γ-alumina nanocatalysts in methanol dehydration to dimethyl ether using factorial experimental design. *Fuel*, 139:40–50.

Yoo, K. S., Kim, J. H., Park, M. J., Kim, S. J., Joo, O. S., and Jung, K. D. (2007). Influence of solid acid catalyst on DME production directly from synthesis gas over the admixed catalyst of Cu/ZnO/Al_2O_3 and various SAPO catalysts. *Applied Catalysis A: General*, 330:57–62.

Yoshihiro, S., Takamasa, S., Na-oki, I., and Toshimitsu, S. (2000). Dehydrogenation of ethylbenzene with an activated carbon-supported vanadium catalyst. *Applied Catalysis A: General*, 192(2):281–288.

Yu, B., Diao, Z. F., Guo, C. X., and He, L. N. (2013). Carboxylation of olefins/alkynes with CO_2 to industrially relevant acrylic acid derivatives. *Journal of CO_2 Utilization*, 1:60–68.

Zhang, C., W., J. K., Gao, R., Kwak, G., and Park, H. G. (2017). Carbon dioxide utilization in a gas-to-methanol process combined with CO_2/steam-mixed reforming: Techno-economic analysis. *Fuel*, 190:303–311.

Zhang, M. H., Liu, Z. M., Lin, G. D., and Zhang, H. B. (2013). Pd/CNT-promoted $CuZrO_2$/HZSM-5 hybrid catalysts for direct synthesis of DME from CO_2/H_2. *Applied Catalysis A: General*, 451:28–35.

Zhang, S., Chen, S. L., Dong, P., Yuan, G., and Xu, K. (2007). Characterization and hydroisomerization performance of sapo-11 molecular sieves synthesized in different media. *Applied Catalysis A: General*, 332(1):46 – 55.

Zhang, Y., Li, D., Zhang, Y., Cao, Y., Zhang, S., Wang, K., Ding, F., and Wu, J. (2014). V-modified CuO–ZnO–ZrO_2/HZSM-5 catalyst for efficient direct synthesis of DME from CO_2 hydrogenation. *Catalysis Communications*, 55:49–52.

Zheng, B., Hua, W., Yue, Y., and Gao, Z. (2005). Dehydrogenation of propane to propene over different polymorphs of gallium oxide. *Journal of Catalysis*, 232(1):143–151.

Zhou, C., Wang, N., Qian, Y., Liu, X., Caro, J., and Huang, A. (2016a). Efficient synthesis of dimethyl ether from methanol in a bifunctional zeolite membrane reactor. *Angewandte Chemie International Edition*, 55(41):12678–12682.

Zhou, X., Su, T., Jiang, Y., Qin, Z., Ji, H., and Guo, Z. (2016b). CuO-Fe_2O_3-CeO_2/HZSM-5 bifunctional catalyst hydrogenated CO_2 for enhanced dimethyl ether synthesis. *Chemical Engineering Science*, 153:10–20.

Zhu, X. M., Schön, M., Bartmann, U., van Veen, A. C., and Muhler, M. (2004). The dehydrogenation of ethylbenzene to styrene over a potassium-promoted iron oxide-based catalyst: a transient kinetic study. *Applied Catalysis A: General*, 266(1):99–108.